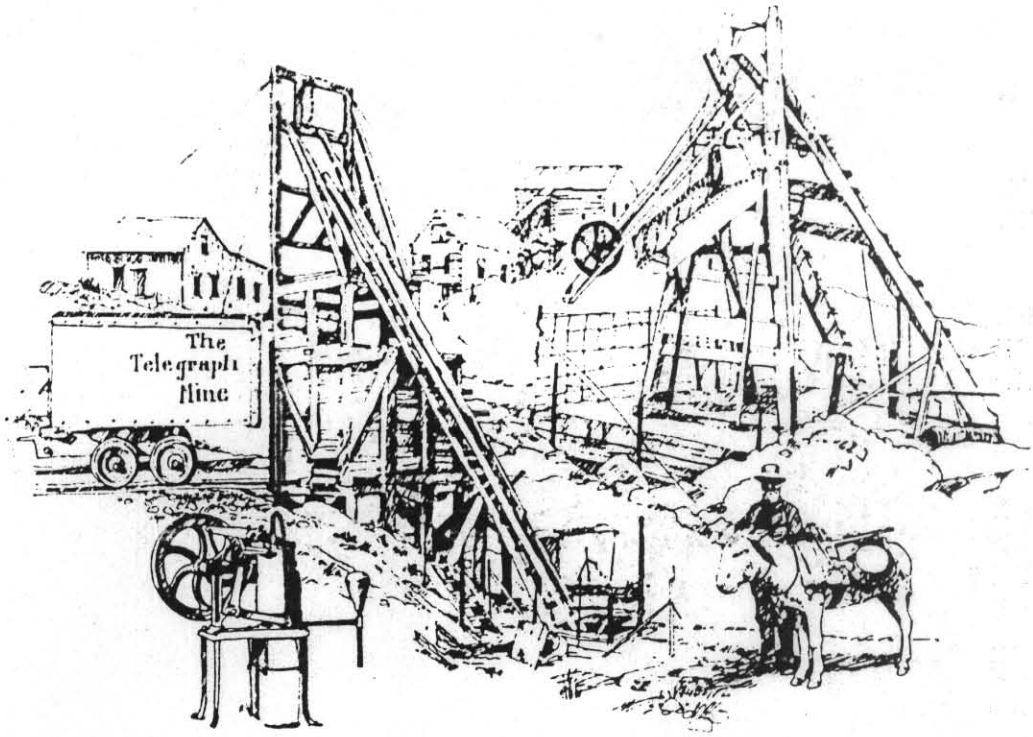

A STUDY OF THE

GEOLOGY, AGE, PRECIOUS METAL DISTRIBUTION OF THE TELEGRAPH MINE HYDROTHERMAL BRECCIA SYSTEM.

BY
PETER LANGE

1984-1987

CASCADE
ENERGY & METALS
CORPORATION

Table Of Contents

VIII FORMATION MODEL OF THE TELEGRAPH SYSTEM

List of Tables

List of Figures

List of Plates

I
INTRODUCTION

Purpose

This study describes the geology, age, precious-metal distribution and physicochemical characteristics of the Telegraph Mine tectono-hydrothermal breccia system.

Methods of Investigation

The field work for this report commenced in April 1984 and continued through January of 1985. 50 samples of wall rock alteration and vein mineralization samples were taken and studied. District mapping on aerial photographs and on 1:2400 scale topographic maps, including detailed surface and underground mapping at 1:240 scale along the Telegraph and Gold Dike trends was completed. In addition a total of 55 VLF-EM survey lines were surveyed and plotted.

Over 500 rock-chip geochemistry samples were cut throughout the area. Of 290 geochemistry samples, 184 separate analyses for Au, Ag, Hg, As, Cu were performed. Thirty six samples were selected for wall rock alteration clay analysis by X-ray diffraction. Due to the highly variable fragment size and distribution characteristics of the Telegraph breccias, sixty five select breccia-vein segment samples were slabbed,

stained and examined. Thirty of these samples were chosen for breccia fragment-rock flour-hydrothermal mineral volume analysis using the grid-controlled, binocular microscope methods of Hutchinson (1974). Finer details of hydrothermal mineralogy were determined by standard petrographic techniques on ninety two thin sections. Modal analyses of intrusive rocks utilized standard point counting techniques on thirty two thin sections (a total 200-400 points counted per section). Seventeen doubly polished plates were prepared from a total of ninety thin sections of vein rocks for fluid inclusion work.

Nearly complete oxidization of ore samples precluded detailed ore-petrographic analysis of most breccia-vein rocks. Polished grain-mounts of sample 968 (Fig. 45) were analyzed by microprobe to detect the presence exsolved gold or silver in pyrite. Samples 968 and 1056 were disaggregated and manually sorted, and discrete mineral-stage separates were analyzed. Sample 922, a quartz-carbonate vein, was disaggregated and acid-treated; the residual was analyzed geochemically and by X-ray diffraction. Adularia separates for age dating were drilled-out of sample 971.

Drill chips representing two-foot segments from nineteen Cascade shallow drill holes cut along the Telegraph fissure were logged to provide a database for the distribution analysis. Surface and drill hole location, alteration, mineralization and assay data were encoded into LOTUS 1-2-3 micro-computer files; the results are listed in Appendices C,D,E and F.

GEOGRAPHY

The Telegraph Mine area is located 24 km east of Baker, California, in the eastern Mojave desert (Fig. 1). It is readily accessible by dirt roads from the Halloran Summit or Halloran Springs exits from Interstate 15. The area encompasses 5.3 km^2 of low-relief high desert pediment terrain of the East Halloran Springs Mining District (unorganized). The Southern Halloran Hills block is a deeply eroded Mesozoic intrusive dome complex bounded to the north by basalt-capped plateaus of the Halloran Hills and bounded to the southeast by Cima Dome and the Cima Volcanic Field (Fig. 2).

Very low annual rainfall and poorly developed "C" horizon soils support sparse typical high desert flora and joshua, yucca, mesquite and sage brush. Although vegetative cover is low, good bedrock exposures in many areas are poor due to low relief (130m maximum) and extensive sheet-wash alluvial cover. The summit of the local dome complex is located 2 km east of the area, and drainage systems extend east towards the Ivanpah valley, and west to Baker.

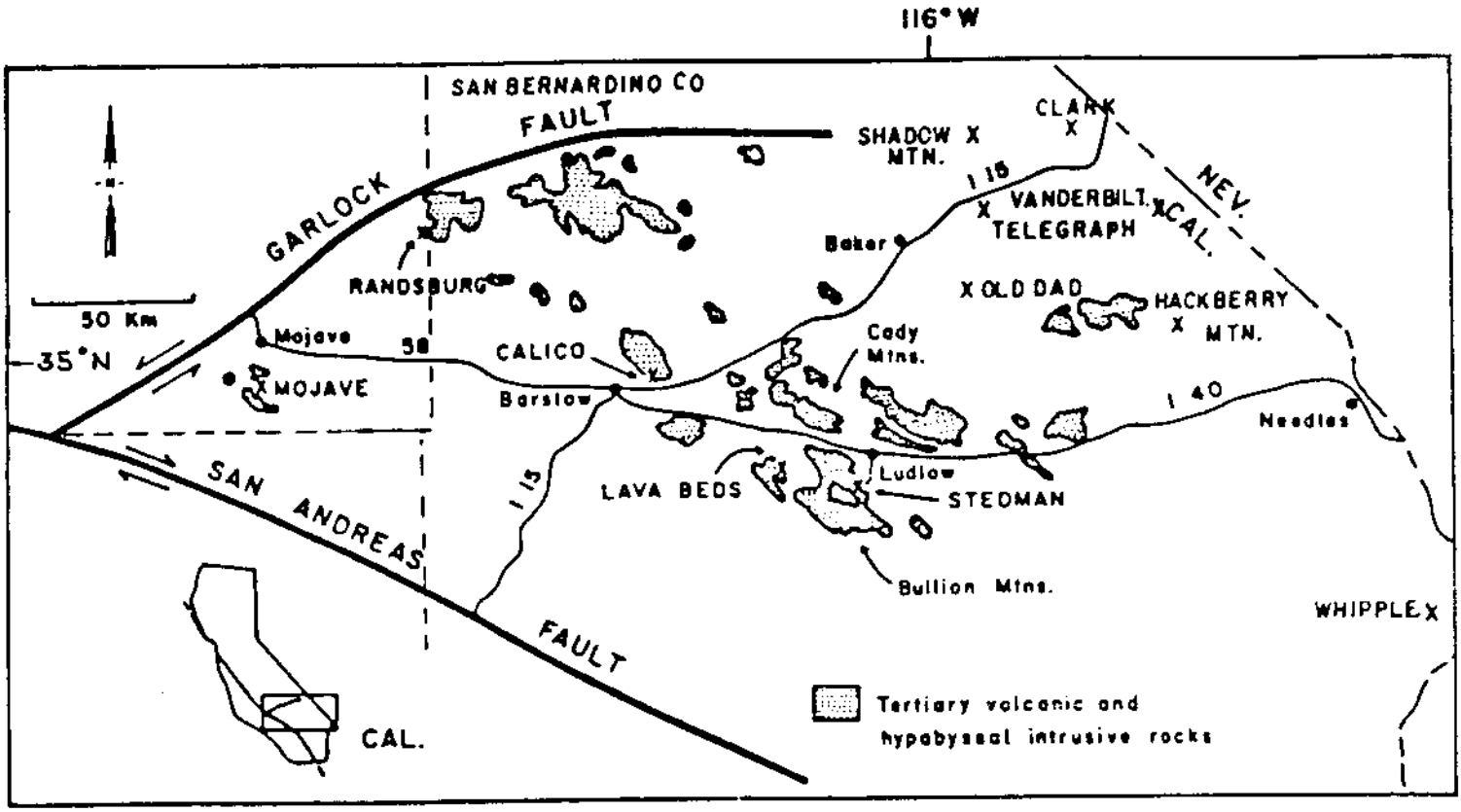

Figure 1. Location map of the Mojave Desert region. The distribution of Tertiary volcanic and hypabyssal intrusive rocks and selected gold deposits are shown (Modified from Polovina, 1984.)

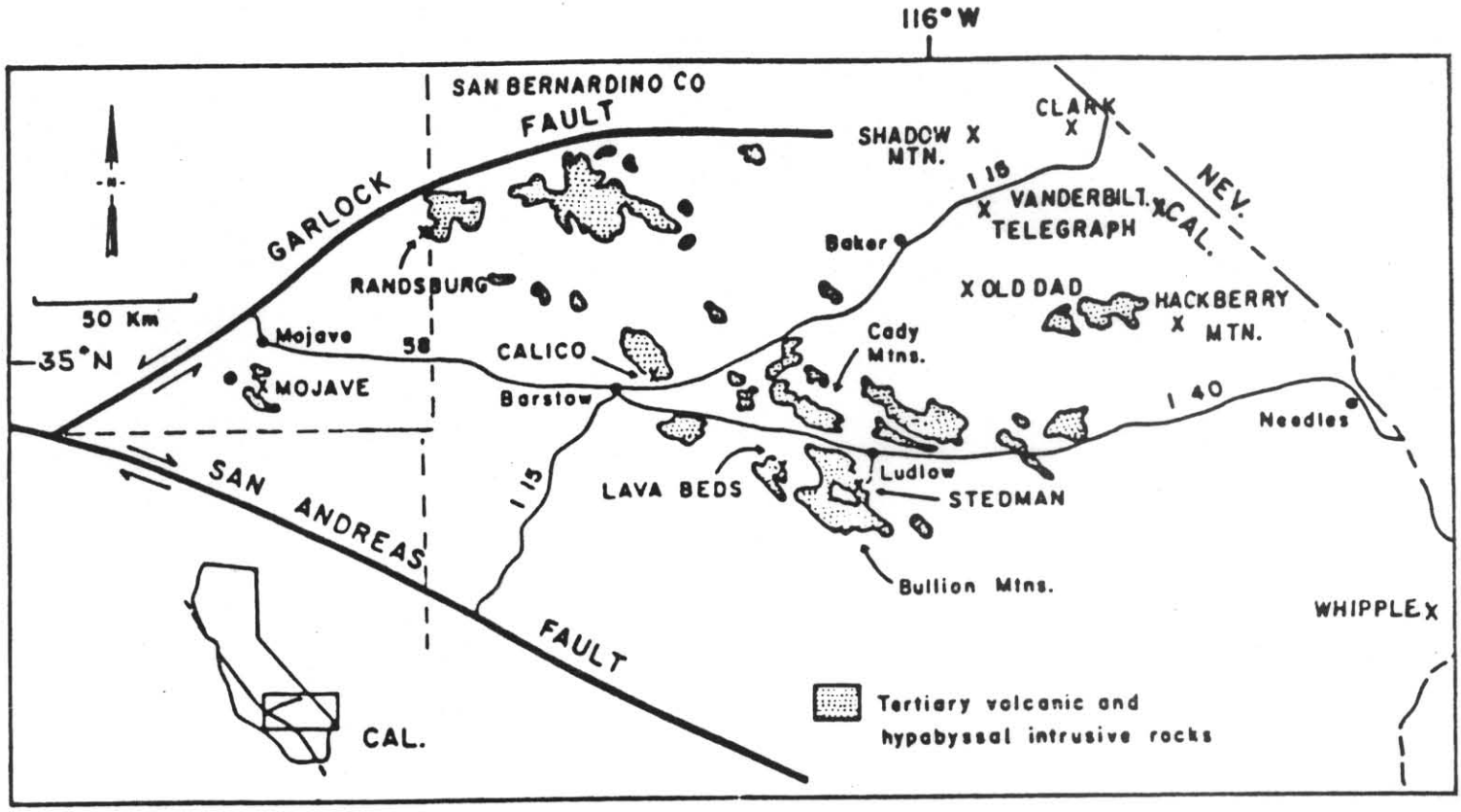

Figure 1. Location map of the Mojave Desert region. The distribution of Tertiary volcanic and hypabyssal intrusive rocks and selected gold deposits are shown (Modified from Polovina, 1984.)

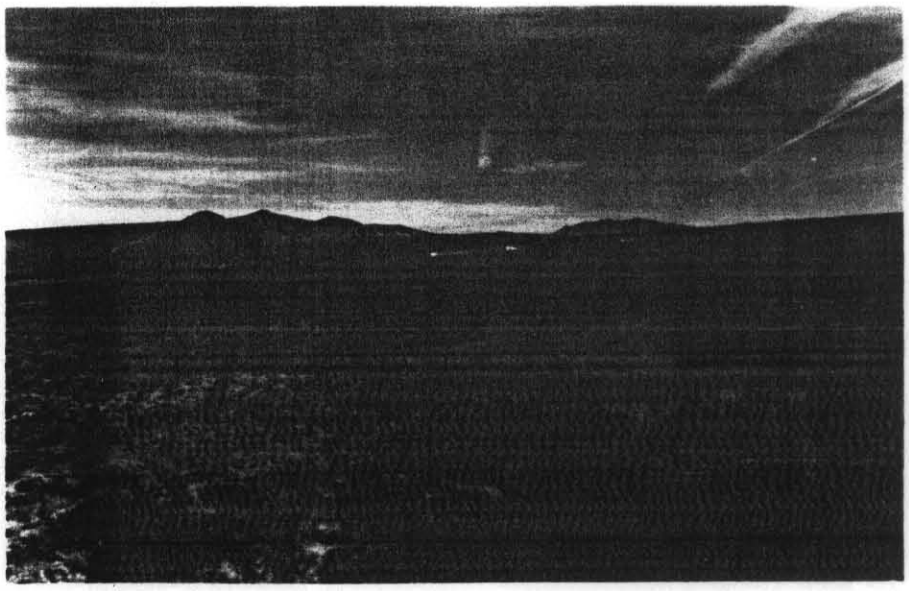

Figure 2. View looking northeast of the study area. The Telegraph Mine workings are in the center of the photograph, the northern Halloran Hills are capped by Cima basalt flows in the background.

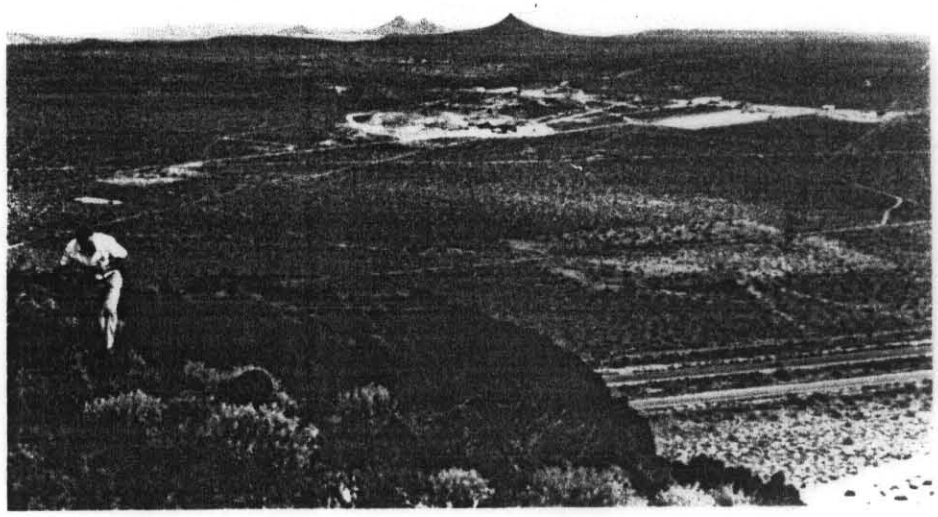

Figure 2A. View looking Southeast in the opposite direction of Figure 2. as taken from the Cima basalt flows. The Telegraph Mine workings are in the center of the photograph

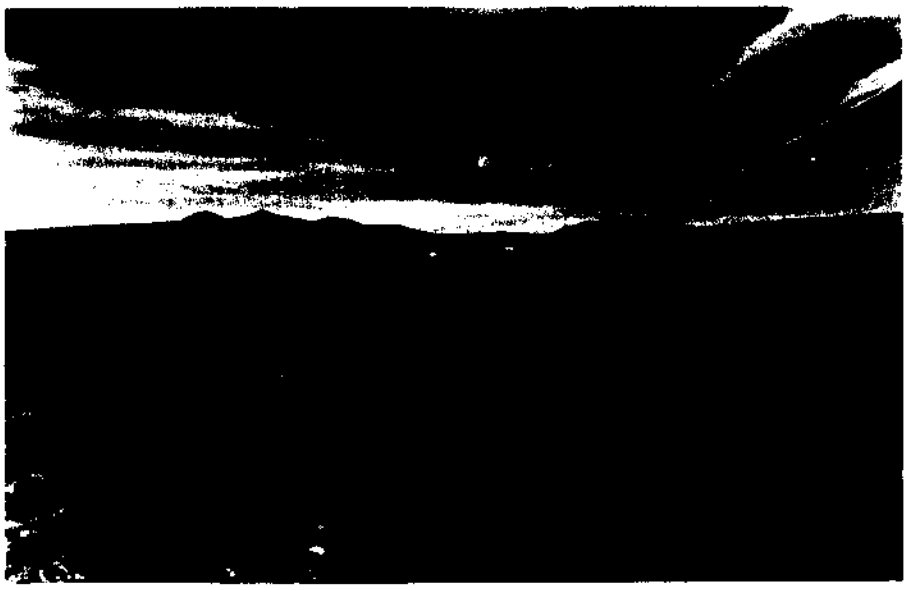

Figure 2. View looking northeast of the study area. The Telegraph Mine workings are in the center of the photograph, the northern Halloran Hills are capped by Cima basalt flows in the background.

Figure 2A. View looking Southeast in the opposite direction of Figure 2, as taken from the Cima basalt flows. The Telegraph Mine workings are in the center of the photograph.

MINING HISTORY

Lode claims along the exposed outcrop of the mineralized Telegraph fault were located by Ralph and H. H. Brown of Salida, Utah, in 1930 (Hewitt, 1956). Subsequent active development over a ten year period from 1932 to 1948 included nine shafts and about thirteen discovery dozer cuts along the 900 m exposure of the vein (Owens, 1980). During this period, a total of 2749 tons of ore yielding 2559 ounces of recoverable gold (average grade of 0.93 oz/ton) and 5423 ounces of silver (average grade of 1.97 oz/ton) were extracted from workings covering over 320 m along strike at 113 m downdip (Ito, 1968). Mining methods were geared toward extracting high grade material along drifts down-dip on the vein on Hill 1 and Hill 2 (Plt. 4).

Underground workings included, from north to south:

1) Telegraph Extension Shaft 3: 100 m deep on a 35° incline, exposing a 1.0 to 1.5 m silicified breccia zone-fissure vein system (see cross section, Plt. 4).

2) Telegraph Shaft 2 : an 80° incline shaft with crosscuts at the 3800 ft. and 3750 ft. levels with 30 m drifts developed along the breccia-vein system (Fig. 17). The main stope (new caved) of 1.2- 3m width, extended from the 3800 ft. level to the surface. A lower stope (inaccessible) extends from the 3750 ft. level to the 3800 ft. level.

3) South Telegraph Shaft 1 (located on the southwest edge of Hill 1, now secured and covered): reportedly a 30°- 53° incline shaft with drifts at the 3775 ft., 3725 ft., and 3575 ft.(unconfirmed) levels. State records (Tucker and Sampson, 1943) reported a 2 in. (5cm) pocket of "high grade" ore in footwall of the south Telegraph shaft contained 18.5 oz/ton gold and 25.5 oz/ton silver.

Intermittent work apparently continued into the 1950's, when the lessors of the property hired Harrison Salsbury (later of the U.S. Bureau of Mines) who used the first cyanide heap-leaching methods to process the micron-sized ore (Ito, 1968). In 1969, eight diamond drill holes totaling 640 m were drilled on the property under contractual agreement with the OME. Tomo Ito, the applicant geologist estimated measured ore reserves on an average vein width of 1.5 m totaling 72,000 tons of 0.51 oz/ton Au and 1.16 oz/ton silver. Core samples were not available for this study.

During renewed development of the property in 1981, more than forty shallow exploration holes were drilled along strike (Plt. 5). Selected results from the resulting 790 m of drilling are included as Appendix F.

PREVIOUS INVESTIGATIONS

The earliest comprehensive geological and mineral potential study of the eastern Mojave region was completed by Hewett

(1956), covering 10,140 km^2 of the Ivanpah Quadrangle in southwestern Nevada and southeastern California. Miller (1946) first described the Halloran Complex of crystalline Precambrian and Mesozoic rocks outside of Baker. Building on Miller's study, Warnke (1969) reviewed the Halloran Hills geology north of I-15, emphasizing the domal, multiple intrusive relationships of the Mesozoic diorite to "tonolite" stocks.

More recently, Hall (1972) investigated Cu-Mo mineralization apparently related to hypabyssal porphyry intrusives at the East Camp of the Turquoise Mountain District, 4 km north of the Telegraph mine, (Fig. 3). Robinson (1979) distinguished three multiple intrusive domes north of Cima , while Turrin and Dohrenwend (1985) have dated and mapped the overlying basalt sequence from Cima to the southern Halloran Hills. Dewitt's (1980) study is the most comprehensive work to date in the immediate area, emphasizing the geochronology of the Halloran metamorphic core complex and zoned Mesozoic domes. The mine reports of Ito (1968), Joseph Owens (1980) and M.L. Jensen (1981) as confirmed by this study have adequately evaluated ore reserves and mine development criteria based on the drilling programs. (See Exhibit "A")

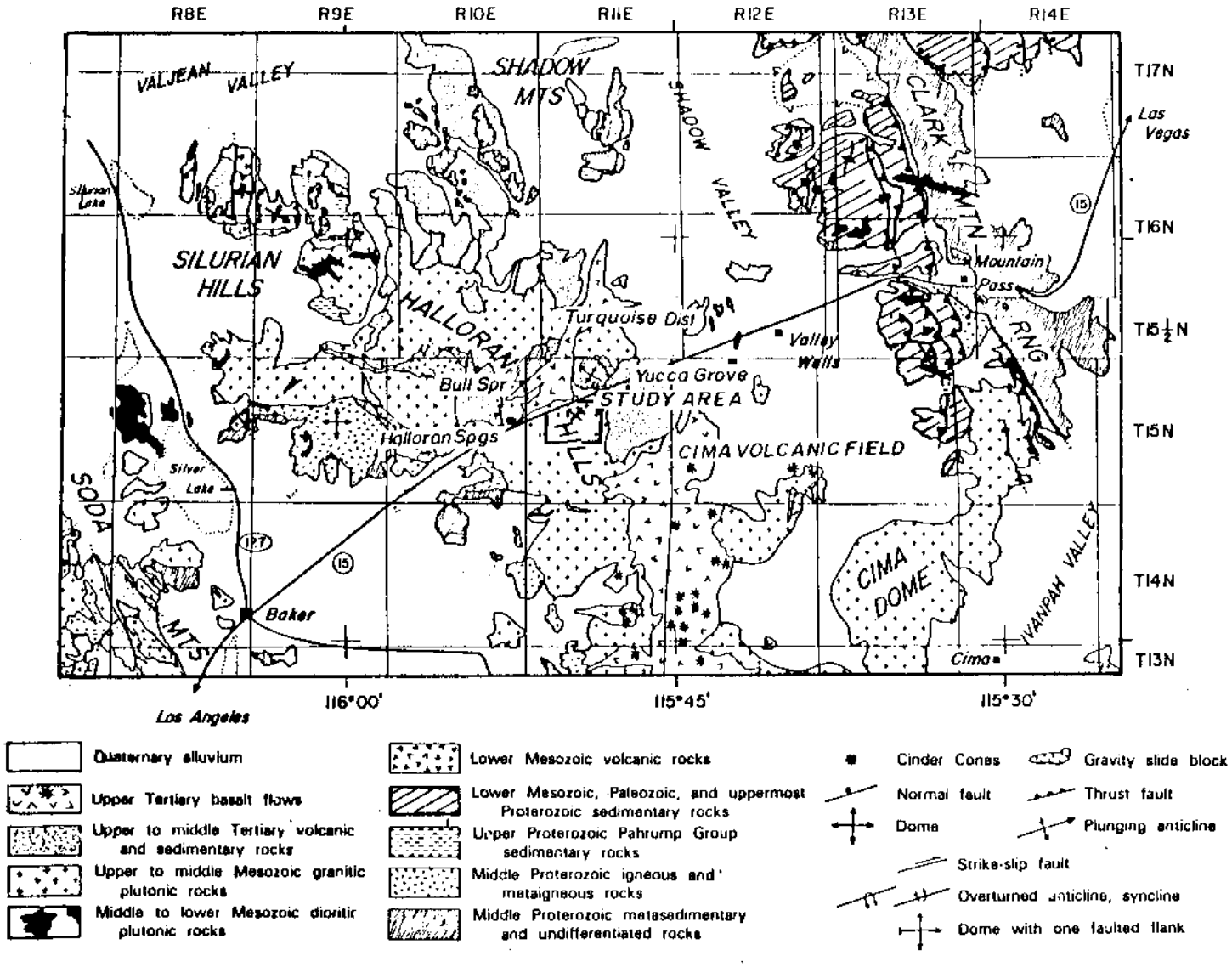

Figure 3. Geologic map of the Halloran Hills (Modified from DeWitt, 1980.)

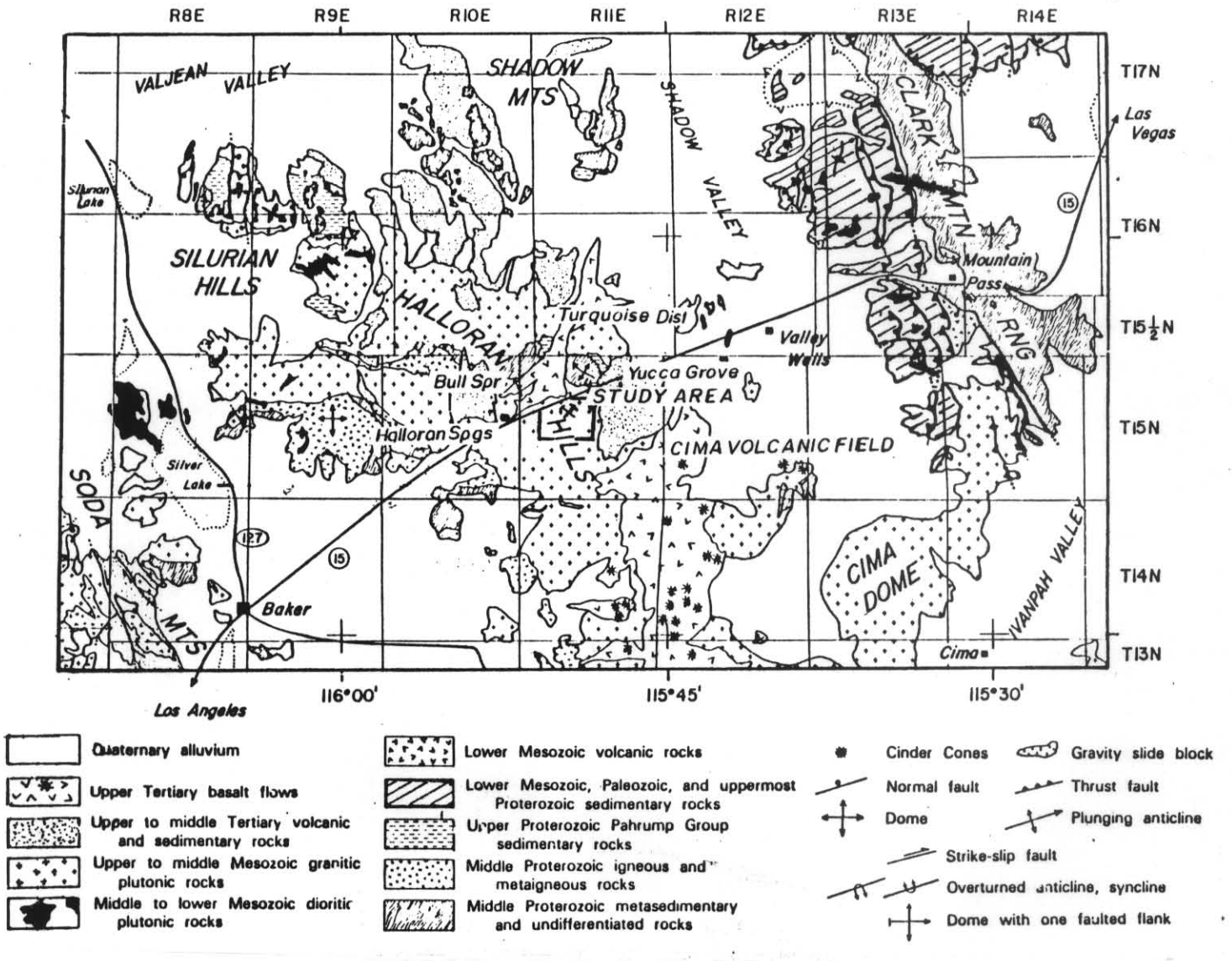

Figure 3. Geologic map of the Halloran Hills (Modified from DeWitt, 1980.)

II

DISTRICT PETROLOGY

Cretaceous plutons that host East Halloran Springs District mineralization are exposed on a low-relief pediment surface. Intrusive relationships help define a petrogenic sequence, although actual contacts are often very poorly exposed. A complete investigation of compositional and textural variations within these composite bodies was not attempted in this study. The following descriptions are based on reconnaissance mapping and selective sampling in the study area (see Plt. 1).

Mesozoic Intrusive Rocks

Quartz Diorite

A dark gray, coarsely crystalline biotite hornblende quartz diorite crops out in a linear band 2591 m long and 300 m to 600 m wide, extending from the southeastern part of Sec. 21 to the western half of Sec. 20 (Plt. 1). Owing to a high percentage of ferromagnesian minerals and calcic plagioclase, the rock is not resistant and erodes to gentle slopes of black talus and black-mica sands. Intrusive relationships with the Teutonia quartz monzonite are visible only in the Aqua Dulce area of Sec. 19-20 (Fig. 4). Here, outcrop patterns and local attitudes suggest the diorite is a thin remnant roof of a larger pluton. The diorite occurs as xenoliths in quartzmonzonite

Fig. 4. Injection of Cretaceous Teutonia quartz monzonite into Mesozoic quartz diorite. Contacts in the Aqua Dulce area, Sec. 19 (see Plt. 1).

Figure 5. Quartz diorite xenoliths in Teutonia quartz monzonite in outcrop, Sec. 20, Plate 1.

visible only in the Aqua Dulce area of Sec. 19-20 (Fig. 4).

Fig. 4. Injection of Cretaceous Teutonia quartz monzonite into Mesozoic quartz diorite. Contacts in the Aqua Dulce area, Sec. 19 (see Plt. 1).

Figure 5. Quartz diorite xenoliths in Teutonia quartz monzonite in outcrop, Sec. 20, Plate 1.

visible only in the Aqua Dulce area of Sec. 19-20 (Fig. 4).

and granite throughout Secs. 21 and Sec. 16, and in isolated outcrops of quartz monzonite in Sec. 20.

Microscopically, the rock is idiomorphic to hypidiomorphic equigranular composed of 45 to 62% plagioclase, up to 14% interstitial quartz, 13% euhedral hornblende, 10 to 14% euhedral biotite, 5 to 10% anhedral perthite. Andesine (An 33-36) laths (1.0 to 2.5 mm) shows little zonation, with 10 to 50% cleavage-controlled deuteric sericite alteration. Poikilitic perthite with microlites of andesine and quartz shows dustings of albite-controlled sericite alteration. Hornblende (1-5mm) is often poikilitic with quartz, biotite, magnetite, ilmenite and shows from 20 to 100% alteration to a chlorite-epidote-calcite assemblage. Accessories include trace amounts of coarse euhedral sphene (to 1 mm), zircon (0.1mm), magnetite (0.2mm), and apatite (0.05 to 0.01 mm).

Quartz Monzonite / Monzodiorite

The major rock type in the study area is a light pink-gray to gray-green, locally porphyritic biotite hornblende quartz monzonite to monzodiorite originally mapped as the "Teutonia quartz monzonite" by Hewitt (1956). The rock takes on an almost ubiquitous green-gray hue from deuteric alteration of biotite and hornblende to chlorite (Fig. 6), locally pronounced in highly sheared or weakly propylitized zones where en-echelon joint sets are infilled with chlorite. Low erosion resistance restricts good outcrops to creek beds and inselbergs in the NW part of Sec. 20 and Sec. 16 where the rock is locally rich in

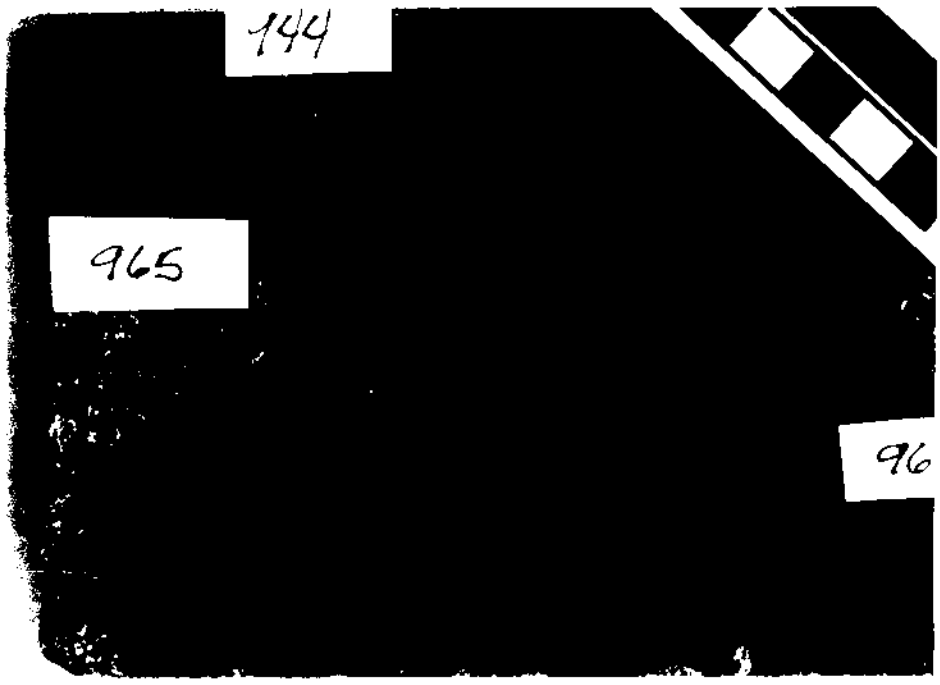

Figure 6. Various hand samples of the Teutonia quartz monzonite. Sample 965 shows weak propylitic alteration consisting of greenish epidote-bearing saussurite core with a white montmorillinite-rich rind. Sample 964 displays more advanced propylitic alteration, in which all biotite has been converted to chlorite and plagioclase to montmorillinte-mixed layer clays. Sample 944 displays more pervasive, augmented chlorite alteration of the rock developed along the unsilicified breccia of the Telegraph system wall rocks (see Chapter VII).

locally pronounced in highly sheared or weakly propylitized zones where en-echelon joint sets are infilled with chlor-

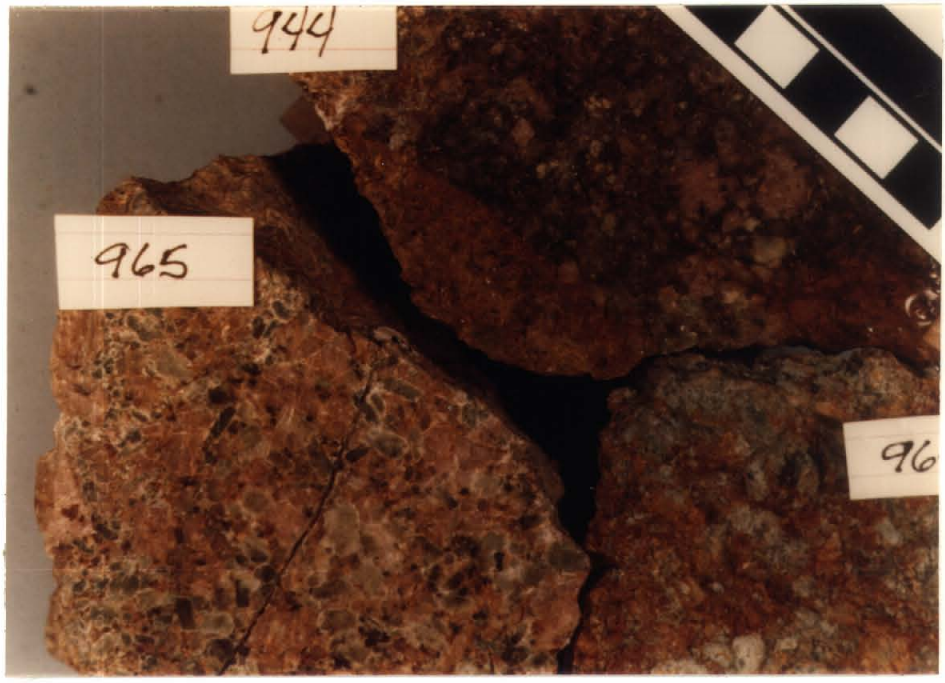

Figure 6. Various hand samples of the Teutonia quartz monzonite. Sample 965 shows weak propylitic alteration consisting of greenish epidote-bearing saussurite core with a white montmorillinite-rich rind. Sample 964 displays more advanced propylitic alteration, in which all biotite has been converted to chlorite and plagioclase to montmorillinte-mixed layer clays. Sample 944 displays more pervasive, augmented chlorite alteration of the rock developed along the unsilicified breccia of the Telegraph system wall rocks (see Chapter VII).

locally pronounced in highly sheared or weakly propylitized zones where en-echelon joint sets are infilled with chlor-

rounded (5-10 cm) xenoliths of quartz diorite (Fig. 5). Measured xenolith foliations do not reflect any particular districtwide fabric trends. Intrusive contacts are visible only where more resistant granite and aplite dikes support exposed hills.

Microscopically, the rock is hypidiomorphic granular, locally glomeroporphyritic with 23 to 40 % subhedral plagioclase, 24 to 36 % perthite, anhedral interstitial quartz, 5 to 12% subhedral biotite, 1 to 15% euhedral hornblende. Andesine laths (An 33-34) (1.5-3 mm) show core and cleavage deuteric sausserite replacement while poikilitic perthite, with plagioclase and apatite, exhibits minor alteration to sericite. Biotite is partially to completely altered to by chlorite with inclusions of rutile, leucoxene, and hematite. Hornblende, often poikilitic with inclusions of plagioclase, exhibits core replacements by felty masses of biotite-altered to chlorite and epidote. Accessories include magnetite (0.1mm microlites), sphene (1mm), zircon (0.%mm) and apatite (0.05mm).

Granite / Quartz Adamellite

A dark pink, coarsely crystalline leucocratic composite stock of granite to quartz adamellite intrudes quartz monzonite in exposures in Sections 19 and 20 (Plt. 1). Modal sample compositions suggest a differentiated composite pluton with a true granite phase and a quartz adamellite phase (as classified by Dewitt, 1980), based upon variations in the orthoclase/-plagioclase ratio. True granite has a K-feldspar/plagioclase

ratio of 2:1 and appears reddish pink in outcrop due to 1 % hematitic clay alteration. Quartz adamellite has a perthite/plagioclase ratio of 1:1 and is light pink in outcrop, exhibiting little hematitic alteration.

Granites in thin section are dominantly idiomorphic equigranular with 34 to 46% subhedral to euhedral perthite (to 6mm), 23 to 34 % euhedral sodic plagioclase (An~ 14, 6mm), 27 to 30 % anhedral intragranular quartz (to 7mm), and 1 to 4% euhedral biotite (3mm). Perthite and quartz often display mosaic, micrographic and myrmekitic intergrowth textures. Accessories include magnetite (0.01mm), muscovite, and apatite (0.05 mm).

No attempt was made to map these distinct intrusive phases based on subtle variations in pluton composition. Distinct regional rock fabric foliation trends were not observed.

Aplite / Pegmatite Dikes

Intruding all plutons in the region is a swarm of light to dark pink aplitic to locally pegmatitic alaskite-granite dikes. These resistant dikes often form light colored, low-relief ridges and linear hills (Fig. 9). They range from 5 cm to 15 m in width and are generally discontinuous; a few form continuous segments in excess of 800 m (Plt. 1). Texture, grain size and compositional variations often accompany variations in dike widths; pegmatite phases generally occupy central zones in fairly wide aplite phases. This is true for the dikes near

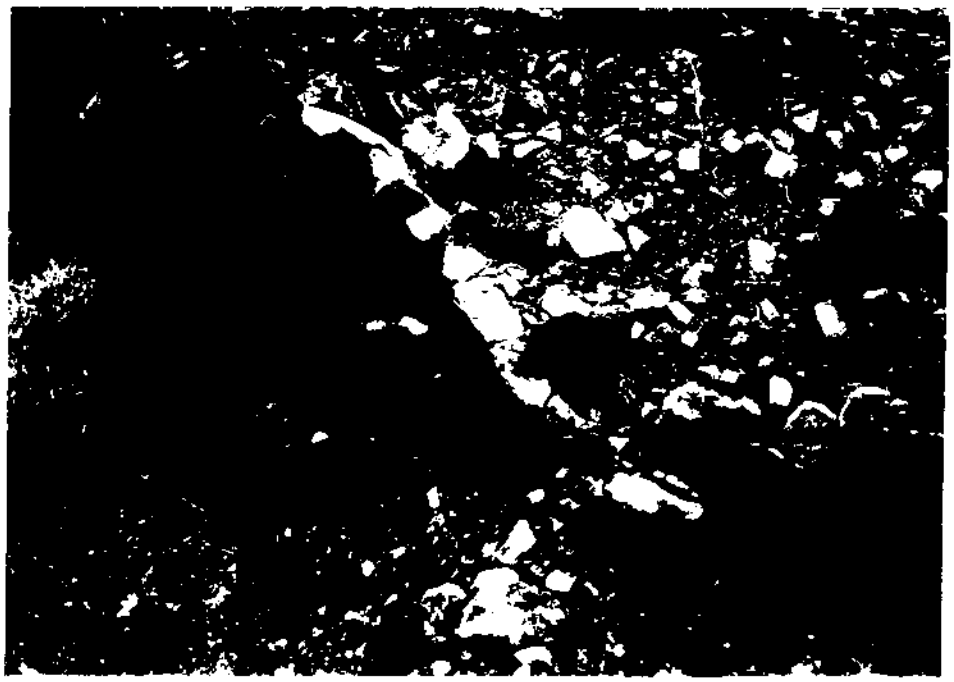

Figure 7. Exposure of fine grained aplite dike within quartz diorite (in out crop in Section 19, Plate 1).

low-relief ridges and linear hills (Fig. 9). They range from 5 cm to 15 m in width and are generally discontinuous; a few form continuous segments in excess of 800 m (Plt. 1). Texture, grain size and compositional variations often

Figure 7. Exposure of fine grained aplite dike within quartz diorite (in out crop in Section 19, Plate 1).

low-relief ridges and linear hills (Fig. 9). They range from 5 cm to 15 m in width and are generally discontinuous; a few form continuous segments in excess of 800 m (Plt. 1). Texture, grain size and compositional variations often

the Telegraph Mine, south of the Gold Dike and in Sec. 21 (see Plts. 1 and 3). Plagioclase-rich dikes, plotting toward the "quartz adamellite" field of Figure 12, are coarse aphanites to fine phanerites and also form in wider zones ("footwall aplite" of Hill 2., Plt. 4).

Granite aplite hand specimen color differs depending on quartz content, from dark pink (35 % quartz) to very pale pink (50 % quartz). In thin section, the rock displays a fine allotriomorphic to micrographic equigranular texture with microperthite (0.5 to 1.5 mm), subhedral sodic plagioclase (An 14-30) laths (0.1 to 1.0 mm), interstitial quartz (0.2 to 0.5 mm) and minor subhedral muscovite (0.35 mm). Accessories include apatite (0.01mm), zircon (0.05mm), sphene (0.1 mm), magnetite (0.1mm), allanite (0.05mm), and garnet (0.05mm).

Tertiary Rocks

Quartz Latite Porphyry Dikes

Isolated, 1 to 3 m wide discontinuous pink-grey to greenish grey quartz latite porphyry dikes, are clustered in the southeast corner of mapped area (Sec. 21, Plt. 1). They intrude granite (on the northeast slope of Squaw Tit) and quartz diorite (west central Sec. 21) and appear to strike parallel or crosscut aplite dikes in Sec. 21 (Plt. 1). The dikes tend to follow predominantly N 30° to 35° E and N 60° to 65° E trends (see Section "Stuctural Geology") but are

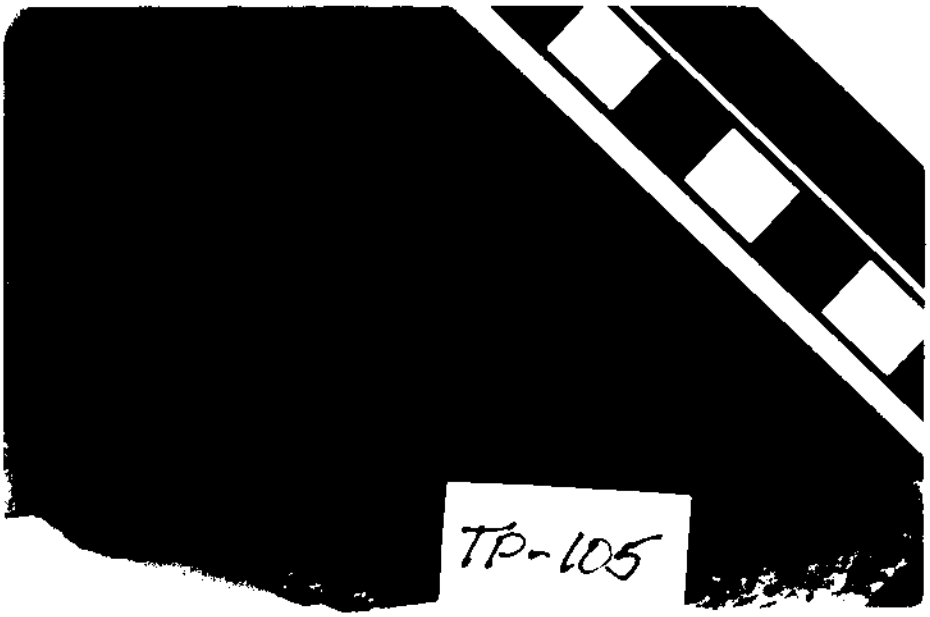

Figure 8. Hand sample of Tertiary quartz latite showing well-developed porphyritic texture.

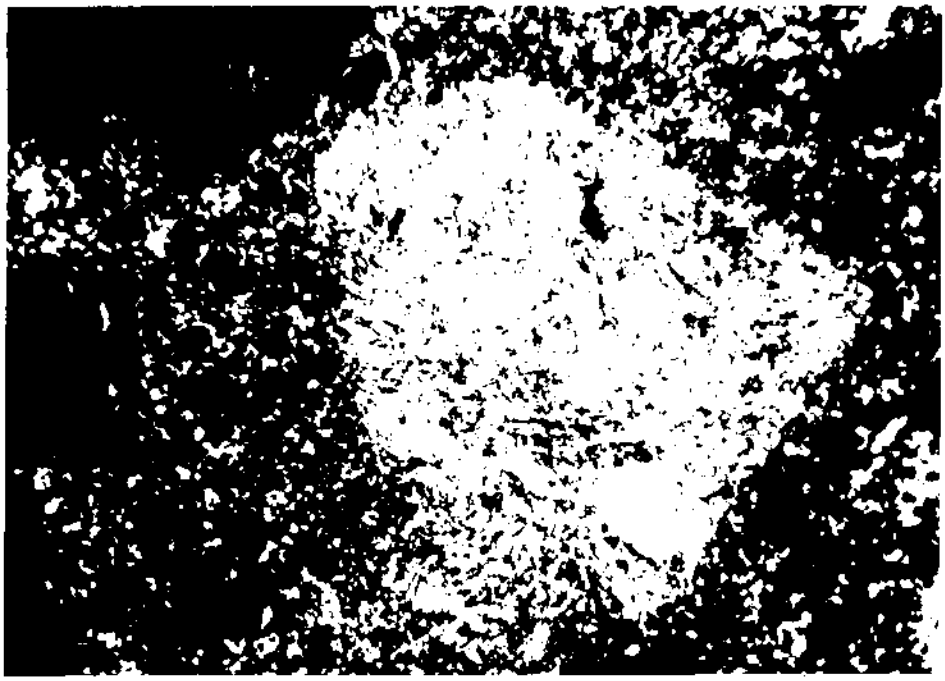

Figure 9. Photomicrograph of TP-105 showing pervasive alteration of plagioclase to sericite. Note resorption of quartz phenocryst in lower right hand corner.

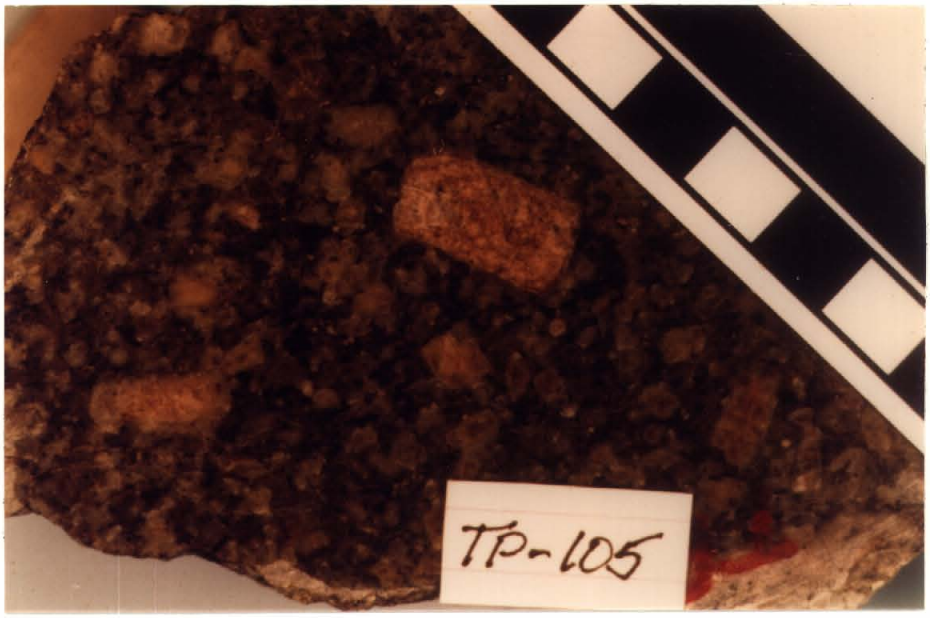

Figure 8. Hand sample of Tertiary quartz latite showing well-developed porphyritic texture.

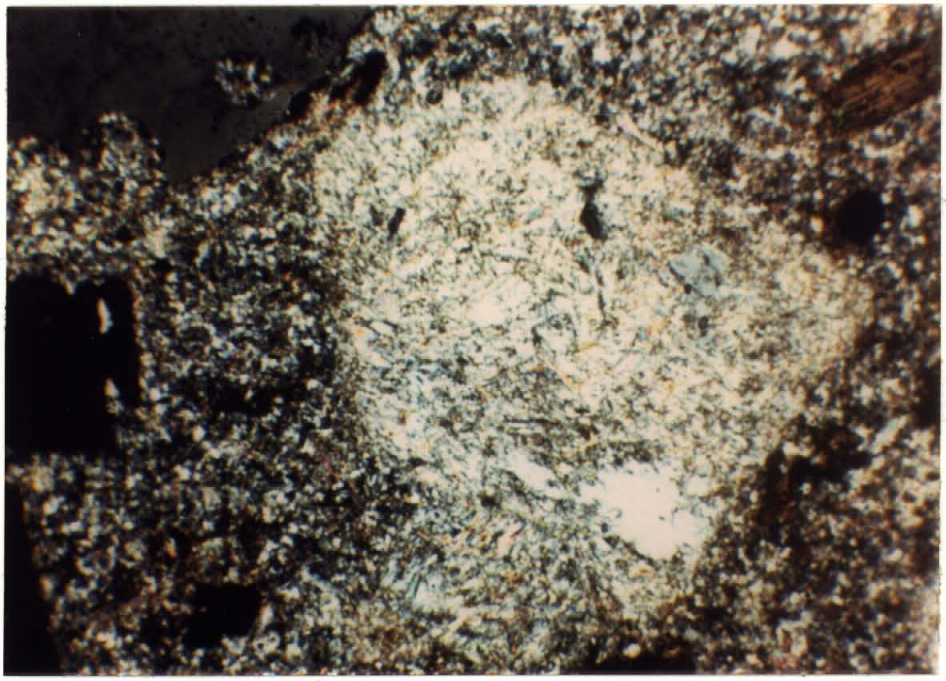

Figure 9. Photomicrograph of TP-105 showing pervasive alteration of plagioclase to sericite. Note resorption of quartz phenocryst in lower right hand corner.

ridges throughout the area.

Tertiary basalt flows that cap Squaw Tit and plateaus north and south of Halloran Summit represent remnants of a once continuous field that covered the district about 4.5 million years ago. The individual flows have been dated and the regional basaltic volcanism chronology has been the subject of recent investigation (Dohrenwend, 1984). Mass-wasted basalt from Squaw Tit butte is mapped as Quaternary colluviun (see Fig 1). The special significance of the flow chronology to geologic reconstruction of the Telegraph system is fully developed in Section X.

Recent Alluvium

Modern pediment alluvium is composed of coarse, unconsolidated sand and gravel, from 0.25 to 2.0 m thick, with caliche interbeds and locally extensive cold spring calcite deposits. Caliche is especially well developed along permeable zones above recent clay-rich interbeds. Small cold spring tufa deposits form along fracture systems and intrusive contacts, especially along the granite-quartz monzonite contact in Sec. 20 (Plt. 1).

Age and Correlation

Dewitt's (1980) mapping placed the Halloran Springs District quartz monzonite pluton within the "quartz monzodiorite peripheral phase" of his zoned pluton, dated at 140

to 90 m.y. by Ar-Ar techniques. Selective modal analysis in this study suggests a dominantly quartz monzonite composition in the immediate study area. He mapped the granitic rocks as "quartz adamellite"; this study identifies true granites in the suite (over 66 % Kspar), as exposed in the eastern half of Secs. 18 and 19 (Plt. 1). He mapped exposures in Sec. 20 and 21 (Plt. 1) of quartz diorite as questionable "Older Precambrian biotite gneiss"; this study confirms the "quartz diorite" designation based on petrographic compositional and textural evidence from outcrop samples and xenoliths of quartz monzonite. The Mesozoic quartz diorite intrusives in the area have been dated at 126 m.y. to 129 m.y.

Aplite dike "swarms" are apparently more common in the study area than elsewhere in the Ivanpah Quadrangle (Hewitt, 1956), and are mentioned by Dewitt (1980) and Hall (1972) in the Halloran Hills to the north of the highway. Although no radiometric dating of the dikes was attempted, Dewitt considered the Halloran Springs aplite dikes and Turquoise Mountain intrusive plugs (see Fig. 3) as correlative phases of his Late Cretaceous "muscovite-garnet adamellite" unit. Quartz latite dikes of Sec. 20 may be correlative to the latite dike suite described by Hall (1972) at Turquoise Mountain, based on compositional, textural and alteration similarities. He believes the sericitically altered latite porphyry dikes within the Turquoise Mountain quartz monzonite are genetically related to magmato-hydrothermal Cu-Mo mineralization hosted by

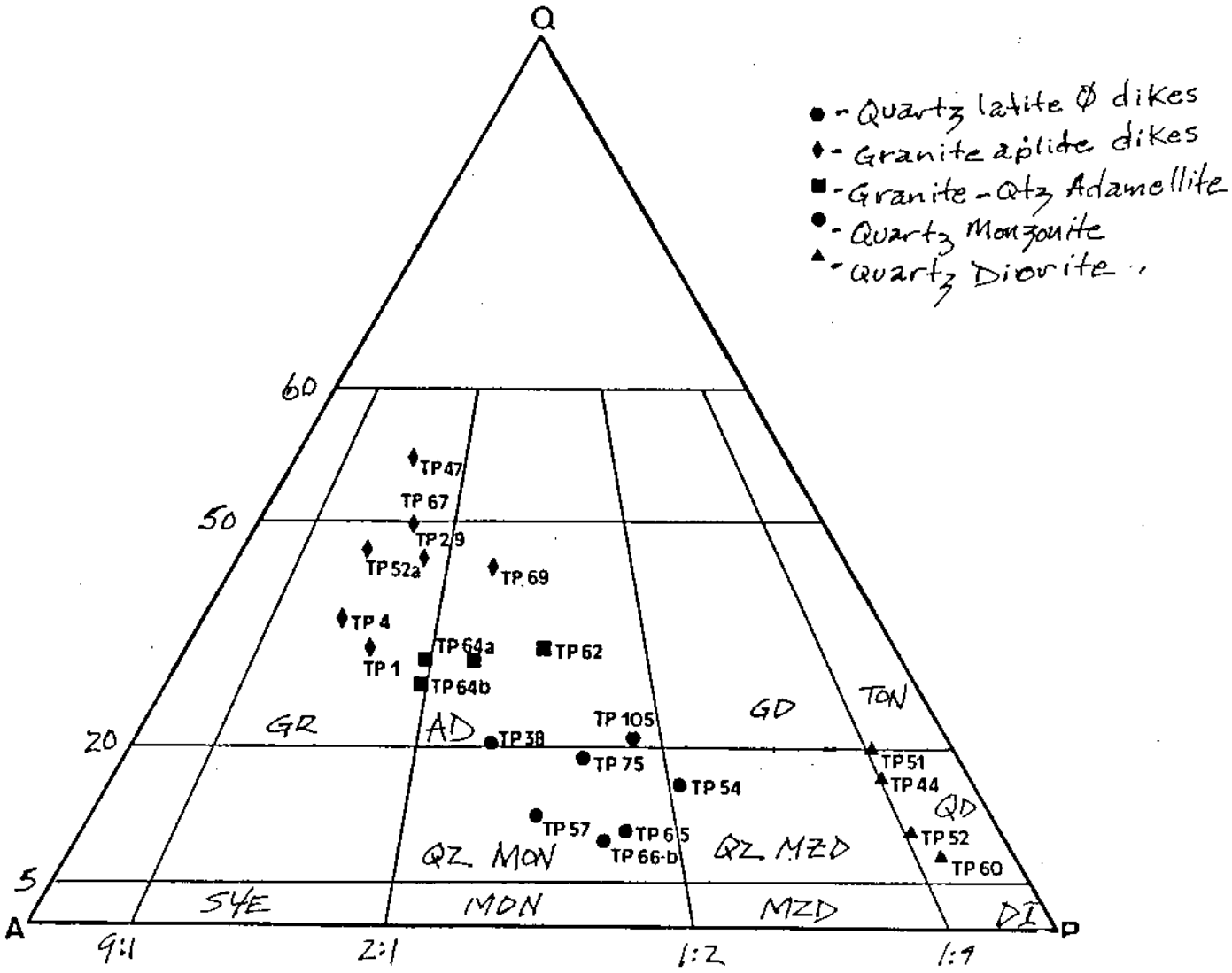

Figure 10. Triangular composition diagram for Mesozoic/Cenozoic intrusive rocks. Data from point-counted modal compositions. Specific regions, their compositional boundaries and nomenclature from I.U.G.S. system.

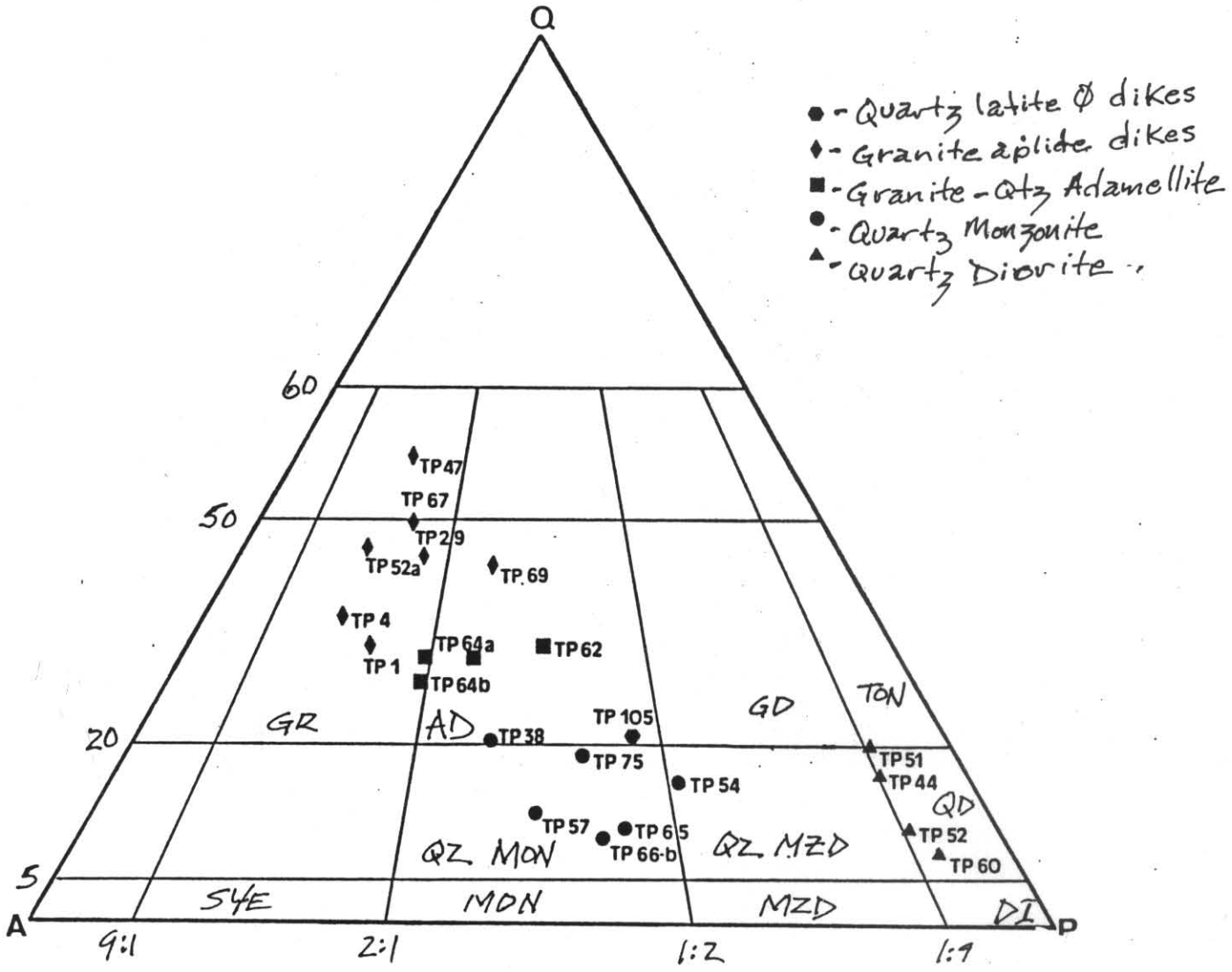

Figure 10. Triangular composition diagram for Mesozoic/Cenozoic intrusive rocks. Data from point-counted modal compositions. Specific regions, their compositional boundaries and nomenclature from I.U.G.S. system.

the pluton. He interprets granophyric textures and strong sericitization of latite porphyry dikes and breccia pipes as evidence of the cooling of through-going hybrid magmaticmeteoric fluids. Apparently, early magmatic-dominated fluids migrated upward in the host stock, forming breccia pipes and zoned potassic alteration. Later-stage, meteoric-dominated hydrothermal fluid migration along northwest trending shears is represented by fracture-controlled alteration and mineralization. These relationships suggest that similar processes may have contributed to hydrothermal mineralization at the Telegraph Mine.

III

STRUCTURAL GEOLOGY

The structural features of the Halloran Springs District are the result of an overprinted sequence of intrusive igneous, extensional and transform tectonic events. Districtwide structural analysis was undertaken to reveal the spatial and genetic relationships between post-Laramide structure and mineralization. A reconstruction of events using cross-cutting relationships of joints, faults and veins reveal structural controls for district-wide and Telegraph system mineralization.

District Structure

Structural data collected throughout the property was

plotted onto circular histograms (Rose diagrams), to facilitate the analysis, correlation and interpretation of discrete elements. The database included strikes of dikes, joint sets, faults and fault zones, and vein deposits. Plate 3 was constructed by isolating the data into local structural provinces, then arranging it by type of structural information and host rock. A complete pi-plot structural analysis was not attempted because few dip measurements could be measured with precision.

Dikes

A preliminary examination of vein outcrops indicated possible correlations between fault-hosted breccias, fissure-vein mineralization and dike distribution at the Telegraph. As noted in other districts, dikes and dike swarms often serve as foci for vein-related mineralization even though the veins may be genetically unrelated to the dikes (Park and MacDiarmid, 1975).

If the Halloran Hills aplite/pegmatite dikes represent a late stage, residual intrusive pulse of the granitic plutons, it follows that attitudes and distributions of dikes probably reflect tensional stresses related to the updoming of the zoned pluton (Dewitt, 1980 and Hewitt, 1956.) Figure 11 exhibits the wide scatter in aplite dike attitudes throughout the area and strong districtwide trends are not readily observable. However, Sectional segregations of dike strike distributions exhibit local trends (Plt. 3).

In Sections 16 and 17, the dominant aplite strike trends

are N 50°-55° NW, and N 50°-55° NE, with a subordinate set trending N 30°- 35° NE. In Sections 20 and 21, the dominant trend appears to be N 20°-25° NW, with the subordinate sets at N 55°-65° NW and N 60°-65° NE (Plt. 3).

Exposures of "felsic dikes" (predominantly of latitic composition) are restricted to the northwestern portion of Sec. 21. Most of latite dike attitudes are between N 25°-35° E or N 60°-65° E (Fig. 12); attitudes which are also represented in a large portion of the middle set (J_2) of joints throughout the area (see Figs. 13, 14, and 15). The N 25°-35° E trend is also reflected in the modal distributions of veins and joints along both the Gold Dike and Telegraph trends (Plt. 3). This empirical correlation is interesting considering that the dikes may be genetically related to the hydrothermal system responsible for both mineralized systems. Basalt dikes are restricted to Sections 19, 20, and 21 (Plt. 1), and are also constrained by local structure to N 60°-70° W strikes (Fig. 12). This trend is within the strong, districtwide N 50°-70° W range of attitudes displayed by late set joints (J_3 in Figs. 13 and 14) and faults (Fig. 16). The mode distribution for Telegraph post-mineral wallrock faults is also between N 60° and 70° W (Plt. 3). These relations indicate that ascending basaltic magmas took advantage of relatively young extensional fracture regimes.

Joint Sets

Twenty five structure control stations located throughout the study area provided joint-development chronologies based

on cross-cutting relationships (Figures 13 and 14). The lack of primary fabric foliations in intrusive rocks hosting these structures prevented drawing relationships between joint attitudes and stresses related to intrusive events. The purpose of this study was to:

1) examine the variety (ie. tensional, extensional or shear) and spatial distribution of post-Laramide joints (see Plt. 3),

2) establish a relative chronology of structural events and related stress regimes and

3) suggest possible correlations between joint sets, faults and district-wide mineralization.

The granitic rocks and quartz diorite in Sections 20 and 21 exhibit a predominance of northeastern joints, from N 40°-60° E and subordinately N 15°-35° E. Northwestern sets are N 50°- 60° W with subordinate N 10°-15° W (Plt. 3). Trends in quartz monzonite district-wide are more bimodal:

1) strong eastern trends at N 20°-25° E and N 35°-40° E, perhaps mimicking extensional-shear mimicking faulting (as at the Telegraph itself) and,

2) N 45°-55° E, reflecting pre-existing aplite orientations (see Fig. 11).

Sub-horizontal tensional joints are found in all larger igneous body exposures and represent the release of isotropic lithostatic stress. These unloading structures appear to host "bull quartz" veins in Section 17 (Plt. 2).

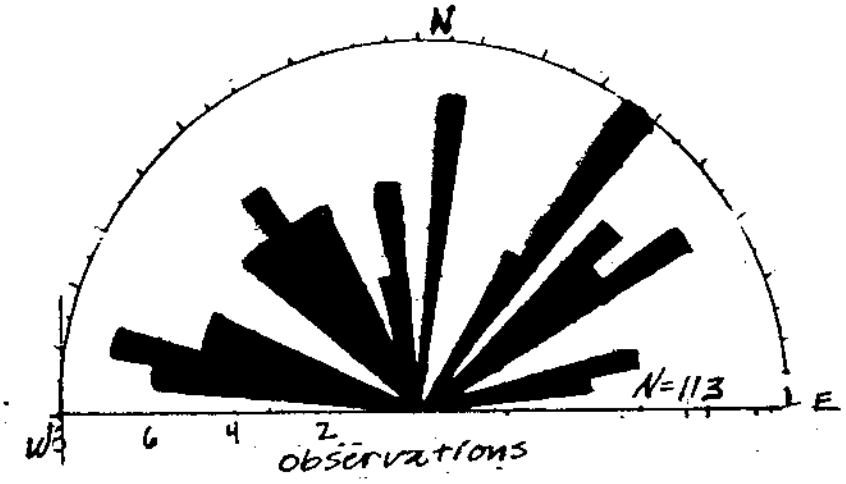

Figure 11. Distribution of Cretaceous-Tertiary dike orientations throughout study area. This diagram represents all measurements shown on Plate 3.

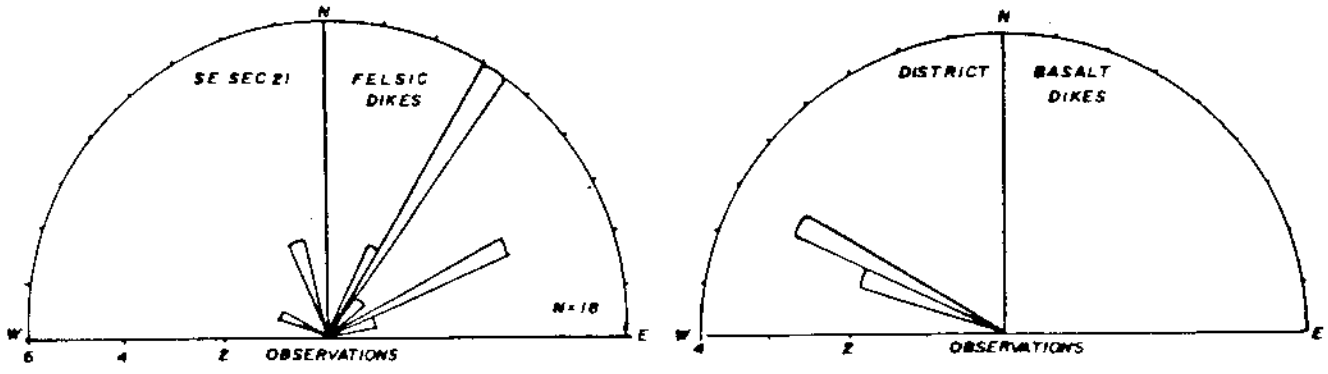

Figure 12. Distribution of felsic and basalt dikes. Felsic dikes (generally of quartz latite composition) are exposed in the northwestern corner, Sec. 21, and Cima-equivalent basalt dikes, exposed mainly in Sections 19, 20 and 21 (Plt. 1).

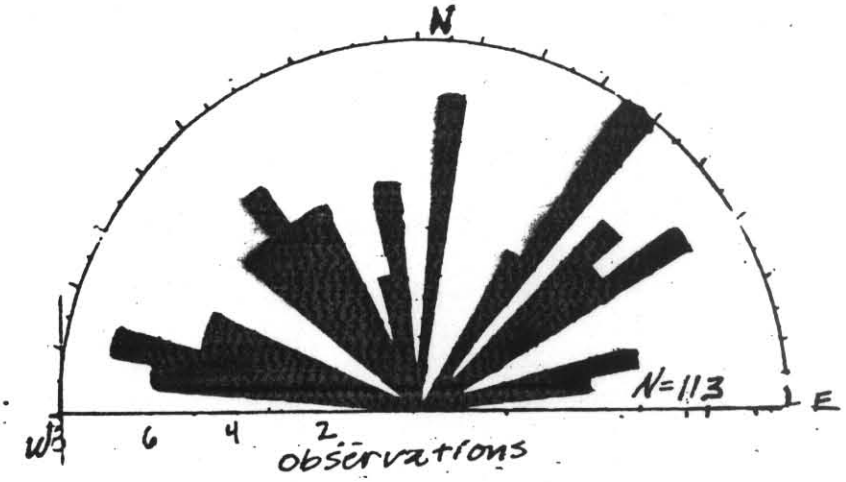

Figure 11. Distribution of Cretaceous-Tertiary dike orientations throughout study area. This diagram represents all measurements shown on Plate 3.

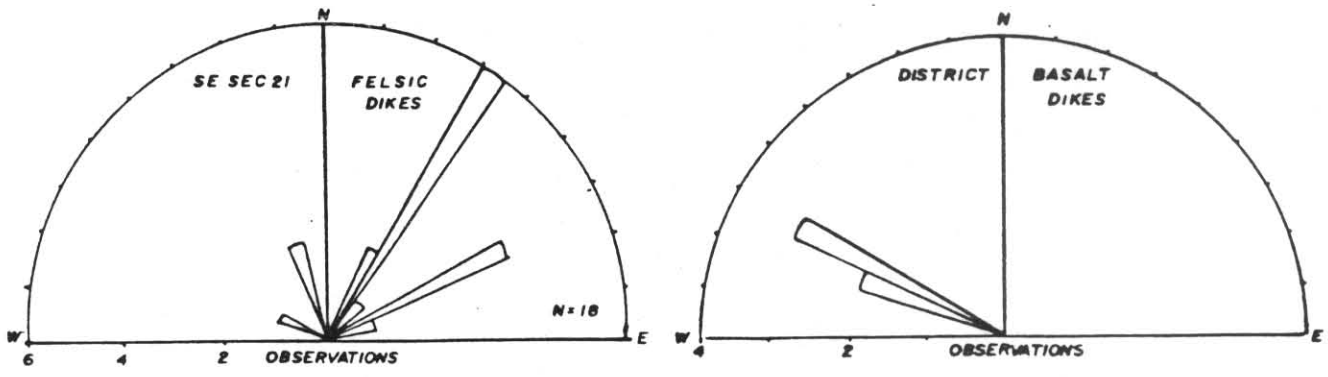

Figure 12. Distribution of felsic and basalt dikes. Felsic dikes (generally of quartz latite composition) are exposed in the northwestern corner, Sec. 21. and Cima-equivalent basalt dikes, exposed mainly in Sections 19, 20 and 21 (Plt. 1).

Faults

A strong correlation between certain fault trends and vein attitudes was expected. Because so few faults could be clearly identified in poor exposures throughout most of the area, Section by Section distributions were not prepared. Figure 16, representing all measured faults in the area and is somewhat biased toward exposures in Section 17 (Plt. 3).

Explanation for Figures 13 and 14

J_1 - Early Set: often offset by J_2 and J_3.

Dominated primarily N 15°-40° W, with subordinate trends at N 15°-30° E. Almost all of the joints are tensional (i.e. they do not offset dikes), are present with a frequency of between 5 and 20 per meter and have chlorite selvages (if developed inquartz monzonite.)

J_2 - Middle Set: cut-off by J_3.

Dominantly N 40°-65° E and subordinately N 20°-30° E. All sets are well represented in granite of Sec. 20 where they are clearly visible on aerial photographs (predominantly N 60° E sets). They exhibit either extensional or shear separation with minor offset of dike or earlier joints. They have an average density of 20 per meter and are often chlorite infilled.

J_3 - Late Set: Offsetting all other sets.

Dominantly N 40°-60° W with subordinate set at N 20°-65° E. They are mostly extensional with lower density, 5 to 10 per meter, and tend to have no selvage infilling material.

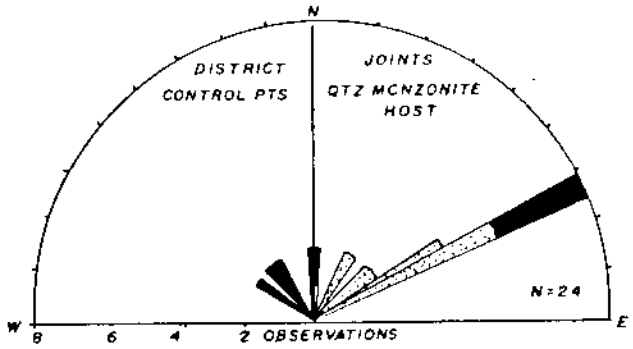

Figure 13. Distribution of joints in Teutonia quartz monzonite from districtwide control point measurements. All dip attitudes recorded were between 60° and 90°.

*EXPLANATION

- Early Set : often cut-off, offset by later joints
- Middle Set : cut-off by Late Set
- Late Set : Offsets all other sets

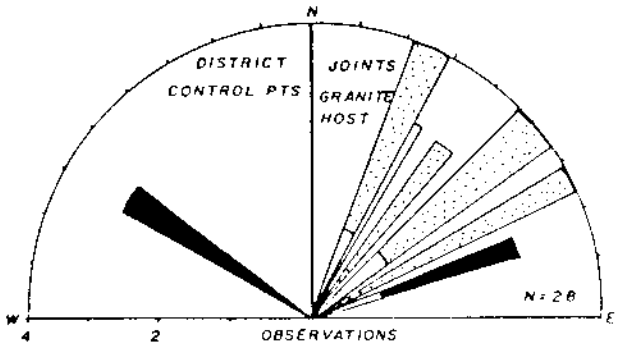

Figure 14. Distribution of joints in granite from districtwide control point measurements.

Modal attitudes of mapped normal dip-slip faults are northwest-dominant at N 50°-65° W (Fig. 16). Many of these fault attitudes were recorded in the "chaotic zone", southeast of the Telegraph trend in Section 17 (Plt. 3.). A number of N 60°-75° E normal oblique-slip (with dominantly left-lateral map separations) faults are concentrated in the "chaotic zone" as well, representing either conjugate fault development or antithetic structures to the main Telegraph shear zone (see Table 1 and Fig. 61). In quartz monzonite host rocks, an apparently later N 75° W to E-W trend (Plt. 3).

Veins

Fine-grained silica fissure vein trends tend to mimic certain fault and aplite dike orientations, as these structures provide permeable zones for ascending fluids. Due to the high frequency of exposed veins in the "chaotic zone" of Sec. 17 (Plt. 2) and along the Gold Dike trend (Plt. 2), attitude distributions are biased in favor of veins developed in these areas (generally hosted in quartz monzonite.)

In the Gold Dike area, veins follow or mimic dike trends of N 40°-55° E and fault trends of N 25°-30° E (Plt. 3). The two breccia systems here may be en-echelon to the main Telegraph trends (some 1 km to the southeast.) Veins in the "chaotic zone" (within 400 m east of the Telegraph system) have dominant N 35°-60° E trends (similar to the middle joint set) and subordinate N 40°-65° W trends (mimicking late joint set).

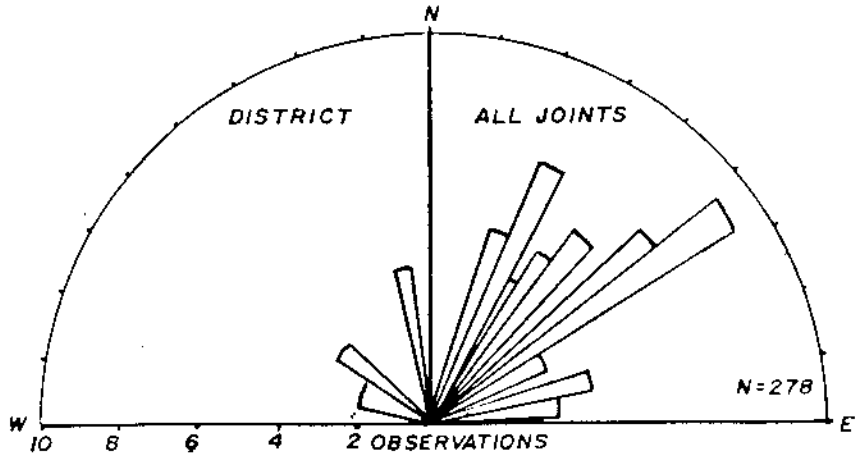

Figure 15. Distribution of all joint orientations throughout the district. The diagram represents all measurements recorded on Plate 3.

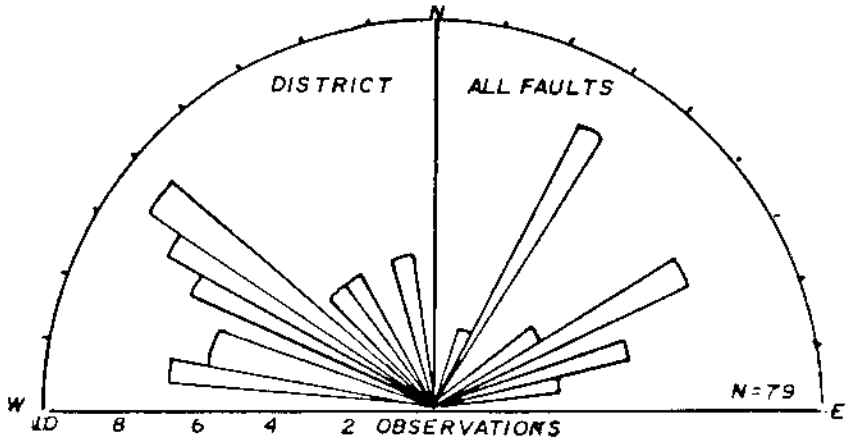

Figure 16. Distribution of all fault measurements.

TELEGRAPH SYSTEM STRUCTURE

The N 25°-30° E trending Telegraph fault zone hosts five separate mineralization loci along its 610 m (2000 ft.) exposure. The Telegraph fault can be classified as a normal right-slip fault, which displays a undulatory curvature throughout its length. Table 1 lists the features which demonstrate both dip and strike-slip components of movement; Section IX "Formation Model of the Telegraph System" discusses the relationships between fault development and mineralization.

As related to districtwide structural elements, the following conclusions can be drawn from distributions given on Plate 3:

1) A strong empirical correlation exists between the N 25°-40° E strike trends of joints and wallrock veins and the main Telegraph silicified breccia zone.

2) District control point observations suggest that the mineralized Telegraph system fault correlates with the "middle stage" of joint formation. This observation is supported by the extensional-shear nature of middle stage joints and fault zones throughout the study area (see Hill 1, Plate 4).

3) Late stage- and post-mineral faults with orientations of N 60°-75° E and N 60°-85° W in Telegraph wallrocks are aligned with the late stage joint chronology and with the dominant fault trends

throughout the area. Minor mineralization occurs along these trends.

TELEGRAPH MINE ORE CONTROLS

In order to fully understand the local structural style and ore controls developed along the Telegraph fault, additional analytical tools were used. Detailed surface (Plts. 3 and 4) and underground (Fig. 17) mapping at 1:240 scale along the fault trace was essential to the interpretation of tectonic controls on mineralization. The sub-surface continuity of the shear zone was delineated by VLF-EM geophysical surveys (Plt. 6) and vein contouring of Hill 2 (Fig. 18) illustrated how local variations in fault plane geometry affected ore deposition.

Plate 4 clearly illustrates the effects of right lateral and normal separation along the Telegraph fault. A summary of the elements indicating oblique-slip movement is given in Table 1; the tectonic development of the system is covered completely in the Section entitled Formation Model of the Telegraph System.

Profile-Dip Contouring

Irregularities in fault plane surfaces have long been known to be a major structural control of ore shoots in vein systems. Vein dilation and profile-dip contouring of vein deposits are among the most useful techniques in determining how irregularities in fault surfaces affect the

TABLE 1

Evidence of Movement on the Telegraph Fault

LOCATION	FEATURE and INTERPRETATION
Entire exposure: Plate 1 Plate 4 Plate 6	Regular, undulatory curvature of fault trace. Mineralized breccias are best developed where fault bends to the right, indicating right-lateral sense of separation. Spacing of eastward bends is nearly periodic at 213m (700ft) intervals.
All surface: excavations	En echelon distribution of wide breccia segments. Dilation occured where footwall concavity Plate 4 was oriented more easterly with relative movement of hangingwall to the northeast.
Plate 4: Surface and Underground	40 to 60 degree dip of main fault plane. Inclined transform fault suggests lateral shearing was acted upon by imposed E-W extension stress and causing normal dip slip.
Plate 4: S, 200 W Figure	Footwall slickensides show 18 degree northeast pitch from vertical. Latest(?) movement along the fault plane is dominantly dip-slip, with minor right-lateral component. 2350
Plate 4: 2300 S, 150 W 3050 S, 100 W	Map separation of of dikes adjacent to main fault is right lateral. Some of the apparent lateral separation is atributable to dip-slip movement.
Plate 4: 3050 S, 150 W 2350 S, 150 W 2300 S, 200 W	Late-stage mineralized hangingwall tensional structures with acute angle oriented away from direction of lateral displacement. These secondary structures are found only where dilatant zone is produced by fault curvature.
Plate 4: 2300 S, 50 W 300 S, 250 W Plate 1: Choas zone	East-northeast and west-northwest post-mineral faults show left-lateral map separation of dikes and veins. These represent secondary "antithetic" structures, oriented at a high angle to the primary structure exhibiting opposite sense of lateral offset (see Wilcox, 19).
Plate 4: 100 N, 150 W	Narrow, high angle, north-northeast mineralized structures forming "horsetail" shear zone. These faults are common hangingwall features at the terminus of transform faults. Sense of movement is right lateral, oblique-slip (due to imposed E-W extension).

EXPLANATION

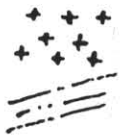
- Cretaceous Teutonia quartz monzonite, showing weak propylitic alteration.

- Propylitized quartz monzonite wall rock


- Argillically altered wall rock - developed both parallel to main Stage III and IV trends and along cross-cutting structures.


- Tan, unsilicified microbreccia- gouge. Most likely developed during Stage II tectonic event.


- Silicified breccia zone, including both Stage III, IV.


- Fine-grained Stage V crackle breccia cementation


- Fine- grained Stage V isolated fissure veins


- Black Mn-calcite-quartz fissure veins of Stage VI


- Strike & Dip of Veins


- Strike & Dip of fractures


- Strike & Dip of Faults


- Ore shoot


- Inaccessible Stopes

.1054 - Geochemical Sample

.TP-60 - Hand Sample

Details concerning the construction of contoured L-sections are given in Appendix A, only the results will be discussed here.

Preliminary relationships between ore-shoot position within the brecciated/mineralized dilatant zones, vein width

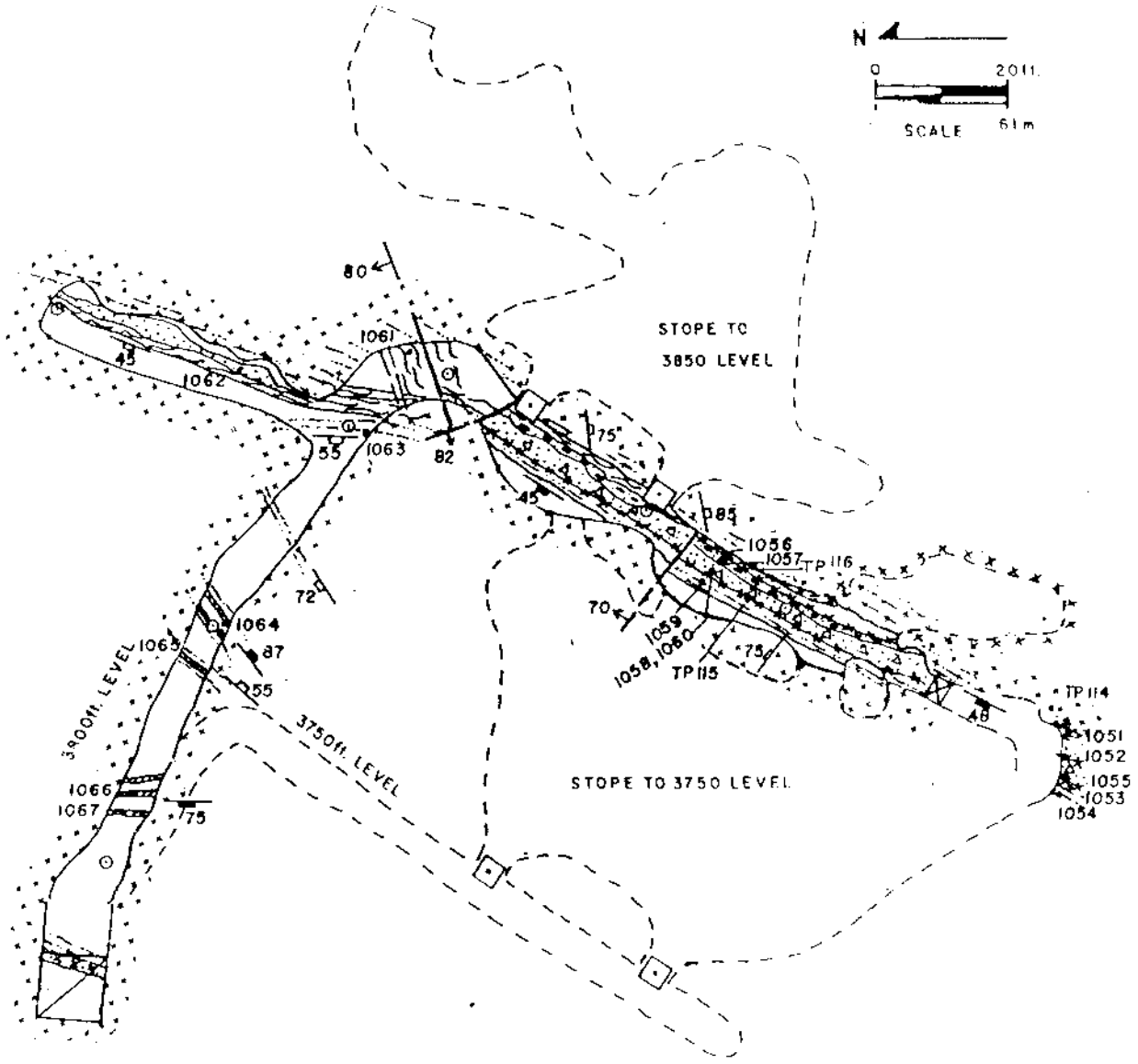

Figure 17. Underground map of the 3800ft. and 3750ft. (projected) of Shaft 2, Hill 2 of Plate 4 and 5. 3800ft. level geologic mapping by Peter C. Lange, stope outline projections, and 3700ft. level projections are from Tomo Ito, 1981.

and assay values indicate that:

1) There is a maximum of 20° total variation in local dip of the system. Local flattening in dip towards dip direction (convex curve toward hangingwall) favored the creation of dilatant zones (vein widths from 2 to 3 m) representing increased brecciation/replacement mineralization and fissure vein mineralization. These wider zones also tend to be the richest part of the vein system - probably due to multiple hypogene enrichment with successive episodic stages.

2) The bulk of the ore mined on Hill 2 was taken from shoots where vein attitudes are between 45° and 55°; vein dips greater than 55° and less than 45° were less favored.

3) Variations in strike also exerted influence on ore shoot formation: fault plane deflections toward the hangingwall created somewhat wider dilation zones. Ore shoot formation on right-hand deflections from the average strike of the fault were a consequence of right-lateral, oblique movement of the fault.

4) Post-mineral faults controlled mining and exposure of the system as indicated by the correlation of the shape and orientation of stopes within the ore shoots (see Figs. 17 and 18).

Explanation for Figure 18

A: Dip profile L - section of Telegraph system Hill 2.

Features

- Dome-like form of contours on the footwall on the normal fault at 2300 S probably represents a steady flattening of dip the 3860 ft. level, then a reversal, to steeper dips, to the 3800 ft. level.

- The overall horizontal pitch of dilatant zones caused by convex fault plane curvature towards the hangingwall is shown by "ridge lines" marked with antiform symbols. Note that high grade ore shoots, from drill hole data and projection of stopes, are distributed about the ridge lines where dip contours vary between 40° and 50°.

- Truncation of contour lines are interpreted as disruption of the main fault trend by post-mineral faulting as documented on the surface (see Plt. 4), underground(see Fig. 31) and from vein-contour maps (not presented here).

B: Plan view (A-A'), of true shape and width of vein from drill hole data.

- Vein widths are presented accross average dip to give true representation of shape and width. Note that abrupt curvature toward the footwall appears to form pinch zone, and the wider portions of the vein occurs where curvature is towards the hangingwall.

- Truncation of contours is interpreted as offsets by post mineral faults, as discussed above.

C: Vertical cross-sectional view of dip contours along B-B'.

- Evenly spaced, horizontal contours from the 3860 ft. level to the 3750 ft. level probably indicate a steady flattening of dip over this interval, while widely spaced contours above 3860' level indicate a steeper overall dip. This is generally the trend from 2200 S to 2300 S.

- Inflection point of the profile represents the ridge line of the hangingwall-directed curvature.

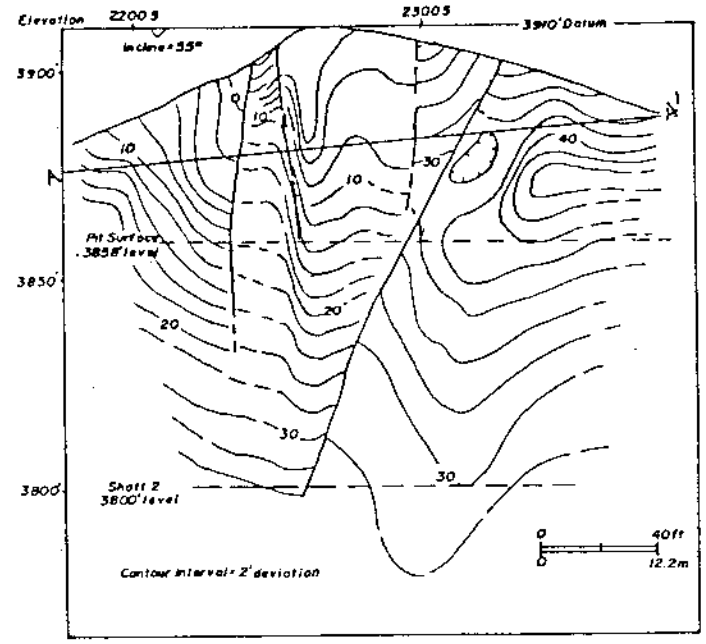

VEIN CONTOUR SECTION

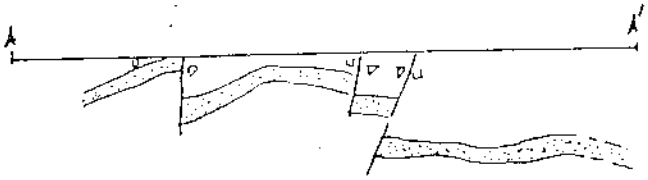

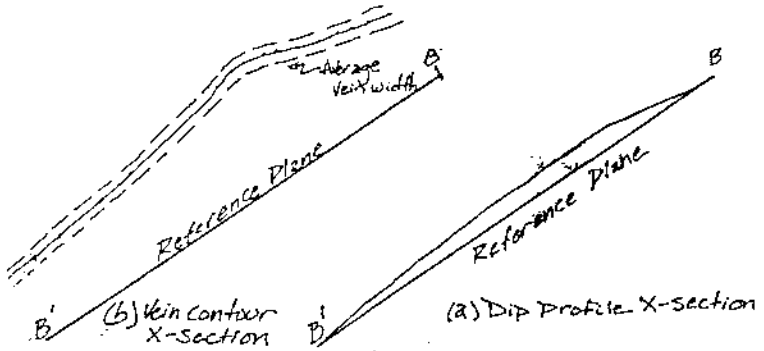

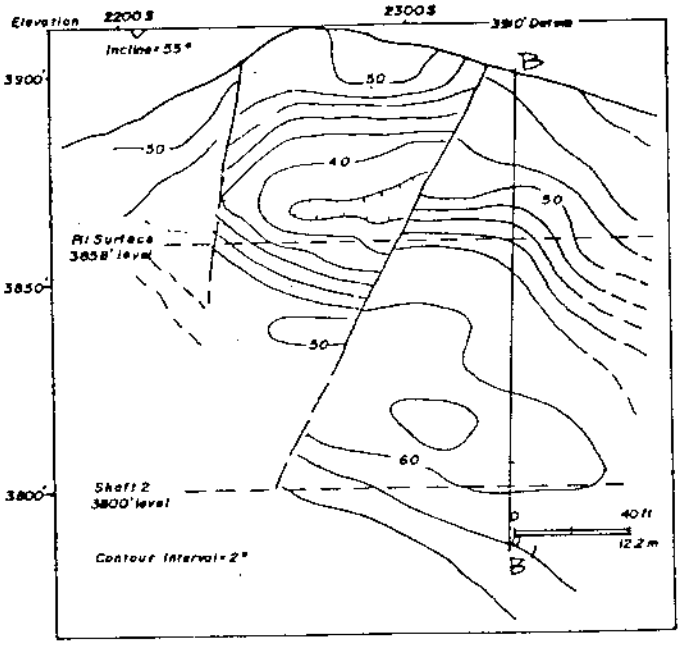

DIP PROFILE SECTION

Figure 18. Dip-contour L-section (A) with horizontal(B) and vertical(C) cross sections. See Plate 5 for location of datum reference plane and Appendix A for construction details.

Very Low Frequency Electromagnetic Survey

VLF-EM geophysical survey was conducted at the Telegraph Mine as this geophysical tool has been found to be effective in prospecting for buried sulfide bodies, and for mapping contrasting rock types and buried faults (Teleford, 1976; Paterson and Ronka, 1969). The method provides a sensitive, inexpensive and time-effective way to investigate buried, water-filled geologic structure that respond as weak electromagnetic conductors. Appendix B discusses variable parameters and survey procedures and Frasier filtering techniques.

A contour map of filtered VLF-EM dip data and field strength peaks was constructed on grid base maps of the Telegraph system (Plt. 6). In-phase dip, quadrature and field-strength profiles across the system were plotted by computer from LOTUS files (Fig. 19). The profiles show the correlation between the dip crossovers and field strength peaks.

As Plate 6 and Table 2 illustrate, contoured "crossover" peaks form straight ridges that approximate the average N 28° E to N 30° E strike of the buried Telegraph system. Ridge asymmetry yields some indication of fault dip; more closely spaced contours occur on the footwall side of the structure and spacing decreases on the down-dip side.

TABLE 2

Features of Telegraph Fault VLF-EM Surveys

PROVINCE	FEATURE	INTERPRETATION
Southern Section:		
2660 - 3000 S	parallel anomaly ridges	en echelon shears or offshoot shear veins.
2600 S	disruption of contours post-mineral fault.	northeast striking,
2300 - 2600 S	30.5m contour ridge offest to the west	down-dip estension of water-saturated surface.
2100 - 2250 S	change in contour ridge	offsetting structure
2200 - 2000 S	N 70° E trending contour	offsetting fault.
1800 - 1950 S	strong anomaly (Fig. 34)	represents higher sulfide content of local ore (?).
Northern Extension		
1300 - 900 S	symmetrical anomaly ridges	45° constant dip (?).
1300 - 400 S	N 12° - 16° E strike of ridge anomaly	undulatory nature of fault curvature
1300 - 200 S	good correlation between ridges and field strength	peiziometric surface accurately located
200 S	N 28° E strike change	curvature to parallel main trends

TABLE 2

Features of Telegraph Fault VLF-EM Surveys (Plate 6)

PROVINCE	FEATURE	INTERPRETATION
Southern Section:		
2660 - 3000 S	parallel anomaly ridges	en echelon shears or offshoot shear veins.
2600 S	disruption of contours post-mineral fault.	northeast striking,
2300 - 2600 S	30.5m contour ridge offset to the west	down-dip extension of water-saturatedsurface.
2100 - 2250 S	change in contour ridge	offsetting structure
2200 - 2000 S	N 70° E trending contour	offsetting fault.
1800 - 1950 S	strong anomaly (Fig. 19)	represents higher sulfide content of local ore (?).
Northern Extension		
1300 - 900 S	symmetrical anomaly ridges	45° constant dip (?).
1300 - 400 S	N 12° - 16° E strike of ridge anomaly	undulatory nature of fault curvature
1300 - 200 S	good correlation between ridges and field strength	piezometric surface accurately located
200 S	N 28° E strike change	curvature to parallel main trends

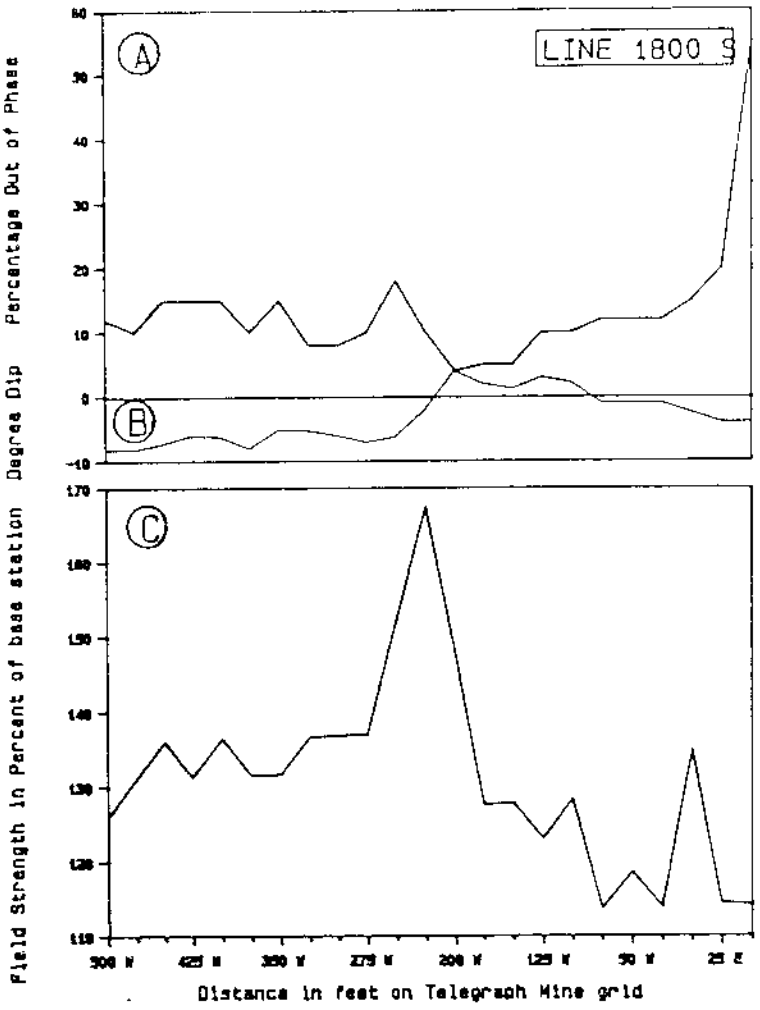

Figure 19. VLF-EM survey profiles at 1800 ft. S. on Telegraph Mine grid running W - E on Plate 6 - Southern Section. (A) Indicates the percentage "out of Phase" of horizontal field component, (B) indicates the vertical dip component, in degrees converted from E-W dip measurements (E dips are negative, W dips are positive). (C) Shows the local field strength. Note that the classic cross-over behavior of percent out-of-phase and vertical component dip, and their correlation to local maximum field strength.

Ore Control Summary

Dilatant zones, acting as open conduits or as breccia-filled high permeability zones, are the foci of all mineralization along the fault. Key elements in the location, shape, width, depth, and continuity of dilatant zones as ore shoots include: 1) the location and attitude of aplite dikes near the fault trace, and 2) fault zone pattern and shape.

Association of Dikes with Fault Zone

The spacial association between Mesozoic aplite dikes, faults and mineralization is a districtwide phenomena. The dikes apparently provided convenient surfaces of structural weakness along which Cenozoic faults and fracture systems propagated. Although mineralized fault planes are not restricted to or dependent on dike presence, width or attitude, dikes did act as local deflectors of the fault attitudes due to their influence in distributing applied stress in an inhomogeneous manner. Such deflections, when directed away from the fault footwall, were favorable to the development of wider fault dilation, whereas deflections toward the footwall were unfavorable.

Fault Zone Pattern

Fault zone mineralization is locally irregular but generally along strike, changes in attitude result in consistent trends. As mapping (Table 1 and Fig. 17), fault plane contours

(Fig. 18) and VLF patterns (Table 2) suggest, strike deflections toward the footwall (to the East) tend to close-off open dilatant areas and swings toward the hangingwall (to the West) favor wider breccia and dilatant zones forming "shingle" en-echelon breccia-veins (see Hill 1 and 2, Plt. 4) and cymoid-style branching (see Hill 1 and 2 ,Plt. 4). Radical strike deflections toward the hangingwall accentuate vein branching and the development of "horsetail"-style, fan-shaped vein system terminations at the north end of the Northern Extension exposures and south end of Hill 1.

Fault zones exhibiting all five mineralization stages occur only within N 25° E to N 35° E trend and between 45° to 55° SW dip along the fault surface. En-echelon breccias are usually of similar strike and dip, whereas the branching veins off the main structure tend to be of more northerly or easterly strike and higher angle of dip. Post-mineral fault orientations differ markedly from hangingwall joint and vein trends. They are strongly oriented N 55°- 85° W as illustrated on Plate 3, Plate 4, . These faults do not show significant quartz vein infilling.

These features reflect the effects of low angle oblique-slip kinematics operating along the Telegraph fault that opened-up the structure to through-going hydrothermal fluids (Jaroszewski, 1984). The spacing, width and shape of mineralized breccia-veins are directly related to the location and attitudes of the original breaks along the fault trace. The proposed formation model in

Section X discusses the evolution of these structural features.

IV

DISTRICT MINERALIZATION

Over seventy five fissure veins and silicified breccias, excluding the Telegraph system itself, are exposed in the Telegraph area. All of the veins are developed along faults or major fracture systems within quartz monzonite and quartz diorite; often also spatially associated with aplite dikes (Sec. 17 of Plt. 3). In order to gain a more complete understanding of the Telegraph system itself, these mineralized structures were examined to:

1) determine relationships between the host structures, mineralogy, or alteration effects between the district-wide veins and the Telegraph, and

2) locate, through specific sampling procedures, those systems with particularly anomalous precious metal content or characteristic trace elements.

Analytical Methods

Mapping and sampling within the study area was designed to test veins that showed typical upper-level epithermal assemblages. Quartz-carbonate, gossan-bearing fissure veins and silicified breccias were analyzed for the typical epithermal trace element suite - Hg, Sb, As, and Cu - to discover whether the dispersion of trace elements reflect Au and Ag content. Economic considerations resulted in a sampling bias toward

structures exhibiting relatively strong alteration and mineralization; the conclusions drawn in this report are therefore only preliminary.

Geochemical distributions were constructed from samples collected throughout the district to compare metal concentrations of Gold Dike and Telegraph breccias with unrelated fissure-veins. The small size and large variability of the sample population precluded the determination of "threshold" statistics (for identifying anomalous metal values) through rigorous means such as log-probability distribution plots (Sinclair, 1974). Although a rigorous statistical treatment of the data was not attempted, cumulative frequency graphs (Figs. 20 and 21), summary trace element statistics (Tables 4 and 5) and correlation matrices (Tables 6 and 7) were constructed from frequency distributions of log-transformed assay results on LOTUS 1-2-3 files (see Appendices C and D). Since an anomalous population is often considered to represent the upper 5% of the distribution (Lepeltier, 1969), an approximation of the anomalous precious-metal population can be read directly from Figures 20 and 21.

Breccia Systems

Mineralized tectonic and tectono-hydrothermal breccia deposits occur primarily along the Gold Dike trend, the Owl Shafts and in the fault zones southeast of the Aqua Dulce workings (Plts. 1 and 2). The breccias are developed in dilatant sections of fairly well defined but discontinuous faults hosted in quartz

monzonite and quartz diorite rocks. In the Gold Dike area, the breccias and host structures are spatially associated with the occurrence of Mesozoic aplite dikes.

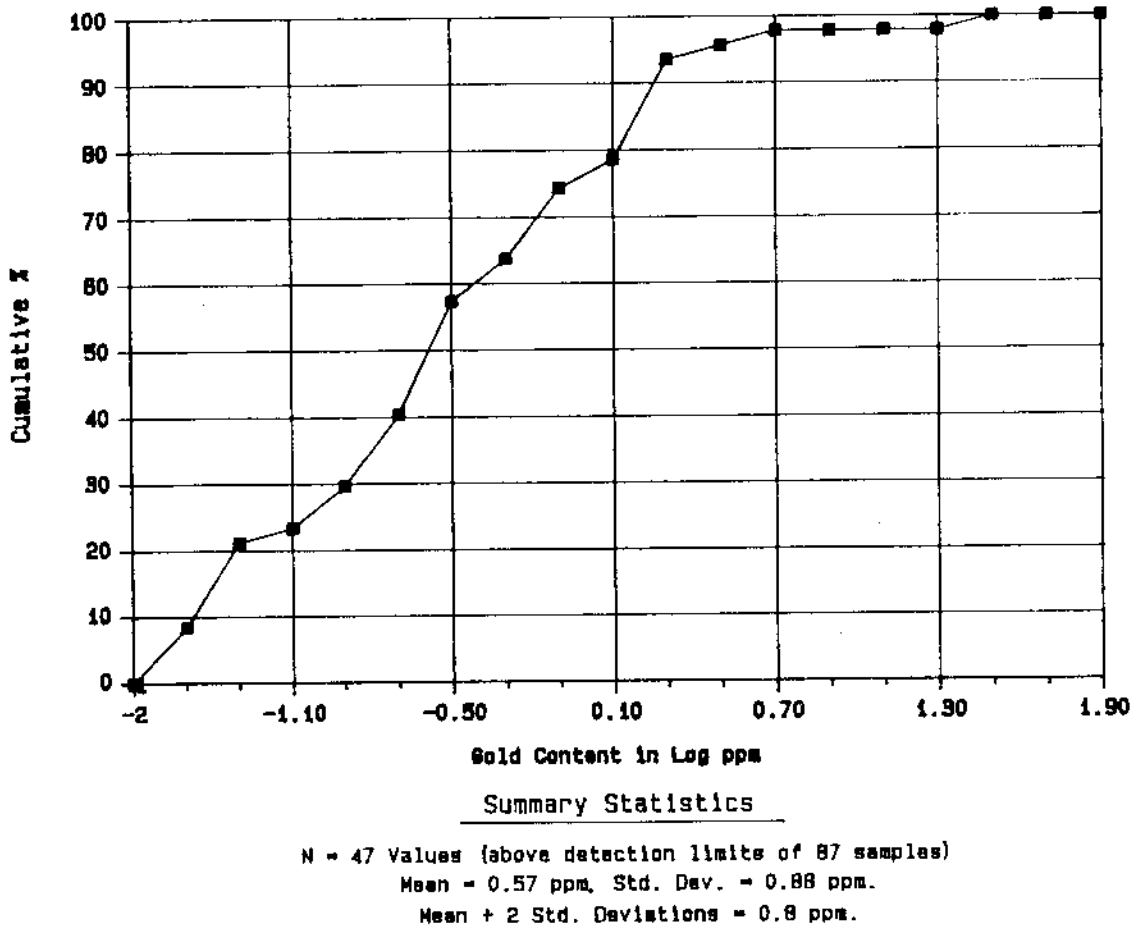

Figure 20. East Halloran Springs District gold distribution. This distribution is exclusive of the Telegraph Mine samples or any samples located on mine grid maps, Plate 5.

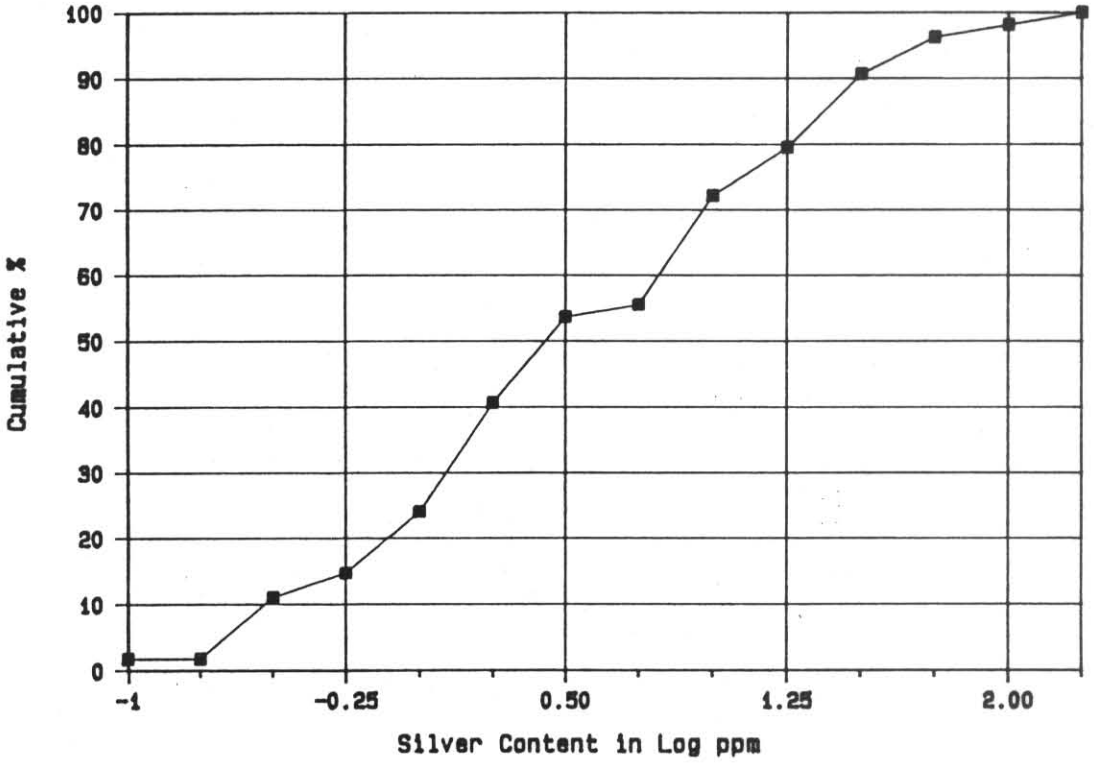

Summary Statistics

N = 54 Values (above detection limits of 87 samples)
Geo. Mean. = 0.52 ppm, Std. Dev. = 0.72 ppm.
Mean + 2 Std. Deviations = 1.88 ppm

Figure 21. East Halloran Springs District silver distribution. This distribution is exclusive of the Telegraph Mine.

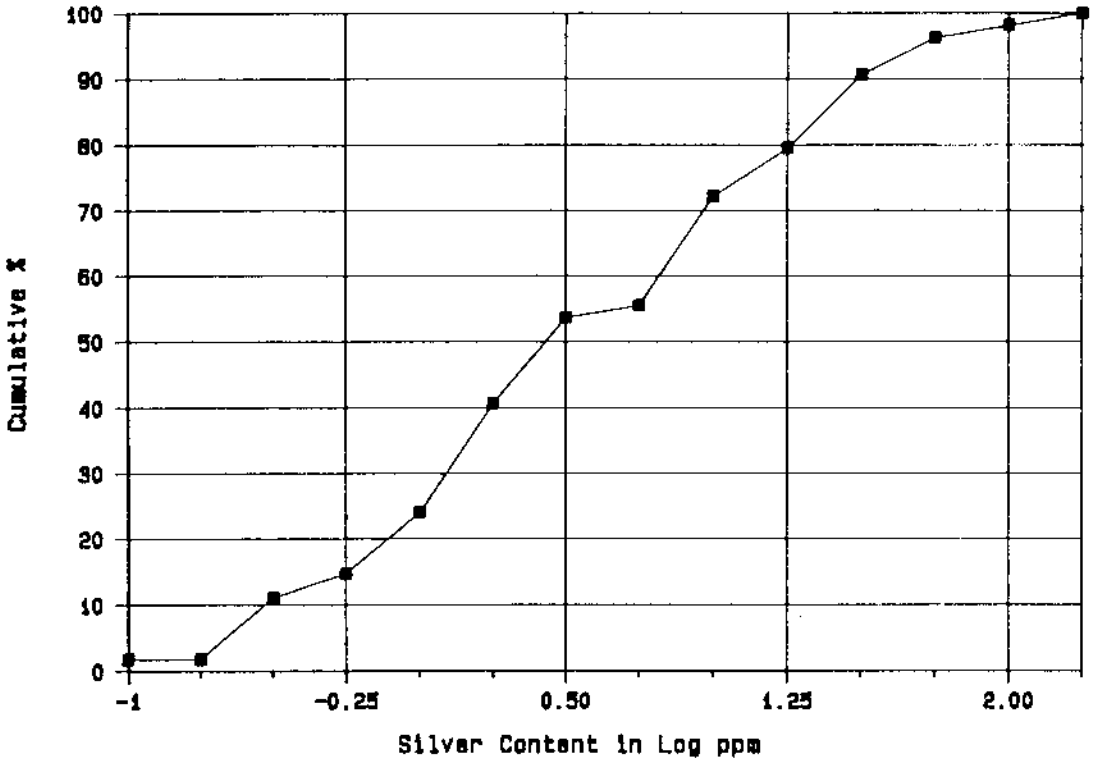

Summary Statistics

N = 54 Values (above detection limits of 87 samples)
Geo. Mean. = 0.52 ppm, Std. Dev. = 0.72 ppm.
Mean + 2 Std. Deviations = 1.88 ppm

Figure 21. East Halloran Springs District silver distribution. This distribution is exclusive of the Telegraph Mine.

Excluding the Telegraph system itself, the width of mineralized breccias seldom exceed 1 m (in the Gold Dike area); width and strength of mineralization and selvage alteration exhibits great differences along host fault exposures. As noted with the Telegraph breccias, considerable diminution of fragments, an increase in the ratio of hydrothermal cement material to rock flour + rock fragments and evidence of re-brecciation with episodic mineralization are common in the wider portions to the fault zone. This is especially true in the Gold Dike workings.

The Gold Dike hydrothermal breccias developed along a N 55°-60° E trend (see Fig. 22, and Plt. 5), show the development of an alteration/mineralization assemblage sequence very similar to the Telegraph Stages III, IV, V and VI. An early quartz-chlorite-adularia stage breccia cement assemblage is followed by quartz-sericite-pyrite mineralization and late stage vug-filling quartz and quartz-carbonate assemblage (Fig. 23). Ten of the fifteen regional samples containing over the 0.57 ppm mean Au content (Fig. 20) are found along the Gold Dike trend, and ten of the eighteen Gold Dike samples are above average in precious metal content (Appendix C). Half of these are concentrated in quartz-sericite-pyrite altered breccias; these samples average 1.33 ppm Au, from 0 to 41 ppm Ag, 3.8 ppm Hg and from 0 to 55 ppm As.

Both gold and silver apparently occur in submicron particles; no discrete crystals were seen in oxidized samples from

the deposit. Preliminary fluid inclusions temperature measurements for the quartz-sericite-pyrite assemblage are approximately 260° to 330°C, and 200° to 238°C for the quartz-adularia-pyrite assemblage (see Table 11, Section VI "Fluid Inclusions"). Fluid transportation and deposition conditions were probably similar to those as described for Stages IV to V for the Telegraph system (see Section VII).

Tectonic breccias developed along high angle faults in southwestern Section 20 and on the Owl Shafts trend in Section 16 (Plt. 2), are distinctly different from the Telegraph/Gold Dike group. Hematitic-chalcedonic quartz-healed tectonic breccias in Section 20 (Plt. 2) apparently developed along a pre-existing aplite dike. Angular 0.2 to 3cm angular aplite clasts are cemented by a small amount of cryptocrystalline quartz (Fig. 24). Aside from quartz cementation, the breccia is essentially unmineralized.

The blue-grey microbreccias of the Owl Shafts occur along a 0.5m-wide N 20° E fault. One to 5mmm angular quartz monzonite clasts are supported by a matrix of fine rock flour, cryptocrystalline quartz and finely-disseminated sulfides (Fig. 25). Very few unoxidized samples were found; polished sections of TP-80 revealed that early 0.10mm pyrite cubes were subsequently replaced by chalcopyrite and galena. Samples 601 to 606 indicate that these breccias do not contain significant disseminated precious metals (see Appendix D).

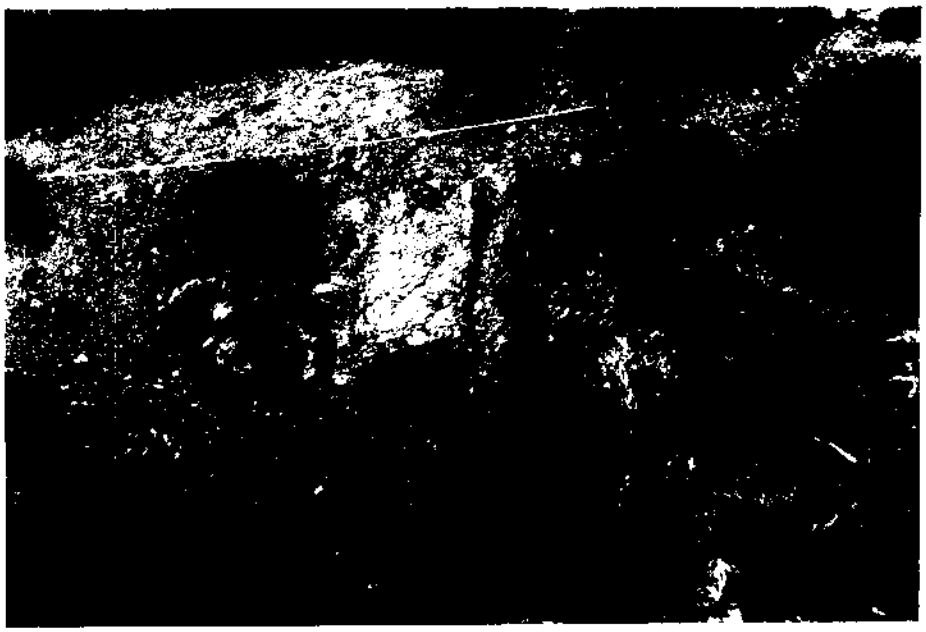

Figure 22. Surface exposure of the Gold Dike system in the extreme west edge of Sec. 17. The view is to the NE. Note the silicified breccia zone adjacent to the light colored aplite dike (footwall side) and the extensive argillized zone (footwall side).

Figure 23. Stained slab of quartz-sericite-pyrite dominant Gold Dike microbreccia. Sample from the inner part of the breccia zone (at 12" chisel on outcrop). Note the similarity to Telegraph Mine specimens (Chapter VII).

flour, cryptocrystalline quartz and finely-disseminated sulfides (Fig. 25). Very few unoxidized samples were found; polished sections of TP-80 revealed that early 0.10mm pyrite

Figure 22. Surface exposure of the Gold Dike system in the extreme west edge of Sec. 17. The view is to the NE. Note the silicified breccia zone adjacent to the light colored aplite dike (footwall side) and the extensive argillized zone (footwall side).

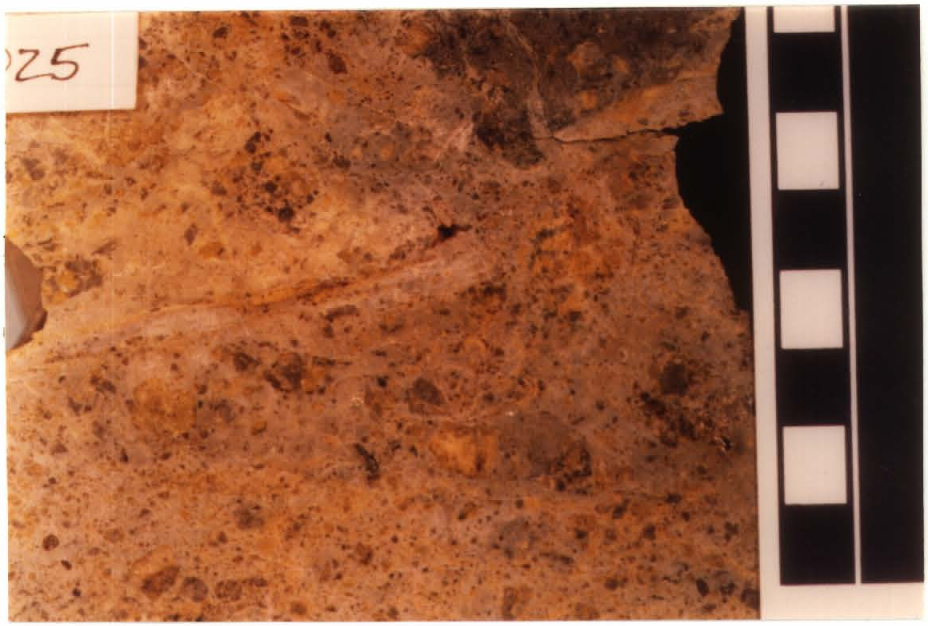

Figure 23. Stained slab of quartz-sericite-pyrite dominant Gold Dike microbreccia. Sample from the inner part of the breccia zone (at 12" chisel on outcrop). Note the similarity to Telegraph Mine specimens (Chapter VII).

flour, cryptocrystalline quartz and finely-disseminated sulfides (Fig. 25). Very few unoxidized samples were found; polished sections of TP-80 revealed that early 0.10mm pyrite

FISSURE VEIN SYSTEMS

Three distinct types of fissure vein deposits are found throughout the district. These types are distinguished by dominant hydrothermal mineralization assemblages:

1) low-sulfide, vug-filling veins occur mainly in high-angle "chaotic zone" structures to the east of the Telegraph system (Fig. 26),

2) gossan-bearing, high temperature Cu-Pb-Ag quartz veins that are concentrated in high-angle faults in quartz diorite (southeast Sec. 21 and in the Aqua Dulce area, Plt. 2), and

(3) Quartz-Manganiferous calcite veins (Fig. 27) are found as late stage fissure-filling deposits along the main breccia deposits (at the Telegraph and Gold Dike) and in discontinuous faults northeast of the Gold Dike (Plt. 2).

Width and precious metal content of these quartz and quartz-carbonate veins ranges greatly. Type (1) veins, in the "chaotic zone" carry very little significant metal at all, whereas type (2) gossans are characteristically enriched in Cu-As-Ag and locally carry significant Au (see sample 1014, Appendix D). For example, the 0.5 m wide, N 60° W trending gossan-bearing fissure vein system in Sec. 21 (Plt. 2) contains 0.50 ppm gold and 41.0 ppm silver (sample 634, Appendix D); and the gossan-rich, thin veins at the Rattler Shafts run the highest in Au (20.43 ppm). Type (3) veins can be anomalous in both gold and

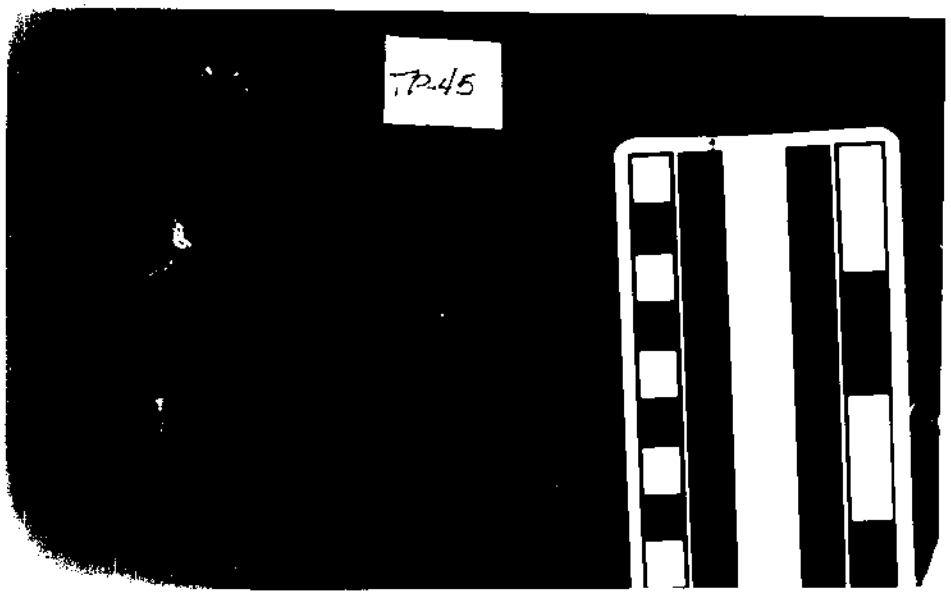

Figure 24. Tectonic breccia, cemented by chalcedonic quartz, developed in aplite. Note the larger fragment size, greater angularity and greater homogeneity of fragment type than the Telegraph mineralized breccias. Scale in cm.

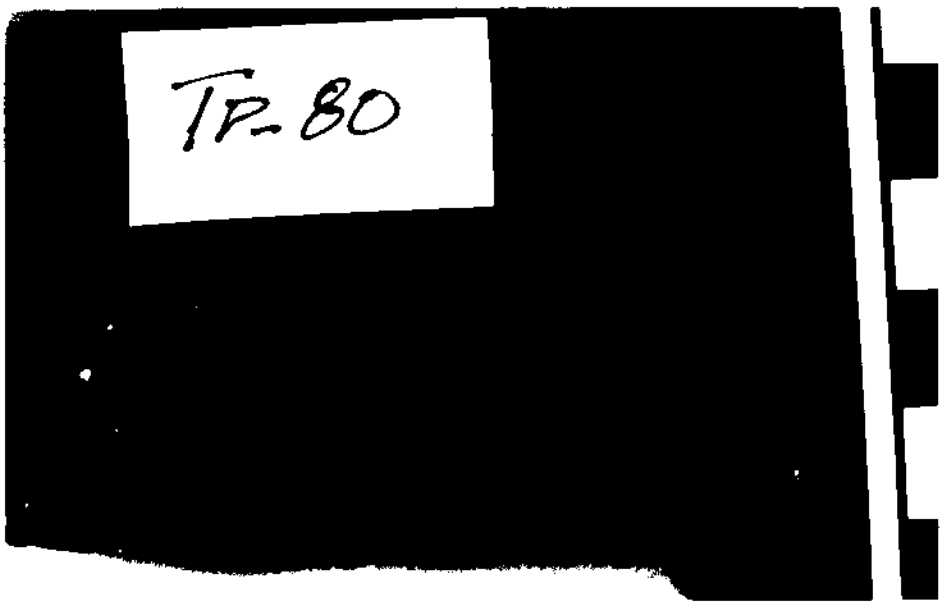

Figure 25. Hand sample of Owl Shaft silicified microbreccia. Note blue chalcedonic quartz matrix and unaltered quartz monzonite fragments. Most of the rock is unoxidized, containing original galena, chalcopyrite and pyrite encased in quartz. Scale in cm.

Figure 24. Tectonic breccia, cemented by chalcedonic quartz, developed in aplite. Note the larger fragment size, greater angularity and greater homogeneity of fragment type than the Telegraph mineralized breccias. Scale in cm.

Figure 25. Hand sample of Owl Shaft silicified microbreccia. Note blue chalcedonic quartz matrix and unaltered quartz monzonite fragments. Most of the rock is unoxidized, containing original galena, chalcopyrite and pyrite encased in quartz. Scale in cm.

Figure 24. Tectonic breccia, cemented by chalcedonic quartz, developed in aplite. Note the larger fragment size, greater angularity and greater homogeneity of fragment type than the Telegraph mineralized breccias. Scale in cm.

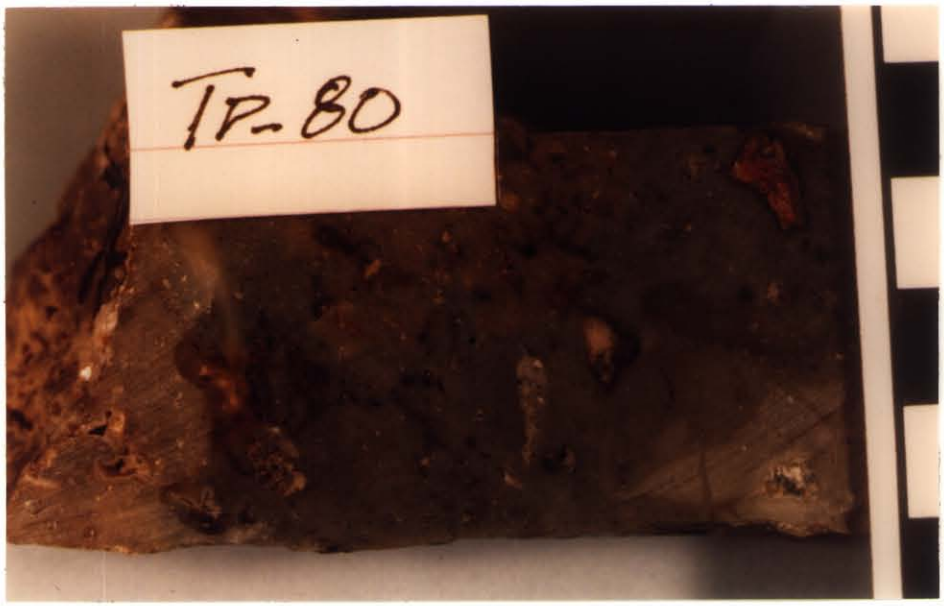

Figure 25. Hand sample of Owl Shaft silicified microbreccia. Note blue chalcedonic quartz matrix and unaltered quartz monzonite fragments. Most of the rock is unoxidized, containing original galena, chalcopyrite and pyrite encased in quartz. Scale in cm.

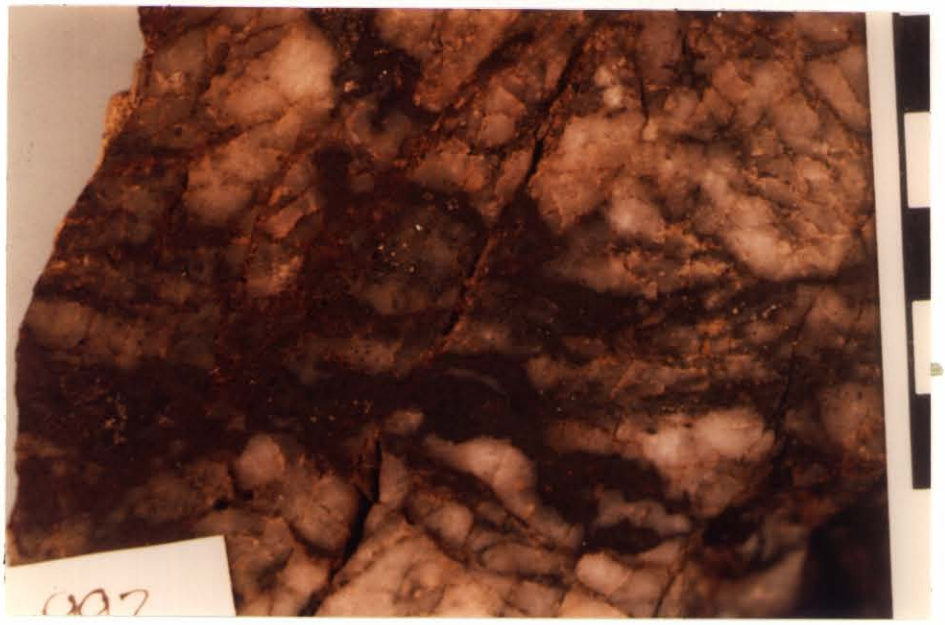

Figure 26. Typical base metal, gossan-bearing bull quartz fissure vein.

Figure 27. Outcrop of typical quartz-manganiferous calcite vein in quartz monzonite in western Section 17. Scale in cm.

the "chaotic zone" carry very little significant metal at all, whereas type (2) gossans are characteristically enriched in Cu-As-Ag and locally carry significant Au (see sample 1014, Appendix D). For example, the 0.5 m wide, N 60° W trending gossan-bearing fissure vein system in Sec. 21 (Plt.

silver. The 20 cm black calcite-quartz veins to the south of Rattler Shaft, locally following the Gold Dike breccia trend, are anomalous in gold (sample 1024 =0.82 and 1040= 1.17 ppm Au) and tend to be high in silver (sample 1024= 35.31 and 1040 = 159.09 ppm Ag). It is not unusual for manganiferous calcite to be anomalous in silver (Hewitt and Radtke, 1967; Andrusenko, 1979).

METAL GEOCHEMISTRY AND DISTRIBUTION

Central tendency statistics in Tables 4 and 5 show that Gold Dike breccias contain significantly elevated concentrations of all trace elements and precious metals compared to district fissure-veins. In general, distributions indicate that breccias show less random variability in metal content, as evidenced by their greater tendency to follow log-normal behavior (less dispersion about the geometric mean and lower coefficients of deviation for all elements.)

Trace element distributions seem to indicate that strong positive correlations do not exist between precious metal concentrations and the usual epithermal suite of pathfinder elements in either breccia or vein deposits. Indeed, gold shows a significantly negative correlation with arsenic in Gold Dike breccia samples, whereas copper seems to form a strongly positive trend with gold (Table 6). In both veins and breccias, gold seems to respond marginally with silver (Tables 6 and 7). It is clear that gold itself is the only reliable pathfinder for gold in district deposits.

Given that alteration mineralogy and fluid inclusions favor an epithermal temperature regime for the Gold Dike system- and most quartz vein deposits- the correlation matrices results indicates a more complex natural dispersion of elements than is found in many epithermal deposits. For example, gold may be associated with chalcopyrite in the primary breccia matrix or alternatively, copper may have been simply introduced into precious metal bearing rock by supergene processes.

Table 3. Metal distribution summary statistics for Gold Dike system breccias samples. Assay results (Appendix C) were tabulated and transformed into concentrations, in ppm, from log distributions for each element. The mean, median and mode statistics are all geometric in accordance with approximate log-normal behavior of the distribution. Detection limits for Au, Ag, As and Cu are 0.02 ppm, and 5.0 ppm for Hg. N = 15.

Element	Range (ppm)	Mean (ppm)	Median (ppm)	Mode (ppm)	Std. Dev.
Au	0.17 - 20.43	0.78	1.00	0.51	0.54
Ag	0.02 - 159.09	12.30	6.46	39.81	5.62
As	5.00 - 75.00	11.22	10.00	6.31	2.40
Hg	0.27 - 10.40	2.04	1.58	1.58	1.74
Cu	10.00 - 695.00	37.15	39.81	100.00	4.27

Table 4. Metal distribution summary statistics for districtwide Tertiary mineralization. This distribution is exclusive of Telegraph or Gold Dike mineralization. Log distributions were constructed from Appendix D, all statistics below are geometric. Detection limits for Au, Ag, As and Cu are as reported in Table 4.
N = 44.

(Table 4. cont.)

Element	Range (ppm)	Mean (ppm)	Median (ppm)	Mode (ppm)	Std. Dev.
Au	0.02 - 1.50	0.13	0.02	0.04	0.32
Ag	0.20 - 41.00	6.42	1.70	1.70	13.16
As	5.00 - 85.00	14.09	5.00	5.00	9.27
Hg	0.02 - 2.50	0.19	0.09	0.20	0.27
Cu	0.01 - 870.00	104.78	10.00	15.00	215.90

Table 5. Metal correlation coefficient ("r" statistic) matrix for Gold Dike breccia samples. At the 5% level of significance, r values exceeding 0.51 would indicate significant correlation between values for this population (based on data of Snedecor and Cochran,1967). Results were calculated on LOTUS program by Dougherty, 1986.

	Au	Ag	As	Hg	Cu
Au	1.00	0.45	-0.59	0.27	0.70
Ag	0.45	1.00	-0.01	0.55	0.46
As	-0.59	-0.01	1.00	0.23	-0.55
Hg	0.27	0.55	0.23	1.00	0.28
Cu	0.70	0.46	-0.55	0.28	1.00

Table 6. Metal correlation coefficient matrix for district-wide vein samples. At the 5% level of significance, r values exceeding 0.30 would indicate significant correlation between values for this population (based on data of Snedecor and Cochran, 1967). N = 44.

	Au	Ag	As	Hg	Cu
Au	1.00	0.28	0.08	0.04	-0.11
Ag	0.28	1.00	0.16	0.01	-0.09
As	0.08	0.16	1.00	0.42	0.25
Hg	0.04	0.01	0.42	1.00	-0.09
Cu	-0.11	-0.09	0.25	-0.09	1.00

V

TELEGRAPH MINE ALTERATION AND MINERALIZATION

The Telegraph breccia vein system is composed of rebrecciated wall rock fragments replaced and cemented by five stages of hydrothermal fluids. The main breccia zone ranges in width from 0.3m to 3.3m and is bounded by hydrothermally altered wall rocks extending 0.5m to 24m from the main zone. Each distinct structural-mineralizing event is documented by its inclusion in intraclasts of subsequent rebrecciated assemblages. Central regions of the fault zone contain a larger percentage of rebrecciated clasts, smaller clast size ranges, better "sorting" of transported fragmental material and a higher percentage of open-space hydrothermal matrix. Peripheral regions consist of large, angular un-transported fragments (to 10cm) to angular blocks that show little translation, and are cemented with late-stage quartz (Stages IV and V), similar to the "crackle-breccia" of many investigators (Sillitoe,1985).

Telegraph breccia genetic classification is complicated by a record of consanguineous operation of mechanical fracturing and fluid flow with subsequent open-space and replacement mineralization. Figure 28 illustrates intra-zonal variations between tectonic fragmental material, including weakly altered host rock "clasts" and "rock flour", and hydrothermally derived "matrix" including secondary quartz, adularia, pyrite, sericite, chlorite, illite-montmorillinite clays. Careful petrographic examinations of many breccia samples was required

Location	Inner Footwall	Outer Footwall	Silicified Breccia
Alteration Zone	Propylitic to weak Argillic	Fresh Rock to weak Propylitic	Quartz - Illite to Quartz - Sericite
Width Main :	0.1 to 2.0 m	1.0 to 9.0 m	0.6 to 3.3 m
Width North :	0.5 to 2.0 m	1.0 to 6.0 m	0.3 to 1.5 m
Effects on :			
Quartz	Nil to locally Augmented	Nil	Greatly Augmented
Plagioclase	Montmorillinite(100%) to Sericite (0 - 80%)	Montmorillinite Calcite + Epidote	Illite (to 100%) Kaolinite (North)
K-feldspar	Sericite (trace) to Unaltered	Sericite (trace) to Unaltered	Sericite + Quartz (locally to 100%)
Biotite	Swelling Chlorite + Montronite	Mg-Chlorite+Rutile Montronite	Fe-Chlorite (added)
Hornblende	Chlorite	Mg-Chlorite + Epidote	Chlorite
Samples	910, 942, 961, 956	9078, 943	Numerous

Location	Inner Hangingwall	Outer Hangingwall
Alteration Zone	Argillic to strong Propylitic	weak Propylitic to Fresh Rock
Width Main :	0.3 to 3.5 m	3.0 to 15 m
Width North :	1.0 to 2.0 m	6.0 to 20 m
Effects on :		
Quartz	Nil to locally Augmented	Nil
Plagioclase	Montmorillinite to Sericite (0 to 5%)	Montmorillinite(0-50%)
K-feldspar	Sericite (trace) to Kaolinite (North)	Unaltered
Biotite	Swelling Chlorite	Mg-Chlorite to Unaltered
Hornblende	Chlorite + Montronite	Chlorite to Unaltered
Samples	912b, 918, 919, 920	965, 989

Table 7. Generalized diagram of Telegraph breccia-zone alteration. Clay identification was developed mainly through X-ray diffraction techniques, other mineral identification by through optical methods.

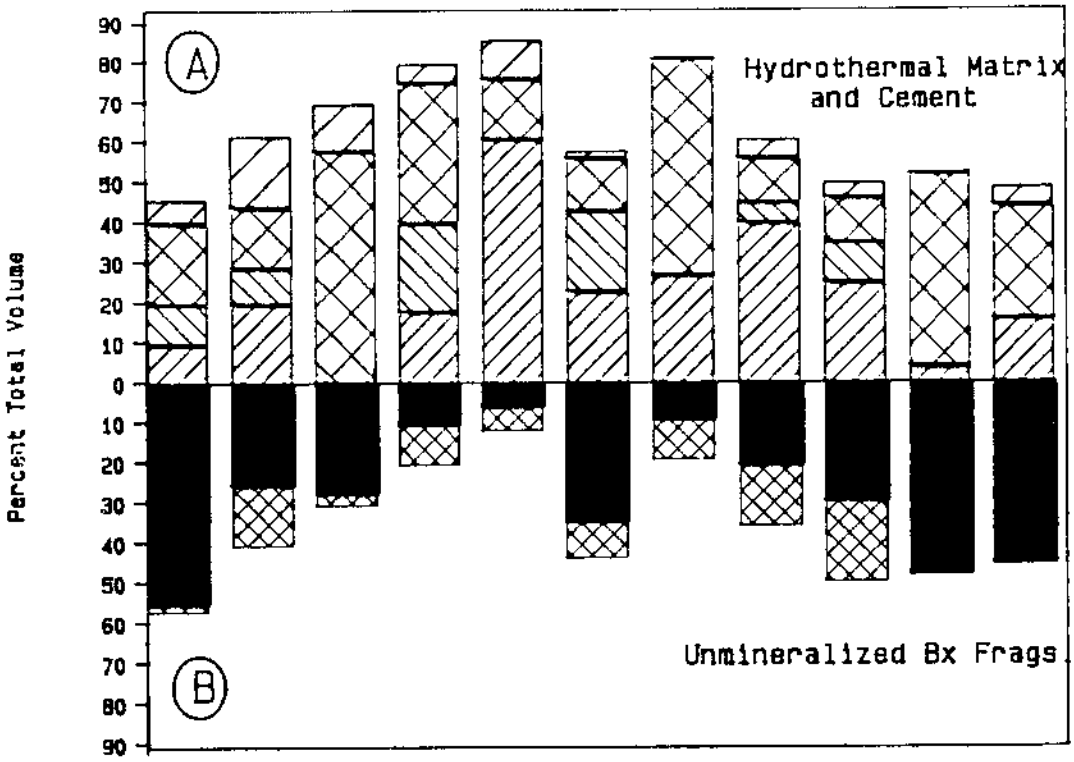

Figure 28. Volume distribution, in percent, of surface breccia-zone hand samples, Hill 2, Plate 5 - Southern Section. (A) total volume of introduced hydrothermal gangue including matrix cements of Stages III, IV and V breccia systems, and Stage VI fissure-filling veins. (B) Total volume of wall rock breccia clasts, either un-altered or weakly propylitically altered.

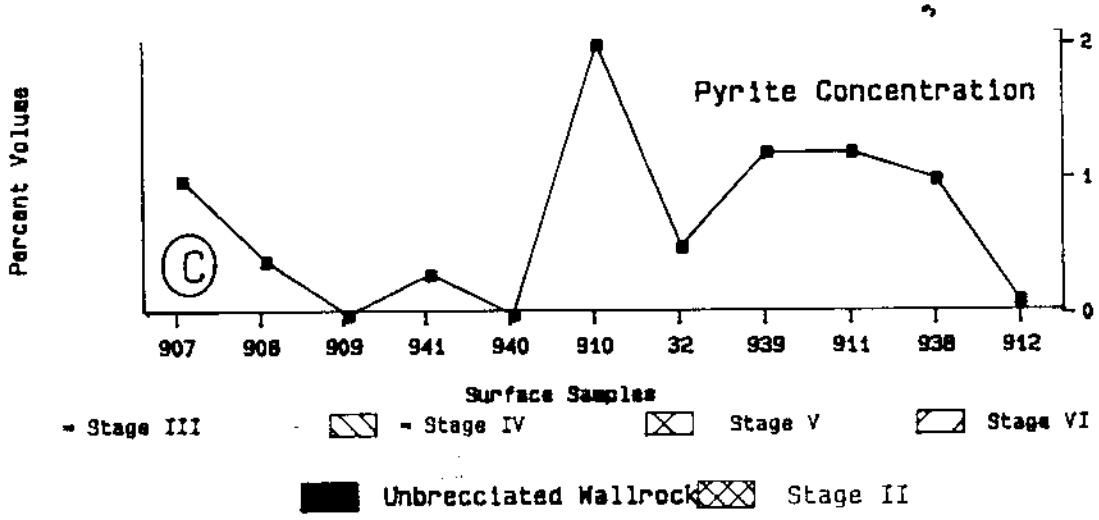

Figure 29. Pyrite distribution of Hill 2 breccias, in percent by volume.

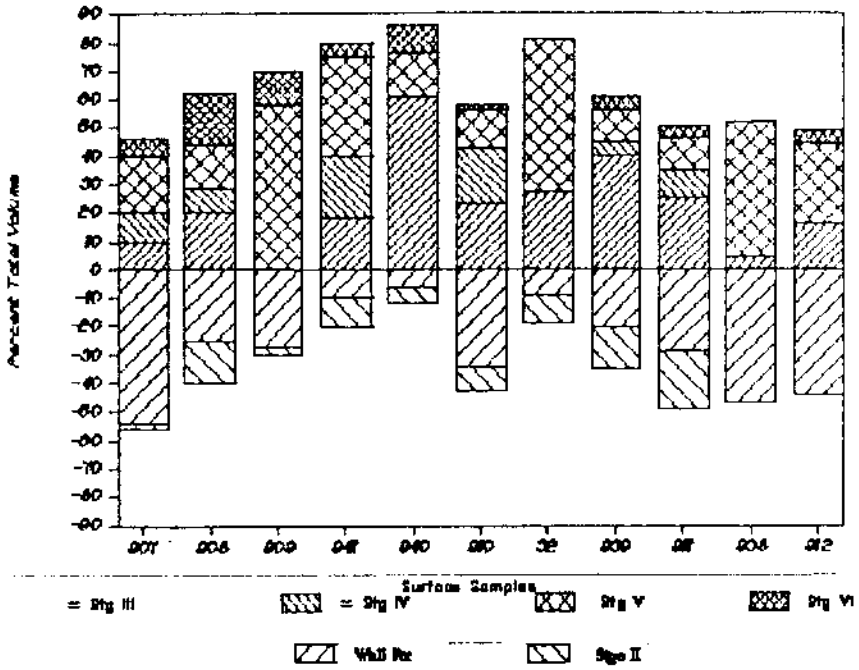

Figure 28. Volume distribution, in percent, of surface breccia-zone hand samples, Hill 2, Plate 5 - Southern Section. (A) total volume of introduced hydrothermal gangue including matrix cements of Stages III, IV and V breccia systems, and Stage VI fissure-filling veins. (B) Total volume of wall rock breccia clasts, either un-altered or weakly propylitically altered.

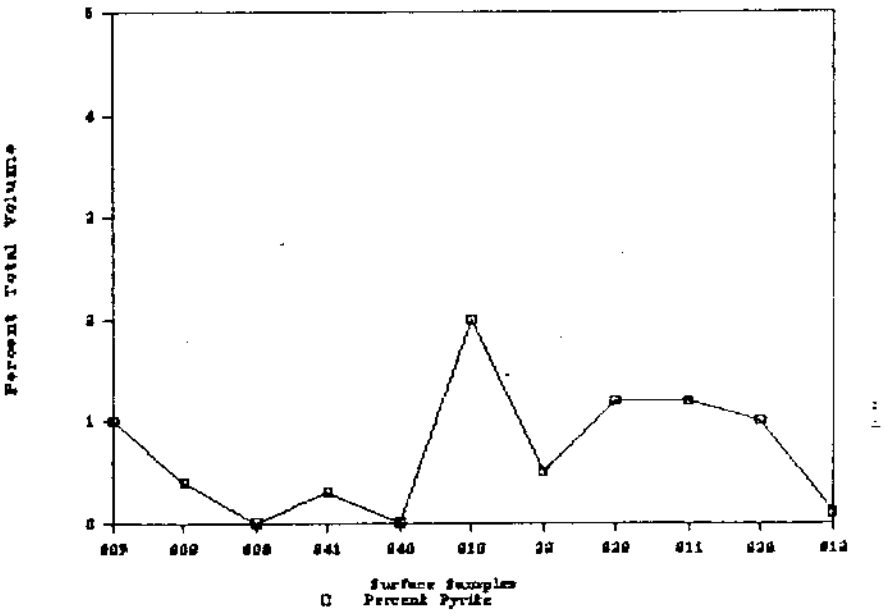

Figure 29. Pyrite distribution of Hill 2 breccias, in percent by volume.

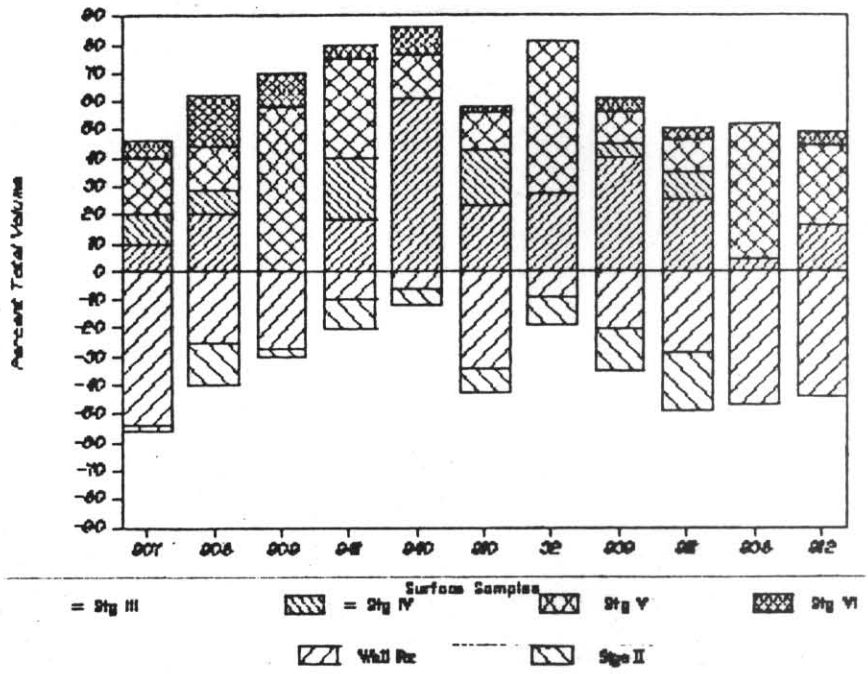

Figure 28. Volume distribution, in percent, of surface breccia-zone hand samples, Hill 2, Plate 5 - Southern Section. (A) total volume of introduced hydrothermal gangue including matrix cements of Stages III, IV and V breccia systems, and Stage VI fissure-filling veins. (B) Total volume of wall rock breccia clasts, either un-altered or weakly propylitically altered.

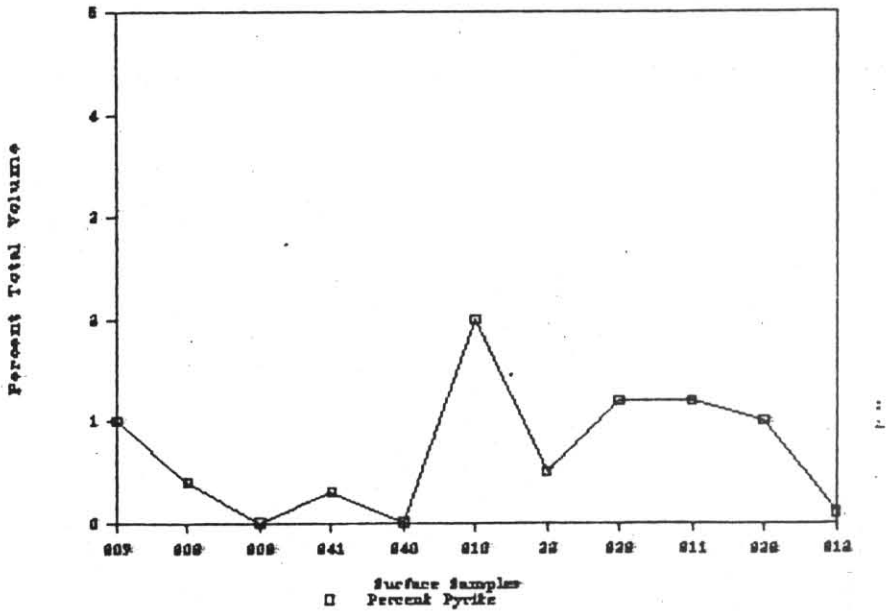

Figure 29. Pyrite distribution of Hill 2 breccias, in percent by volume.

HYDROTHERMAL MINERAL PARAGENESIS

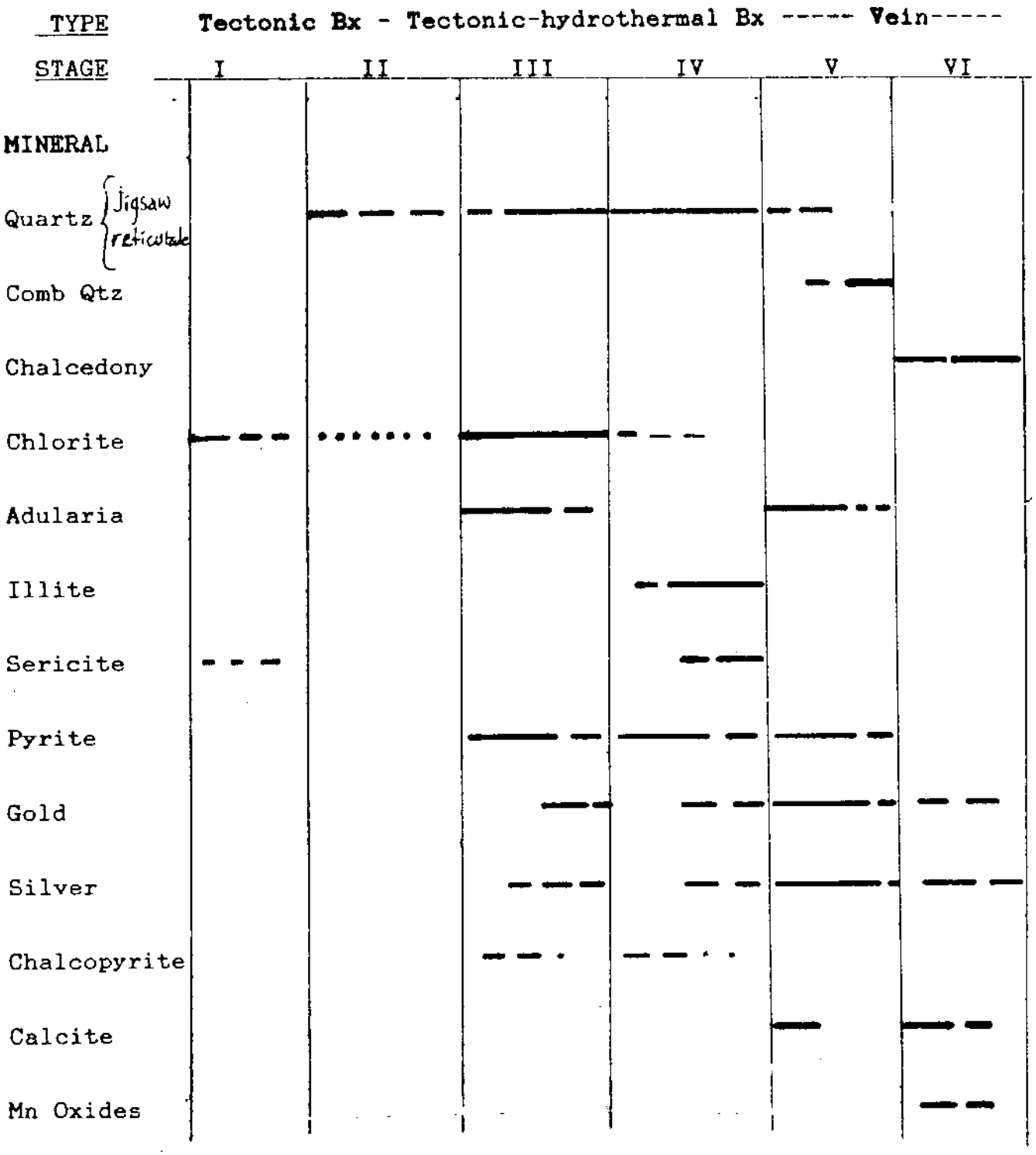

Figure 30. Paragenetic diagram of the Telegraph system mineralization.

to unravel the sequence of overprinted events, and it is clear that both hydrothermal and tectonic factors contributed to the physical fragment diminution of each stage. Broad-based genetic classifications of Sillitoe (1985) were used for proposing the "tectono-hydrothermal" designation for the Telegraph breccias.

HYDROTHERMAL ALTERATION SEQUENCE

Stage I

Initial oblique-slip normal faulting along the Telegraph system during Stage I provided the primary ground preparation for subsequent, through-going hydrothermal solutions. Wallrock quartz monzonite and alaskite-aplite fragments range in size from in-situ blocks (>10cm) to discrete angular rock clasts (0.02mm to 10mm). As intraclasts of later stages, the fragments commonly show significant size diminution and rounding. Homogeneity in clast size, shape and sorting of Stage I fragments is a function of re-brecciation such that central-zone segments contain a high percentage of discrete primary crystals of quartz monzonite and peripheral-zone breccias contain a higher percentage of quartz monzonite rock fragments.

Stage I solutions altered quartz monzonite plagioclase and biotite to a propylitic assemblage of montmorillinite-calcite-epidote and chlorite-nontronite in the breccia-zone wallrocks. Unaltered primary quartz and orthoclase are the main components of angular rebrecciated fragments and strongly comminuted rock

flour within the latter stages brecciation where they constitute from as little as 5% to 90% total volume (see Fig. 28). Wallrock and breccia-zone alteration of primary minerals is summarized in Table 8.

Stage II

Stage II tectonic events produced finely pulverized microbreccias and fault gouge with only minor hydrothermal alteration effects. As intraclasts within younger breccias, Stage II rock fragments constitute from 10% to 15% total breccia zone volume and are more common in the fringe segments of the zone (Table 8). Microbreccias are fragment supported, have a clast to rock flour matrix ratio of 4:1, and are moderately to poorly sorted. Fragments consist of very angular rebrecciated Stage I fragments (0.5mm to 2.5mm dia.), angular primary quartz (0.1mm dia.), angular orthoclase (0.1mm dia.), subangular to subrounded montmorillinite-replaced plagioclase (0.5mm) in a rock flour matrix of pulverized quartz and orthoclase (0.005mm dia.).

Hydrothermal effects are minimal with minor chlorite and montmorillinite alteration and quartz-replacement of intraclastic material, and the addition of "jigsaw" secondary quartz (0.01 to 0.005mm dia.) in the matrix.

Stage III

Stage III tectonic and hydrothermal events mark the initial onset of significant fluid-flow through the fault system. These

breccias consist of rebrecciated Stage I and II rock fragments in a matrix of rock flour and secondary quartz-chlorite-adularia-pyrite. The fragment:rock flour: hydrothermal matrix ratio (F:RF:M ratio) of Stage III breccias ranges from 2:1:1.3 on the footwall side of the zone, to 1.5:1:7 in the central zone (see Fig. 28). Angular to subangular intraclasts (1 to 10mm dia.) of Stage I rock fragments are moderately sorted with subrounded intraclasts (0.5mm to 10mm dia.) of Stage II microbreccias within a rock flour/hydrothermal matrix.

Stage III breccias generally comprise the largest volume of mineralized material within the zone, ranging from 15% in the central area to 75% on the fringes (Fig. 28). There is considerable variation along strike in the volume of Stage III material, however, as the Northern Extension exposures contain only 5% Stage III material. The Northern region brecciation and mineralization may represents a structurally higher geothermal level during Stage III time.

Secondary hydrothermal minerals occur both as replacements in permeable portions of the rock flour matrix and as pervasive open-space fillings in dilatant segments of the breccia zone. Rock flour contains as much as 10% intergranular chlorite in fine (0.01mm long) blades along with fine "jigsaw-texture" quartz replacements and locally abundant disseminated pyrite. Finely crystalline quartz, showing jigsaw, "reticulate" (up to 0.04mm dia.), and optically-continuous "streaked" replacement textures constitute 50% to 75% of the total open space volume.

Open-texture quartz encapsulates as much as 20% (by volume) high temperature chlorite occurring as discrete rosettes (Fig. 31). The index of refraction, birefringence and optic sign of the chlorite species suggest it is diabanite a chlorite with 4.0% total Fe and FE/Mg ratio of 0.5. Euhedral rhombs of adularia (5% to 35% of open space volume) occur with chlorite and reticulate quartz (Fig. 32). Pyrite, in euhedral pyritohedrons, occurs in discrete 1cm to 5cm replacement fronts in rock flour (Fig. 33) and disseminated throughout the assemblage.

Stage IV

Stage IV breccia is dominant in the central and inner footwall side of the Telegraph zone on Hills 1 and 2; occupying 0% to 40% of the total breccia zone volume. Stage IV breccias tend to be hydrothermal matrix-dominant, but have highly variable F:RF:SM ratios from 1:1:2 to 10:1:60, averaging 1:1:7 (Fig. 28). Moderately sorted, subangular fragments and broken crystals of Stage I (1mm to 6mm dia.), Stage II (0.5mm to 6mm-dia.) and Stage III (2mm to 10mm dia.) are set in a matrix of finely comminuted rock flour (0.05mm dia.) and an open-space assemblage of quartz-illite-(chlorite)-sericite-pyrite (Fig. 34).

Secondary hypogene mineralization occurs as disseminated replacements in rock flour, in minute replacement fronts in Stage III material and as open-space filling deposits. Fine jigsaw and streaked quartz comprises from 25% to 50% of the

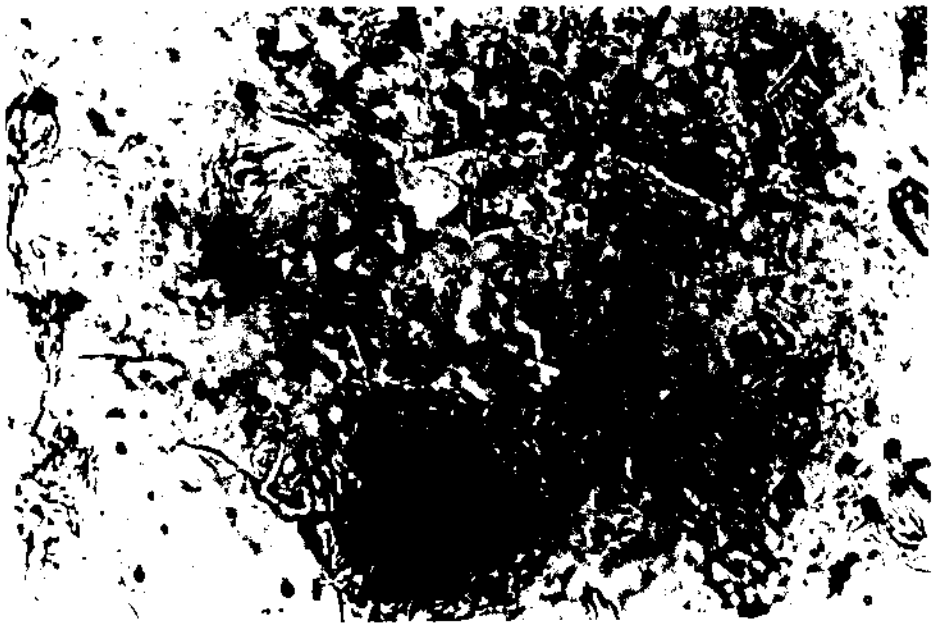

Figure 31. Photomicrograph of Stage III quartz-adularia-chlorite hydrothermal mineralization, sample TP-32. Note minute, rhombohedral adularia (a) and large chlorite rosette (b). Plane polarized. Field of view = 3 mm.

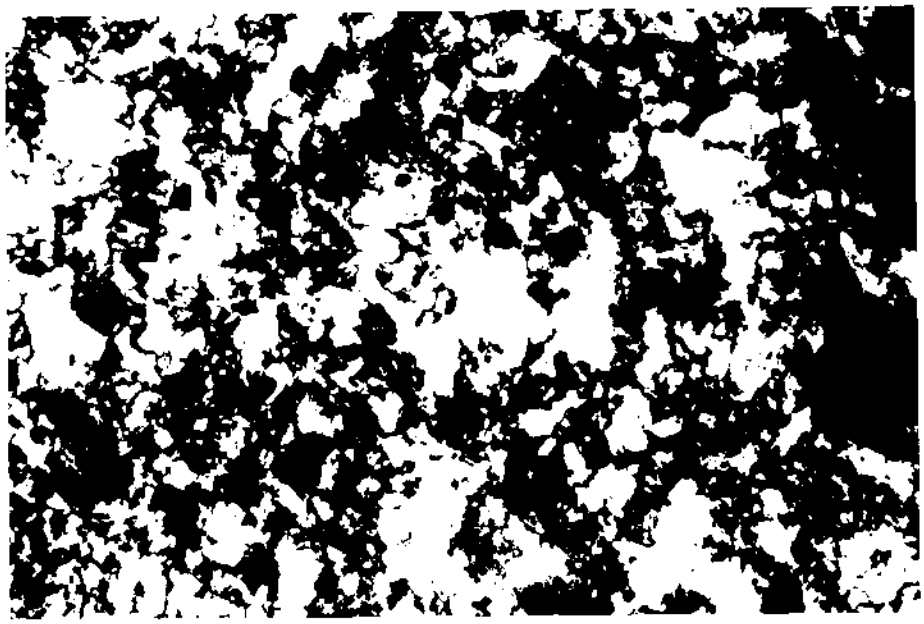

Figure 32. Photomicrograph of sample TP-32 Stage III mineralization- cross polarized. Note anhedral quartz crystallinity, adularia crystals (a) and euhedral hematite pseudomorphs after pyritohedrons (b). Cross polarized. Field of view = 3 mm.

Stage II (0.5mm to 6mm dia.) and Stage III (2mm to 10mm

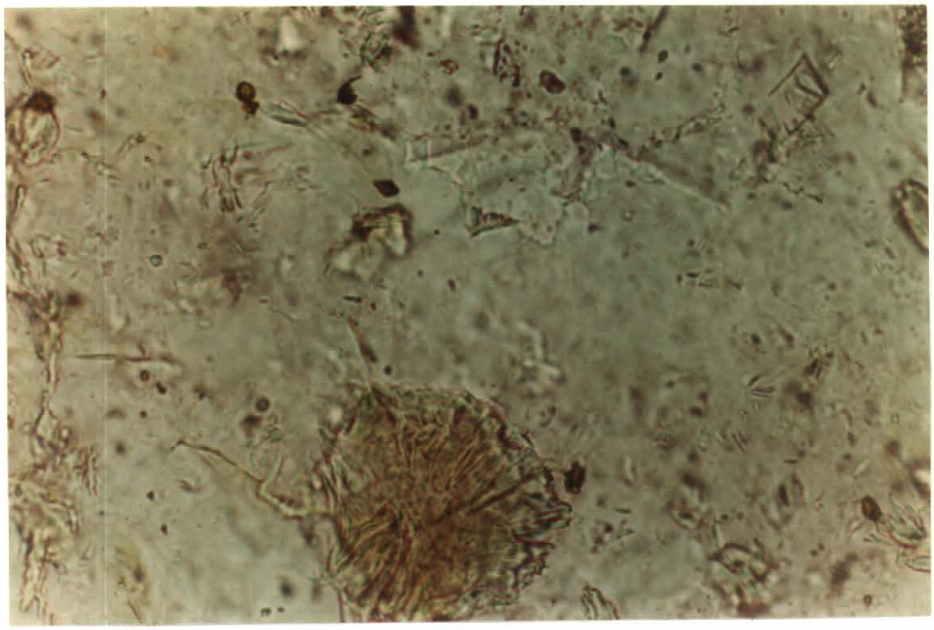

Figure 31. Photomicrograph of Stage III quartz-adularia-chlorite hydrothermal mineralization, sample TP-32. Note minute, rhombohedral adularia (a) and large chlorite rosette (b). Plane polarized. Field of view = 3 mm.

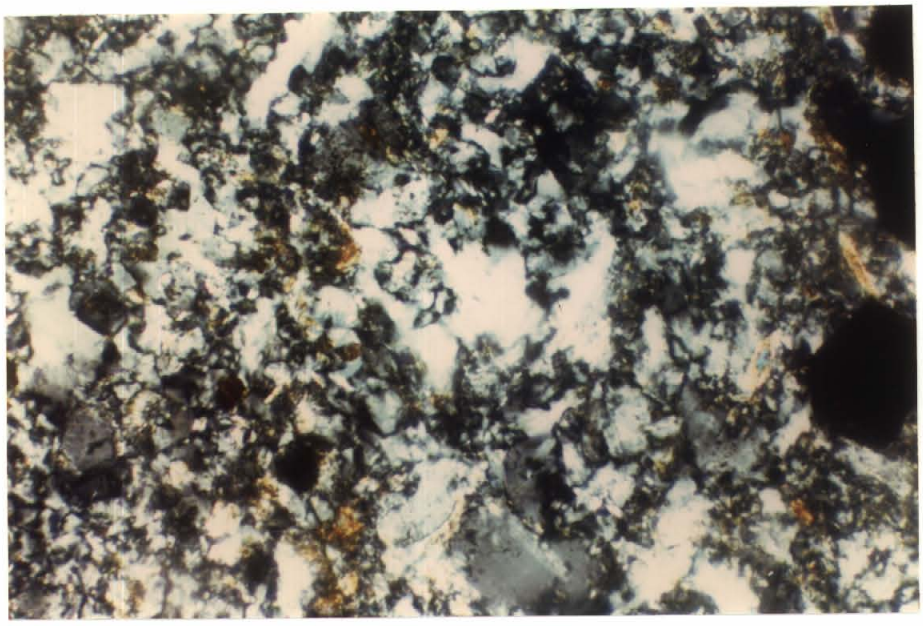

Figure 32. Photomicrograph of sample TP-32 Stage III mineralization- cross polarized. Note anhedral quartz crystallinity, adularia crystals (a) and euhedral hematite pseudomorphs after pyritohedrons (b). Cross polarized. Field of view = 3 mm.

Stage II (0.5mm to 6mm dia.) and Stage III (2mm to 10mm

total open-space volume along with 5% to 20% disseminated illite (hydromuscovite) in fine discrete blades (0.05mm dia.) and felty aggregates (Fig. 34). Up to 10% sericite and up to 15% pyrite (in pyritohedral form from 0.02mm to 0.12mm dia.) accompanies illite within 1cm to 5cm replacement fronts in permeable rock-flour. Up to 10% chlorite occurs in illite-bearing, open-texture silicification. The chlorite may be residual from Stage III events or may represent a genetically-related transition from Stage III to Stage IV events.

Stage V

Stage V mineralization occurs as cement and fine veinlets in crackle breccias of peripheral zones and as open-space fissure veins of the central zone. Percent total volume occupied by Stage V is a function of the original width of fault-induced dilatant fractures and the volume ranges from 0% to 75% of zone width . Although host rocks are highly fractured and intraclasts show rotation/translation within central dilatant zones, there is very little pulverized rock flour within Stage V breccias and the F:RM:HM ratio ranges from 9:0:1, in crackle breccias of Hill 2, to 1:0:1, in Northern Extension fissures (Fig. 36). Fragment size and angularity varies with width of affected zone: from 1 mm discrete subangular fragments in the central zone to greater than 20 cm angular crackle blocks of wall rock in annular zones (Fig. 35).

As illustrated in the Figures 37 and 38, Stage V mineralization occurs in three distinct pulses exhibiting character-

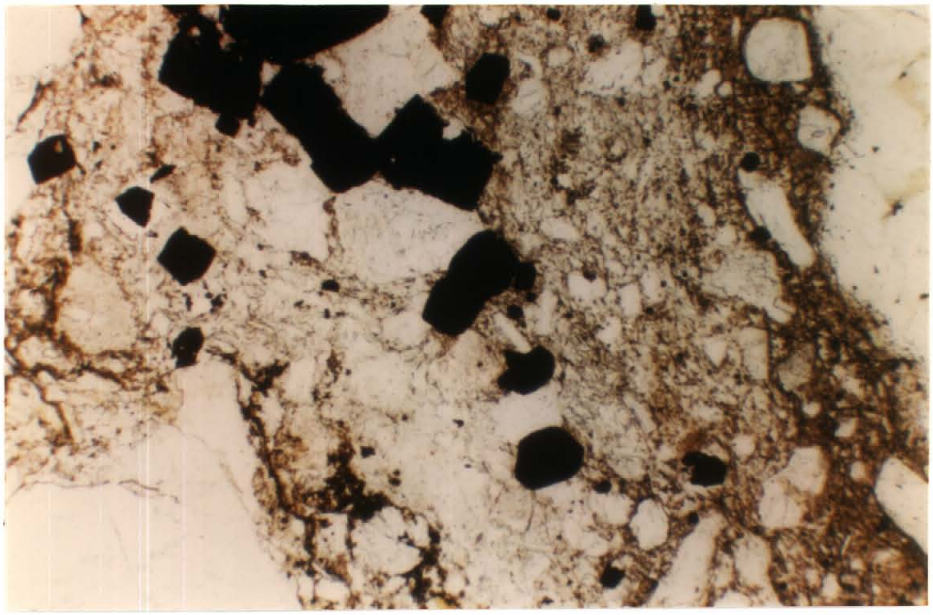

Figure 33. Photomicrograph of Stage IV breccia mineralization showing "pyrite front" developed between Stage I and II clasts and mineral fragments. Plane polarized. Field of view = 2.25 mm.

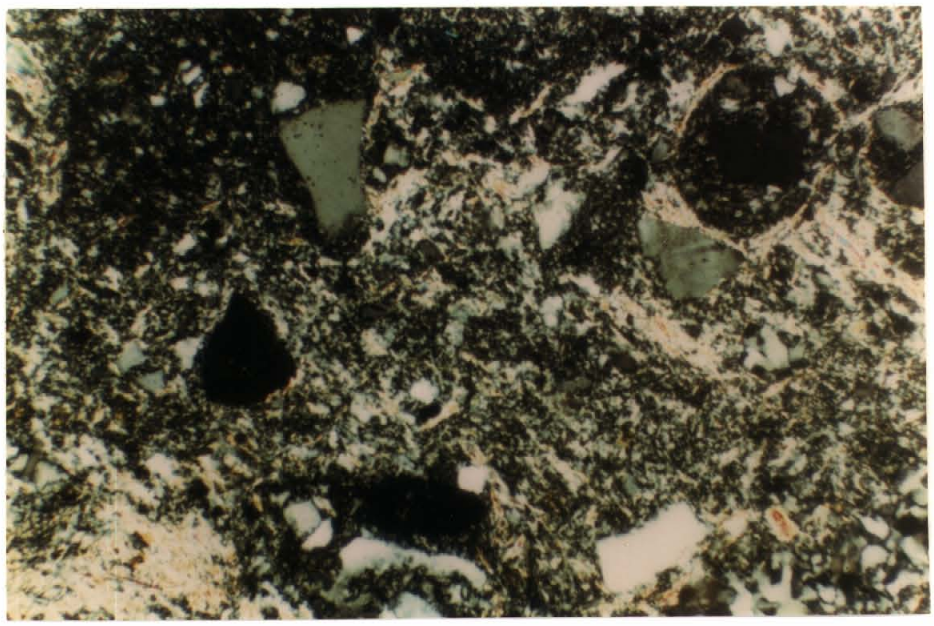

Figure 34. Photomicrograph of well-developed Stage IV breccia. Photo shows massive quartz-illite-sericite hydrothermal cementation and replacement of clasts. Note rounding of Stage II microbreccia-silicified gouge at (a). Cross-polarized. Field of view = 3 mm.

fractured and intraclasts show rotation/translation within

central dilatant zones, there is very little pulverized rock

istic quartz textures and accessory mineral assemblages. An early "reticulate" anhedral quartz (0.05 mm) comprises 80% to 100% of the total volume with 0 to 20% euhedral adularia rhombs (0.005 to 0.075 mm) and minor pyrite. This early pulse often forms as banded crusts on brecciated Stage IV fragments (Fig. 37).

A second pulse characteristically forms euhedral hexagonal comb quartz in open vugs often associated with coarsely crystalline adularia and euhedral pyrite. This phase of Stage V quartz contains the most useful primary fluid inclusions and the only "explosion texture" inclusions of the suite (Figs. 52 and 53, Section VI "Fluid Inclusions").

Late-pulse gold-silver mineralization is spatially restricted and is closely allied with comb quartz, adularia and pyrite. This last pulse is characterized by comb quartz crystals (0.5mm) with well developed explosion textures in close association with 5% to 25 % coarse-grained, flattened rhombohedral bladed calcite crystals - or "snowflake" calcite of Ellis (1979). The snowflake crystals commonly show anhedral quartz pseudomorphs (Fig. 38). This late pulse forms composes an impressive volume of Shaft 3 mineralization.

Stage VI

The latest fissure vein mineralization exposed along the Telegraph (and Gold Dike) system, is a repeated assemblage of banded manganese oxide-bearing calcite and chalcedonic quartz (Fig. 39). In general, the veins range from 1 to 30 cm wide to

Figure 47. Hand sample of sample 1056 showing Stage V-healed "crackle breccia" collected at the 3800' level, Shaft 2 (see Fig. 31) Stage III (a), IV (b) and V (c) are represented.

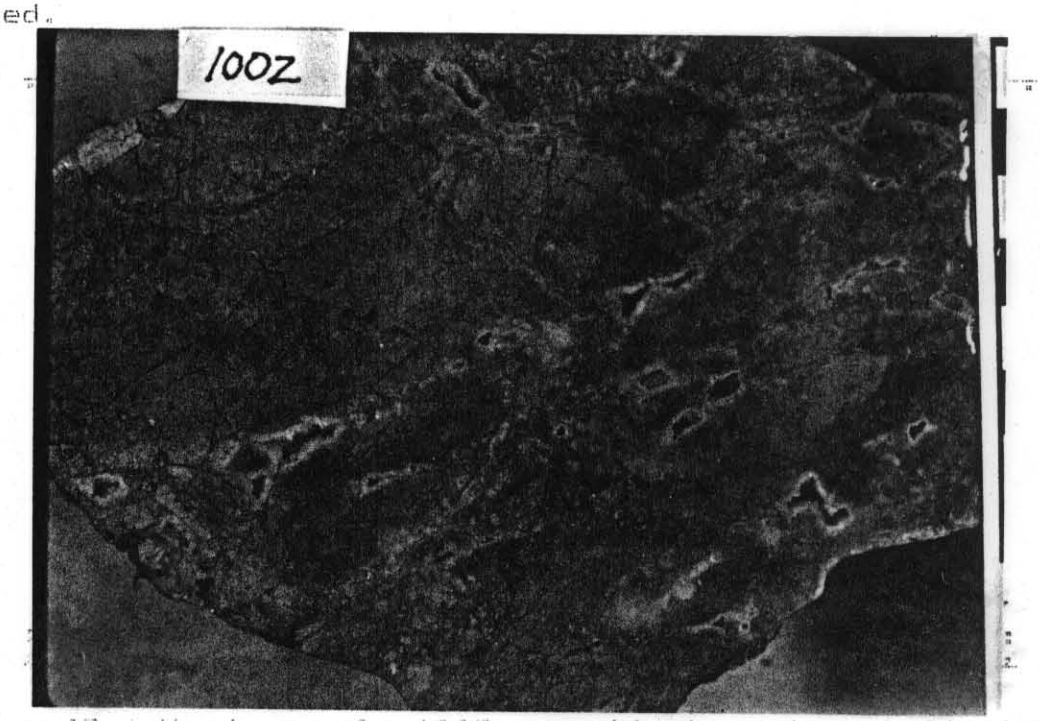

Figure 48. Hand sample 1002 crackle breccia, collected in breccia zone at 250 S., Northern Extension of Plate 5. Note that fragments composed almost exclusively of Stage IV silicified microbreccia with very fine Stage V healing.

a maximum of 0.5m in the west pit of Hill 2 (Plt. 4). This Stage normally constitutes 5% to 30 % of the total breccia zone. Stage IV often clearly exhibits alternating episodic bands of black calcite-dominant and white quartz-dominant mineralization. Early chalcedony is encrusted by initial blooms of snowflake calcite and later coarse grained iceland spar with irregular blebs of manganese oxides concentrated along twin planes. The oxides are a mixture of MnO_2 + $Mn(OH)_2$ and possibly $Mn_4Mg(AsO_4)_2(OH)_2$, as determined by x-ray diffraction patterns from dissolved, coarse-grained calcite separates. Thin chalcedony crusts, pseudomorphous after snowflake calcite, are common in late fractures developed in the breccia zone (Fig. 40).

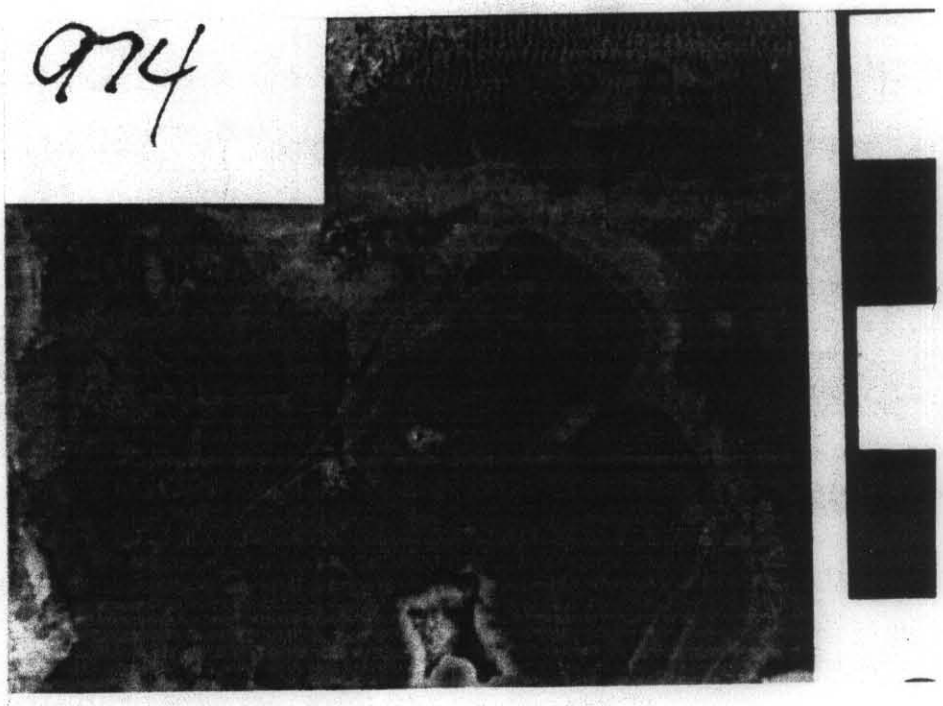

Figure 37. Stained slab of hand sample 974 (Hill 1, Southern Section, Plate 5). Note Stages I (a), III (b) and IV (c) fragments and overgrowths of coarse-grained Stage V adularia on Stage V quartz, adularia is stained yellow (c). Scale in cm.

a maximum of 0.5m in the west pit of Hill 2 (Plt. 4). This Stage normally constitutes 5% to 30 % of the total breccia zone. Stage IV often clearly exhibits alternating episodic bands of black calcite-dominant and white quartz-dominant mineralization. Early chalcedony is encrusted by initial blooms of snowflake calcite and later coarse grained iceland spar with irregular blebs of manganese oxides concentrated along twin planes. The oxides are a mixture of MnO_2 + $Mn(OH)_2$ and possibly $Mn_4Mg(AsO_4)_2(OH)_2$, as determined by x-ray diffraction patterns from dissolved, coarse-grained calcite separates. Thin chalcedony crusts, pseudomorphous after snowflake calcite, are common in late fractures developed in the breccia zone (Fig. 40).

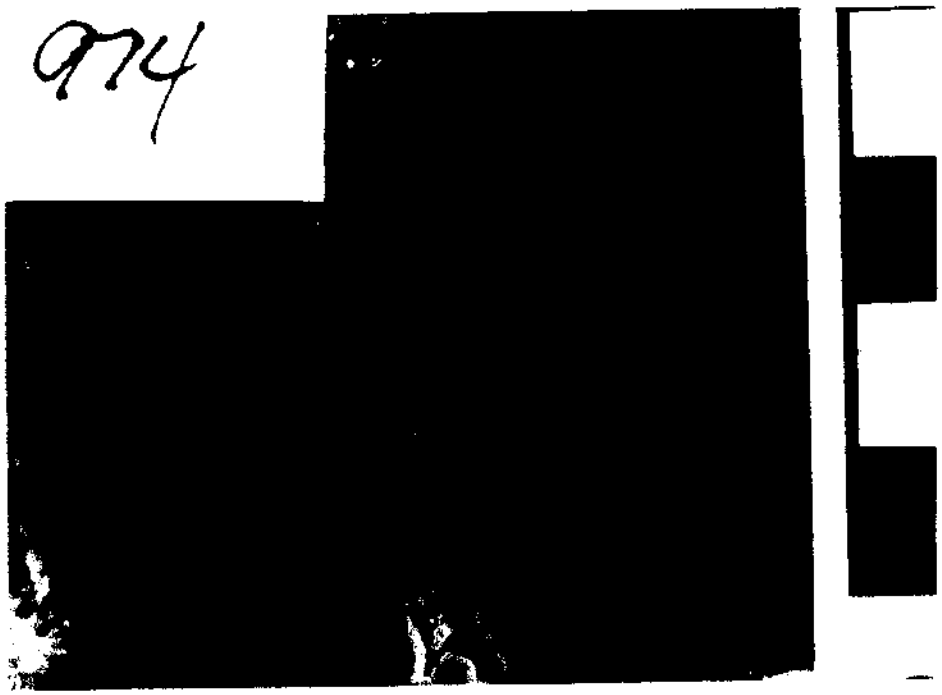

Figure 37. Stained slab of hand sample 974 (Hill 1, Southern Section, Plate 5). Note Stages I (a), III (b) and IV (c) fragments and overgrowths of coarse-grained Stage V adularia on Stage V quartz, adularia is stained yellow (c). Scale in cm

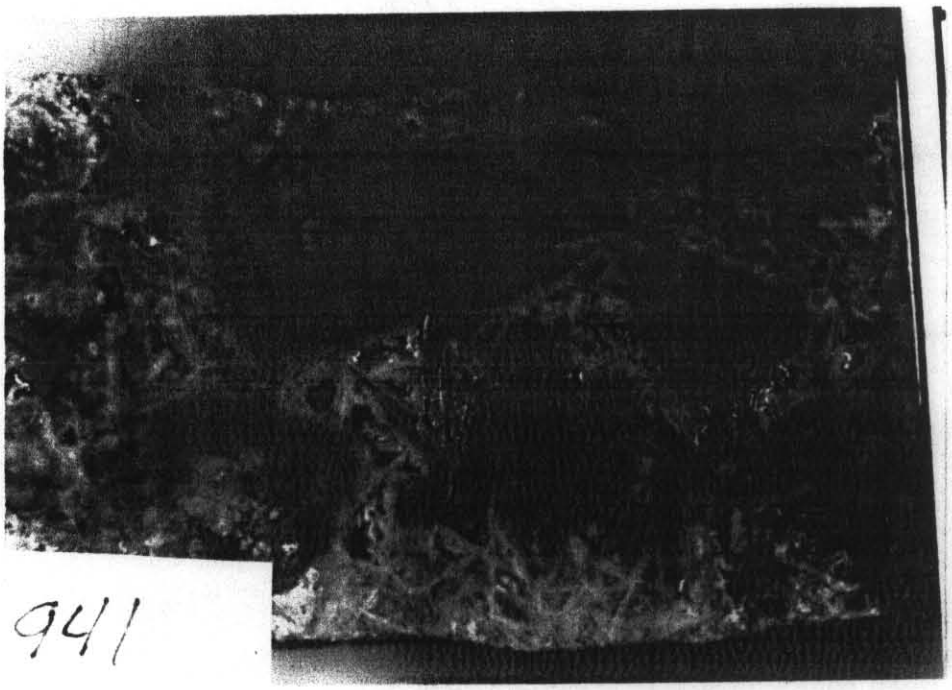

Figure 38. Stained slab hand sample 941 of Stage V- cemented breccia collected on Hill 2 (Plate 5). Note minute adularia overgrowths on fragments (a) and quartz pseudomorphs after "snowflake calcite" (b). Scale in cm .

PRECIOUS METAL GEOCHEMISTRY

Ore Mineralogy

The Telegraph ores are characterized by simple mineralogy typical of low-sulfide, "bonanza-type" precious metal epithermal vein systems. Pyrite and minor chalcopyrite of Stages III, IV, and V were the only sulfides seen in predominantly oxidized surface samples. The chemical parameters under which the system evolved strongly suggest that native gold and silver (perhaps as acanthite) occur as microcrystalline aggregates. No free microscopic gold was found in more than thirty thin sections oxidized ore. It was therefore necessary to collate and categorize all available assay data in order to produce discrete,

Stage-specific precious metal distributions.

Data Reduction

Geochemical data provided by Cascade Energy and Metal's Corporation's atomic absorption lab from drill hole cuttings and rock chip samples specifically taken for this study were compiled into LOTUS 1-2-3 files for reduction and manipulation (see Appendices C through F). Pertinent information concerning sample location, elevation, host lithology, width, host structure, alteration and associated mineralization were encoded along with assay data into the computer files. Completed files represent nearly complete characterizations of each sample.

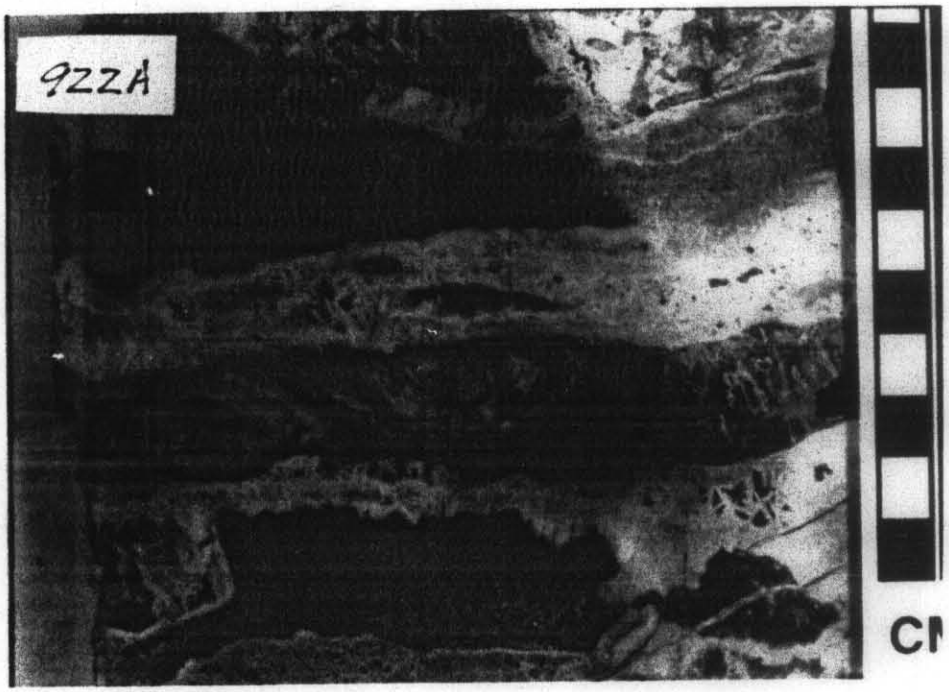

Figure 39. Hand sample 922 collected in the west pit, Hill 1 (Plt. 5). Note rhythmic manganiferous calcite-dominant versus chalcedonic quartz-"snowflake" calcite dominant banding. Note Stage IV breccia fragments near the wall rock edge (a) that shows Stage V quartz cementing. Scale in cm.

Figure 39. Hand sample 922 collected in the west pit, Hill 1 (Plt. 5). Note rhythmic manganiferous calcite-dominant versus chalcedonic quartz-"snowflake" calcite dominant banding. Note Stage IV breccia fragments near the wall rock edge (a) that shows Stage V quartz cementing. Scale in cm.

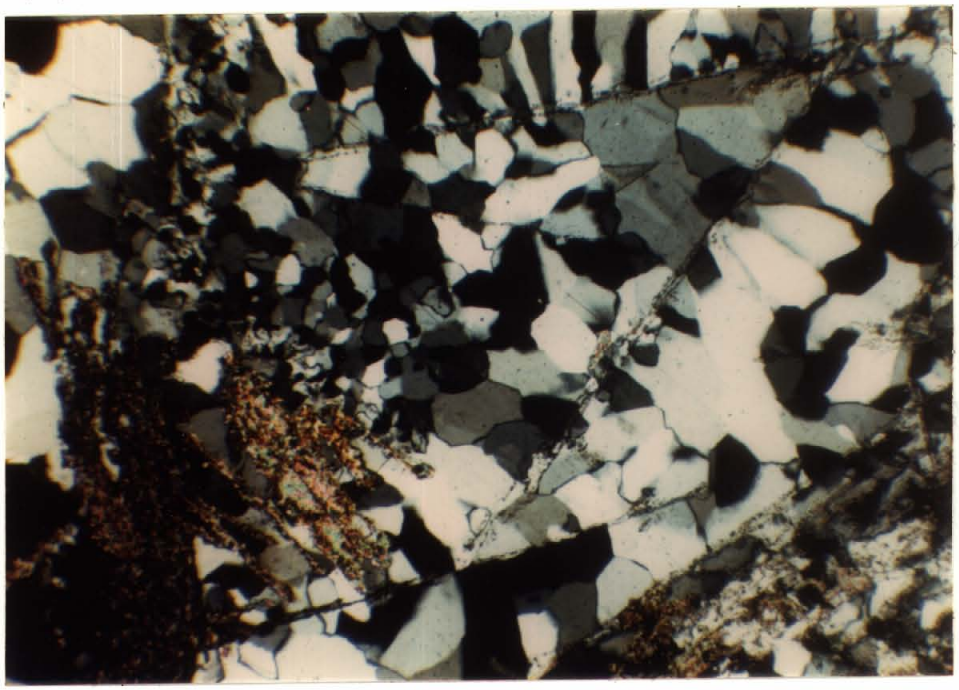

Figure 40. Photomicrograph of Stage VI mineralization. Photo shows manganiferous snowflake calcite (a) and quartz pseudomorphs after calcite (b) in recrystallized quartz matrix.

The sorting capabilities of the 1-2-3 program allowed

Figure 40. Photomicrograph of Stage VI mineralization. Photo shows manganiferous snowflake calcite (a) and quartz pseudomorphs after calcite (b) in recrystallized quartz matrix.

The sorting capabilities of the 1-2-3 program allowed for numerous specialized sample groupings, each sorted population having some particular characteristic in common. Sorting procedures split the large heterogeneous population into several much smaller, nearly homogeneous sample populations. Although the initial sorting reduced to a minimum the intra-sample variance, the resulting sample populations were often too small to perform statistically rigorous variance analyses.

Preliminary frequency analysis of sorted assay data sets indicated log normal behavior within discrete populations. All values (in ppm) were subsequently log-transformed (base 10) before final distribution plots were made. Frequency distribution analyses objectives were:

1) To determine true mean and modal assay values and dispersion tendencies in gold and silver content within

and between populations,

2) to evaluate overprinting enrichment of metals,

3) to allow rudimentary correlation analysis between elements within discrete populations,

4) to detect lateral zoning trends (from Au/Ag ratio), and

5) to evaluate possible chemical partioning of gold and silver.

Breccia-vein System Distribution

The highest absolute and relative mean gold and silver values were obtained from fine-grained, anhedral quartz-adularia-veins of Stage V breccia , especially in late-stage structures on Hill 1 (Plts. 4 and 5). Figure 41 illustrates the surface Stage V Au and Ag value distributions. Note the considerable dispersion of values, from very enriched to just above detectable. Comb quartz-adularia veinlets averaged 4.47 ppm Au and 47.5 ppm Ag. Separates of the 3800ft level sample 1056 confirmed these high late-stage quartz vein values, with values assaying at 35 ppm Au (1.0 oz/t) and 37.7 ppm Ag (1.1 oz/t).

Stage VI veins averaged 1.30 ppm Au and 19.20 ppm Ag. The pronounced enrichment of silver over gold in "black calcite"-chalcedony is perhaps a common phenomena, reported in other districts (Andrusenko,1979; Hewitt and Radtke,1967; Silberman, 1985).

Significant gold and silver mineralization occurs in breccia replacement matrix and breccia cement of Stage III and Stage IV. Stage III plots show moderate dispersion (Fig. 42) with a

suggestion of bimodal distribution of both gold and silver. Dispersion is prominent in breccia matrix and replaced fragments represent both Stage III and IV mineralization (Fig. 44) and is the result of enrichment overprinting of Stage IV over Stage III. Stage IV distribution dispersion (Fig. 43) is intermediate between these extremes with similar modes and similar mean values. Although Rocky Mountain Geochemical Corp. fire assay results are generally lower than reported drill hole data, both sources indicate pronounced gold enrichment of Stage III and over the later, Stage IV mineralization.

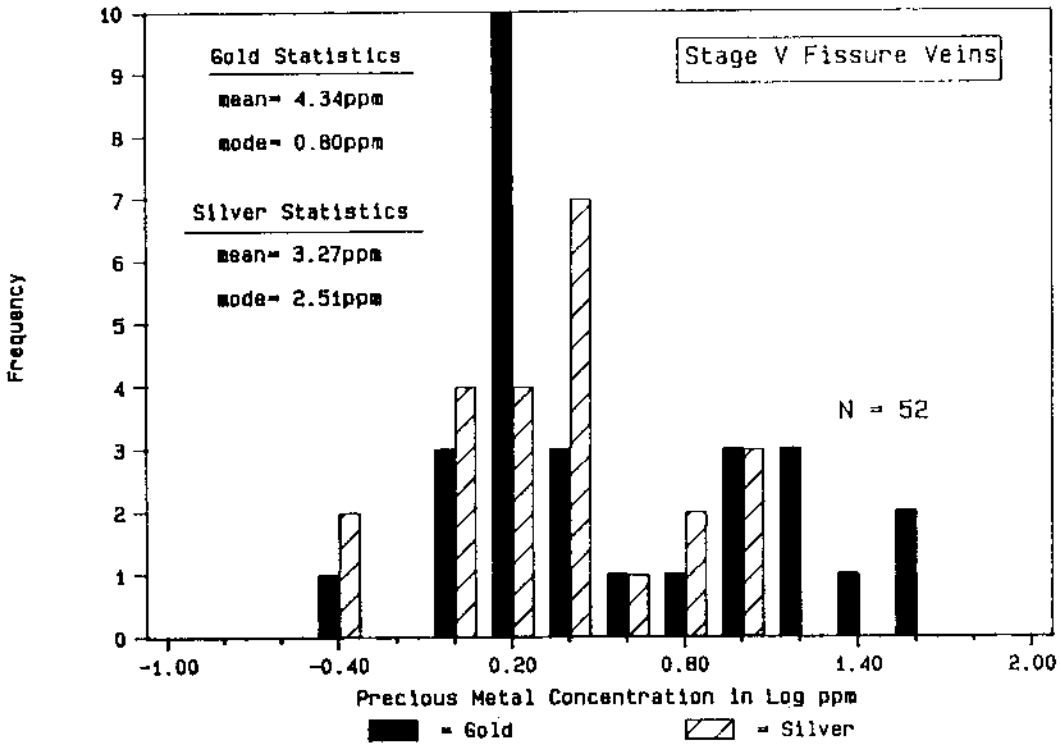

Figure 41. Rotary drill sample geochemical distribution of Stage V fissure veins. All data from sorted LOTUS files, Appendix F.

suggestion of bimodal distribution of both gold and silver. Dispersion is prominent in breccia matrix and replaced fragments represent both Stage III and IV mineralization (Fig. 44) and is the result of enrichment overprinting of Stage IV over Stage III. Stage IV distribution dispersion (Fig. 43) is intermediate between these extremes with similar modes and similar mean values. Although Rocky Mountain Geochemical Corp. fire assay results are generally lower than reported drill hole data, both sources indicate pronounced gold enrichment of Stage III and over the later, Stage IV mineralization.

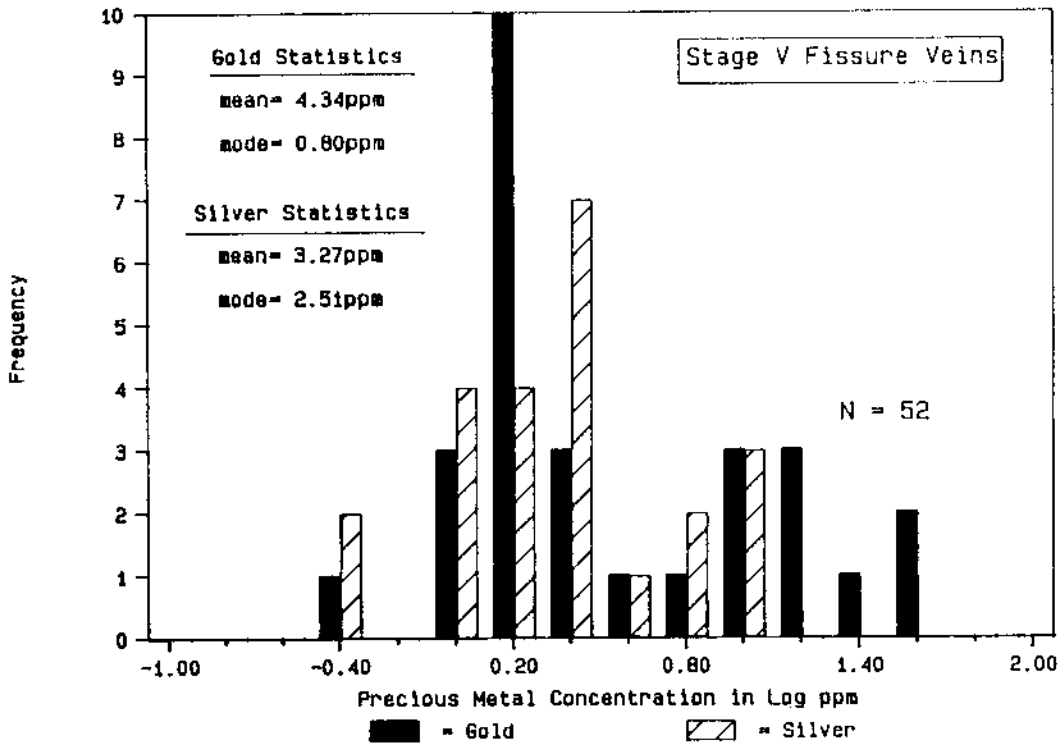

Figure 41. Rotary drill sample geochemical distribution of Stage V fissure veins. All data from sorted LOTUS files, Appendix F.

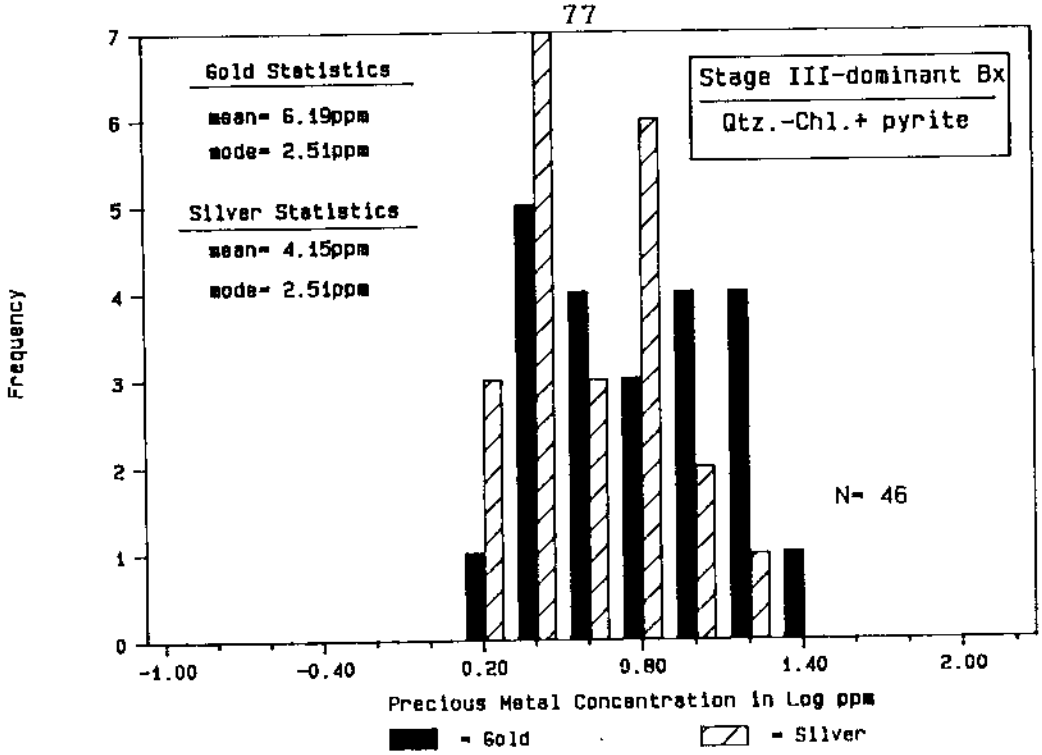

Figure 42. Rotary drill hole geochemical distribution of Stage III-dominant breccia samples. Results from CEM Corp. assay logs, listed in sorted LOTUS files, Appendix F. Explanation in text.

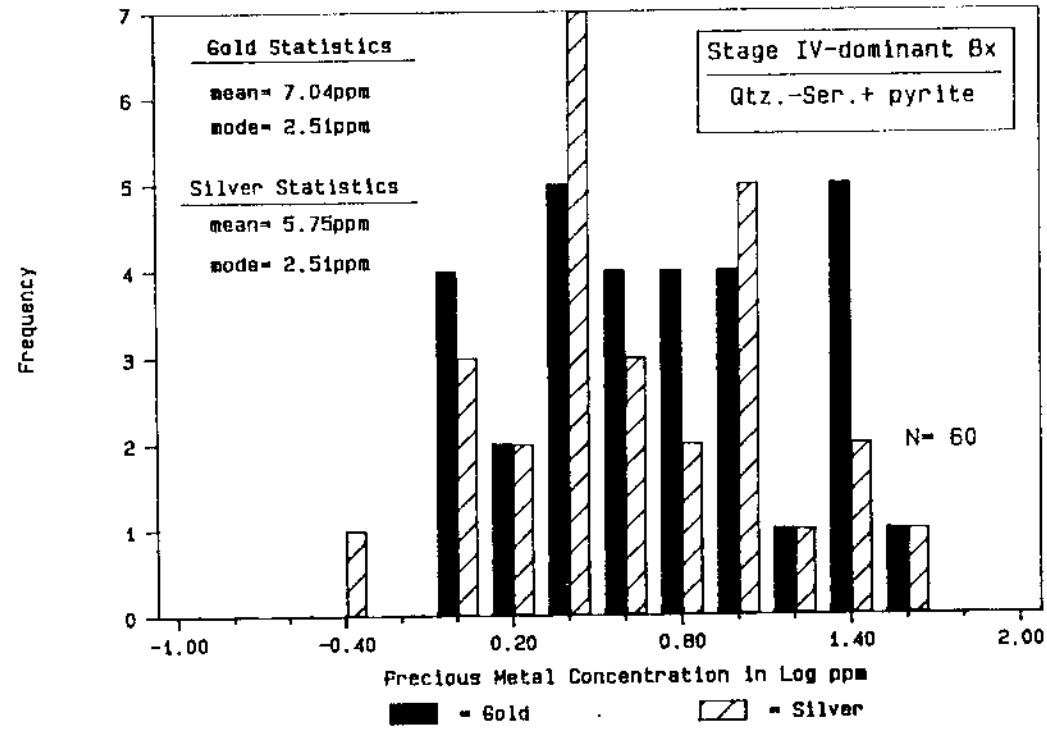

Figure 43. Rotary drill hole geochemical distribution of Stage IV-dominant breccia samples. Results from CEM Corp. assay logs in sorted LOTUS files, Appendix F. Explanation in text.

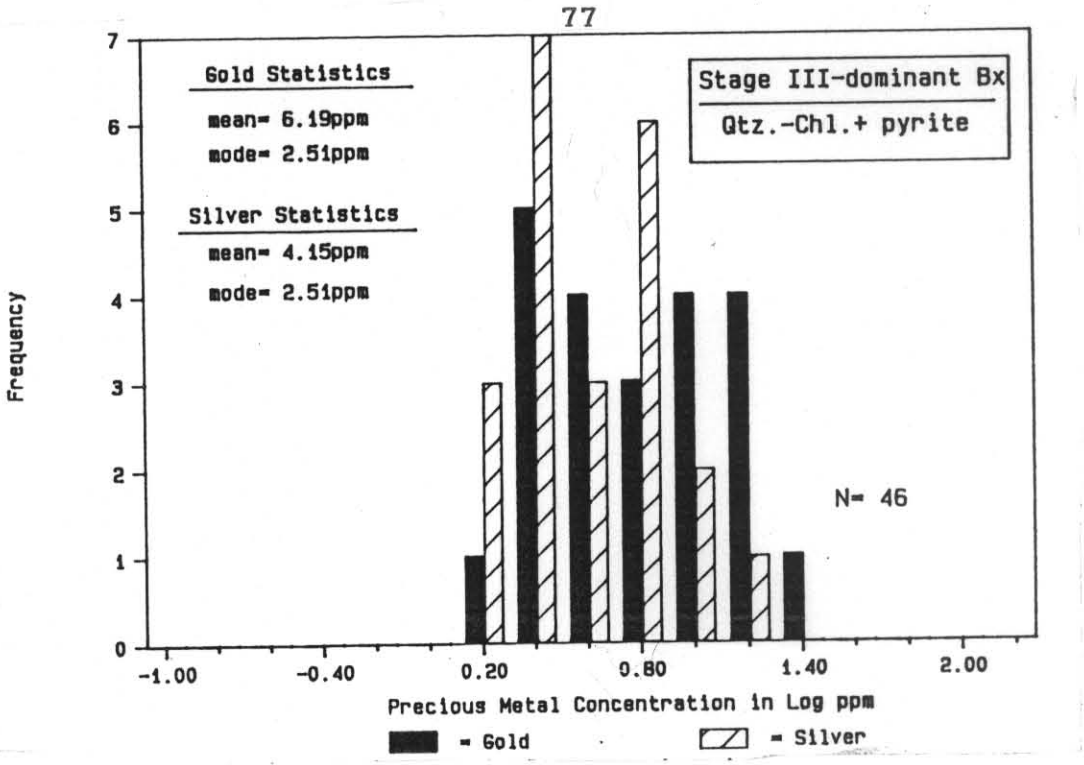

Figure 42. Rotary drill hole geochemical distribution of Stage III-dominant breccia samples. Results from CEM Corp. assay logs, listed in sorted LOTUS files, Appendix F. Explanation in text.

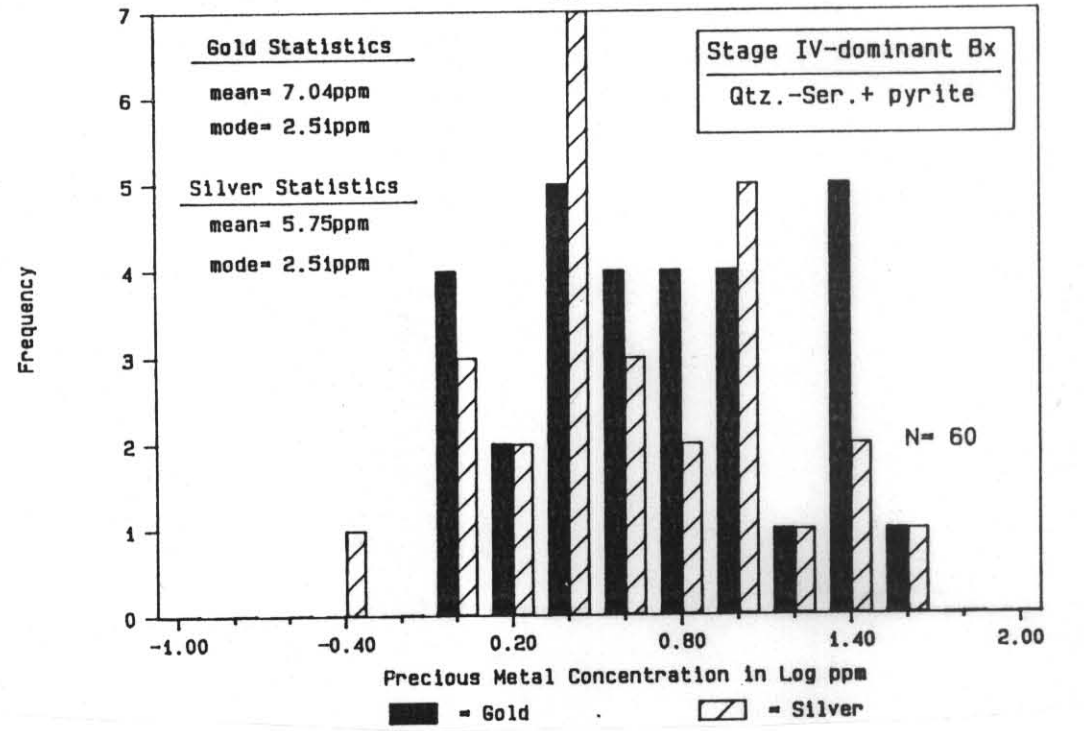

Figure 43. Rotary drill hole geochemical distribution of Stage IV-dominant breccia samples. Results from CEM Corp. assay logs in sorted LOTUS files, Appendix F. Explanation in text.

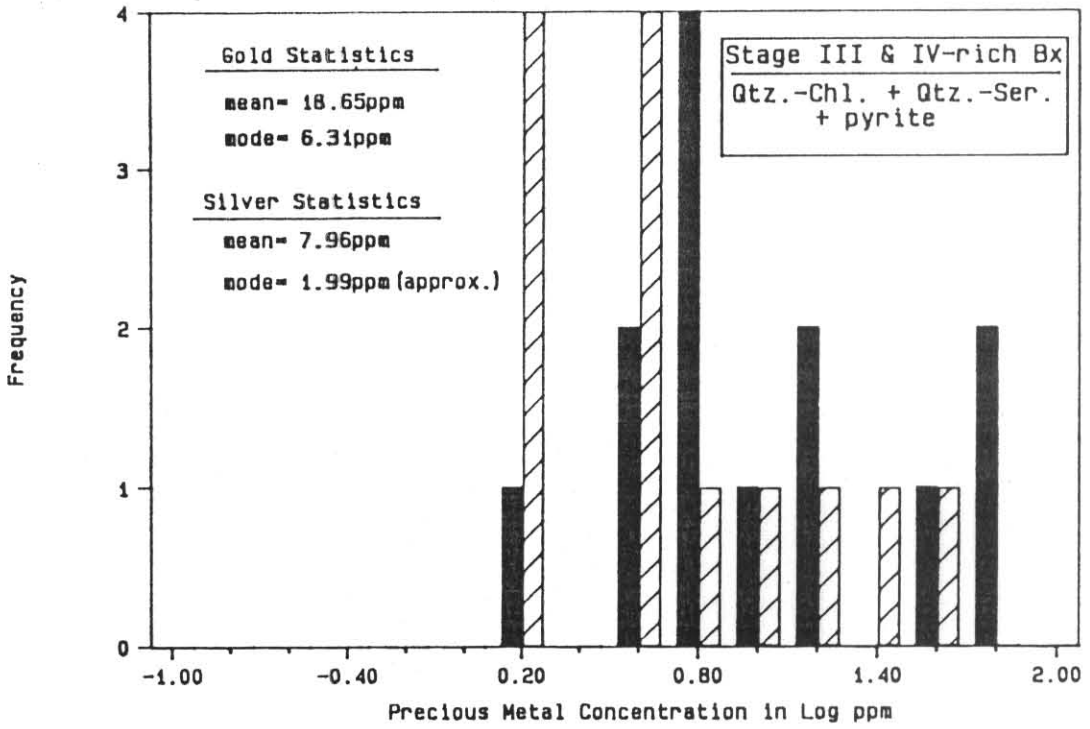

Figure 44. Rotary drill hole geochemical distribution of Stage III + IV-dominant breccia samples. Results from CEM Corp. assay logs listed in Appendix F. Explanation in text.

Curiously, those samples rich in pyrite were not necessarily enriched in precious metals. Pyrite (oxidized to hematite) content does not appear to directly correlate with elevated values in drill hole or surface samples. Microprobe analysis of pyrite on the only unoxidized Stage IV-dominant sample of Stage IV (Fig. 45) did not confirm the presence of exsolved gold. However, minute blebs of co-precipitating pure K-feldspar (presumably adularia?) were identified.

Wallrocks

Fortunately, a large population of wall rock alteration assay data from drill hole samples is available. The positively skewed distribution of altered footwall propylitic zone values

shown on Figure 46 indicates slight enrichment of Ag over Au; hangingwall samples (Fig. 47) show a similar, yet less pronounced trend.

The hangingwall argillic zone is relatively enriched in Au and Ag. There is a subtle shift in the distribution of gold vs silver apparent in the argillic vs propylitic (Fig. 47) hangingwall assemblages. The argillic zone adjacent to the main breccia-feeder zone is enriched in gold over silver, but further away from the main vein, the propylitized zone exhibits Ag enrichment relative to Au. Many of the extremely high Ag values can be attributed to traces of fine-grained quartz-bearing veinlets which are relatively enriched in Ag. Enrichment of Au near the vein (argillic zone) is probably due to the proximity to the main system.

Gold/Silver Ratios

Au/Ag ratio distribution of the Telegraph system, as calculated from drill results, appears to exhibit log-normal behavior (Fig. 49). Surface rock-chip samples have substantially lower ratios than the drill interval samples (2 ft. composites): the drill results have a mean of 2.0 Au/Ag, while rock chip samples average 0.15 Au/Ag. This discrepancy is probably due to the selective drilling in the ore zone on Hill 1 and 2, yielding higher precious metal values overall. Positive skewness of the drill data (Fig. 49) results from above average ratios for breccia-vein intervals versus wall rock intervals: breccia-vein intervals average 2.3 Au/Ag (N=

Figure 45. Stained slab and hand sample 968. Sample collected on Hill 1, Southern Section of Plate 5. Note un-oxidized pyrite-rich Stage IV breccia fragments and oxidized, pyrite bearing fine-grained Stage V quartz healing.

98), while wall rock intervals average 1.09 Au/Ag (N=232). Examination of Appendix F indicates that these higher ratios are probably due to substantial increases in gold values in the breccia vein zone compared to the wall rock zone, while silver values are less variable accross the vein into the wall rocks.

Au/Ag ratios near or above unity have been cited as indicators of shallow-level precious metal deposition within an epithermal regime. Cole and Drummond (1986) discuss the temperature zonation and physicochemical implications of high gold-to-silver ratios and conclude that a majority of epithermal deposits with high ratios were formed from fluids between 200 to 250°C. They note that higher Au/Ag ratios in vein deposits are found typically in the upper parts of systems because shallow ores are relatively gold enriched. `Ratios often decrease with increasing depth due to increasing concentrations of silver (along with base metals) in deep ores. Their experimental data indicate that the boiling of metal-bearing fluids with initially low CO_2 / H_2S ratios, high concentrations of H_2S and high pH (5-6) is a likely cause of high Au/Ag ratios in some epithermal ores.

Estimations of fluid temperatures and chemistry for the Telegraph ores fall within these parameters and variations in ratios probably reflect local variations in fluid temperature (see Section VI) and chemistry (see Section VII). The overprinting of several stages of mineralization also contributed to both the variation and aerial distribution of high Au/Ag ratios. Figure

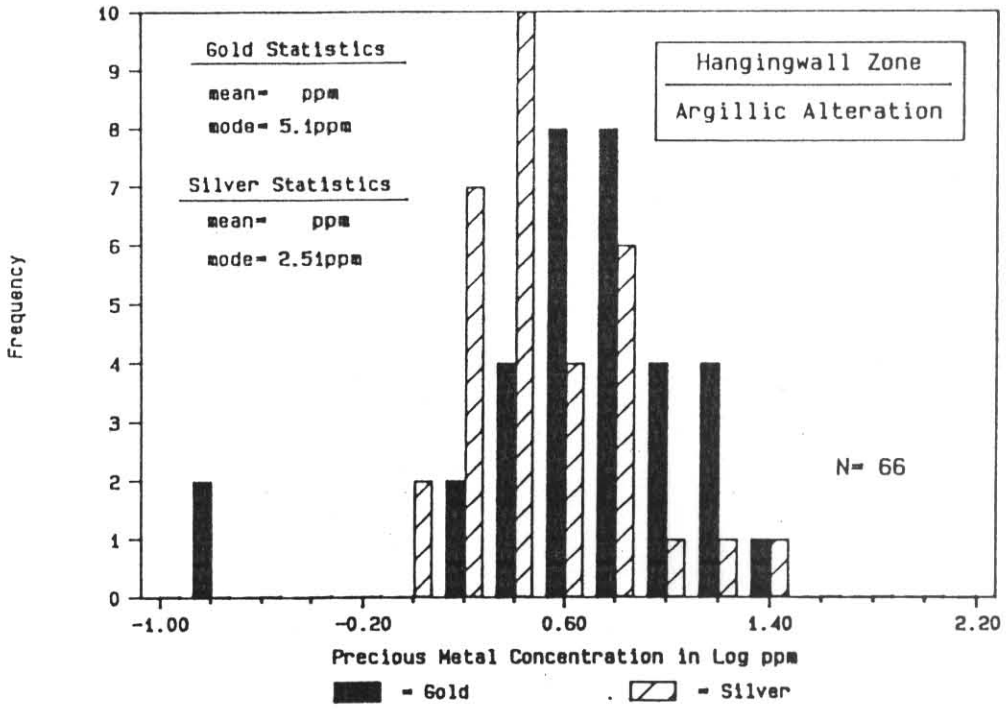

Figure 48. Rotary drill hole precious metal distribution of argillically-altered hangingwall samples. Results listed in sorted Appendix F. Explanation in text.

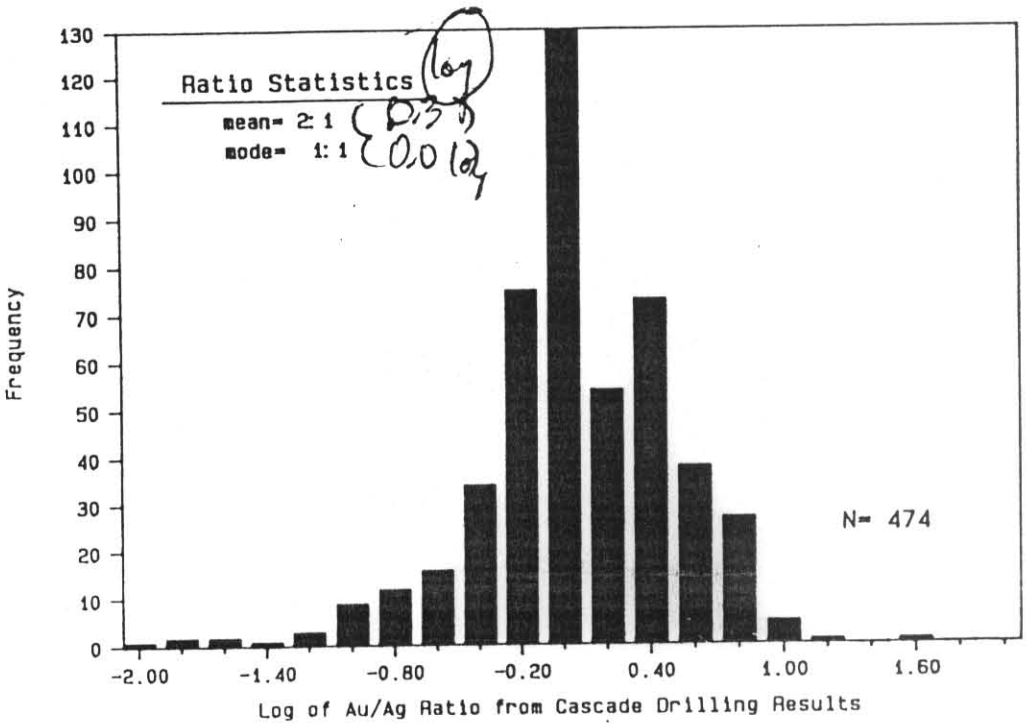

Figure 49. Distribution of gold/silver ratios from all rotary drill hole samples taken along the Telegraph trend (Appendix F). Explanation in text.

98), while wall rock intervals average 1.09 Au/Ag (N=232). Examination of Appendix F indicates that these higher ratios are probably due to substantial increases in gold values in the breccia vein zone compared to the wall rock zone, while silver values are less variable accross the vein into the wall rocks.

Au/Ag ratios near or above unity have been cited as indicators of shallow-level precious metal deposition within an epithermal regime. Cole and Drummond (1986) discuss the temperature zonation and physicochemical implications of high gold-to-silver ratios and conclude that a majority of epithermal deposits with high ratios were formed from fluids between 200 to 250°C. They note that higher Au/Ag ratios in vein deposits are found typically in the upper parts of systems because shallow ores are relatively gold enriched. `Ratios often decrease with increasing depth due to increasing concentrations of silver (along with base metals) in deep ores. Their experimental data indicate that the boiling of metal-bearing fluids with initially low CO_2 / H_2S ratios, high concentrations of H_2S and high pH (5-6) is a likely cause of high Au/Ag ratios in some epithermal ores.

Estimations of fluid temperatures and chemistry for the Telegraph ores fall within these parameters and variations in ratios probably reflect local variations in fluid temperature (see Section VI) and chemistry (see Section VII). The overprinting of several stages of mineralization also contributed to both the variation and aerial distribution of high Au/Ag ratios. Figure

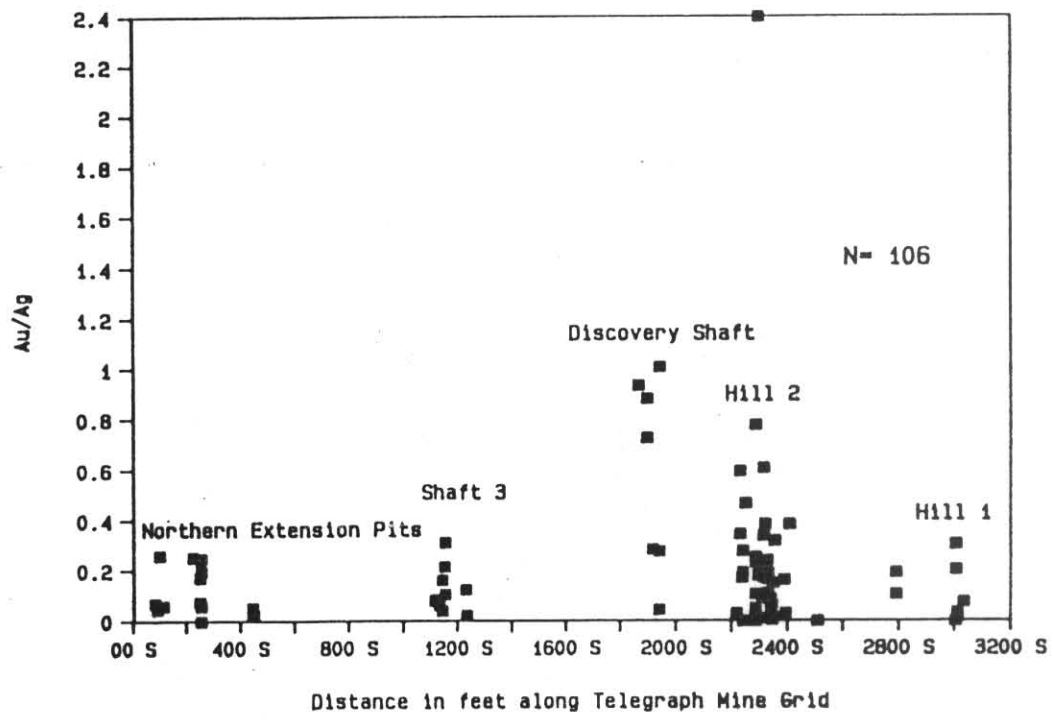

Figure 50. Surface distribution of gold/silver ratios from all rock-chip samples taken along the Telegraph trend, from north to south. Individual samples are listed in Appendix E, and locations are given on Plate 5.

50 indicates that samples collected in areas where the breccia-vein development is widest (ie. Hill 2) have the highest ratios, probably reflecting the greatest re-brecciation and highest periodic fluid-flow along the Telegraph fault.

TRACE ELEMENT DISTRIBUTION

A complete trace element analysis of the breccia system has not been made, however, key surface samples were selected for a preliminary investigation of dispersion patterns. An element suite typically exhibiting some correlation to Au/Ag distribution in epithermal deposits was evaluated. Initial geochemical analysis indicated that only Cu, Hg and As seemed to show any significant enrichment in the Telegraph system; Sb and Tl were removed from consideration early on. Preliminary correlation coefficients run on surface data indicate a moderate correlation of Au values with Ag values (r= 0.57), and moderate to low correlation of Au values with Hg (r= 0.31) (see Fig. 51).

Examination of Appendix E suggests that the inner argillic and propylitic zones of the hangingwall are relatively enriched in Hg, perhaps in association with the presence of hematite-filled ("Fe-Ox") fractures. Arsenic appears to be relatively enriched in FeOx as well, especially of the argillic hangingwall. These relations probably reflect supergene enrichment of these mobile trace elements.

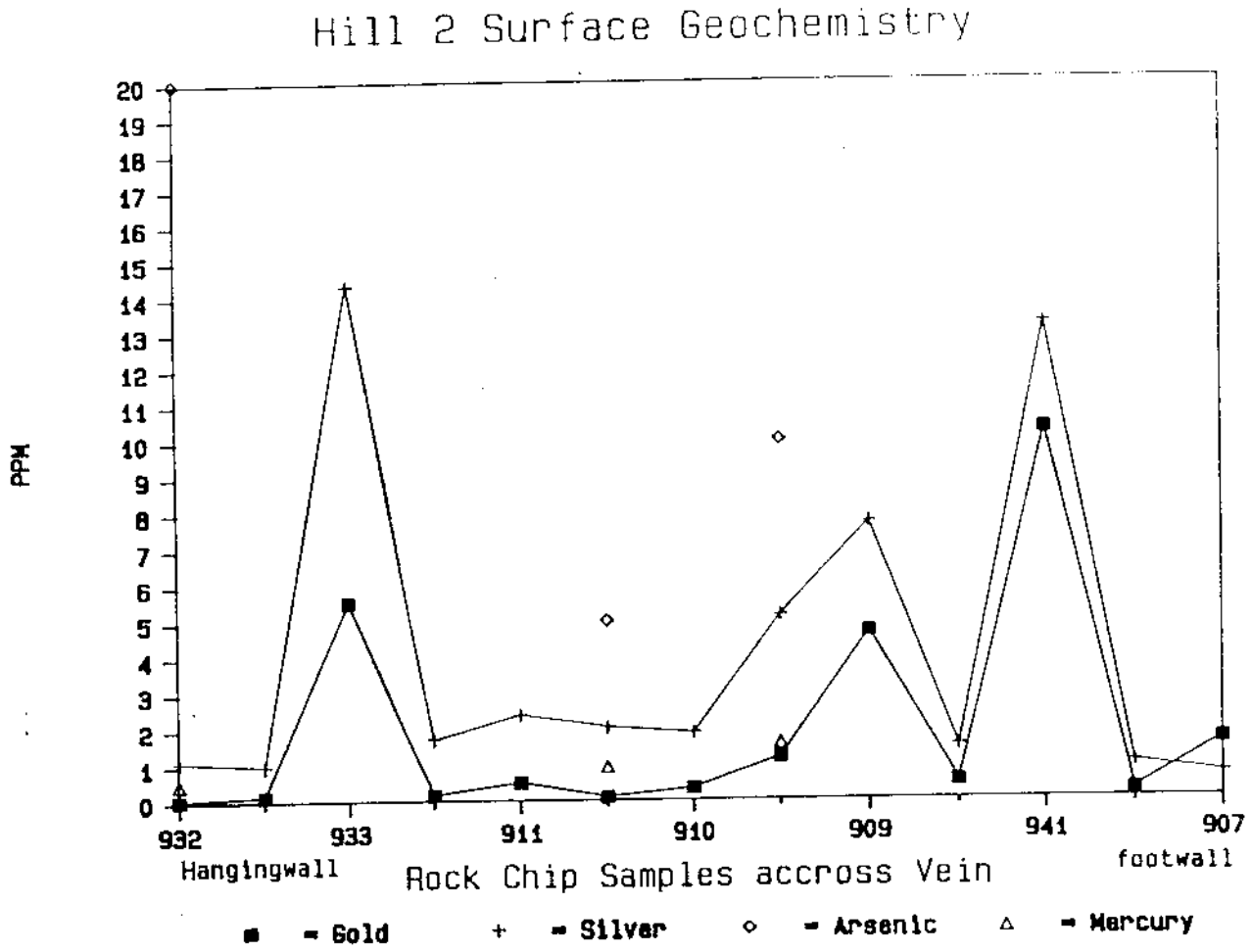

Figure 51. Trace Element distribution accross vein, Hill 2.

Table 8. Summary statistics from log-normal metal distributions for rock-chip samples of Telegraph system mineralization listed in Appendix E. Mean, median and mode statistics are geometric. Detection limits are as given on Table 4. N = 88.

Element	Range (ppm)	Mean (ppm)	Median (ppm)	Mode (ppm)	Std. Dev.
Au	0.17 - 35.31	1.62	0.48	0.63	3.14
Ag	0.10 - 122.74	13.66	5.42	10.00	21.54
As	5.00 - 45.00	11.00	5.00	7.50	19.00
Hg	0.26 - 10.00	2.12	1.50	2.51	1.50

Table 9. Correlation coefficient ("r" statistic) matrix for Telegraph rock-chip breccia samples (Appendix E). At the 5% level of significance, r values exceeding 0.27 would indicate significant correlation between values for this population (based on data of Snedecor and Cochran, 1967). N = 52.

	Au	Ag	As	Hg
Au	1.00	0.57	0.10	0.31
Ag	0.57	1.00	-0.12	0.11
As	0.10	-0.12	1.00	0.19
Hg	0.31	0.11	0.19	1.00

VI

FLUID INCLUSIONS

A preliminary fluid inclusion analysis of the Telegraph breccia-vein system was conducted to :

1) document certain aspects of fluid chemistry such as temperature, solution salinity, and fluid pressure,

2) develop possible fluid pressure/mineralization depth regime for the evolution of the system, and

3) document any direct association between the Gold Dike system and the Telegraph system.

Analytical Methods

Twenty doubly polished plates were prepared from a collection of over 90 breccia and vein thin-sectioned specimens collected on the surface and underground along the Telegraph and Gold Dike trends. Selection criteria included: 1) optimized inclusion size, 2) proof of primary origin, and 3) unambiguous representation of individual thermal events. However carefully chosen, the final plates contained few usable inclusion populations. Although large secondary inclusions were common, true primary inclusions were extremely rare and most were <0.002 mm in diameter. Only primary inclusions >0.004 mm were utilized for this study.

The homogenization temperature, $T/_{h}$, and melting point temperature, $T/_{m}$, determinations were made with a Roman Science heating-freezing stage. Replicate determinations were perform-

ed on each heating and freezing run, noting any metastable activity, inclusion decrepitation or vapor leakage. Particularly large primary inclusions were singled-out for both freezing work and crushing studies.

Several different crushing techniques were applied to document the presence of dissolved CO_2. Crushing individual isolated inclusions under oil with a probe while viewing the operation at high magnification proved to be most satisfactory.

Fluid Inclusion Parameters

Dissolved CO2

Crushing studies can reveal the presence of "overpressured", or CO_2-bearing inclusions (Roedder,1984), and "double freezing" or clathrate measurements can provide estimations of actual CO_2 content (Collins, 1979). Unfortunately, the very minute CO_2 concentrations reported for most geothermal systems and precious metal deposits (where reported) may not be detectable in crushing studies. Bodnar and Bethke (1985) point out that greater than 0.2m % dissolved CO_2 is required to detect vapor bubble expansion beyond the internal volume of an inclusion 0.010 mm in diameter.

Recently, a number of researchers emphasize that low levels of dissolved CO_2 significantly contributes to, or even dominates observed freezing point depression measurements, especially in low NaCl systems (Hedenquist and Henley, 1985a). The inference can be drawn that salinity estimates ranging from

<1 to 10 equiv. wt.% NaCl reported for many epithermal deposits can be grossly in error if CO_2 was not considered.

It is clear that, although crushing studies did not detect CO_2 in Telegraph inclusions, the likelihood that minute quantities of CO_2 were dissolved in the original fluids is great. Therefore, the measured salinities in this study should be considered apparent only, with an assumed CO_2 content of less than 0.2 m equiv. wt. %. Since this is easily within the range where the influence of NaCl dominates over CO_2 in the freezing point measurement, the margin of error between apparent salinity and true salinity is small.

Influence of Boiling on Tt

Boiling produces a two-phase fluid consisting of separate liquid and vapor phases. The condition is reflected in a coeval suite of inclusions yielding highly variable liquid-to-vapor ratio estimates and variable Th measurements. In heating runs, those inclusions trapping some liquid phase and some vapor phase will yield erroneously high Th measurements. Since inclusions trapping solely the liquid or vapor phase reflect homogenization temperatures nearest the critical curve, the lowest Th value in this suite approximates the true trapping temperature for the boiling fluid (Roedder, 1984.)

Inclusion Types

All data reported in this study were measured from liquid-

vapor primary inclusions trapped in quartz crystals of open-space breccia cement or discrete fissure veinlets. By far the most common inclusions were equant to slightly elongated "negative crystal" forms; some, especially in Stage V quartz, were spherical.

Large (to >0.20 mm) secondary inclusions concentrated in subparallel planes along healed tectonic microfractures in both primary-magmatic and hydrothermal quartz were very common in all breccia samples.

Elongated and tubular-shaped "empty" inclusions, containing no originally trapped liquid or vapor, radiating from outer growth zones of euhedral comb quartz are characteristic of late Stage V quartz (Figs. 52 and 53). This variety of "explosion texture" inclusions is often cited as evidence of fluid boiling (Roedder, 1984).

Stage III, IV and V quartz yielded very few usable inclusions, while Stage I, II and VI quartz provided none. Pre-ore Stage I and II events lacked sufficient deposition of hydrothermal quartz, and Stage VI chalcedony was free of large inclusions. Inclusion data gathered from chalcedony or amorphous silica deposits are of dubious value in any case (Fournier, 1985b).

Analytical Results

Stage III Inclusions

Minute 0.004 to 0.006mm primary equant, negative crystal two-phase liquid-rich inclusions in fine-grained anhedral quartz cement (with adularia-chlorite-pyrite) of Stage III breccia were examined from a suite of Hill 2 surface samples. Viewing was

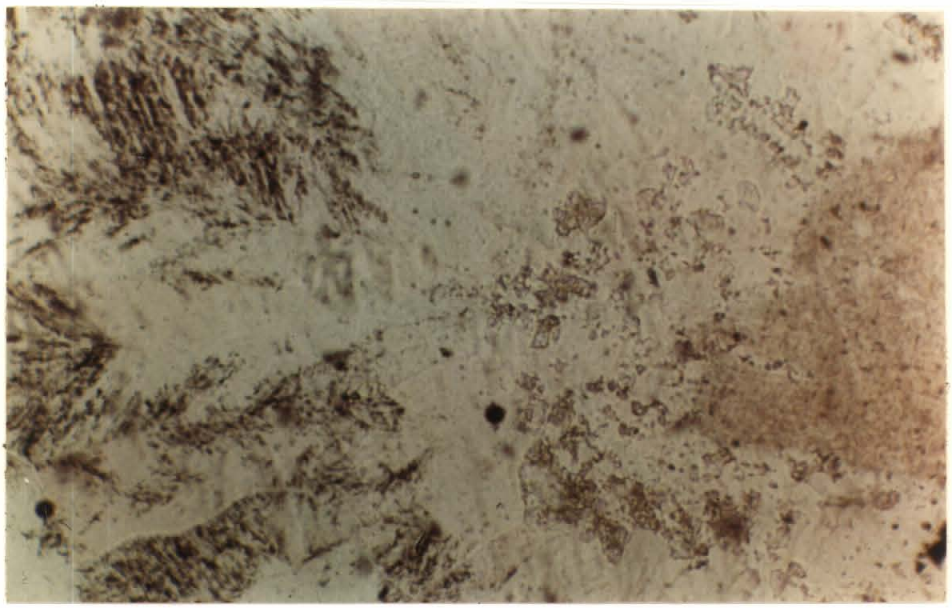

Figure 52. Photomicrograph of Stage V comb quartz of sample 1004. Sample collected in the Northern Extension of the Telegraph system, Plate 5. Note darkly shaded, empty "explosion" or pseudo-secondary inclusions fanning away from the Stage IV fragment (see below). and minute adularia rhombs in early Stage V quartz. Plane-polarized.

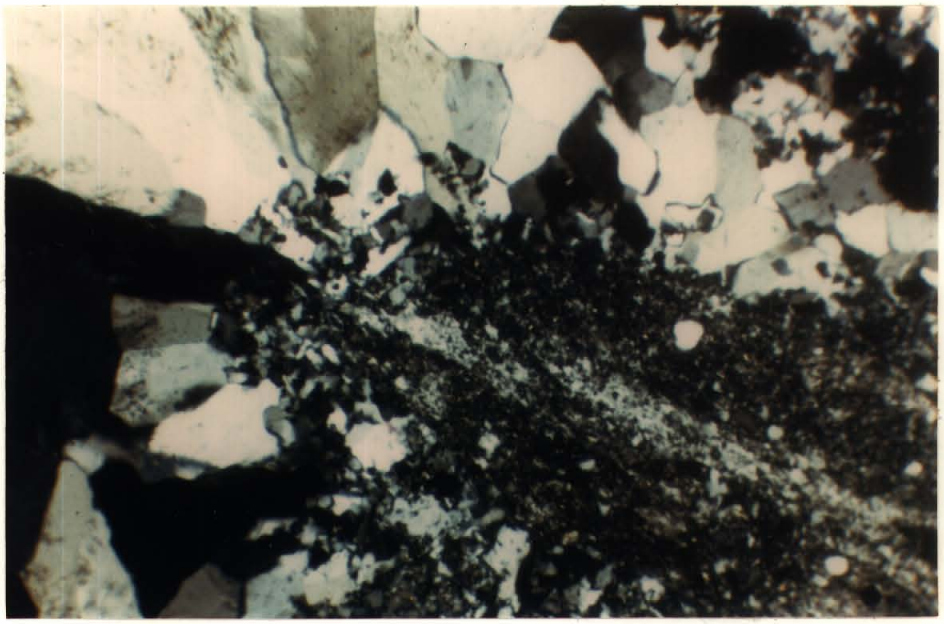

Figure 53. Cross-polarized photomicrograph of sample 1004. Photo shows Stage IV microbreccia fragment (a), radiating Stage V comb-textured quartz.

particularly difficult due to local clustering of radial chlorite rosettes, and only sample TP-32 contained inclusions suitable for both heating and freezing determinations. Th ranged from 282°C to 362°C and l:v ratios ranged from 19:1 to 1:1; both parameters indicate that a two-phase, boiling fluid was trapped (Roedder, 1984). The true trapping temperature, therefore is approximately 282°C.

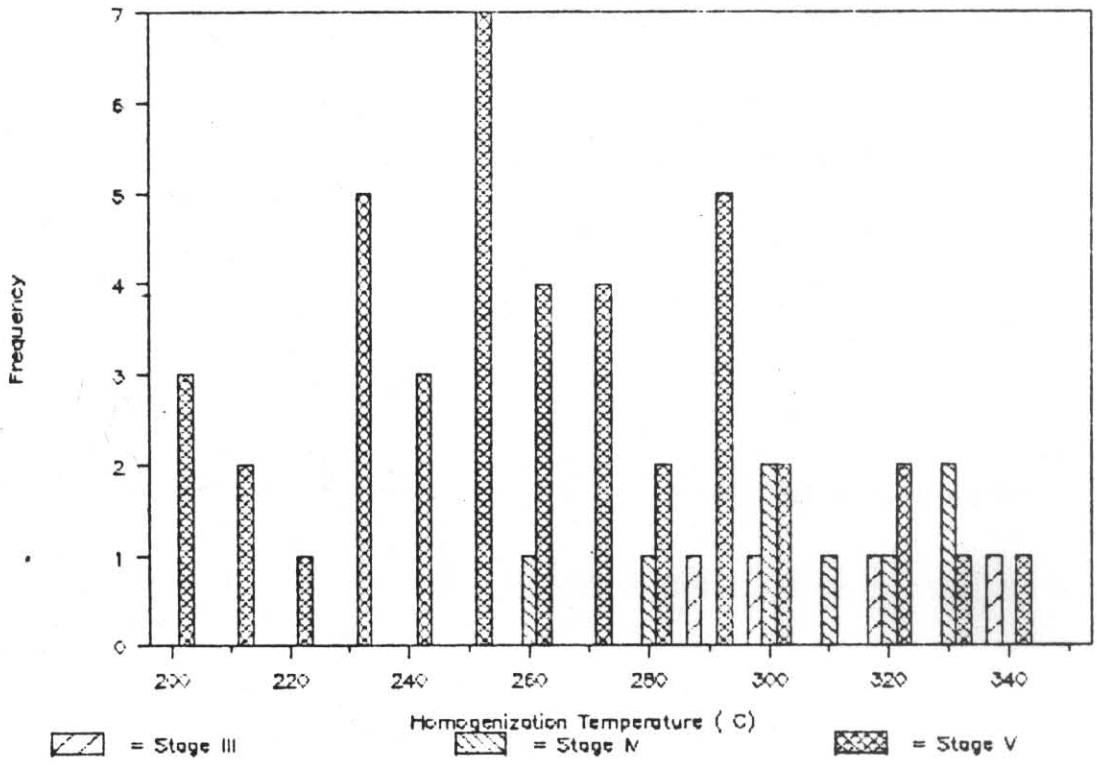

Figure 54. Distribution of fluid inclusion homogenization temperatures from Telegraph System Stage III, IV and V quartz Details are given in Table 11.

Table 10. Summary table of fluid inclusion data.

Location (elev.)	Sample No.	Stage (number of inclusions)	L:V max. min.	T_h(°C) range (mean)	T_m(°C) range (mean)	Salinity equiv.wt.% (mean)
Telegraph Breccia						
Hill 2 (3850ft.)	Tp-32	III (5)	20:1 1:1	280 to 362 (318)	-3.0 to 3.9 (-2.8)	5.0, 6.3 (5.6)
Hill 2 (3800ft.)	1052	IV (2)	5.7:1 1.2:1	263 to 315	-	-
N. Ext.	1000A	IV (3)	9.1:1 1.2:1	260 to 276	-2.0 to -2.1	3.1
Hill 2 (3880ft.)	909A	V (5)	11.5:1 1:1	210 to 340 (261)	-0.7 to -1.4 (-0.9)	1.2 to 2.5 (2.0)
Hill 2 (3880ft.)	907B (3)	V	9:1 1.9:1	203 to 289 (239)	-	-
Hill 2 (3860ft.)	941	V (4)	19:1 4:1	218 to 319 (271)	-	-
Hill 1 (3880ft.)	961	V (2)	9:1	242 to 250	-	-
HIll 1 (3880 ft.)	974	V (2)	19:1	243 to 265	-	-
Hill 1 (3890ft.)	990	V (2)	4:1 1.5:1	224 to 321	-	-
CEM Well	3451ft.	V (2)	11.5:1 5.6:1	228 to 274	-1.5, -2.0	2.5, 3.0
CEM Well	3757ft.	V (2)	9:11 1:1	254, 295	-	-
N. Exten. (3840ft.)	1000A	V	9:1 (2)	200, 245 5:1	-0.8	1 . 4
Gold Dike Breccia						
Gld. Dke. (3660ft.)	1026	IV (6)	5:1 4:1	258 to 330 (303)	-	-
Gld. Dke. (3660ft.)	1026	V (3)	5.6:1	200 to 238 (224)	-	-

Freezing behavior was recorded to temperatures below-80°C; no visible second freezing (clathration) was observed. The observed freezing point depression was from -3 C to -3.9 C. If [CO_2] was essentially insignificant, most of the freezing point depression was therefore due to dissolved NaCl + KCl solutes (Hedenquist and Henley, 1985a). Using Potter's (1978) regression equations for NaCl solutions, this T_m range corresponds to 4.9 to 6.3 equiv. wt. % NaCl yielding a liquid phase density of 1.03 to 1.04 g/cc. at 25°C (CRC, 1975). Using Bodnar's (1983) empirically derived equations and an average salinity of 5 wt % NaCl, the vapor-saturated H_2O + NaCl liquid density calculated for a trapping temperature of 282°C is 0.801 g/cc.

Stage IV Inclusions

Usable primary inclusions were extremely rare and sparsely distributed in Stage IV quartz-illite-sericite matrix. Data obtained for the Telegraph system (Table 11) consist of Th determinations from one sample on Hill 1 (977), one sample from Hill 2 (1052) and one Northern Extension sample (1000A). Th measurements ranged from 263°C to 388°C and l:v ratio range was between 9:1 to 1.1:1. Evidence for boiling is suggested by these widely varying Th values and l:v ratios, and fine-grained textures (see Table 12, Section VII). If near-hydrostatic conditions prevailed (a reasonable assumption), the minimum Th, or 263°C, approximates Tt. This temperature agrees with the 250°C average formation temperatures reported for many epithermal deposits with identical hydrothermal assemblages

(Buchanan, 1981; Mosier, 1986.) The minimum Th for both the Telegraph and the Gold Dike systems are approximately 260°C, suggesting nearly similar conditions of formation (Table 11).

Freezing-point determinations could be made from one sample only (1000a) due to the paucity of suitable inclusions. A Tm of -2.1 for Stage IV fluids yields a salinity estimate of 3.13 wt % NaCl (Potter, 1978); assuming that NaCl alone was responsible for the freezing point depression. Fluid density for a solution of this salinity is approximately 1.0203 g/cc. at 25° C and the corresponding 260°C fluid density is 0.81 g/cc (from Bodnar,1983 and Haas,1976). The crushing test for CO_2 was negative, although the extremely small size and rarity of inclusions makes these determination preliminary only.

Stage V Inclusions

Stage V yielded more positive results from larger (0.005 to 0.018 mm), more evenly distributed liquid-dominated inclusions in euhedral comb quartz associated with adularia and "snowflake" calcite mineralization. Large, isolated, negative-crystal inclusions enclosed in central growth zones were trapped early in the development of quartz crystals with late-stage, empty, explosion inclusions radiating to the crystals edge (Fig. 65).

Th values, as expected for a boiling fluid, varied widely, from 203°C to 340°C and l:v ratios ranged from 19:1 to 1:1 (Fig. 69). Tt is therefore approximately 203° C, as there is no pressure correction needed for boiling fluids under hydrostatic conditions.

Crushing studies did not reveal the presence of significant CO_2 (ie. over 0.1m % CO_2), but the presence of ubiquitous calcite makes the assumption of CO_2-free inclusions difficult: there must be some HCO_3^- in solution to stabilize calcite in solution (Fournier, 1985-b).

Freezing point depression measurements ranged from -0.6 C to -1.5 C. The range in Tm may be due to analytical error, to the presence of variable concentrations of undetected CO_2, or to local variations in boiling history (as boiling affects residual fluid salinity.) In any event, the average Tm was approximately-1.04 C, which corresponds to a salinity of 1.70 eq. wt. % NaCl. Fluid density at 25 C was 1.0103 g/cc. and 0.860 g/cc at 203°C (Bodnar,1983).

Fluid Pressure and Depth of Formation

Under hydrostatic conditions, the depth to a boiling interface ("initial boiling level") for a saline fluid is a function of water table depth, fluid temperature and the concentration of dissolved solids and volitiles (mainly CO_2). In "open" boiling, the hot fluid column extends unobstructed to the water table surface and boiling occurs at a level where fluid pressures equal hydrostatic pressure, or the weight of the overlying column of water (Haas, 1977). Haas'(1977) steam tables provide both pressures and depths of minimum boiling level for an open, saline fluid system. Higher salinity fluids boil at slightly shallower depth, and gas-rich fluids usually boil at much

deeper levels, for a given temperature (Hendenquist and Henley, 1985a).

If a hydrothermal fluid conduit is not open to the surface, due to wall rock constriction or by mineral deposit "sealing", pressures greater than hydrostatic (approaching lithostatic) are imposed on the fluid column (Roedder and Bodnar, 1980). Theoretically, as the hot fluids are confined, fluid and vapor pressures and temperatures will continually increase in the fluid column until the confining, or "super-hydrostatic", pressures are overcome. Boiling will ensue under these conditions when internal fluid + vapor (steam + gas) pressures exceed the confining pressure, or the constriction is broken by tectonic activity. Suddenly un-confined fluids have an internal energy greater than is required for "hydrostatic boiling" at the shallower elevations, these high-energy fluids therefore boil under sub-hydrostatic conditions.

If trapping pressures greater than hydrostatic were in effect at the time of inclusion formation, then homogenization temperatures would not reflect true trapping temperatures because the fluid would have been subjected to super-heated conditions above the critical behavior curve for water (Roedder, 1984.) However, if the fluids in question were boiling, then near-critical behavior can be assumed and estimates of both trapping temperature (Tt) and trapping pressure (Tp) can be obtained from Th.

A 282°C temperature for Stage III produced a fluid pressure of ~62 bars in a 5 wt.% NaCl fluid which could have boiled, at

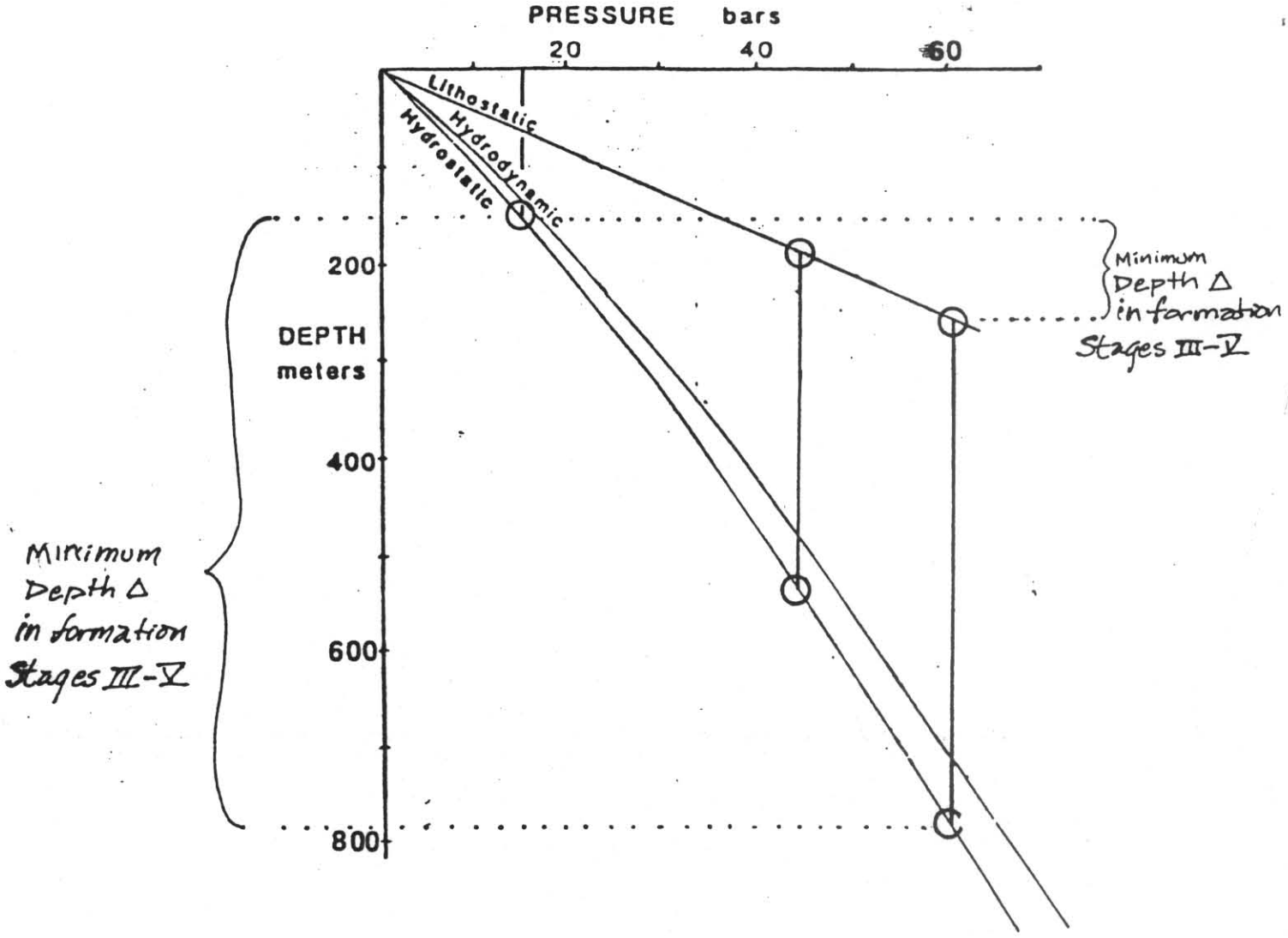

Figure 55. Proposed fluid pressure-depth conditions for the various stages of tectono-hydrothermal brecciation and mineralization. Diagram modified from Henley et al., 1985.

hydrostatic conditions, at a maximum depth of -720 m and a minimum initial boiling depth of ~-250 m if the fluid was confined (Fig. 55). Under hydrostatic conditions, boiling of Stage IV 260°C fluid occurred under approximately 46 bars pressure (data by Haas, 1976) at a depth of -546 m.

Stage V fluids boiled violently at 200°C under 15.3 bars hydrostatic fluid pressure at an estimated initial fluid boiling-level depth of 160 m. Since this figure assumes no dissolved CO_2, it represents a minimum value for the actual depth of formation, as Stage V fluids most probably contained some dissolved CO_2. However, this figure approaches a calculated geologic reconstruction paleo-depth of 188 m to the elevation of Stage V veining (see Section X).

VII

TELEGRAPH MINE FLUID CHEMISTRY

Fluid temperature, pressure, dissolved metal ion concentrations and gas concentrations are important physicochemical parameters affecting mineralization in an epithermal system. At a given temperature, estimations of P_{H_2}, and fO_2 of the original fluid are possible if certain assumptions concerning fluid-mineral equilibria can be reasonably inferred from the hydrothermal mineral assemblage. Calculations and estimates of fluid pH and redox state in this study rely on experimental results on epithermal fluid-mineral equilibria systems.

Unfortunately, natural geologic systems are considerably complex and closed laboratory conditions cannot fully address all reactions possible in epithermal ore deposits. The value of establishing geothermal development fields as modern analogs for epithermal ore deposits is becoming increasingly evident.

Therefore, in establishing reference environments for Telegraph fluids, this study utilizes recent research in modern geothermal systems. Where applicable, epithermal deposits displaying similar alteration, mineralization and fluid inclusion-documented physicochemical characteristics are also cited.

Care was taken to ensure that assumptions concerning estimated fluid parameters were reasonable. In constructing fluid-evolution models for Telegraph fluids, the following general assumptions were made:

1) The hydrothermal fluids were in, or nearly in, equilibrium with precipitating mineral phases. "Local equilibrium" conditions were established between mineralizing fluids and wall rocks (Rose and Burt, 1979).

2) Unless otherwise noted, hydrothermal alteration represent stable or metastable mineral assemblages reflecting conditions <u>at the moment</u> of formation (Henley et al., 1985.)

3) The fluids followed the same thermodynamic phase-rule restrictions as the reference-environment fluids cited.

4) From a chemical standpoint, the Telegraph fluids operated under conditions of nearly hydrostatic pressure.

Fluid Chemistry Parameters

pH Calculations

Temperatures (T_t) and fluid salinities from inclusion studies are used whenever possible in selecting appropriate reference environments. Salinity, actually total NaCl+KCl (or [Na + K]) in solution, is reported here as "apparent salinity" due to the uncertainty in inclusion CO_2 concentrations (hereafter shown as $[CO_2]$). According to extensive empirical data, Na^+/K^+ ratios of many modern geothermal systems appear to vary constantly with temperature from:

Table 11. Alkali ratios of modern hydrothermal systems

Temperature:	200°C	250°C	300°C
Na^+/K^+ :	15:1	10:1	7:1

Source : (Ellis, 1979; and Henley, et al., 1985).

These figures pertain to fluids considered buffered by chloride fluid interactions with K-Al-rich wall rocks (silicic to intermediate igneous rocks) and would not necessarily be valid for excessively acid or basic solutions. These ratios provided an means of estimating total $[K^+]$ of each fluid Stage from fluid inclusion salinities, and also aided selections of reference environments. This $[K^+]$ estimate allowed for independent calculations of fluid pH and ionic strength.

Fluid pH in solution is controlled by redox conditions

(measured as fO_2 or fH_2), and the action of mineral buffers in solution. In recent thermodynamic studies of modern geothermal fields, Henley and Brown (1985) have reported a convenient method of calculating fluid pH from measured fluid salinities. Assuming that fluid pH is buffered by the familiar K-feldspar K-mica hydrolysis reaction,

$$3\ KAlSi_3O_8 + 2\ H^+ \rightleftharpoons KAl_3Si_3O_{10}(OH)_2 + 6\ SiO_2 + 2\ K^+ \quad \text{(eq. 9.1)}$$

pH is calculated from the measured (or estimated) potassium ion molality (mK^+) and activity (aK^+) where $aK^+ = K_t (mK^+)$ (eq. 9.2)

and K_t = empirical activity coefficient for K^+ at a given temperature/salinity (tabulated by Henley et al, 1985).

An equilibrium constant (K_t) for equation (9.1) for a fluid of given temperature (T, in °Kelvin) can be calculated using Henley and Brown's relation:

$$\log K_t = 5.1062 + 6.31 \times 10^{-4} (T) + 1302.5/(T) \quad \text{(eq. 9.3)}$$

And finally, fluid pH is determined from the relation,

$$\log K_t = 2 \log mK^+ + 2 \log K^+ + 2\ pH \quad \text{(eq. 9.4)}$$

Equation (9.4) is similar to the more familiar exponential form:

$$K_t = (aK^+ / aH^+)2 \quad \text{(eq.9.5)}$$

often calculated for reaction (9.1). The familiar pH vs fO_2 activity-activity fluid equilibria diagrams of many epithermal studies are based on this buffering reaction.

Oxidation State Estimation

Fluid oxidation state is primarily examined in terms of fO_2, and redox conditions can be estimated from stable co-existing

mineral assemblages. For appropriate pH and temperature conditions, fO_2 vs pH diagrams provide valuable links between experimental and natural systems. In natural geothermal systems, fO_2 (and fH_2) is primarily controlled by fluid Fe^{2+} Fe^{3+} and S^{-2} - S_2^{-2} redox equilibria. Redox conditions are therefore important in assessing the stability of bisulfide and thiosulfide metal complexing species in solution.

CO_2 Estimation

Although $[CO_2]$ is apparently low in all stages of Telegraph fluids, it cannot be completely ignored as significant quantities are always measured in studies of geothermal systems (Ellis, 1979). Giggenbach (1980) arrived at empirical estimates of $[CO_2]$ from alteration studies of active geothermal systems where chlorite/epidote calcite are stable phases; fCO_2 is calculated primarily as a function of temperature. Shikazono (1985) collated fluid inclusion analyses, Giggenbach's results and experimental fluid equilibria based on stable alteration assemblage data from many Neogene Au-Ag and Ag-Pb-Zn epithermal deposits of Japan. His regression analysis trends for assemblages and temperatures very similar to the Telegraph indicate that Telegraph fluids probably contained less than 0.5m CO_2.

Chemical Effects of Boiling

Simple cooling, wallrock-fluid interactions, hydrothermal fluid/meteoric water mixing, and boiling are all common precip-

itation mechanisms called upon in studies of epithermal deposits. Fluid Inclusion data, mineral textures and speciation, and most recently, mineral paragenesis, have been variously cited as evidence for boiling-dominated fluid systems. Gangue paragenesis pertaining to the initial boiling of Telegraph fluids is discussed in Table 13.

The Telegraph system mineral paragenesis clearly documents episodic boiling along with concurrent tectonic events. Recurrent hot fluid-pressure build-up followed by pressure release and subsequent boiling produces overprinted mineralization at a particular elevation or isolated area that reflects local physicochemical conditions at a particular time. The physicochemical variables include: water-table elevation, heat flux in the ascending fluid, dissolved gas content, and possibility of hydrothermal/surface fluid mixing (Reed and Spycher, 1985). Repeated constriction and expansion of the pressure-temperature-depth boiling regimes may explain the mineral banding and in-situ overprinting of radically different alteration assemblages in breccia-vein deposits (Reed and Spycher, 1986). Buchanan (1981) eludes to this mechanism for the formation of discrete, repetitive mineral banding and "telescoping" ore zones in epithermal veins.

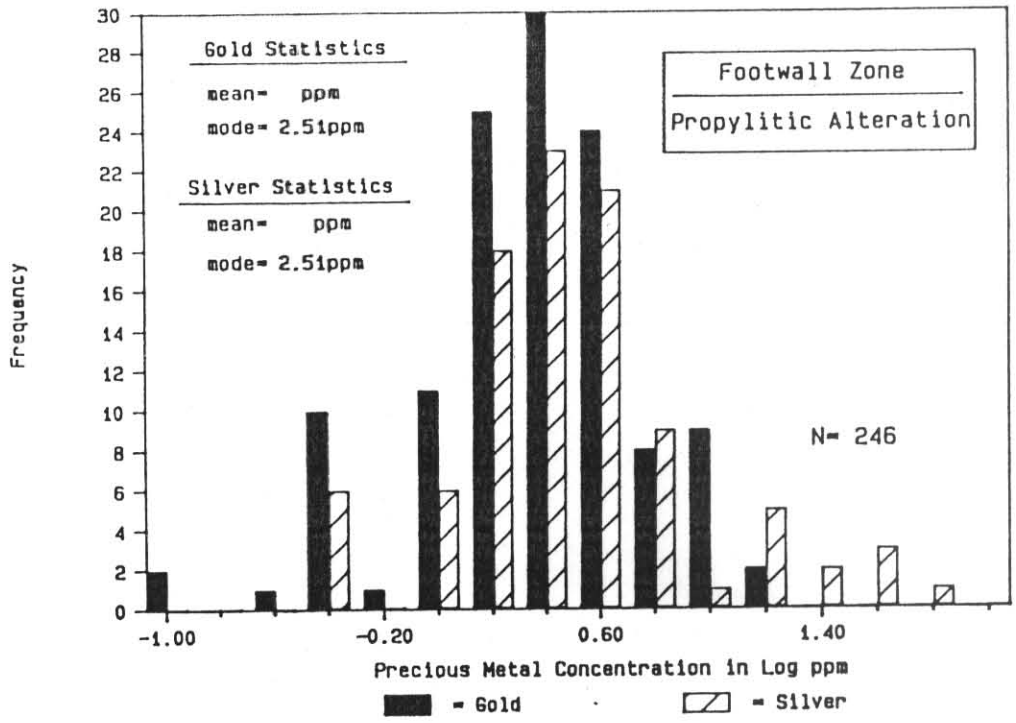

Figure 46. Rotary drill hole precious metal distribution of propylitically-altered footwall samples. Data from CEM Corp. assay logs listed in Appendix F. Explanation in text.

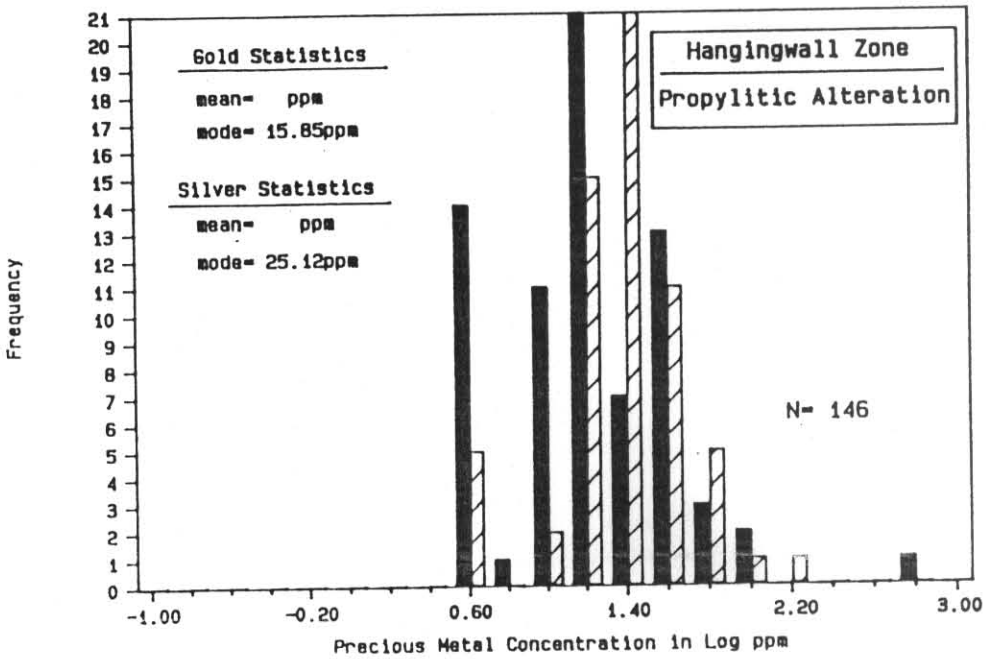

Figure 47. Rotary drill hole precious metal distribution of propylitically-altered hangingwall samples. Results from CEM Corp. assay log listed in Appendix F. Explanation in text.

TABLE 12. Specific chemical and mineralogical fractionation changes accompanying boiling from 1 to 5% (of phase conversion from liquid to vapor by weight).

1) Degassing of CO_2, H_2, and H_2S to the vapor phase.

-The loss of volitiles increases fluid pH as [H] decreases.

-90% loss of CO_2 increases pH by over one unit (Henden-quist and Henley, 1985a). A low initial [CO_2] tends to force a larger relative pH shift (Drummond and Ohmoto, 1985).

2) Metal-bisulfide complexes and chloride complexes are destabilized.

-base metal sulfides (Au and Ag) accompany calcite precipitation. An absence of base metal sulfides at the Telegraph suggests either a low initial total m (Cu^+ + Pb^+ + Zn^+), or the present erosion level exposes only the upper intervals of boiling (normally depleted in base metal sulfides.)

3) The aK^+/aH^+ ratio increases dramatically.

-adularia forms as the stable K-Al silicate phase early in the depositional sequence as Al is liberated from destabilization of $Al(OH_4)^-$. Chlorite precipi-tates with the available Al and Fe from $Fe(OH)_4^-$ (Reed and Spycher, 1986).

4) If violent boiling occurs, supersaturation of fluid with respect to silica causes fine-grained quartz deposition.

-Normally, copious silica precipitation dominates later stages of boiling primarily because cooling (not redox/pH changes) dominates silica solubility and deposition (Founier,1985).

5) At higher initial temperatures, cooling during open boiling destabilizes chloride complexes causing deposition of gold.

-Bisulfide complexed gold will remain stable until the later stages of boiling (between 5 and 90% boiling) when disruption of fluid redox state dominates mineral deposition.

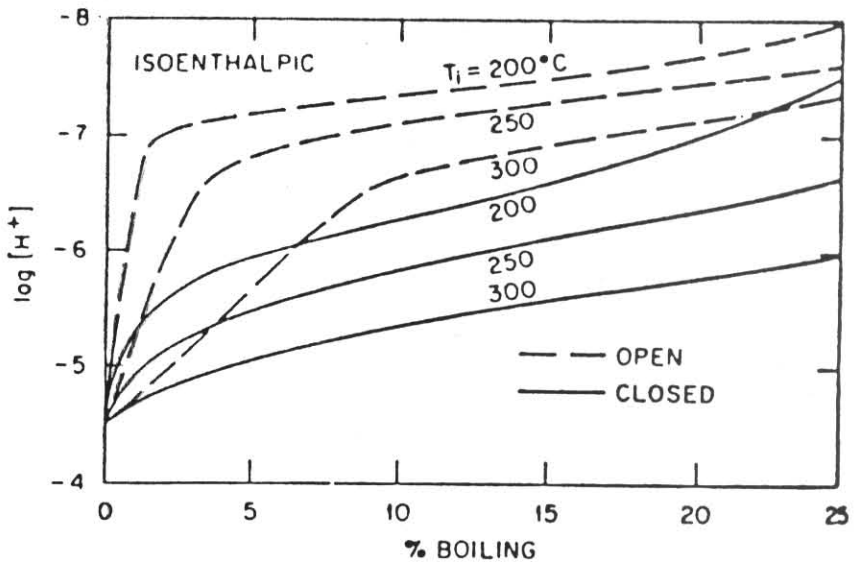

Figure 56. Boiling paths for open and closed boiling under isoenthalpic (not isothermal) conditions. Note major pH shift for open systems within the first 5% of boiling. Initial conditions: $H^+ = 10^{-4.5}$, Cl= 1.0, Na= 0.9, K= 0.1, Ca= 0.003, Mg= 0.001, CO_2= 0.3, H_2S= 0.003, $SO_4 = 3 \times 10^{-3}$. (From Drummond and Ohmoto, 1985).

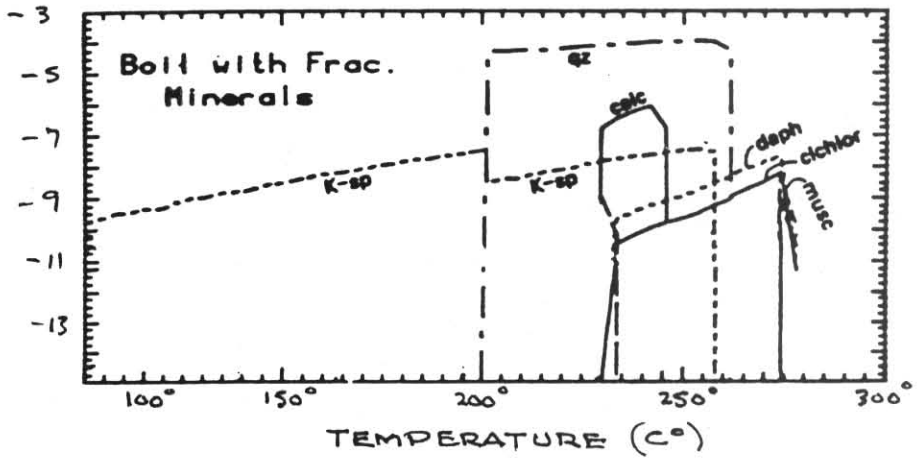

Figure 57. Calculated isoenthalpic boiling of a "Broadlands-like" water with mineral fractionation showing mineral precipitation rate in moles per degree temperature change. "daph" and "clchlor" refer to the Fe-Al rich chlorites daphnite and clinochlore; "calc" , "qz", "musc" and "K-sp" are abbreviations for calcite, quartz, muscovite and K-feldspar, respectively (From Reed and Spycher, 1985).

Fluid Chemistry and Deposition

Stage I and II Fluids

Pervasive propylitic wall rock alteration was due to hydrolysis of plagioclase and biotite. The stable Kfeldspar-quartz-montmorillinite-chlorite (pyrite) assemblage aided in bracketing fluid temperatures (in the absence of fluid inclusions) between 140° and 200°C (data from active geothermal wells, Henley et al., 1985, pg. 66.). Inner propylitic-to-argillic zone temperatures could have reached a maximum of 225 degrees C, based on the presence of mixed-layer montmorillinite-illite. The original fluids were slightly acidic (driving hydrolytic reactions) but fluid pH was buffered by the plagioclase + H_2CO_3 = 'clay' + $CaCO_3$ reaction (in this case, epidote-chlorite stability dominated over calcite.) The stability of K-feldspar ensured that fluids were buffered to near-neutral pH.0

Enrichment of SiO_2, Na^+, Fe^{++} in through-going solutions probably occurred under fairly reducing conditions (low fO_2). These solutions eventually deposited Na-Ca clays, carbonates, and free silica in the inner argillic zone (documented also at Butte by Meyer et al.,1968). Propylitic zone pyrite indicates an initially low fluid fO_2 caused the reduction of Fe^{+++} © Fe^{++} from Ktqm-wallrock magnetite-fluid interactions (Raymahashay and Holland, 1969.)

Stage III Fluid Chemistry

Stage III fluid parameters can be estimated from fluid-

mineral equilibria for the quartz-chlorite-adularia-pyrite assemblage at ~280°C and an apparent salinity of 5.0 equiv. wt% (NaCl + KCl). The total alkali concentration in the original fluid, in mg/kg, was $[Na^+ + K^+] = 1.0m$ and estimated $[K^+]$ is ~0.13m (from Table 9.1). Ionic strength was approximately 0.5 (for dilute solutions over 250°C). CO_2 concentration was probably less than 0.2m %, similar to deep Creede solutions at 1.0 m NaCl (Barton et al., 1977); Giggenbach's method (1981) would predict a maximum of 0.3m % CO_2.

Solution pH was primarily buffered by fluid-Kfeldspar equilibria and can be calculated using equation (9.4). Using equilibria constant, $\log K_{280} = 7.81$ (from equation 9.3), an individual activity constant of $K_{300} = 0.36$ (from tables in Henley, et al.,1985) equation (9.4) takes the form:

$$7.81 = 2 \log(0.13) + 2 \log(0.36) + 2\ pH$$

and $pH_{280} = 5.2$ (neutral pH at 300°C is 5.5)

This very simple picture was undoubtedly complicated by initial wall rock-fluid buffering effects and hydrothermal chlorite-fluid equilibria. The stable assemblage adularia-chlorite-pyrite for the Creede fluids (at 300°C, 1.0 m NaCl, 0.02m S) indicate a pH $\geq$ 5.2 (Barton et al.,1977). In any case, the "high pH" assemblage suggests a shift to higher alkalinity during mineral fractionation from the original fluid (Fig. 58).

Stage III oxidation state can be deduced from chlorite-pyrite stable assemblage with reference to equilibria calculations of Romberger (1982) or Barton et al. (1977). At a pH of approxi-

mately 5.2, Romberger's work suggests a log fO_2 < -30; if the Creede fluids are referenced for comparison, estimated oxidation for log fO_2 is between -35 and -40 (see Fig. 58).

The relatively high-temperature, moderately-saline, reducing, slightly acid to neutral pH Stage III fluid conditions probably favored chloride complexing for precious metal ions in solution. Romberger (1982) showed that $AuCl_2$ is increasingly stable with temperatures above 250°C, log fO_2 less than -30 and acidic to neutral pH.

Deposition of Stage III silicate and sulfide phases seems to require a pH shift, increased oxidation state and temperature decrease. Euhedral chlorite rosettes, adularia rhombs and pyrite crystals in a fine-grained anhedral quartz matrix indicates that redox potential and pH shift operated prior to significant fluid cooling (see Table 13). Since quartz texture is sensitive to cooling rate (Fournier, 1985a), the anhedral textures developed in Stage III indicate that cooling was probably subordinate to other chemical changes. Based on fluid inclusion evidence, stable mineral assemblages, silicate paragenesis and textures, moderate boiling with cooling was probably the dominant precipitation mechanism.

Stage IV Fluid Chemistry

Stage IV assemblage at 260°C, had an apparent salinity of 3.13 equiv. wt. % NaCl. The alkali concentration was therefore

$[Na^+ + K^+]$ = 0.55 mg/kg and the estimated $[K^+]$ was ~0.055m (Table 12). Assuming the fluid was buffered by fluid-Kmica equilibria (see eq. 9.1), the estimated solution pH can be calculated from equation (9.4), with an equilibria constant, $\log K_{263+}$ = 7.9 (from equation 9.3), an individual activity constant of K_{260} = 0.70 (from Henley, et al.,1985):

$$7.9 = 2 \log (0.055) + 2 \log (0.7) + 2\ pH$$

and pH_{260} = 5.4 (neutral pH at 250°C is 5.6)

Hendenquist and Henley's study (1985b) of the Waiotapu geothermal breccias serve as an appropriate reference as the fluid temperatures and salinities are very similar to those of the Telegraph. Their work indicates that the boiling 250°C to 300°C fluids were buffered by the Kmica-Kfeldspar reaction, and "white mica" + pyrite was stable in a pH range of 5 to 6.5 and $\log fO_2$ = -33 to -39.

The reducing, neutral, low salinity Stage IV fluid would fix H_2S as the stable sulfur species and AuH_2S as the dominant gold complex species in solution (Romberger, 1982). The stability of $AuCl_2$ requires considerably higher oxidation conditions in order to be stable at temperatures below 300°C. Identifying the dominant silver species is problematical as both $AgCl_2^-$ and AgH_2S may be stable under these fluid constraints. At the above conditions, the aCl- would be far greater than aH_2S and the chloride complex would probably dominate over the bisulfide complex.

Fluid inclusion, breccia formation and textural/mineralogical evidence argue for a <u>probable</u> boiling-related evolution

Stage V Fluid Chemistry

Stage V fluids boiled violently at 200°C, at a total apparent salinity of 1.5 eq. wt % NaCl and resulted in the distinctly characteristic quartz-adularia-calcite-pyrite stable assemblage. Since calcite solubility required significant dissolved CO_2 (Fournier,1985b), the apparent salinity is probably anomalously high, CO_2 probably contributing to inclusion freezing-point depression. If CO_2 is present to 0.1m to 0.2m (see Section VII), then the true salinity is probably closer to 1.0 equiv. wt.% NaCl or 0.17m [NaCl+ KCl]. At 200°C, the empirical estimate of $[K^+]$ = 0.01m (from Table 12).

Stage V fluid pH was probably buffered both by calcite-fluid equilibria and Kfeldspar-fluid equilibria, but only the latter can be calculated with current data. Using a log K^+_{200} = 8.16 and an individual ion coefficient K^+_{200} = 0.68 (Henley et al., 1985), the calculated fluid pH from equation (9.4) is 6.3 (neutral pH ~ 5.7 at 200°C). Romberger's (1980) fO_2 vs pH diagrams indicate that the stable Stage V assemblage required a pH of $\geq$6.8 with redox conditions between -38 and -40 log fO_2 (Fig. 60).

The lower temperature, alkaline and reducing conditions favored bisulfide complexing for Stage V gold and silver. Cole and Drummond's (1986) boiling-zone modelling trends indicate that the $Au(HS)_2^-$ species dominates gold solubility in low CO_2, alkaline to neutral pH fluids between 200-250°C. Although little is known about silver bisulfide, Henley and Brown (1985) suggests

that HS_2^- may contribute to Ag solubility in low salinity, "Broadlands-type" fluids.

The violent, probably episodic boiling of Stage V fluids resulted in the multi-pulsed mineralization assemblage characterized by fine-grained quartz, coarse adularia, snowflake calcite and relatively high gold and silver values. Initial decompression of super-heated fluid caused fine-grained quartz deposition promoted by silica super-saturation along with an elevation of pH and adularia precipitation. As H_2 was evolved into the gas phase, the residual fluid became sulfate-enriched and bisulfide complexes with gold and silver were destablized, forcing the precipitation of native gold and silver (Romberger, 1982). This mechanism produced shallow level, high-grade gold and associated increased Au/Ag ratio (see p. 111).

Since the initial $[Ca^{++}]$ was probably low, calcite remained in solution until the fluid was within about one log unit of calcite saturation (Drummond and Ohmoto, 1985). The encrusting snowflake calcite with quartz precipitated in response to this saturated condition. Further cooling of the boiling fluid promoted increasingly well-crystallized silica deposition, with vug-filling comb quartz dominating. The inverse solubility of calcite with respect to quartz in a cooling environment caused late stage pseudomorphous replacement of snowflake calcite with quartz.

Stage VI Fluid Chemistry

The absence of fluid inclusions from Stage VI mineraliz-

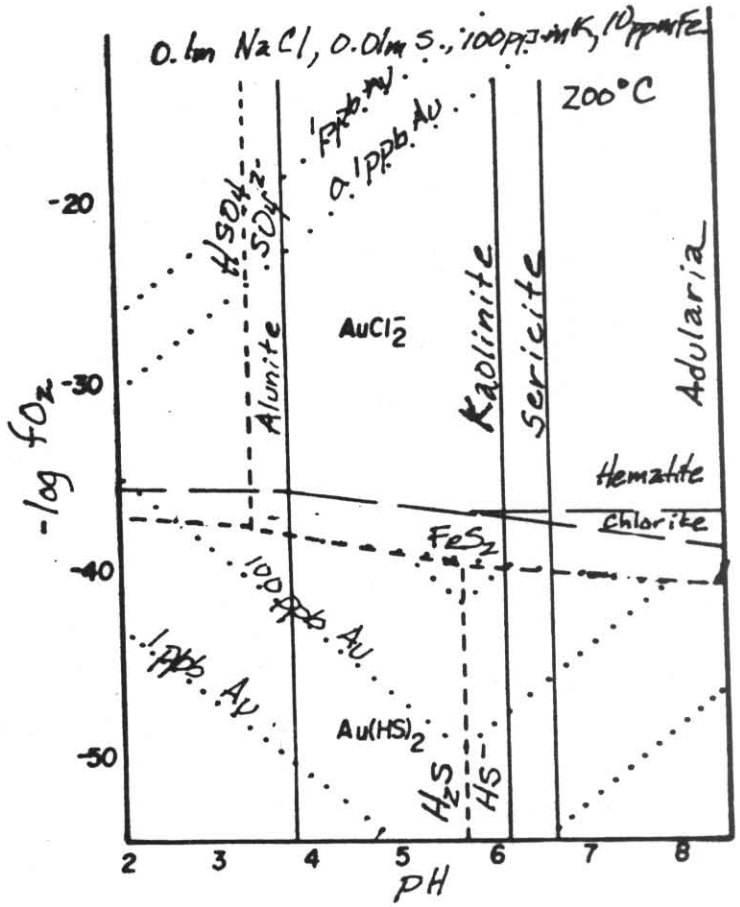

Figure 60. pH vs log fO_2 diagram for a Stage V-like Au-bearing fluid at 200°C. The initial conditions are: 200°C, 0.1mNaCl, 0.01m S, 100ppm K^+. Shading shows possible trajectory of Stage IV fluid during boiling. (From Romberger, 1980).

ation restricts the interpretation of physicochemical conditions, but enough is known about the mineral equilibria of silica and carbonate to bracket chemical conditions during Stage VI. Chalcedony is the dominant silica phase at temperatures below 180° C (Fournier, 1985b). Andrusenko's (1979) summary of temperature-alteration zonation in epithermal deposits brackets the mangano-calcite + quartz-Au-Ag assemblage formation temperature from a high of 270°C to a low of 140°C.

The lack of any salinity data makes pH estimations impossible it is likely that fluids conditions were slightly acidic (less than neutral pH of 5.7 at 200°C), and reducing (Krauskopf, 1979). Unfortunately, little is know about high temperature MnO-fluid equilibria; the oxidation state for Stage VI fluids were certainly lower than log $fO_2 < -40$.

Analysis of sample 922.1 indicate, precious metals were probably transported in solution and precipitated along with the manganiferous-calcite and quartz. If the fluids were considerably reduced, then $Au(HS)_2^-$ and $Ag(HS)_2^-$ could both be stable at low to neutral pH (Romberger,1982). If the fluids were more oxidizing, other complexing possibilities are possible. Experiments of Miller and Fisher (1973) indicate that gold will dissolve in the presence of Cl^- and MnO_2 as an oxidizing agent, forming the relatively stable $AuCl_4^-$ complex (Au oxidized to Au^{+3}).

Repetitive quartz-calcite banding in Stage VI indicates at least three separate fissure-filling, rhythmic quartz-MnO_2 -

calcite depositional episodes occurred. Snowflake calcite with amorphous Mn-O inclusions were overgrown and replaced by chalcedonic silica. Stage VI was apparently far more enriched in both Ca^{++} and CO_2, and again the evidence points to rapid decompression during boiling to account for the textural relations. Clearly, to precipitate Mn-O with calcite, an increase in oxidation state concomitant with pH shift was important, and some mixing with oxygenated surface waters was likely. Cooling would eventually promote silica supersaturation and calcite dissolution, causing the characteristic pseudomorphous silica precipitation observed in both Stage V and Stage VI. Repeated fluid boiling , recharge and reboiling would tend to develop the observed banding, similar to the banded vein formation of many epithermal deposits (Buchanan, 1981).

These relations are supported by considering the distribution of manganiferous calcite in other hydrothermal systems. Manganiferous calcite is found just below the acid-alunite zone, 8 meters below the water table, at Steamboat Springs (Silberman and Berger, 1985). Mn-oxides, enriched in silver, are abundant in low-angle veins in halos adjacent to the breccia zones at Round Mountain (Berger & Silberman, 1985).

VIII

FORMATION MODEL OF THE TELEGRAPH SYSTEM

Repeated tectono-hydrothermal brecciation, successive overprinting of alteration and mineralization, evidence of widespread boiling, repetitive mineral banding (in Stages V and VI) and a fault geometry reflecting numerous irregularities are all present along the Telegraph system. This strongly suggests an environment where periodic constriction-expansion of the boiling depth regime occurred repeatedly in conjunction with the tectonic evolution of normal-right lateral fault.

Age of the Telegraph System

Numerous epithermal vein deposits have been radiometrically dated using a variety of systems, most notably K-Ar analysis from hydrothermal sericite or adularia (Silberman et al., 1972). A 3 gram sample of pure, coarsely crystalline adularia was disaggregated from Stage V vug-filling quartz from sample 971 from Hill 1 (Plate 5). No perthitic intergrowth impurities were detected in X-ray diffraction analysis; the specimen contained an average of 11.710 % K.

Geochron Laboratories analyzed the sample and obtained a 40+Ar/40K ratio of 0.000599 with a calculated age of 10.3 (+/- 0.4) m.y. The sample was probably not subjected to significant post-crystallization thermal or tectonic stress that might have otherwise resulted in loss of Ar, and produced an erroneously

"young" date (Halliday, 1977).

Geologic Reconstruction

The Cima Volcanic field is composed of a series of coalescing Miocene - Pliocene basalt flows covering an area of 150 km^2 (Fig. 76). The flows are widespread, uniformly thin, and flow surfaces generally lay parallel to the paleo-pediment surfaces. 41 radiometric dates taken on flows throughout the region outlined 3 principal periods of Cima volcanism and provided a unique data set to evaluate the rate of Cenozoic landscape degradation in the region (Turrin and Dohrenwend, 1985). The average rate of continuous pediment downgrading has been calculated at 2.41 $cm/10^3$ years. The local erosion rate was calculated for Hill 2 using three-point projections of the paleoslope and an estimation basalt thickness. This independent value is 2.62cm/1000 year.

If an assumption of nearly continuous local erosion is extended 6 m.y., to include the time elapsed since Stage V mineralization, the calculated estimate of eroded overburden thickness above the developing system is 188m. This is almost certainly a minimum thickness, considering that gentle regional uplift has probably changed geomorphic conditions on site during the 5.2 m.y. interval. This figure, then, represents the amount of erosion that has taken place to the present erosion level on Hill 2. It approaches the calculated Stage V boiling level depth (160m), thereby confirming shallow-level precipitation of Stage

V fluids. Regional reconstruction prior to 10.5 m.y. ago is not attempted here. Dating of Stage III mineralization, to provide an elapsed time period for erosion, cannot be done with confidence as adularia is too susceptible to Ar loss during later stage thermal events. Projecting erosion rates into the Early Miocene is also highly problematical.

Tectonic Evolution of the System

Pre-Mineral Development

In the early stages, the Telegraph fault consisted of individual segments with relatively shallow dip, reflecting the NW-SE and NE-SW strikes of other normal faults in the region. The initial breaks were probably focused near post-Laramide aplite dikes, which determined where the first effects of strike-slip movement would appear. The orientation of these segments was profoundly effected by right lateral movement - significant right lateral shearing commenced sometime after 20 m.a., in response to the establishment of a NW-SE shear couple (Dokka, 1983). During this stage, minor brecciation and alteration along the breaks occurred, as evidenced by Stage I and II alteration (see Fig. 61).

Main Stage Sequence

Significant lateral displacement along the established trends, acting in concert with an active deep hydrothermal system, created Stage III and IV tectono-hydrothermal breccias. Initially, mineral distribution of quartz-chlorite-adularia-pyrite alteration

developed only in areas of favorable, northeastery curvature (as evidenced by thickest Stage III development at Hills 1 and 2.) At this time, the "fault" was still a series of en echelon NE-SW tension gashes, separated by minute NW-SE compression shears (see Fig. 61).

A period of erosion was followed by the Stage IV shearing event, which was re-opened and extended brecciated segments and promoted greater continuity of the system. All surface excavations exhibit fairly wide Stage IV zones and fluids apparently infiltrated the less favorable structures, where curvature is northerly or northwesterly (see Fig.). Stage IV mineralogy reflects shallower level boiling and possible mixing.

Late Stage Vein Sequence

As the system matured, secondary structures developed in response to both lateral shear and increased E-W extension. The widest extensional structures were superimposed on hangingwall breccias at an acute angle to the main shear. Stage V quartz-adularia-calcite-pyrite mineralization infilled the tension fractures from an episodically active hydrothermal system. Cymoidal vein systems were established at Hills 1 and 2. The northern terminus of the main fault was established by horsetail splay faults , which were opened by transtension and subsequently hosts to chalcedonic quartz (see Fig. 61).

Minor parallel fractures developed along oblique shears in the Gold Dike and Chaos Zone areas. Tension fractures developed

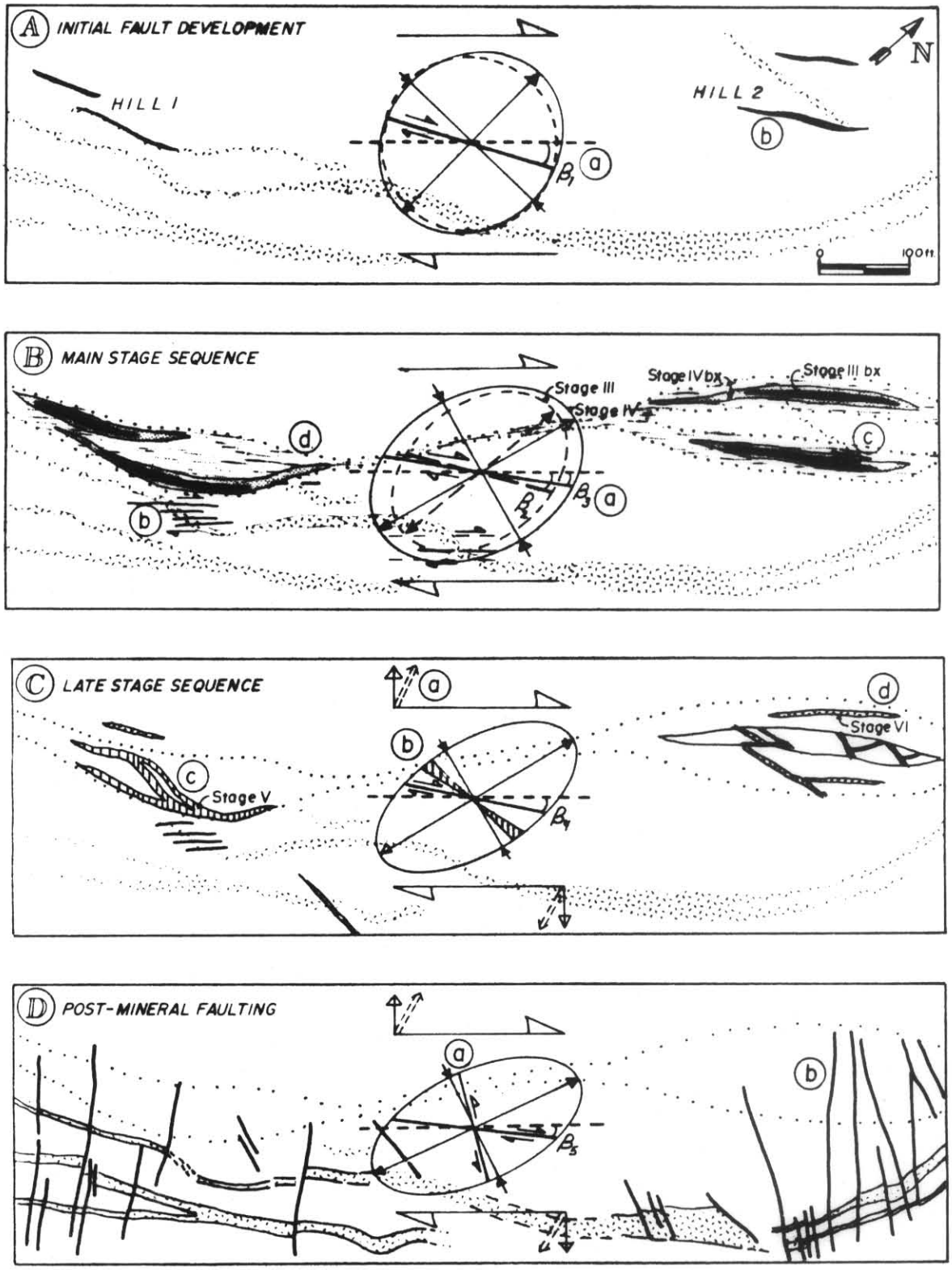

Figure 61. Tectono-hydrothermal evolution of the Telegraph system.

parallel to the main shear but from dominant E-W extension, hosted episodic, shallow quartz-carbonate mineralization of Stage VI (Fig. 61).

Post Mineral Sequence

Although normal, dip-slip faulting dominated the later development of the system, continued right lateral stress created secondary structures off the main trend (see Fig. 61). East--northeast and west-northwest high angle faults show significant left-lateral and dip slip, characteristic of antithetic faults in a transtension regime.

Later, northwest extension structures developed in response to development of Basin and Range NE-SW extension. Some of these structures offset main lateral trends and others host Pliocene and Holocene basalt dikes.

Discussion

Evidence of mid-Cenozoic intermediate to silicic volcanism is found nearly everywhere in association with well-known, low angle fault-hosted epithermal deposits. The lack of volcanism near the Telegraph deposit is conspicuous. Aside from the isolated, discontinuous quartz latite dikes found in the SE corner of the property, and the "porphyry intrusive" described by Hall (1972) in the Turquoise Mountain District, there is little evidence that a volcanic served as the main heat source for the Telegraph fluids. However, the regional elevated heat flow of the mid-Miocene Mojave plutonic arc probably provided enough heat for the development of the Telegraph system.

REFERENCES CITED

Albers, John P., 1967, Belt of sigmoidal bending and right-lateral faulting in the western Great Basin: Geol. Soc. America Bull., v. 78, p. 143-156.

Andrusenko, N. I., 1978, Temperature zonation of gold-silver deposits: Inter. Geol. Rev., v. 21, no. 7., p. 164-182.

Barton, P.B. Jr., Bethke, P.M., and Roedder, E., 1977, Environment of ore deposition in the Creede Mining District, San Juan Mountains, Colorado: Part III. Progress toward interpretation of the chemistry of the ore-forming fluids of the OH vein: Econ.-Geol., v. 72., p. 1-25.

Berger, B.R., and Silberman, M.L., 1985, Relationships of trace element patterns to geology in hot-spring type precious-metal deposits, in Berger, B.R., and Bethke, P.M., eds., Geology and geochemistry of epithermal systems: Reviews in Economic Geology, v. 2, Econ. Geol. Publishing Co., El Paso, TX., p. 233-247.

Bodnar, R. J., 1983, A method of calculating fluid inclusion volumes based on vapor bubble diameters and P-V-T-X properties of inclusion fluids: Econ. Geol., v. 78, p. 535-542.

_____ , Reynolds, T.J., and Kuehn, C.A., 1985, Fluid inclusion systematics in epithermal systems, in Berger, B.R., and Bethke, P.M., eds., Geology and geochemistry of epithermal systems: Reviews in Economic Geology, v. 2, Econ. Geol. Publishing Co., El Paso, TX., p. 73-96.

Buchanan, L. J., 1981, Precious metal deposits associated with volcanic environments in the southwest, in Dickinson, W.R. and Payne, L.S., eds., Relations of tectonics to ore deposits in the southern Cordillera: Ariz. Geol. Soc. Digest., v. 14, p. 237-262.

Cheadle, M.J., Czuchra, B.T., Ando, C.J., Oliver, J.E., Brown, L.P. and Kaufman, S., 1986, The deep crustal structure of the Mojave Desert, California, from COCORP seismic reflection data: Tectonics, Vol. 5, No. 2, p. 293-320.

CRC, 1975, Handbook of Chemistry and Physics: Weast, R. C., ed., Chem. Rubber Co. Press, Inc., pp. D-224-225.

Cole, D.R. and Drummond, S.E., 1986, The effect of transport-

ation and boiling of Ag/Au ratios in hydrothermal solutions: A preliminary assessment and possible implications for the formation of epithermal precious metal deposits: Jour. of Geochem., Vol. 25, p. 45-79.

Collins, P. L. F., 1979, Gas hydrates in CO_2-bearing inclusions and the use of freezing data from estimation of salinity: Econ. Geol., Vol. 74, p. 1435-1444.

Conolly, H. J. C., 1935, A contour method of revealing ore structures: Econ. Geol., Vol. 31, p. 259-271.

DeWitt, E., 1980, Geology and geochronology of the Halloran Hills are southeastern California, and implications concerning Mesozoic tectonics of the southeastern Cordillera: Unpublished PhD. dissertation, Pennsylvania State University, University Park, 269 pp.

Dickinson, W. R., 1981, Plate tectonic evolution of the southern Cordillera, in Dickinson, W. R., and Payne, W. D., eds., Relations of tectonics to ore deposits in the southern Cordillera: Arizona Geol. Soc. Digest, Vol. 14, p. 113-131.

Dougherty, R., 1986, Template for calculation of correlation coefficients with LOTUS 123: Unpublished public domain program, Colorado State University (avail. on disk only).

Dohrenwend, J. C., McFadden, L. D., Turrin, B. D., and Wells, S.G., 1984, Rates and trends of Late Cenozoic landscape degradation in the are of the Cima Volcanic Field, eastern Mojave Desert, California, in Western Geological Excursions, Mackey School of Mines-Geol. Soc. America 1984 Annual Meeting Guidebook, Reno, Nevada, v. 1, p. 178-190.

Dokka, R.K., 1986, Patterns and modes of early Miocene crustal extension, central Mojave Desert, California, in Mayer, L., ed., Extensional tectonics of the southeastern U.S.: A perspective on Processes and kinematics: Geol. Soc. America Special Paper 208, p. 75-95.

Drier, John, 1984, Regional tectonic control of epithermal veins in the western United States and Mexico: Ariz. Geol.-Soc. Digest, v. 15, pp. 28-50.

Drummond, S.E., and Ohmoto, H.,1985, Chemical evolution and mineral deposition in boiling hydrothermal systems: Econ-Geol., v. 80, pp.126-147

Eaton, Gordon P.,1980, Geophysical and geological characteristics of the crust of the Basin and Range: in Studies in geophysics: Continental Tectonics: Geophysics Study Committee of Geophysics Research Board, eds., National Academy of Sciences, Washington D. C., p. 96-126.

Ellis, James, A., 1979, explored geothermal systems, in Barnes, H. L., ed., Geochemistry of hydrothermal ore deposits: John Wiley & Sons, New York, 798 p.

Emmons, R.C., 1969, Strike slip rupture patterns in sand models: Tectonophysics, v. 7,

Fournier, Robert O., 1985a, Silica minerals as indicators of conditions during gold deposition, in Tooker, E.W. (ed.),Geologic Characteristics of Sediment and Volcanic-
hosted Types of Gold Deposits: U.S. Geol. Survey Bull. 1646, p. 15-26.

_____ , 1985b, The behavior of silica in hydrothermal solutions: in Berger, B.R., and Bethke, P.M., eds., Geology and Geochemistry of Epithermal Systems: Reviews in Economic Geology, v. 2, Econ. Geol. Publishing Co., El Paso, TX., p. 45-61.

_____ , 1985c, Carbonate transport and deposition in epithermal environments: in Berger, B.R., and Bethke, P.M., eds., Geology and Geochemistry of Epithermal Systems: Reviews in Economic Geology, v. 2, Econ. Geol. Publishing Co., El Paso, TX., p. 63-72.

Fraser, D. C., 1969, Contouring of VLF-EM data: Geophysics, v. 34, p. 958-967.

Garfunkel, Z., 1974, Model for the Late Cenozoic tectonic history of the Mojave Desert, California, and for its relation to adjacent regions: Geol. Soc. America Bull., v. 85, p. 1931-1944.

Giggenbach, W. F., 1981, Geothermal-mineral equilibria: Geochem. et Cosmochimica Acta, v. 45, p. 393-410.

Gough, D., 1965, Structural analysis of ore shoots at Greenside lead mine, Cumberland, England: Econ. Geol., v. 60, p. 1459-1477.

Haas, J. L. Jr., 1976, Physical properties of the coexisting phases and thermochemical properties of the H20 component in boiling NaCl solutions: U. S. Geol. Survey Bull. 1421-A, 73 p.

_____ , 1971, The effect of salinity on the maximum thermal

gradient of a hydrothermal system at hydrostatic pressure: Econ. Geol., v. 66, pp. 940-946

Hall, D. K., 1972, Hydrothermal alteration and mineralization in the East Camp of the Turquoise District, San Bernardino Co., California: M. S. thesis, Department of Geosciences, University of Arizona, 137 p.

Halliday, A. N., 1977, K-Ar Dating of mineralization episodes- a discussion: Econ. Geol. v. 72, pp. 870-871.

Hedenquist, J. W., and Henley, R.W., 1985a, The importance of CO_2 on freezing point measurements of fluid inclusions: Evidence from Active Geothermal Systems and Implications for Epithermal Ore Deposition: Econ.
Geol.,v. 80, pp. 1379-1406.

_____, 1985b, Hydrothermal eruptions in the Waiotapu geothermal system, New Zealand: Their origin, associated breccias, and relation to precious metal mineralization:
Econ. Geol., v. 80, pp. 1640-1688.

Henderson, G. V., 1984, Geology of the Silvers Hills lead-silver deposit, Silurian Hills, California, in Fife, D. L., ed., Geology and Mineral Wealth of the California Desert: So. Coast Geol. Soc. Digest, p. 349-351.

Henley, R.W., and Brown, K.L., 1985, The geothermal framework of epithermal deposits: in Berger, B.R., and Bethke, P.M., eds., Geology and Geochemistry of Epithermal Systems: Reviews in Economic Geology, v. 2, Econ. Geol. Publishing Co., El Paso, TX., p. 25-43

_____, Truesdell, A. H., and Barton, P. B., 1985, Fluid Equilibria in Hydrothermal Systems: in Henley, R.W., Truesdell, A.H. and Barton, P.B., eds., Reviews in Economic Geology, v. 1, Society of Economic Geologists, El Paso, TX, 266 p.

Hewett, D. F., and Radtke A. S., 1967, Silver-bearing black calcite in western districts: Econ. Geol. Bull., v. 62, no. 1, p. 1-19.

Hewett, D. F., 1956, Geology and mineral resources of the Ivanpah Quadrangle, California and Nevada: U. S. Geol. Survey Prof. Paper 225, 171 p.

Hutchinson, C.S., 1974, Laboratory Handbook of Petrographic Techniques: J. Wiley and Sons, N.Y., 527 p.

Ito, T., 1968, The Telegraph Mine, San Bernardino Co., Califor-

nia: Unpub. report with proposal to the U. S. Geol. Survey Off. Min. Explor., 20 p.

Jaroszewski, W., 1984, Fault and Fold Tectonics: Ellis Harwood, Ltd, Chichester, U.K., 565 p.

Jensen, M. L., 1981, Review report on the Telegraph Mining Venture, San Bernardino Co., California: Unpub. consultant report for Telegraph Gold, Inc., 13 p.

Krauskopf, K.B., 1979, Introduction to Geochemistry: McGraw--Hill, N.Y., 698 p.

Lawrence, C. R., 1976, Strike-slip faulting terminates the Basin and Range Province in Oregon: Geol. Soc. America Bull., v. 87, p. 846-850.

Lepeltier, C., 1969, A simplified statistical treatment of geochemical data by graphical representation: Econ. Geol., v.64, pp. 538-550.

Mckinstry, H. E., 1948, Mining Geology: Prentice Hall, N.Y., 680 p.

McCurry,M., 1984, A preliminary report of a large silicic volcanic center in the eastern Mojave Desert, San Bernardino Co., California, in Fife, D.L., ed., Geology and Mineral Wealth of the California Desert: So. Coast Geol. Soc. Digest, pp. 242-247.

Mosier, D. L., Menzie, W.D., and Kleinhampl, F.J., 1986, Geologic and grade tonnage information on Tertiary epithermal precious and base metal vein districts associated with volcanic rocks: U.S. Geol. Survey Bull. 1666, 37 p.

Miller, A. D., and Fisher, E. I., 1973, Oxidation by MnO2: Geochem. Inter., v. 10, p. 656-663.

Nielsen, R.L., 1965, Right lateral strike-slip faulting in the Walker Lane, west central Nevada: Geol. Soc. America Bull., v. 76, p. 1301-1308.

Owens, J., 1980, Report of examination of the Telegraph Mine, San Bernardino Co., California: Cascade Energy and Metals Corp. Report, 25 p.

Park, C.F. Jr., and McDiarmid, R.A., 1975, Ore Deposits: W.H. Freeman and Co., San Francisco, 530 p.

Paterson, N. R., and Ronka, V., 1969, Five years of surveying with the VLF- E.M. method: Soc. Explor. Geophys.,

Annual International meeting, 9 p.

Polovina, J. S., 1984, Origin and structural evolution of gold-silver-copper bearing hydrothermal breccias in the Sleeper Mining District, southeastern California: Ariz. Geol. Soc. Digest, v. 15, p. 159-165.

Potter, R. W. II, Clyne, M. A., and Brown, D. L., 1977, Freezing point depression of aqueous sodium chloride solutions: Econ.-Geol., v.73, p. 284-285.

Reed, M. H. and Spycher, N. F., 1985, Boiling, cooling, and oxidation in epithermal systems: a numerical approach, in Berger, B.R., and Bethke, P.M., eds., Geology and Geochemistry of Epithermal Systems: Reviews in Economic Geology, v. 2, Econ. Geol. Publishing Co., El Paso, TX., p. 249-272.

Robinson, J. P., 1979, Petrology and petrochemistry of granitic intrusions of the Cima Dome-south Ivanpah Mountains area, southeastern California: M. S. thesis, University of Southern California at Los Angeles, 125 p.

Roedder, E., 1984, Fluid Inclusions, in Ribbe, P.H., ed., Reviews in Mineralogy: Mineral. Soc. America, v. 12, 643 p.

_____ , and Bodnar, R. J., 1980, Geologic pressure determinations from fluid inclusion studies: Ann. Rev. Earth Planet. Sci., v. 8, p. 263-301.

Romberger, S.R., 1982, Geochemistry of Precious Metal Hydrothermal Systems: Unpub. short course, 68 p.

Rose, A. W.,and Burt, D. M., 1979, Hydrothermal alteration, in Barnes, H. L., ed., Geochemistry of Hydrothermal Ore Deposits: John Wiley & Sons, New York, 798 p.

Shikazono, N., 1985, Gangue minerals from Neogene vein-type deposits in Japan and an estimate of their CO_2 fugacity: Econ Geol., v. 80, p. 574-768.

Silberman, M. L. and Berger, B. R., 1985, Relationship of trace element patterns to alteration and morphology in epithermal precious metal deposits, in Berger, B.R., and Bethke, P.M., eds., Geology and Geochemistry of Epithermal Systems: Reviews in Economic Geology, v. 2, Econ. Geol. Publishing Co., El Paso,TX., p. 203-232.

_____, 1985, Geochronology of hydrothermal alteration and mineralization: Tertiary epithermal precious metal

deposits in the Great Basin, in Tooker, E. W., ed., Geologic Characteristics of Sediment- and Volcanic-Hosted Disseminated Gold Deposits: Geol. Soc. America Bull. 1646, P. 55-70.

_____, Chesterman, C. W., Klienhampl, F. J., and Gray, C. H. Jr., 1972, K-Ar ages of volcanic rocks and gold-bearing quartz-adularia veins in the Bodie Mining District, Mono Co., California: Econ. Geol., v. 67, p. 597-604.

Sillitoe, R. H., 1985, Ore-related breccias in volcano plutonic arcs: Econ. Geol., v. 80, p.1467-1514.

Sinclair, A. J., 1974, Selection of threshold values in geochemical data using probability graphs: Jour. of Geochem. Explor., v. 3, p. 129-149.

Smith, D. M., Albinson T., and Sawkins, F. J., 1982, Geologic and fluid inclusion studies of the Tayalotita silver-gold vein deposit, Durango, Mexico: Econ. Geol., v. 77, p. 1120-1145.

Snedecor, G. W., and Cochran, W. G., 1967, Statistical Methods: Iowa University Press, Ames, Iowa, 593 p.

Tanner, W. F., 1962, Surface structural patterns obtained from strike-slip models: Jour. Geol., v. 70, p. 101-107.

Teleford, W. M., 1976, VLF mapping of geologic structure Geol. Survey Canada Paper 76-25, 15 p.

Tucker, W. B., and Sampson, R., 1943, Mineral resources of San Bernardino Co., California: Calif. Jour. Mines and Geol., v. 39, p. 427-545.

Turrin, B. D., and Dohrenwend, J. C., 1985, Potassium-Argon ages from the Cima volcanic field, eastern Mojave Desert, California: U. S. Geol. Survey Appendix Data File, 20 p.

Warnke, D. A., 1969, A geologic investigation of the Halloran Hills, central Mojave Desert, California: Geol. Rund., v. 58, no. 3, p. 998-1047.

Wilcox, R. E., Harding, T. P., and Seely, D. R., 1973, Basic wrench tectonics, American Assoc. Petrol. Geol. Bull., v. 57, no. 1, p. 74-90.

Wilkins, J. Jr., 1984, The distribution of gold- and silver--bearing deposits in the Basin and Range Province, western United States: Ariz. Geol. Soc. Digest, v. 15, p. 1-27.

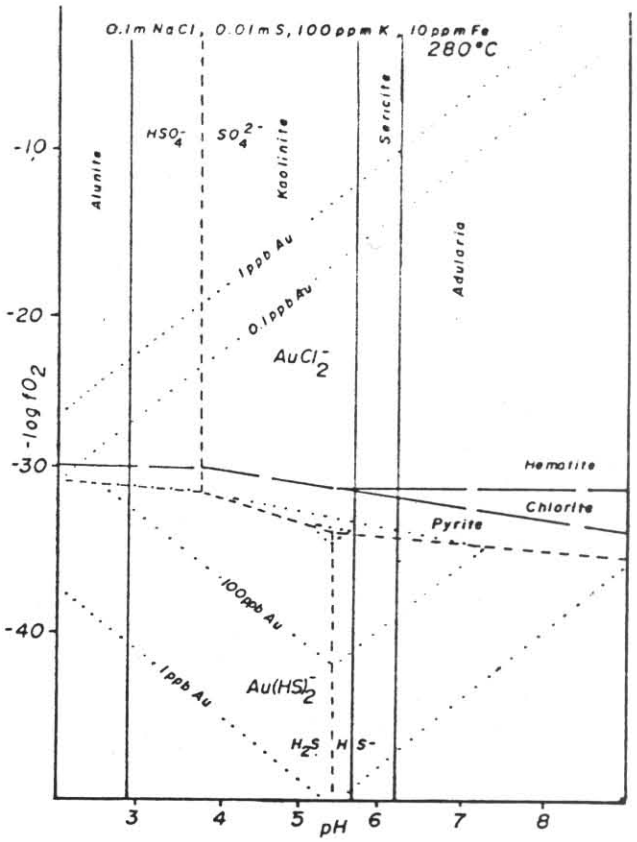

Figure 58. pH vs log fO_2 diagram for Au-bearing fluid at 280°C under initial conditions shown. Shading shows possible trajectory of Stage III-like fluid during boiling, based on stable equilibrium assemblage and initial conditions. (Modified from Romberger, 1980)

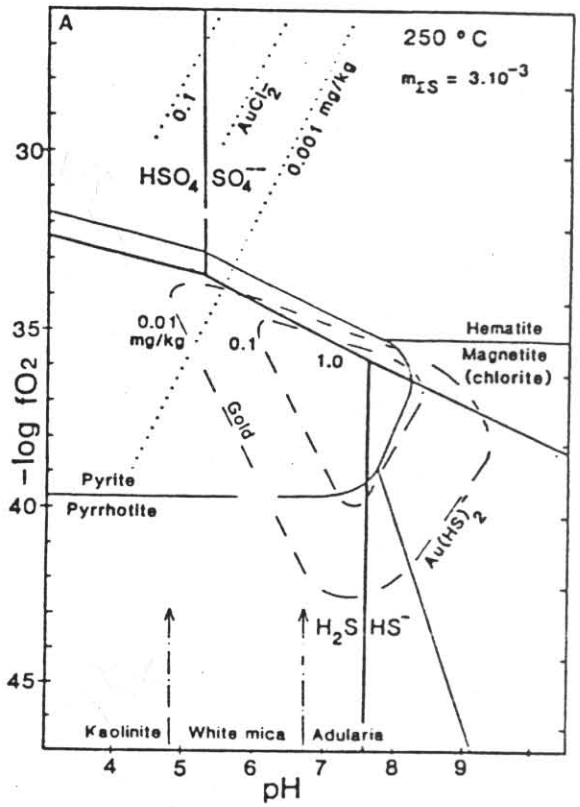

Figure 59. pH vs log fO_2 diagram for Au-bearing fluid at 250°C for the Waiotapu geothermal system fluids. Conditions are similar to those estimated for Stage IV. Shading shows possible trajectory of Stage IV-like fluid during boiling/-cooling, based on stable equilibrium assemblage and initial conditions (Modified from Hedenquist and Henley, 1985a).

APPENDICES

Appendix A
Vein Contouring

The following procedures apply to the Telegraph sections: (References to "the vein" correspond to the composite, open-space cemented breccia zone and incorporated late-stage fissure veins.)

1. A reference plane of N 28° E, 55° SW was drawn from 2200 S to 2400 S at 100 W on the grid maps at a 3910ft. level datum plane (see Hill 2, Plt. 5). These grid maps were used as composite horizontal plans (at various elevations) for plotting surface data, air-track intercepts and underground workings (at the 3800ft. and 3700ft. levels).

2. Projections of the inclined reference plane at various elevations were drawn onto the horizontal plan.

3. Vein dip between intercepts and the reference plane projections at the same elevation were measured. Vein dips centers, rather than footwall or hangingwall intercepts were estimated due to incomplete drill hole data.

4. Deviation distances were projected onto a 55° inclined longitudinal section (representing an undistorted, sectional plan-view of the idealized vein surface.) These distances were, in effect, exactly like elevations-above-sea-level for surface topography on a plan map.

5. Equidistant deviations from the ideal plane were contoured on the inclined section. The finished L-section therefore represents the "topography" of the vein surface. The contours are preliminary only, as the data are incomplete and unevenly distributed.

6. Cross-sectional slices representing edge-on views of the vein normal to the reference plane, were constructed from the contoured section where there was sufficient drill hole control on vein width. The cross sections helped distinguish between "pinch and swell zones" of the vein and zones of equal-thickness that bend into and away from the reference plane (Fig. 31).

The dip-profile contouring (Fig. 32) provided another way of distinguishing the effects of dilation from equal-thickness deviation because the measurements are based upon surface and underground breccia zone attitude measurements and fairly accurate drill hole footwall intercept projections (where possible). The contours were constructed in a manner similar to dilation contours except that dip information at vein intercepts were plotted according to the procedure described by Gough (1965). Before contouring points of equivalent dip, the raw data were smoothed by applying a 20ft. x 20ft. moving average procedure over the inclined longitudinal section. Averaging was necessary because the lack of complete raw data gave an erratic picture of localized variations in dip.

Where possible, vein-width data, along with assay values were projected onto the contoured sections in order to document obvious correlations between vein shape and precious metal content. Unfortunately, records were not kept of stope width or assay values between the 3750ft. and 3800ft. levels, or above the 3800ft. level.

Appendix B

Very Low Frequency Electromagnetic Survey

A complete discussion of the theoretical and technical principles involved in collection and interpretation of VLF-EM

data is beyond the scope of this study. GEONICS EM-16 and CRONE RADEM VLF-EM operation manuals and supplementary technical articles are good reference sources.

This technique takes advantage of the worldwide network of military navigation stations that transmit very low frequency radio signals, the groundwave component of which penetrates the earth's surface. The electrical component of the groundwave is oriented vertically, the magnetic component oriented horizontally, 90° with respect to the ground surface. Sensitive VLF-EM receivers (a CRONE RADEM receiver was used in this study) measure local deflections in the magnetic component as the groundwave traverses rocks or soils of contrasting electrical conductivity. Groundwave depth of penetration and signal attenuation are functions of:

1) Depth to a conducting surface (so-called "target zone"),

2) attitude, shape and conductivity of the target zone, and

3) the conductivity of the surrounding rock or soil.

The complex interplay of so many variables makes precise interpretation of VLF-EM data difficult.. Moreover, VLF-EM is one of the few electrical methods that can be used to delineate very weak conductors, such as water-filled fault zones.

Three measured parameters help define the shape of the magnetic field at any particular location:

Dip Angle: The deviation in the normally horizontal component of the magnetic field (Hx); caused by the

electromagnetic interference of a buried conductive target zone.

Quadrature: The "Percent out-of-phase". Usually small, this is the percent phase shift in the vertical component (Hz) caused by the interception of a conductor.

Field Strength: The relative amplitude attenuation of the total magnetic field at any location - measured as a percentage of the field strength recorded at a nearby control base station at a particular time of day. Hourly fluctuations of the earth's magnetic field cause a drift in measured values at any particular location. Field strength drift is compensated for by:

a) distributing the "error" between two successive base station readings, usually taken two hours apart, and

b) subtracting or adding these incremental values from individual station readings.

Dip angle and relative field strength proved most useful for delineating basic structure along the Telegraph trend.

Methodological control for this survey consisted of short test traverses over exposed parts of the Telegraph system at 100 N and 2900 S across the main grid (Plt. 6). Results of these tests guided the selection of a regional base station, an appropriate transmitter station (NLK- Seattle, at a frequency of 18.6 KHz), trend of survey line (N 28° E) and the most effective station spacing (50ft.) for the survey. More than 1158.5m (3800 ft.) along the average strike of the Telegraph structure was covered at an average width of 183m (600ft.). Fifty foot station spacing offered optimum coverage for Frasier-method contouring applications. Obvious effects of buried cables, fence lines and phone lines were noted and were filtered out of the final data. Base station measurements of field

strength were taken at intervals of about two hours; more frequently at dawn and dusk each day.

Procedures

Raw VLF data were entered into LOTUS worksheets by Erik Kauzmann and field strength drift corrections were calculated by computer. Directional dip measurements were converted to pure values following the convention: southern and eastern dips were recorded as negative; northern and western dips were recorded as positive values. These conversions allowed the raw data to be Frasier-filtered.

The Fraser (1969) filter was used to transform data into contourable form by reducing signal noise, enhancing shallow dip anomalies and amplifying significant local anomalies. The filter applies "a difference operator to transform zero-crossings (of dip data) into peaks, and a low-pass smoothing generator to reduce noise" (Frasier,1969, p. 958). The plotted function has the form: $f(m2,m3) = (m3 + m4) - (m1 + m2)$ where m1...m4 are successive station dip measurements. The filtered data have the following characteristics:

1) All dip angles are phase-shifted by 90°; crossovers and local inflections are transformed into contourable peaks.

2) The resolution of local anomalies is accentuated by eliminating noise with a wavelength equal to station spacing (i.e. 50ft. in this study) and direct current bias (from larger wavelength signal attenuation from nearby sources).

3) Maximum amplitude occurs for wavelengths of 76m (250ft.); the method functions optimally for conductor within the upper 91.2m (300ft.) of the surface.

Application of this filter was required in this study because:

a) the target surface is a weak to very weak conductor with highly variable electrical response properties,

b) highly conductive materials in the area- pipes, wires, equipment, buried rails- have the potential to contribute to noise of unacceptable levels, and

c) target response expected to depths much less than total skin depth penetration level. Skin depth was estimated at 250m from the surface, using a skin-depth nomogram (Campbell, et al, 1981) for a quartz monzonite rock medium of a conductivity of 5000 ohm-m (Dobrin, 1960).

APPENDIX C

TELEGRAPH MINE
GOLD DIKE AREA GEOCHEMISTRY RESULTS

Sample Number	NS Coordinates	EW	Length Meter	Type	Alt	Min	Strike	Dip	auppm	agppm	asppm	hgppm	cuppm	RATIO Au/Ag
1008	-2865	2900	0.2	Vn	0	Qcmn	205	50	0.51	0.00	0.00	1.00	10.0	
1010	-2680	2950	0.1	Bx	QCSP	Qvg	235	90	1.71	0.00	10.00	1.10	20.0	
1012	-1950	2920	0.2	Bx	Ain	Qfn	205	90	1.82	30.17	15.00	2.10	25.0	0.060
1014	-3510	3080	0.2	Bx	Ain	Goss	205	90	20.43	17.83	0.00	1.90	695.0	1.146
1015	-3510	3080	0.2	Vn	0	Qcmn	205	90	0.41	0.00	0.00	0.88	50.0	
1017			0.3	Bx	Aout	FeO	235	80	0.34	0.00	55.00	1.40	10.0	
1018	-3980	3290	0.1	Bx	QSP	FeO	244	85	1.75	0.00	10.00	3.70	60.0	
1023	-4000	3310	0.3	Bx	QCSP	Qfn	244	80	0.17	0.69	5.00	1.60		0.250
1024	-4080	3350	0.3	Vn	0	Qcmn	244	80	0.82	35.31	15.00	10.40	85.0	0.023
1025	-4050	3340	0.2	Fw	Ain	Qfn	242	80	0.00	0.00	0.00	1.40	70.0	
1026	-4100	3360	0.4	Bx	QSP	FeO	240	80	0.27	0.00	5.00	1.50	10.0	
1027	-4210	3425	0.2	Bx	QSP	QFe	230	80	1.30	6.51	10.00	6.60	70.0	0.200
1028	-4050	3535	0.0	Vn	0	Qmp	230	90	4.63	0.00	75.00	6.70	575.0	
1038	-4600	3600	0.6	Bx	Ain	Qfn	230	90	0.17	5.83	5.00	1.80	45.0	0.029
1039	-4570	3590	0.5	Fw	Ain	Qfnp	230	90	0.58	0.00	0.00	1.10	85.0	
1040	-4580	3600	0.2	Bx	0	Qcmn	230	90	1.17	******	35.00	2.90	80.0	0.007
1041	-5160	3850	0.3	Bx	QSP	Qfn	230	90	1.27	36.34	45.00	5.30	40.0	0.035
1042	-5060	3840	0.0	Hw	Aout	Qfnp	230	90	0.27	0.00	5.00	1.40	25.0	
1043	-5160	3850	0.3	Bx	QSP	Qfn	215	90	0.62	6.51	5.00	3.00	125.0	0.095
1044	-5170	3900	0.2	Vn	0	Qfnp	40	45	0.31	0.00	0.00	0.27	125.0	

APPENDIX D

TELEGRAPH MINE
DISTRICT AREA GEOCHEMISTRY RESULTS

Sample Number	Length Meter	H	Description Type	Alt	Min	Strike	Dip	auppm	agppm	asppm	hgppm	cuppm	sbpp	Ratio Au/Ag
tp37	0.00	m	Co	Aout	FeO	90	90	0.00	0.00	5.00			3	
tp40	0.00	m	Vn	0	Qmp	345	21	0.00	0.00	-5.00	0.29		-1	
tp41	0.10	m	Vn	Ain	Qmp	20	26	0.00	0.00	5.00	0.13		-1	
tp46	0.50	d	Bx	Ain	Goss	82	69	0.51	1.03	10.00	0.52		-1	0.500
tp48	0.30	m	Fw	Pin	Goss	82	69	0.21	0.00	-5.00			-1	
tp49	0.10	d	Vn	QS	Goss	82	70	0.00	1.03	5.00	0.36		1	0.000
tp50	0.60	m	Hw	Pin	FeO	82	69	0.00	2.06	-5.00	0.24		-1	0.000
601	0.00	m	Bx	QSP	FeO	242	78	0.12	0.90	10.00	0.29	10.0	29	0.133
602	0.00	m	Bx	QSP	Qfnp	200	87	0.28	1.00	20.00	0.15	10.0	27	0.280
603	0.00	m	Hw	Ain	QFe	242	78	0.00	1.20	15.00	0.50	35.0	24	0.000
604	0.00	m	Bx	QSP	QFe	200	87	0.00	0.20	5.00	0.46	15.0	5	0.000
605	0.00	m	Vn	0	Qcmn	200	87	0.00	0.20	5.00	0.28	5.0	2	0.000
606	0.00	m	Bx	QC	Qvn	200	87	0.00	0.20	5.00	0.33	10.0	2	0.000
607	0.00	m	Vn	QS	CuO	220	77	0.02	11.00	60.00	0.83	0.0	-1	0.002
608	0.50	m	Vn	QS	CuO	240	61	0.00	4.00	25.00	2.20	0.0	-1	0.000
609	0.25	m	Vn	QS	CuO	210	46	0.08	9.10	35.00	0.07	0.0	-1	0.009
610	0.15	a	Vn	QC	0	355	65	0.00	0.90	5.00	0.02	605.0	15	0.000
611	0.30	m	Vn	QS	Goss	348	42	0.00	7.50	10.00	0.06	0.0	-1	0.000
612	0.20	a	Fw	QS	FeO	348	42	0.00	2.80	5.00	0.05	870.0	-1	0.000
613	0.10	a	Vn	0	Qmp	150	15	0.00	1.70	-5.00	0.02	250.0	-1	0.000
614	1.50	m	Bx	Ain	Qmp	225	90	0.00	1.70	-5.00	0.59	60.0	2	0.000
615	0.00	m	Bx	QS	Qfnp	225	90	0.00	1.70	15.00	1.10	90.0	8	0.000
616	0.00	m	Bx	Ain	Qmp	265	45	0.14	21.00	25.00	0.22	0.0	-1	0.007
617	0.00	m	Vn	0	QFe	315	90	0.08	9.20	-5.00	0.15	0.0	-1	0.009
618	1.50	g	Bx	Ain	FeO	190	90	0.00	0.00	-5.00	0.07	40.0	-1	
619	0.30	m	Vn	0	QFe	345	21	0.00	0.40	-5.00	0.04	0.0	-1	0.000

Sample Number	Length Meter	H	Description Type	Alt	Min	Strike	Dip	auppm	agppm	asppm	hgppm	cuppm	sbppm	Ratio Au/Ag
620	0.00	m	Vn	0	CuO	125	42	0.22	74.00	40.00	0.13	0.1	1	0.003
621	0.00	m	Vn	0	QFe	198	90	0.00	0.20	-5.00	0.01	130.0	-1	0.000
622	0.50	m	Vn	0	CuO	328	37	0.00	5.80	30.00	0.02	0.0	-1	0.000
623	0.40	m	Vn	0	Goss	328	37	0.00	1.70	25.00	0.03	0.0	-1	0.000
624	0.03	a	Vn	0	Goss	347	90	0.04	2.10	85.00	2.50	0.0	-1	0.019
625	0.00	a	Vn	0	Goss	115	85	0.24	6.90	35.00	0.43	0.0	-1	0.035
626	0.30	m	Vn	0	QFe	0	0	0.04	1.20	15.00	0.02	480.0	-1	0.033
627	0.00	g	Bx	QS	Qfnp	265	85	0.00	0.00	-5.00	0.04	25.0	-1	
628	0.00	d	Vn	0	Goss	50	75	2.60	7.10	35.00	0.64	0.0	-1	0.366
629	0.50	d	Vn	0	Goss	125	86	1.40	13.00	-5.00	0.10	30.0	-1	0.108
630	0.00	d	Vn	0	Qmp	125	86	0.62	22.00	5.00	0.12	15.0	-1	0.028
631	0.00	d	Hw	Ain	FeO	125	86	0.02	0.50	-5.00	0.05	20.0	-1	0.040
632	0.00	a	Vn	QS	QFe	111	74	0.00	0.00	10.00	0.15	60.0	-1	
633	0.50	d	Hw	Pin	Qvn	111	74	0.04	3.10	-5.00	0.02	170.0	-1	0.013
634	0.25	d	Bx	QS	QFe	112	90	0.50	41.00	-5.00	0.24	10.0	-1	0.012
635	0.00	g	Vn	0	QFe	140	40	1.50	20.00	10.00	0.09	0.0	-1	0.075
636	0.00	d	Vn	0	Qmp	137	73	0.00	2.30	55.00	0.09	765.0	-1	0.000
637	0.00	d	Vn	0	Qfnp			0.04	2.90	-5.00	0.42	130.0	-1	0.014
638	0.00	m	Vn	0	Goss	280	90	0.28	11.00	75.00	0.03	630.0	-1	0.025
639	4.00	g	Hw	Ain	FeO	210	90	0.00	0.00	5.00	0.06	10.0	-1	
640	0.50	m	Hw	Ain	FeO	210	90	0.00	0.00	-5.00	0.05	5.0	-1	
641	2.50	g	Hw	Ain	FeO	250	90	0.00	0.00	5.00	0.02	10.0	-1	
642	1.50	g	Hw	Ain	FeO	250	90	0.04	0.00	10.00	0.02	25.0	2	
643	1.50	d	Bx	QS	Goss	300	90	0.02	0.00	10.00	0.03	40.0	-1	
644	1.00	d	Bx	QS	QFe	294	90	0.00	0.30	5.00	0.03	60.0	-1	0.000
645	2.00	d	Hw	Aout	0	195	90	0.00	0.00	5.00	0.02	10.0	-1	
646	8.00	d	Hw	Aout	0	225	90	0.00	0.00	25.00	0.05	10.0	3	
647	1.25	d	Hw	Aout	Qfn	240	90	0.00	0.00	15.00	0.02	30.0	-1	
648	0.50	d	Vn	QSP	FeO	140	65	0.00	0.00	5.00	0.02	10.0	3	
650	0.50	d	Bx	QSP	FeO	65	75	0.00	0.00	10.00	0.05	140.0	-1	
651	0.00	d	Bx	QSP	FeO	65	75	0.02	1.40	45.00	1.00	550.0	1	0.014

Sample Number	Length Meter	H	Description Type	Alt	Min	Strike	Dip	auppm	agppm	asppm	hgppm	cuppm	sbpp	Ratio Au/Ag
652	1.30	m	Vn	0	Qfn	175	53	0.14	0.90	25.00	0.13	25.0	16	0.156
653	0.50	m	Hw	Pin	FeO	175	53	0.00	0.00	20.00	0.14	125.0	3	
654	2.50	m	Fw	Pin	Qcmn	175	53	0.00	0.10	20.00	0.05	10.0	1	0.000
655	1.00	a	Vn	0	Qmp	306	45	0.00	0.00	45.00	0.08	0.0	9	
656	0.00	m	Co	QS	0	304	45	0.04	18.00	-5.00	0.05	0.0	-1	0.002
657	0.50	m	Vn	0	Qmp	280	32	0.06	2.90	10.00	0.10	0.0	-1	0.021
953	0.2	a	Vn	0	Qvg	320	58	0.17	16.11	5.00	1.30			0.011

APPENDIX E

TELEGRAPH MINE
BRECCIA-VEIN SURFACE GEOCHEMICAL RESULTS

(Rocky Mountain Geochemical Laboratory)

Sample Number	NS Coordinates	EW	Length Meter	Type	Alt	Strike	Dip	auppm	agppm	asppm	hgppm	cuppm	sbpp	au/ag
tp14	-250	185		Bx	QSP	210	50	0.21	7.89	5.00			21	0.026
tp16	-250	190	1.00	Vn	0	210	50	0.21	6.86	-5.00	0.33		3	0.030
tp22	-1155	107	0.50	Vn	0	210	50	2.98	17.14	10.00	7.20		17	0.174
tp27	-1865	0	1.00	Bx	Pout	325	44	0.00	2.06	-5.00	0.26		-1	0.000
tp33	-2330	165	1.00	Bx	QCS	200	60	1.20	5.14	10.00	1.60		13	0.233
tp34	-2330	170	1.00	Hw	QC	205	60	0.10	2.06	5.00	0.95		6	0.050
tp35	-3032	137	0.50	Bx	QCS	245	55	2.30	15.09	20.00	2.40		19	0.152
tp36	-3032	137	0.25	Vn	0	245	55	0.58	36.00	-5.00	8.50		46	0.016
658	-1940	310	4.00	Fw	Pin	205	40	0.22	3.50	5.00	1.70	95.0	2	0.063
659	-1940	310	2.00	Vn	0	205	40	1.80	21.00	-5.00	0.30	30.0	32	0.086
661	-1880	290	1.00	Vn	0	202	40	1.30	25.00	-5.00	0.50	45.0	20	0.052
671	81	75	4.00	Fw	Pout	218	65	0.00	0.10	5.00	1.20			0.000
675	90	94	6.00	Hw	Pout	210	60	0.00	0.31	10.00	0.73			0.000
677	98	137	1.00	Hw	Pin	5	20	0.00	0.51	10.00	0.95			0.000
679	112	165	33.00	Hw	Pout	20	80	0.00	0.21	5.00	0.49			0.000
698	-445	122	3.30	Fw	Pout	195	50	0.00	0.10	-5.00	1.50			0.000
699	-447	147	1.20	Fw	Pin	195	50	0.00	0.51	15.00	4.70			0.000
901	-449	168	3.00	Hw	Pout	195	50	0.00	0.21	5.00	4.40			0.000
902	-1231	142	3.00	Fw	Pout	230	50	0.00	0.62	5.00	0.68			0.000
904	-1234	155	0.05	Hw	0	230	65	0.14	1.71	10.00	4.60			0.080
907	-2340	140	5.0	Fw	Pout	210	50	1.65	0.69					2.400
908	-2355	155	2.0	Fw	Pin	215	60	0.51	1.51					0.341
909	-2348	160	0.5	Bx	QCP	215	80	4.70	7.71					0.609
910	-2341	167	0.5	Bx	QSP	215	70	0.34	1.89					0.182

Sample Number	NS Coordinates	EW	Length Meter	Type	Alt	Strike	Dip	auppm	agppm	asppm	hgppm	cuppm	sbpp	au/ag
911	-2343	170	0.5	Bx	QCSP	215	70	0.51	2.40					0.214
912	-2346	180	0.5	Bx	Pin	205	90	0.17	1.71					0.100
913	-2347	190	3.0	Hw	Pout	205	60	0.17	0.99					0.172
918	-2510	210	0.30	Vn	0	207	86	0.65	27.09	10.00	3.30			0.024
919	-2290	247	2.00	Bx	Ain	210	45	0.69	3.39	105.00	4.30			0.202
920	-2294	246	3.00	Hw	Ain	210	45	0.07	2.19	75.00	2.20			0.031
922	-2315	238	0.30	Vn	0	208	46	0.00	1.99					0.000
922	-2315	238	0.3	Vn	0	208	46	1.51	5.42					0.278
922.1	-2315	238	0.30	Vn	0	208	46	0.00	4.80					0.000
923	-2310	238	0.6	Bx	QCSP	208	46	1.41	4.49					0.313
924	-2305	238	0.5	Bx	QC	208	46	0.82	7.71					0.107
932	-2393	218	4.00	Bx	Ain	200	76	0.07	1.13	20.00	0.52			0.061
933	-2389	184	0.5	Bx	QCP	208	80	5.55	14.33					0.388
934	-2407	150	5.0	Bx	Pin	215	90	0.24	0.99					0.241
935	-2218	115	0.1	Bx	QS	205	90	0.14	0.69	-5.00	2.00			0.200
941	-2332	155	0.2	Bx	QCSP	245	65	0.29	13.20					0.779
942.1	-2320	161	0.6	Fw	Pin	215	65	0.17	0.89					0.192
956	-3066	200	0.2	Bx	Pin	215	50	3.53	11.52					0.307
957	-3047	195	1.6	Hw	Ain	210	60	0.07	3.02	35.00	6.80			0.023
958	-3052	206	1.6	Hw	Aout	205	60	0.14	1.10	30.00	3.50			0.125
959	-3044	190	0.2	Vn	0	215	50	6.55	16.90					0.387
960	-3043	188	2.0	Fw	Aout	215	60	0.69	6.17	10.00	2.90			0.111
961	-3049	185	0.5	Bx	QCP	215	50	5.79	30.03					0.193
962	-3052	184	0.6	Vn	0	215	50	0.29	50.06					0.205
963	-3050	180	0.5	Vn	0	245	80	0.29	96.69					0.106
967	-3005	132	0.3	Vn	0	215	50	7.06	80.23					0.088
968	-3010	133	0.3	Bx	QSP	215	50	0.69	10.70					0.064
968.1	-3010	133	0.30	Bx	QSP	215	70	0.21	3.39					0.061
968.2	-3010	133	0.30	Bx	0	215	70	0.14	25.03					0.005
969	-3004	127	1.3	Fw	Pin	245	55	0.31	1.61					0.191
970	-3006	137	0.3	Vn	0	240	60	0.57	40.11					0.089

Sample Number	NS Coordinates	EW	Length Meter	Type	Alt	Strike	Dip	auppm	agppm	asppm	hgppm	cuppm	sbpp	au/ag
974	-3042	138	1.0	Bx	QCSP	245	55	6.00	18.72					0.321
975	-3042	138	0.3	Bx	QS	220	60	0.82	5.01					0.164
976	-3110	187	4.0	Fw	Pin	225	85	0.62	3.77	10.00	1.10			0.164
977	-3093	197	0.6	Bx	QP	225	86	0.51	33.05					0.016
983	-3172	219	0.2	Bx	Pin	215	42	0.21	2.71					0.076
984	-3170	221	1.6	Fw	Ain	210	90	0.51	26.02					0.020
985	-2791	163	0.3	Bx	Ain	200	55	0.03	0.31					0.111
986	-2791	165	0.6	Fw	Ain	200	55	0.03	0.21					0.167
989	-1895	192	1.5	Hw	Ain	205	45	1.85	76.11	10.00	0.62	20.0		0.024
990	-1895	190	0.8	Vn	0	205	45	3.36	122.74	5.00	0.32	25.0		0.027
991	-1916	96	0.3	Vn	0	270	45	0.00	6.51	5.00	0.28			0.000
993	-1152	100	0.6	Fw	Aout	210	45	0.00	0.51	-5.00	0.53			0.000
994	-1155	103	0.0	Vn	0	205	52	0.00	0.51	15.00	1.70			0.000
995	-1143	106	0.1	Bx	QSP	310	50	0.96	3.77	-5.00	1.40	60.0		0.255
996	-1143	108	0.6	Bx	0	310	50	2.64	37.03	-5.00	1.50	40.0		0.071
997	-1143	109	0.3	Bx	Ain	310	50	0.48	10.29	-5.00	0.43	10.0		0.047
998	-1117	108	0.1	Hw	Ain	205	42	0.58	9.60	-5.00	1.60	25.0		0.061
999	-1133	109	0.6	Hw	Ain	215	50	1.17	4.46	10.00	1.60	20.0		0.262
1000	-255	191	0.5	Bx	QSP	210	42	0.55	17.49	-5.00	3.40			0.031
1001	-255	190	0.5	Vn	0	210	42	1.71	50.06	-5.00	3.70			0.034
1002	-225	189	1.50	Bx	QS	210	42	0.00	19.54	5.00	2.00	60.0		0.000
1003	-255	188	0.2	Vn	0	212	42	0.41	5.14	-5.00	1.70			0.080
1004	-255	185	0.0	Bx	QCSP	210	42	0.55	7.20	5.00	2.10			0.076
1051	-2326	202	0.5	Bx	QSP	215	45	0.55	3.19					0.172
1052	-2327	204	0.9	Bx	Pin	215	45	10.29	17.21					0.598
1053	-2328	206	0.3	Bx	0	220	50	3.26	9.39					0.347
1054	-2329	208	0.2	Bx	QCP	215	70	2.91	6.21					0.470
1056	-2285	204	0.5	Bx	Pin	215	45	10.29	11.62					0.885
1056.1	-2285	204	0.50	Bx	QCP	215	70	5.25	7.20					0.729
1056.2	-2285	204	0.50	Bx	QSP	215	70	0.31	7.54					0.041
1056.3	-2285	204	0.50	Bx	0	215	70	35.31	37.71					0.936

Sample Number	NS Coordinates	EW	Length Meter	Type	Alt	Strike	Dip	auppm	agppm	asppm	hgppm	cuppm	sbpp	au/ag
1057	-2285	206	0.9	Bx	QC	215	45	0.17	0.79					0.217
1058	-2285	208	0.2	Bx	Pin	215	45	10.29	36.00					0.286
1059	-2285	210	0.4	Hw	Ain	215	45	6.86	6.79					1.010
1061	-2250	200	1.30	Hw	Ain	205	45	0.17	0.62	5.00	0.57	50.0		0.278
1062	-2230	210	0.40	Vn	QC	205	45	3.67	33.94	25.00	8.50	135.0		0.108
1062.1	-2230	210	0.50	Hw	Pout	205	45	0.48	1.89	-5.00	1.70	25.0		0.255
1063.1	-2242	230	0.30	Hw	Ain	215	42	0.10	2.30	10.00	2.90	30.0		0.045
1063.2	-2242	230	1.00	Hw	Aout	215	42	0.07	2.19	5.00	1.30	35.0		0.031
1064	-2240	234	0.15	Hw	Pout	30	83	0.14	18.86	-5.00	1.60	45.0		0.007
1065	-2238	250	0.70	Hw	Pout	35	88	0.00	6.17	-5.00	0.62	50.0		0.000
1068	-1115	140	0.8	Vn	0	200	30	4.01	30.17	-5.00	10.00			0.133

(CEMCORP Laboratories)

2000	210	259		Vn	0	165	74	0.86	41.14					0.021
2001	215	235		Vn	0	165	90	2.40	7.20					0.333
2002	144	72		Vn	0	200	58	0.07	1.71					0.040
2003	120	85		Bx	QC	220	65	9.67	42.86					0.226
2004	98	81		Bx	QC	220	60	3.91	10.97					0.356
2005	93	70		Fw	0	0	0	9.60	236.57					0.041
2006	58	88		Bx	QC	220	60	1.58	97.03					0.016
2007	25	98		Bx	QC	215	54	0.62	35.66					0.017
2008	-5	106		Fw	QC	218	54	0.34	13.37					0.026
2009	-27	107		Fw	0	0	0	1.41	15.09					0.093
2010	-41	115		Bx	QS	220	64	0.65	4.11					0.158
2011	-52	120		Vn	0	200	78	0.62	1.71					0.360
2012	-72	121		Vn	0	220	64	0.17	27.77					0.006
2013	-91	146		Vn	0	230	60	0.17	1.71					0.100
2014	-110	155		Vn	0	230	60	0.51	20.57					0.025
2015	-142	165		Vn	0	230	60	1.71	15.43					0.111

Sample Number	NS Coordinates	EW	Length Meter	Type	Alt	Strike	Dip	auppm	agppm	asppm	hgppm	cuppm	sbpp	au/ag
2016	-205	186		Vn	0	230	50	-0.17	5.83					-0.029
2017	-176	179		Vn	0	225	50	2.13	22.29					0.095
2018	-210	182		Vn	0	225	50	3.77	98.74					0.038
2019	-243	184		Vn	0	210	50	0.34	0.17					2.000
2020	-244	196		Vn	0	218	90	0.51	17.49					0.029
2021	-244	200		Vn	0	208	90	0.38	10.97					0.034
2022	-280	191		Hw	0	208	90	0.69	78.86					0.009
2023	-275	196		Hw	0	208	90	0.75	85.72					0.009
2024	-315	188		Bx	QS	208	50	0.51	14.06					0.037
2025	-316	200		Hw	0	208	50	0.17	1.06					0.161
2026	-375	205		Hw	0	208	0	0.17	1.34					0.128
2027	-365	209		Bx	QS	208	50	1.03	52.80					0.019
2028	-343	200		Hw	0	208	0	0.51	16.80					0.031
2029	-343	205		Hw	0	208	0	1.06	15.09					0.070
2030	-358	193		Hw	0	208	0	1.34	26.40					0.051
2031	-391	191		Fw	0	360	0	0.34	34.29					0.010
2032	-394	196		Bx	Pin	208	0	0.27	20.57					0.013
2033	-421	200		Hw	Pin	208	0	0.17	5.49					0.031
2034	-1125	110		Bx	0	200	25	1.03	7.54					0.136
2035	-2200	190		Hw	0	210	50	0.48	20.23					0.024
2036	-2202	118		Fw	0	210	50	0.17	25.37					0.007
2037	-2219	116		Fw	0	210	50	0.51	20.91					0.025
2038	-2208	172		Hw	0	210	50	1.92	24.00					0.080
2039	-2235	147		Hw	0	210	50	4.59	9.87					0.465
2040	-2295	124		Hw	Ain	210	50	0.69	8.91					0.077
2041	-2294	159		Hw	Pin	210	50	0.14	11.25					0.012
2042	-2293	180		Hw	Pout	210	50	1.03	6.17					0.167
2043	-2292	197		Hw	Pout	210	50	1.71	9.33					0.184
2044	-2295	210		Vn	QCS	210	50	51.09	20.23					2.525
2045	-2295	225		Bx	QCS	200	50	4.25	26.74					0.159
2046	-2295	220		Bx	QCS	200	50	0.69	9.60					0.071

APPENDIX C

TELEGRAPH MINE
GOLD DIKE AREA GEOCHEMISTRY RESULTS

Sample Number	NS Coordinates	EW	Length Meter	Type	Alt	Min	Strike	Dip	auppm	agppm	asppm	hgppm	cuppm	RATIO Au/Ag
1008	-2865	2900	0.2	Vn	0	Qcmn	205	50	0.51	0.00	0.00	1.00	10.0	
1010	-2680	2950	0.1	Bx	QCSP	Qvg	235	90	1.71	0.00	10.00	1.10	20.0	
1012	-1950	2920	0.2	Bx	Ain	Qfn	205	90	1.82	30.17	15.00	2.10	25.0	0.060
1014	-3510	3080	0.2	Bx	Ain	Goss	205	90	20.43	17.83	0.00	1.90	695.0	1.146
1015	-3510	3080	0.2	Vn	0	Qcmn	205	90	0.41	0.00	0.00	0.88	50.0	
1017			0.3	Bx	Aout	FeO	235	80	0.34	0.00	55.00	1.40	10.0	
1018	-3980	3290	0.1	Bx	QSP	FeO	244	85	1.75	0.00	10.00	3.70	60.0	
1023	-4000	3310	0.3	Bx	QCSP	Qfn	244	80	0.17	0.69	5.00	1.60		0.250
1024	-4080	3350	0.3	Vn	0	Qcmn	244	80	0.82	35.31	15.00	10.40	85.0	0.023
1025	-4050	3340	0.2	Fw	Ain	Qfn	242	80	0.00	0.00	0.00	1.40	70.0	
1026	-4100	3360	0.4	Bx	QSP	FeO	240	80	0.27	0.00	5.00	1.50	10.0	
1027	-4210	3425	0.2	Bx	QSP	QFe	230	80	1.30	6.51	10.00	6.60	70.0	0.200
1028	-4050	3535	0.0	Vn	0	Qmp	230	90	4.63	0.00	75.00	6.70	575.0	
1038	-4600	3600	0.6	Bx	Ain	Qfn	230	90	0.17	5.83	5.00	1.80	45.0	0.029
1039	-4570	3590	0.5	Fw	Ain	Qfnp	230	90	0.58	0.00	0.00	1.10	85.0	
1040	-4580	3600	0.2	Bx	0	Qcmn	230	90	1.17	******	35.00	2.90	80.0	0.007
1041	-5160	3850	0.3	Bx	QSP	Qfn	230	90	1.27	36.34	45.00	5.30	40.0	0.035
1042	-5060	3840	0.0	Hw	Aout	Qfnp	230	90	0.27	0.00	5.00	1.40	25.0	
1043	-5160	3850	0.3	Bx	QSP	Qfn	215	90	0.62	6.51	5.00	3.00	125.0	0.095
1044	-5170	3900	0.2	Vn	0	Qfnp	40	45	0.31	0.00	0.00	0.27	125.0	

APPENDIX D

TELEGRAPH MINE
DISTRICT AREA GEOCHEMISTRY RESULTS

Sample Number	Length Meter	H	Description Type	Alt	Min	Strike	Dip	auppm	agppm	asppm	hgppm	cuppm	sbpp	Ratio Au/Ag
tp37	0.00	m	Co	Aout	FeO	90	90	0.00	0.00	5.00			3	
tp40	0.00	m	Vn	0	Qmp	345	21	0.00	0.00	-5.00	0.29		-1	
tp41	0.10	m	Vn	Ain	Qmp	20	26	0.00	0.00	5.00	0.13		-1	
tp46	0.50	d	Bx	Ain	Goss	82	69	0.51	1.03	10.00	0.52		-1	0.500
tp48	0.30	m	Fw	Pin	Goss	82	69	0.21	0.00	-5.00			-1	
tp49	0.10	d	Vn	QS	Goss	82	70	0.00	1.03	5.00	0.36		1	0.000
tp50	0.60	m	Hw	Pin	FeO	82	69	0.00	2.06	-5.00	0.24		-1	0.000
601	0.00	m	Bx	QSP	FeO	242	78	0.12	0.90	10.00	0.29	10.0	29	0.133
602	0.00	m	Bx	QSP	Qfnp	200	87	0.28	1.00	20.00	0.15	10.0	27	0.280
603	0.00	m	Hw	Ain	QFe	242	78	0.00	1.20	15.00	0.50	35.0	24	0.000
604	0.00	m	Bx	QSP	QFe	200	87	0.00	0.20	5.00	0.46	15.0	5	0.000
605	0.00	m	Vn	0	Qcmn	200	87	0.00	0.20	5.00	0.28	5.0	2	0.000
606	0.00	m	Bx	QC	Qvn	200	87	0.00	0.20	5.00	0.33	10.0	2	0.000
607	0.00	m	Vn	QS	CuO	220	77	0.02	11.00	60.00	0.83	0.0	-1	0.002
608	0.50	m	Vn	QS	CuO	240	61	0.00	4.00	25.00	2.20	0.0	-1	0.000
609	0.25	m	Vn	QS	CuO	210	46	0.08	9.10	35.00	0.07	0.0	-1	0.009
610	0.15	a	Vn	QC	0	355	65	0.00	0.90	5.00	0.02	605.0	15	0.000
611	0.30	m	Vn	QS	Goss	348	42	0.00	7.50	10.00	0.06	0.0	-1	0.000
612	0.20	a	Fw	QS	FeO	348	42	0.00	2.80	5.00	0.05	870.0	-1	0.000
613	0.10	a	Vn	0	Qmp	150	15	0.00	1.70	-5.00	0.02	250.0	-1	0.000
614	1.50	m	Bx	Ain	Qmp	225	90	0.00	1.70	-5.00	0.59	60.0	2	0.000
615	0.00	m	Bx	QS	Qfnp	225	90	0.00	1.70	15.00	1.10	90.0	8	0.000
616	0.00	m	Bx	Ain	Qmp	265	45	0.14	21.00	25.00	0.22	0.0	-1	0.007
617	0.00	m	Vn	0	QFe	315	90	0.08	9.20	-5.00	0.15	0.0	-1	0.009
618	1.50	g	Bx	Ain	FeO	190	90	0.00	0.00	-5.00	0.07	40.0	-1	
619	0.30	m	Vn	0	QFe	345	21	0.00	0.40	-5.00	0.04	0.0	-1	0.000

Sample Number	Length Meter	H	Description Type	Alt	Min	Strike	Dip	auppm	agppm	asppm	hgppm	cuppm	sbppm	Ratio Au/Ag
620	0.00	m	Vn	0	CuO	125	42	0.22	74.00	40.00	0.13	0.1	1	0.003
621	0.00	m	Vn	0	QFe	198	90	0.00	0.20	-5.00	0.01	130.0	-1	0.000
622	0.50	m	Vn	0	CuO	328	37	0.00	5.80	30.00	0.02	0.0	-1	0.000
623	0.40	m	Vn	0	Goss	328	37	0.00	1.70	25.00	0.03	0.0	-1	0.000
624	0.03	a	Vn	0	Goss	347	90	0.04	2.10	85.00	2.50	0.0	-1	0.019
625	0.00	a	Vn	0	Goss	115	85	0.24	6.90	35.00	0.43	0.0	-1	0.035
626	0.30	m	Vn	0	QFe	0	0	0.04	1.20	15.00	0.02	480.0	-1	0.033
627	0.00	g	Bx	QS	Qfnp	265	85	0.00	0.00	-5.00	0.04	25.0	-1	
628	0.00	d	Vn	0	Goss	50	75	2.60	7.10	35.00	0.64	0.0	-1	0.366
629	0.50	d	Vn	0	Goss	125	86	1.40	13.00	-5.00	0.10	30.0	-1	0.108
630	0.00	d	Vn	0	Qmp	125	86	0.62	22.00	5.00	0.12	15.0	-1	0.028
631	0.00	d	Hw	Ain	FeO	125	86	0.02	0.50	-5.00	0.05	20.0	-1	0.040
632	0.00	a	Vn	QS	QFe	111	74	0.00	0.00	10.00	0.15	60.0	-1	
633	0.50	d	Hw	Pin	Qvn	111	74	0.04	3.10	-5.00	0.02	170.0	-1	0.013
634	0.25	d	Bx	QS	QFe	112	90	0.50	41.00	-5.00	0.24	10.0	-1	0.012
635	0.00	g	Vn	0	QFe	140	40	1.50	20.00	10.00	0.09	0.0	-1	0.075
636	0.00	d	Vn	0	Qmp	137	73	0.00	2.30	55.00	0.09	765.0	-1	0.000
637	0.00	d	Vn	0	Qfnp			0.04	2.90	-5.00	0.42	130.0	-1	0.014
638	0.00	m	Vn	0	Goss	280	90	0.28	11.00	75.00	0.03	630.0	-1	0.025
639	4.00	g	Hw	Ain	FeO	210	90	0.00	0.00	5.00	0.06	10.0	-1	
640	0.50	m	Hw	Ain	FeO	210	90	0.00	0.00	-5.00	0.05	5.0	-1	
641	2.50	g	Hw	Ain	FeO	250	90	0.00	0.00	5.00	0.02	10.0	-1	
642	1.50	g	Hw	Ain	FeO	250	90	0.04	0.00	10.00	0.02	25.0	2	
643	1.50	d	Bx	QS	Goss	300	90	0.02	0.00	10.00	0.03	40.0	-1	
644	1.00	d	Bx	QS	QFe	294	90	0.00	0.30	5.00	0.03	60.0	-1	0.000
645	2.00	d	Hw	Aout	0	195	90	0.00	0.00	5.00	0.02	10.0	-1	
646	8.00	d	Hw	Aout	0	225	90	0.00	0.00	25.00	0.05	10.0	3	
647	1.25	d	Hw	Aout	Qfn	240	90	0.00	0.00	15.00	0.02	30.0	-1	
648	0.50	d	Vn	QSP	FeO	140	65	0.00	0.00	5.00	0.02	10.0	3	
650	0.50	d	Bx	QSP	FeO	65	75	0.00	0.00	10.00	0.05	140.0	-1	
651	0.00	d	Bx	QSP	FeO	65	75	0.02	1.40	45.00	1.00	550.0	1	0.014

Sample Number	Length Meter	H	Description Type	Alt	Min	Strike	Dip	auppm	agppm	asppm	hgppm	cuppm	sbpp	Ratio Au/Ag
652	1.30	m	Vn	0	Qfn	175	53	0.14	0.90	25.00	0.13	25.0	16	0.156
653	0.50	m	Hw	Pin	FeO	175	53	0.00	0.00	20.00	0.14	125.0	3	
654	2.50	m	Fw	Pin	Qcmn	175	53	0.00	0.10	20.00	0.05	10.0	1	0.000
655	1.00	a	Vn	0	Qmp	306	45	0.00	0.00	45.00	0.08	0.0	9	
656	0.00	m	Co	QS	0	304	45	0.04	18.00	-5.00	0.05	0.0	-1	0.002
657	0.50	m	Vn	0	Qmp	280	32	0.06	2.90	10.00	0.10	0.0	-1	0.021
953	0.2	a	Vn	0	Qvg	320	58	0.17	16.11	5.00	1.30			0.011

Sample Number	NS Coordinates	EW	Length Meter	Type	Alt	Strike	Dip	auppm	agppm	asppm	hgppm	cuppm	sbpp	au/ag
911	-2343	170	0.5	Bx	QCSP	215	70	0.51	2.40					0.214
912	-2346	180	0.5	Bx	Pin	205	90	0.17	1.71					0.100
913	-2347	190	3.0	Hw	Pout	205	60	0.17	0.99					0.172
918	-2510	210	0.30	Vn	0	207	86	0.65	27.09	10.00	3.30			0.024
919	-2290	247	2.00	Bx	Ain	210	45	0.69	3.39	105.00	4.30			0.202
920	-2294	246	3.00	Hw	Ain	210	45	0.07	2.19	75.00	2.20			0.031
922	-2315	238	0.30	Vn	0	208	46	0.00	1.99					0.000
922	-2315	238	0.3	Vn	0	208	46	1.51	5.42					0.278
922.1	-2315	238	0.30	Vn	0	208	46	0.00	4.80					0.000
923	-2310	238	0.6	Bx	QCSP	208	46	1.41	4.49					0.313
924	-2305	238	0.5	Bx	QC	208	46	0.82	7.71					0.107
932	-2393	218	4.00	Bx	Ain	200	76	0.07	1.13	20.00	0.52			0.061
933	-2389	184	0.5	Bx	QCP	208	80	5.55	14.33					0.388
934	-2407	150	5.0	Bx	Pin	215	90	0.24	0.99					0.241
935	-2218	115	0.1	Bx	QS	205	90	0.14	0.69	-5.00	2.00			0.200
941	-2332	155	0.2	Bx	QCSP	245	65	0.29	13.20					0.779
942.1	-2320	161	0.6	Fw	Pin	215	65	0.17	0.89					0.192
956	-3066	200	0.2	Bx	Pin	215	50	3.53	11.52					0.307
957	-3047	195	1.6	Hw	Ain	210	60	0.07	3.02	35.00	6.80			0.023
958	-3052	206	1.6	Hw	Aout	205	60	0.14	1.10	30.00	3.50			0.125
959	-3044	190	0.2	Vn	0	215	50	6.55	16.90					0.387
960	-3043	188	2.0	Fw	Aout	215	60	0.69	6.17	10.00	2.90			0.111
961	-3049	185	0.5	Bx	QCP	215	50	5.79	30.03					0.193
962	-3052	184	0.6	Vn	0	215	50	0.29	50.06					0.205
963	-3050	180	0.5	Vn	0	245	80	0.29	96.69					0.106
967	-3005	132	0.3	Vn	0	215	50	7.06	80.23					0.088
968	-3010	133	0.3	Bx	QSP	215	50	0.69	10.70					0.064
968.1	-3010	133	0.30	Bx	QSP	215	70	0.21	3.39					0.061
968.2	-3010	133	0.30	Bx	0	215	70	0.14	25.03					0.005
969	-3004	127	1.3	Fw	Pin	245	55	0.31	1.61					0.191
970	-3006	137	0.3	Vn	0	240	60	0.57	40.11					0.089

Sample Number	NS Coordinates	EW	Length Meter	Type	Alt	Strike	Dip	auppm	agppm	asppm	hgppm	cuppm	sbpp	au/ag
974	-3042	138	1.0	Bx	QCSP	245	55	6.00	18.72					0.321
975	-3042	138	0.3	Bx	QS	220	60	0.82	5.01					0.164
976	-3110	187	4.0	Fw	Pin	225	85	0.62	3.77	10.00	1.10			0.164
977	-3093	197	0.6	Bx	QP	225	86	0.51	33.05					0.016
983	-3172	219	0.2	Bx	Pin	215	42	0.21	2.71					0.076
984	-3170	221	1.6	Fw	Ain	210	90	0.51	26.02					0.020
985	-2791	163	0.3	Bx	Ain	200	55	0.03	0.31					0.111
986	-2791	165	0.6	Fw	Ain	200	55	0.03	0.21					0.167
989	-1895	192	1.5	Hw	Ain	205	45	1.85	76.11	10.00	0.62	20.0		0.024
990	-1895	190	0.8	Vn	0	205	45	3.36	122.74	5.00	0.32	25.0		0.027
991	-1916	96	0.3	Vn	0	270	45	0.00	6.51	5.00	0.28			0.000
993	-1152	100	0.6	Fw	Aout	210	45	0.00	0.51	-5.00	0.53			0.000
994	-1155	103	0.0	Vn	0	205	52	0.00	0.51	15.00	1.70			0.000
995	-1143	106	0.1	Bx	QSP	310	50	0.96	3.77	-5.00	1.40	60.0		0.255
996	-1143	108	0.6	Bx	0	310	50	2.64	37.03	-5.00	1.50	40.0		0.071
997	-1143	109	0.3	Bx	Ain	310	50	0.48	10.29	-5.00	0.43	10.0		0.047
998	-1117	108	0.1	Hw	Ain	205	42	0.58	9.60	-5.00	1.60	25.0		0.061
999	-1133	109	0.6	Hw	Ain	215	50	1.17	4.46	10.00	1.60	20.0		0.262
1000	-255	191	0.5	Bx	QSP	210	42	0.55	17.49	-5.00	3.40			0.031
1001	-255	190	0.5	Vn	0	210	42	1.71	50.06	-5.00	3.70			0.034
1002	-225	189	1.50	Bx	QS	210	42	0.00	19.54	5.00	2.00	60.0		0.000
1003	-255	188	0.2	Vn	0	212	42	0.41	5.14	-5.00	1.70			0.080
1004	-255	185	0.0	Bx	QCSP	210	42	0.55	7.20	5.00	2.10			0.076
1051	-2326	202	0.5	Bx	QSP	215	45	0.55	3.19					0.172
1052	-2327	204	0.9	Bx	Pin	215	45	10.29	17.21					0.598
1053	-2328	206	0.3	Bx	0	220	50	3.26	9.39					0.347
1054	-2329	208	0.2	Bx	QCP	215	70	2.91	6.21					0.470
1056	-2285	204	0.5	Bx	Pin	215	45	10.29	11.62					0.885
1056.1	-2285	204	0.50	Bx	QCP	215	70	5.25	7.20					0.729
1056.2	-2285	204	0.50	Bx	QSP	215	70	0.31	7.54					0.041
1056.3	-2285	204	0.50	Bx	0	215	70	35.31	37.71					0.936

Sample Number	NS Coordinates	EW	Length Meter	Type	Alt	Strike	Dip	auppm	agppm	asppm	hgppm	cuppm	sbpp	au/ag
1057	-2285	206	0.9	Bx	QC	215	45	0.17	0.79					0.217
1058	-2285	208	0.2	Bx	Pin	215	45	10.29	36.00					0.286
1059	-2285	210	0.4	Hw	Ain	215	45	6.86	6.79					1.010
1061	-2250	200	1.30	Hw	Ain	205	45	0.17	0.62	5.00	0.57	50.0		0.278
1062	-2230	210	0.40	Vn	QC	205	45	3.67	33.94	25.00	8.50	135.0		0.108
1062.1	-2230	210	0.50	Hw	Pout	205	45	0.48	1.89	-5.00	1.70	25.0		0.255
1063.1	-2242	230	0.30	Hw	Ain	215	42	0.10	2.30	10.00	2.90	30.0		0.045
1063.2	-2242	230	1.00	Hw	Aout	215	42	0.07	2.19	5.00	1.30	35.0		0.031
1064	-2240	234	0.15	Hw	Pout	30	83	0.14	18.86	-5.00	1.60	45.0		0.007
1065	-2238	250	0.70	Hw	Pout	35	88	0.00	6.17	-5.00	0.62	50.0		0.000
1068	-1115	140	0.8	Vn	0	200	30	4.01	30.17	-5.00	10.00			0.133

(CEMCORP Laboratories)

2000	210	259		Vn	0	165	74	0.86	41.14					0.021
2001	215	235		Vn	0	165	90	2.40	7.20					0.333
2002	144	72		Vn	0	200	58	0.07	1.71					0.040
2003	120	85		Bx	QC	220	65	9.67	42.86					0.226
2004	98	81		Bx	QC	220	60	3.91	10.97					0.356
2005	93	70		Fw	0	0	0	9.60	236.57					0.041
2006	58	88		Bx	QC	220	60	1.58	97.03					0.016
2007	25	98		Bx	QC	215	54	0.62	35.66					0.017
2008	-5	106		Fw	QC	218	54	0.34	13.37					0.026
2009	-27	107		Fw	0	0	0	1.41	15.09					0.093
2010	-41	115		Bx	QS	220	64	0.65	4.11					0.158
2011	-52	120		Vn	0	200	78	0.62	1.71					0.360
2012	-72	121		Vn	0	220	64	0.17	27.77					0.006
2013	-91	146		Vn	0	230	60	0.17	1.71					0.100
2014	-110	155		Vn	0	230	60	0.51	20.57					0.025
2015	-142	165		Vn	0	230	60	1.71	15.43					0.111

Sample Number	NS Coordinates	EW	Length Meter	Type	Alt	Strike	Dip	auppm	agppm	asppm	hgppm	cuppm	sbpp	au/ag
2016	-205	186		Vn	0	230	50	-0.17	5.83					-0.029
2017	-176	179		Vn	0	225	50	2.13	22.29					0.095
2018	-210	182		Vn	0	225	50	3.77	98.74					0.038
2019	-243	184		Vn	0	210	50	0.34	0.17					2.000
2020	-244	196		Vn	0	218	90	0.51	17.49					0.029
2021	-244	200		Vn	0	208	90	0.38	10.97					0.034
2022	-280	191		Hw	0	208	90	0.69	78.86					0.009
2023	-275	196		Hw	0	208	90	0.75	85.72					0.009
2024	-315	188		Bx	QS	208	50	0.51	14.06					0.037
2025	-316	200		Hw	0	208	50	0.17	1.06					0.161
2026	-375	205		Hw	0	208	0	0.17	1.34					0.128
2027	-365	209		Bx	QS	208	50	1.03	52.80					0.019
2028	-343	200		Hw	0	208	0	0.51	16.80					0.031
2029	-343	205		Hw	0	208	0	1.06	15.09					0.070
2030	-358	193		Hw	0	208	0	1.34	26.40					0.051
2031	-391	191		Fw	0	360	0	0.34	34.29					0.010
2032	-394	196		Bx	Pin	208	0	0.27	20.57					0.013
2033	-421	200		Hw	Pin	208	0	0.17	5.49					0.031
2034	-1125	110		Bx	0	200	25	1.03	7.54					0.136
2035	-2200	190		Hw	0	210	50	0.48	20.23					0.024
2036	-2202	118		Fw	0	210	50	0.17	25.37					0.007
2037	-2219	116		Fw	0	210	50	0.51	20.91					0.025
2038	-2208	172		Hw	0	210	50	1.92	24.00					0.080
2039	-2235	147		Hw	0	210	50	4.59	9.87					0.465
2040	-2295	124		Hw	Ain	210	50	0.69	8.91					0.077
2041	-2294	159		Hw	Pin	210	50	0.14	11.25					0.012
2042	-2293	180		Hw	Pout	210	50	1.03	6.17					0.167
2043	-2292	197		Hw	Pout	210	50	1.71	9.33					0.184
2044	-2295	210		Vn	QCS	210	50	51.09	20.23					2.525
2045	-2295	225		Bx	QCS	200	50	4.25	26.74					0.159
2046	-2295	220		Bx	QCS	200	50	0.69	9.60					0.071

Sample Number	NS Coordinates	EW	Length Meter	Type	Alt	Strike	Dip	auppm	agppm	asppm	hgppm	cuppm	sbpp	au/ag
2047	-2314	228		Bx	QCS	200	50	0.69	9.60					0.071
2048	-2336	225		Vn	0	200	50	0.51	1.71					0.300
2049	-2331	209		Vn	0	200	50	0.89	7.34					0.121
2050	-2325	193		Hw	0	210	50	0.82	19.61					0.042
2051	-2323	180		j	0	210	50	0.96	9.12					0.105
2052	-2335	162		Hw	0	225	60	0.21	9.39					0.022
2053	-2360	175		Hw	0	225	60	1.54	6.86					0.225
2054	-2378	220		Bx	0	200	50	0.17	6.86					0.025
2055	-2397	218		Bx	0	200	50	1.54	10.29					0.150
2056	-2417	211		Bx	0	200	50	0.17	3.43					0.050
2057	-2433	197		Bx	0	200	50	1.03	9.94					0.103
2058	-2453	203		Vn	0	226	60	37.71	36.34					1.038
2059	-2470	200		Vn	0	222	80	9.94	83.31					0.119

APPENDIX F
TELEGRAPH MINE
DRILL LOG DATA AND ASSAY RESULTS

	COORDINATE		ALTERATION			VALUE		RATIO
NS	EW	ELEV	TYPE	ALT	MIN	AUppm	AGppm	AU/AG
CDH-1								
202	287.0	3836.0	Hw	Pout	0			
202	290.3	3831.8	Hw	Pout	0			
202	293.7	3827.5	Hw	Pout	0			
202	297.0	3823.3	Hw	Pout	0			
202	300.4	3819.0	Hw	Pout	0	0.686	1.714	0.400
202	303.7	3814.8	Vn	Pout	Qvgp	1.131	1.714	0.660
202	307.1	3810.5	Vn	Pout	Qvgp	1.097	1.714	0.640
202	310.4	3806.3	Hw	Pout	0	1.166	1.714	0.680
202	313.7	3802.1	Hw	Pout	0	1.029	1.714	0.600
202	317.1	3797.8	Hw	Pout	Qvgp	1.509	1.714	0.880
CDH-2								
102	120.0	3847.0						
102	128.3	3838.5						
102	132.4	3834.3				0.686	1.714	0.400
102	136.5	3830.0				0.171	1.714	0.100
102	140.7	3825.8				1.577	1.714	0.920
102	144.8	3821.5				0.891	1.714	0.520
102	148.9	3817.3						
102	153.1	3813.1				1.029	1.714	0.600
102	157.2	3808.8						
CDH-3								
25	155.0	3842.0						
25	159.1	3837.8						
25	163.3	3833.5						
25	167.4	3829.3						
25	171.5	3825.0						
25	175.7	3820.8				1.166	1.714	0.680
25	179.8	3816.5				1.166	1.714	0.680
25	183.9	3812.3				0.514	1.714	0.300
25	188.1	3808.1				0.171	1.714	0.100
25	192.2	3803.8						
CDH-3A								
24	155.0	3833.5						
24	167.4	3829.3						
24	171.6	3825.0						
24	175.7	3820.8				1.303	1.714	0.760
24	179.9	3816.5				0.617	1.714	0.360
24	184.0	3812.3				0.411	1.714	0.240
24	188.2	3808.1				0.274	1.714	0.160
24	192.3	3803.8				0.206	1.714	0.120
CDH-4								
-75	158.0	3825.0	Hw	Pout	0	1.029	1.714	0.600
-75	153.8	3820.8	Hw	Pout	Qvg	0.960	1.714	0.560
-75	149.5	3816.5	Hw	Pout	Qvg	0.411	1.714	0.240
-75	145.3	3812.3	Hw	Pout	Qvg	0.686	1.714	0.400
-75	141.1	3808.1	Hw	Pout	0			
-75	136.8	3803.8	Hw	Pout	0			

	COORDINATE		ALTERATION			VALUE		RATIO
NS	EW	ELEV	TYPE	ALT	MIN	AUppm	AGppm	AU/AG
CDH-5								
-200	230.2	3817.3				0.069	4.800	0.014
-200	223.4	3807.5				0.514	1.714	0.300
-200	219.9	3802.6				0.857	1.714	0.500
-200	213.0	3800.2				0.069	5.829	0.012
-200	216.5	3797.7				1.543	1.714	0.900
-200	210.0	3795.0				0.583	1.714	0.340
-200	213.0	3792.8				0.446	1.714	0.260
-200	207.0	3789.8				0.171	1.714	0.100
-200	204.0	3784.6				0.069	1.714	0.040
-200	201.0	3779.4				0.960	4.457	0.215
-200	198.0	3774.2				1.234	3.429	0.360
CDH-6								
-300	223.5	3828.5	Hw	Aout	0	0.069	1.714	0.040
-300	215.0	3820.0	Hw	Aout	Qfn	0.069	1.714	0.040
-300	210.8	3815.8	Bx	QSP	Qfn	2.229	18.172	0.123
-300	206.5	3811.5	Fw	Aout	Qfn	0.480	22.629	0.021
-300	202.3	3807.3	Fw	Pout	Qfn	1.783	1.714	1.040
CDH-7-8								
-350	214.6	3837.6				1.714	16.800	0.102
-350	213.2	3836.2				3.086	20.229	0.153
-350	211.8	3834.8				1.029	1.714	0.600
-350	210.3	3833.3				1.714	7.886	0.217
-350	208.9	3831.9				2.743	4.457	0.615
-350	207.5	3830.5				1.371	7.543	0.182
-350	206.1	3829.1				0.686	6.857	0.100
-350	204.7	3827.7				1.714	10.286	0.167
-350	225.0	3827.0	Hw	Pin	0	1.029	1.714	0.600
-350	203.3	3826.3				1.029	9.257	0.111
-350	225.0	3825.0	Bx	QC	Qvg	3.566	1.714	2.080
-350	201.9	3824.9				1.029	13.372	0.077
-350	200.4	3823.4				3.771	22.629	0.167
-350	225.0	3823.0	Bx	QSP	Qfn	0.686	1.714	0.400
-350	199.0	3822.0				2.400	7.886	0.304
-350	225.0	3821.0	Bx	QSP	Qfn	0.960	1.714	0.560
-350	197.6	3820.6				2.400	5.486	0.438
-350	196.2	3819.2				0.686	3.086	0.222
-350	225.0	3819.0	Vn	0	Qfn	2.057	1.714	1.200
-350	194.8	3817.8				0.686	1.714	0.400
-350	225.0	3817.0	Vn	QSP	Qfn	10.080	6.514	1.547
-350	225.0	3815.0	Fw	Pin	0	3.429	1.714	2.000
-350	225.0	3813.0	Vn	QSP	Qfn	1.509	1.714	0.880
-350	225.0	3807.0	Fw	Pout	0	0.171	1.714	0.100
-350	225.0	3805.0	Fw	Pout	0	2.537	39.429	0.064
-350	225.0	3803.0	Fw	Pout	0	8.366	54.858	0.152
-350	225.0	3801.0	Fw	Pout	0	0.069	3.429	0.020
-350	225.0	3799.0	Fw	Pout	0	0.549	1.714	0.320
-350	225.0	3797.0	Fw	Pout	0	0.069	13.029	0.005

COORDINATE			ALTERATION			VALUE		RATIO
NS	EW	ELEV	TYPE	ALT	MIN	AUppm	AGppm	AU/AG
CDH-AA								
-500	216.5	3826.5						
-500	212.3	3822.3				0.343	1.714	0.200
-500	208.0	3818.0				2.674	1.714	1.560
-500	203.8	3813.8				0.480	1.714	0.280
-500	199.5	3809.5				1.440	1.714	0.840
-500	195.3	3805.3						
-500	191.1	3801.1						
-500	186.8	3796.8						
-500	182.6	3792.6						
CDH-BB								
-2185	147.6	3872.6				2.057		
-2185	146.2	3871.2				1.029		
-2185	144.8	3869.8				2.057		
-2185	143.3	3868.3				7.886		
-2185	141.9	3866.9				8.572		
-2185	140.5	3865.5				11.314		
-2185	139.1	3864.1				2.057		
-2185	137.7	3862.7				125.487		
-2185	136.3	3861.3				9.943		
-2185	134.9	3859.9				0.343		
-2185	133.4	3858.4				6.171		
-2185	132.0	3857.0				9.600		
CDH-CC								
-2188	147.6	3873.6				1.371		
-2188	146.2	3872.2				3.771		
-2188	144.8	3870.8				9.943		
-2188	143.3	3869.3				11.657		
-2188	141.9	3867.9				46.286		
-2188	140.5	3866.5				6.857		
-2188	139.1	3865.1				5.829		
-2188	137.7	3863.7				17.486		
-2188	136.3	3862.3				0.686		
-2188	134.9	3860.9				1.714		
-2188	133.4	3859.4				6.857		
-2188	132.0	3858.0				3.771		
CDH-DD								
-2194	149.0	3874.2				7.886		
-2194	150.1	3872.8				2.743		
-2194	143.3	3871.3				1.714		
-2194	141.9	3869.9				16.457		
-2194	140.5	3868.5				12.343		
-2194	139.1	3867.1				5.143		
-2194	137.7	3865.7				4.114		
-2194	136.3	3864.3				0.686		
-2194	134.9	3862.9				5.486		
-2194	133.4	3861.4				1.029		
-2194	132.0	3860.0				3.429		

COORDINATE			ALTERATION			VALUE		RATIO
NS	EW	ELEV	TYPE	ALT	MIN	AUppm	AGppm	AU/AG
CDH-9								
-2225	133.6	3886.6	Hw	Aout	0	2.400	2.400	1.000
-2225	132.2	3885.2	Hw	Aout	0	2.057	4.457	0.462
-2225	130.8	3883.8	Hw	Ain	Qfn	8.914	13.714	0.650
-2225	129.3	3882.3	Hw	Ain	0	2.057	4.457	0.462
-2225	127.9	3880.9	Hw	0	Qfnp	39.086	16.457	2.375
-2225	126.5	3879.5	Hw	0	Qfnp	76.458	96.344	0.794
-2225	125.1	3878.1	Hw	0	Qfnp	42.858	19.543	2.193
-2225	123.7	3876.7	Hw	QSP	Qfn	24.000	14.057	1.707
-2225	122.3	3875.3	Bx	QSP	Qfn	20.914	16.114	1.298
-2225	120.9	3873.9	Bx	QSP	Qfn	16.114	6.857	2.350
-2225	119.4	3872.4	Bx	Pin	Qvg	14.743	15.086	0.977
-2225	118.0	3871.0	Fw	Pin	QFe	10.629	20.914	0.508
-2225	116.6	3869.6	Fw	Pin	Qcmn	6.857	11.314	0.606
-2225	115.2	3868.2	Fw	Pin	Qvgp	9.257	29.829	0.310
-2225	113.8	3866.8	Fw	Pin	Qvgp	3.771	2.743	1.375
-2225	112.4	3865.4	Fw	Pin	Qvgp	3.429	3.429	1.000
-2225	111.0	3864.0	Fw	Pout	Qvgp	2.400	3.086	0.778
-2225	109.5	3862.5	Fw	Pout	Qvgp	3.086	2.743	1.125
CDH-10								
-2232	208.6	3861.6				1.371		
-2232	207.2	3860.2				2.400		
-2232	205.8	3858.8				0.686		
-2232	204.3	3857.3				2.057		
-2232	202.9	3855.9				1.029		
-2232	201.5	3854.5				2.057		
-2232	200.1	3853.1				1.029		
-2232	198.7	3851.7				6.857		
-2232	197.3	3850.3				2.057		
-2232	195.9	3848.9				1.029		
-2232	194.4	3847.4				1.029		
-2232	193.0	3846.0				2.057		
-2232	191.6	3844.6				0.343		
-2232	190.2	3843.2				0.686		
-2232	188.8	3841.8				2.057		
-2232	187.4	3840.4				0.686		
CDH-11								
-2240	133.6	3889.6	Hw	Pout	0	2.743	3.086	0.889
-2240	132.2	3888.2	Hw	Pout	0	4.800	5.829	0.824
-2240	130.8	3886.8	Hw	Pout	0	2.743	2.400	1.143
-2240	129.3	3885.3	Hw	Pout	Qfnp	1.371	3.086	0.444
-2240	127.9	3883.9	Hw	Pout	0	3.086	5.486	0.563
-2240	126.5	3882.5	Hw	Pin	0	1.714	3.771	0.455
-2240	125.1	3881.1	Bx	QSP	Qvg	21.600	30.172	0.716
-2240	123.7	3879.7	Bx	QS	Qvg	5.143	6.514	0.789
-2240	122.3	3878.3	Bx	QCSP	Qvg	3.086	5.143	0.600
-2240	120.9	3876.9	Bx	QCP	Qfn	7.200	7.886	0.913
-2240	168.6	3876.6	Hw	Pin		3.429	2.057	1.667
-2240	119.4	3875.4	Fw	Pin	0	4.800	5.829	0.824
-2240	167.2	3875.2	Hw	Pin		3.429	4.114	0.833

COORDINATE			ALTERATION			VALUE		RATIO
NS	EW	ELEV	TYPE	ALT	MIN	AUppm	AGppm	AU/AG
-2240	118.0	3874.0	Fw	Pin	Qvg	5.143	17.486	0.294
-2240	165.8	3873.8	Hw	Pin	Qfn	1.371	0.343	4.000
-2240	116.6	3872.6	Fw	Pout	0	3.086	3.429	0.900
-2240	164.3	3872.3	Hw	Pin	Qfnp	3.429	4.114	0.833
-2240	115.2	3871.2	Fw	Pout	Qcmn	4.457	2.743	1.625
-2240	162.9	3870.9	Bx	Pin	0	3.086	4.114	0.750
-2240	113.8	3869.8	Fw	Pout	Qvg	5.829	2.743	2.125
-2240	161.5	3869.5	Bx	Pin	Qvgp	4.457	0.686	6.500
-2240	112.4	3868.4	Fw	Pout	0	2.057	2.743	0.750
-2240	160.1	3868.1	Bx	QC	Qvgp	1.029	2.400	0.429
-2240	111.0	3867.0	Fw	Pout	0	3.771	3.086	1.222
-2240	158.7	3866.7	Bx	QC	Qvgp	3.771	4.457	0.846
-2240	109.5	3865.5	Fw	Pout	0	8.572	4.457	1.923
-2240	157.3	3865.3	Bx	QC	Qvg	2.057	6.171	0.333
-2240	155.9	3863.9	Fw	Pin	Qvg	1.371	0.686	2.000
CDH-12								
-2250	136.6	3892.6	Hw	Pout	0	2.057	1.371	1.500
-2250	133.6	3891.6	Hw	0	QFe	2.057	1.029	2.000
-2250	135.2	3891.2	Hw	Pout	0			ERR
-2250	132.2	3890.2	Hw	QSP	Qvg	16.114	17.143	0.940
-2250	133.8	3889.8	Hw	Pout	0	3.429	1.714	2.000
-2250	130.8	3888.8	Hw	Pout	Qcmn	9.257	7.886	1.174
-2250	132.3	3888.3	Hw	Pout	0	1.029	1.371	0.750
-2250	129.3	3887.3	Hw	Pout	Qvgp	42.172	10.972	3.844
-2250	130.9	3886.9	Hw	QC	0	1.029	1.371	0.750
-2250	127.9	3885.9	Hw	Pout	Qvg	6.171	5.486	1.125
-2250	129.5	3885.5	Hw	QC	Qvg	2.057	1.714	1.200
-2250	126.5	3884.5	Hw	Pout	0	2.743	2.743	1.000
-2250	128.1	3884.1	Bx	QCSP	Qvg	52.115	22.286	2.338
-2250	125.1	3883.1	Hw	Pin	Qvgp	6.171	2.743	2.250
-2250	126.7	3882.7	Bx	QCS	Qvg	12.686	25.715	0.493
-2250	123.7	3881.7	Bx	QCSP	Qfn	12.686	3.086	4.111
-2250	125.3	3881.3	Bx	QCS	Qvg	3.771	1.371	2.750
-2250	122.3	3880.3	Bx	QCP	Qfn	9.600	3.429	2.800
-2250	123.9	3879.9	Bx	Pin	Qvg	9.600	2.057	4.667
-2250	120.9	3878.9	Bx	QCSP	Qvgp	5.486	1.371	4.000
-2250	122.4	3878.4	Fw	Ain	Qfn	7.886	2.057	3.833
-2250	119.4	3877.4	Bx	QC	Qvg	2.400	2.057	1.167
-2250	121.0	3877.0	Fw	Aout	Qvg	5.829	3.771	1.545
-2250	118.0	3876.0	Bx	QSP	Qvg	2.743	0.686	4.000
-2250	119.6	3875.6	Fw	Aout	Qvg	2.743	5.486	0.500
-2250	116.6	3874.6	Fw	Pin	Qcmn	9.600	1.714	5.600
-2250	118.2	3874.2	Fw	Aout	Qvg	8.229	1.714	4.800
-2250	115.2	3873.2	Fw	QS	FeO	2.743	1.029	2.667
-2250	116.8	3872.8	Fw	Pout	0	1.029	1.371	0.750
-2250	113.8	3871.8	Fw	Pout	FeO	2.057	1.714	1.200
-2250	115.4	3871.4	Fw	Pout	0	1.371	2.743	0.500
-2250	112.4	3870.4	Fw	Pout	FeO	2.743	4.457	0.615
-2250	114.0	3870.0	Fw	Pout	0	0.686	2.400	0.286
-2250	111.0	3869.0	Fw	Pout	Qvgp	8.914	3.771	2.364

COORDINATE			ALTERATION			VALUE		RATIO
NS	EW	ELEV	TYPE	ALT	MIN	AUppm	AGppm	AU/AG
-2280	116.0	3872.0	Fw	Pout	0	2.743	5.143	0.533
-2280	114.5	3870.5	Fw	Pout	0	4.457	2.400	1.857
CDH-15								
-2290	142.6	3896.6	Hw	Pout	0	0.343	0.343	1.000
-2290	141.2	3895.2	Hw	Pout	0	1.029	0.343	3.000
-2290	139.8	3893.8	Hw	Pout	0	1.371	0.343	4.000
-2290	138.3	3892.3	Hw	Pout	0	0.343	0.343	1.000
-2290	136.9	3890.9	Hw	Pout	0	1.714	1.714	1.000
-2290	135.5	3889.5	Hw	Pout	0	1.029	3.086	0.333
-2290	134.1	3888.1	Bx	QSP	Qvg	11.657	0.343	34.000
-2290	132.7	3886.7	Bx	QCP	Qvg	10.629	5.829	1.824
-2290	131.3	3885.3	Bx	QCP	Qfn	13.714	9.943	1.379
-2290	129.9	3883.9	Bx	QCS	Qvg	4.800	1.371	3.500
-2290	128.4	3882.4	Bx	QC	0	11.314	5.486	2.063
-2290	127.0	3881.0	Fw	Aout	Qvgp	2.400	1.371	1.750
-2290	125.6	3879.6	Fw	Pout	Qvg	4.457	0.343	13.000
-2290	124.2	3878.2	Fw	Aout	Qvg	6.857	2.743	2.500
-2290	122.8	3876.8	Fw	Aout	Qvgp	1.371	0.343	4.000
-2290	121.4	3875.4	Fw	Aout	Qvgp	14.743	4.800	3.071
-2290	120.0	3874.0	Fw	Pout	0	2.057	0.343	6.000
-2290	118.5	3872.5	Fw	Pout	0	2.057	1.029	2.000
-2290	117.1	3871.1	Fw	Pout	0	1.371	0.343	4.000
-2290	115.7	3869.7	Fw	Pout	0	1.029	2.057	0.500
-2290	114.3	3868.3	Fw	Pout	Qvgp	2.400	1.371	1.750
-2290	112.9	3866.9	Fw	Pout	0	1.029	32.915	0.031
-2290	111.5	3865.5	Fw	Pout	0	3.429	1.371	2.500
-2290	110.1	3864.1	Fw	Pout	0	0.343	0.686	0.500
CDH-17								
-2291	197.2	3870.2	Hw	Pout	0	1.371	2.400	0.571
-2291	195.8	3868.8	Hw	Pout	0	2.400	1.371	1.750
-2291	194.3	3867.3	Hw	Pout	Qfn	3.429	2.400	1.429
-2291	192.9	3865.9	Hw	Aout	0	3.429	2.057	1.667
-2291	191.5	3864.5	Hw	Aout	0	2.743	1.714	1.600
-2291	190.1	3863.1	Hw	Pin	Qvg	2.743	1.714	1.600
-2291	188.7	3861.7	Hw	Pin	Qvg	1.714	1.714	1.000
-2291	187.3	3860.3	Bx	QCP	Qvg	6.857	2.057	3.333
-2291	185.9	3858.9	Bx	QCP	Qvg	2.057	1.371	1.500
-2291	184.4	3857.4	Hw	Aout	0	2.400	1.371	1.750
-2291	183.0	3856.0	Hw	Aout	0	2.057	1.029	2.000
-2291	181.6	3854.6	Hw	Aout	0	5.143	3.086	1.667
-2291	180.2	3853.2	Hw	Aout	Qfn	3.771	2.057	1.833
-2291	178.8	3851.8	Hw	Aout	Qvg	7.543	4.457	1.692
-2291	177.4	3850.4	Hw	Aout	Qvg	11.657	5.486	2.125
-2291	176.0	3849.0	Bx	QCSP	Qvg	8.229	3.771	2.182
-2291	174.5	3847.5	Bx	QCSP	Qvg	5.829	3.429	1.700
-2291	173.1	3846.1	Bx	QC	Qvg	5.143	1.714	3.000
-2291	171.7	3844.7	Bx	QC	Qvgp	5.829	3.429	1.700
-2291	170.3	3843.3	Hw	Aout	Qvg	3.771	3.429	1.100
-2291	168.9	3841.9	Hw	Aout	0	2.400	3.086	0.778
-2291	167.5	3840.5	Hw	Aout	0	2.057	2.400	0.857

COORDINATE			ALTERATION			VALUE		RATIO
NS	EW	ELEV	TYPE	ALT	MIN	AUppm	AGppm	AU/AG
-2291	166.1	3839.1	Hw	Aout	Qvg	3.429	2.057	1.667
-2291	164.6	3837.6	Hw	Pout	Qvg	9.257	2.743	3.375
CDH-18								
-2305	148.6	3898.6	Hw	Pout	0			ERR
-2305	147.2	3897.2	Hw	Pout	0	3.429	2.400	1.429
-2305	145.8	3895.8	Hw	Pout	0			ERR
-2305	144.3	3894.3	Hw	Pout	0			ERR
-2305	142.9	3892.9	Bx	QSP	Qvgp	3.771	1.371	2.750
-2305	141.5	3891.5	Bx	QSP	Qvgp	1.714	0.686	2.500
-2305	140.1	3890.1	Bx	QCSP	Qvg	27.429	7.543	3.636
-2305	138.7	3888.7	Bx	QCP	Qvg	10.972	4.457	2.462
-2305	137.3	3887.3	Bx	QC	Qvgp	17.829	3.429	5.200
-2305	135.9	3885.9	Bx	QCS	Qvg	4.457	3.771	1.182
-2305	134.4	3884.4	Fw	Pin	Qvg	3.429	1.714	2.000
-2305	133.0	3883.0	Fw	Aout	Qvg			ERR
-2305	131.6	3881.6	Fw	Aout	Qvg	2.743	0.686	4.000
-2305	130.2	3880.2	Fw	Aout	FeO	5.486	1.029	5.333
-2305	128.8	3878.8	Fw	Aout	Qvg	3.771	1.029	3.667
CDH-19								
-2320	68.6	3888.6				1.029	0.343	3.000
-2320	162.6	3888.6	Hw	Pout		2.743	1.371	2.000
-2320	161.2	3887.2	Hw	Pout		3.771	1.371	2.750
-2320	67.2	3887.2				0.343	1.029	0.333
-2320	159.8	3885.8	Hw	Pout		1.371	1.714	0.800
-2320	65.8	3885.8				1.029	1.029	1.000
-2320	158.3	3884.3	Hw	Pout		0.686	1.029	0.667
-2320	64.3	3884.3				0.686	0.000	
-2320	62.9	3882.9				1.029	3.086	0.333
-2320	156.9	3882.9	Hw	Pin	0	0.686	1.371	0.500
-2320	168.6	3881.6				1.029	3.086	0.333
-2320	61.5	3881.5				1.029	3.771	0.273
-2320	155.5	3881.5	Hw	Pin	Qvgp	1.371	1.029	1.333
-2320	167.2	3880.2				0.343	3.086	0.111
-2320	60.1	3880.1				1.029	3.771	0.273
-2320	154.1	3880.1	Hw	QC	Qvg	3.771	1.371	2.750
-2320	165.8	3878.8				2.743	3.771	0.727
-2320	152.7	3878.7	Bx	QC	0	4.457	1.371	3.250
-2320	58.7	3878.7				1.029	3.771	0.273
-2320	164.3	3877.3				2.743	0.686	4.000
-2320	151.3	3877.3	Bx	QSP	Qvg	3.086	1.371	2.250
-2320	57.3	3877.3				0.343	3.429	0.100
-2320	162.9	3875.9				1.714	3.429	0.500
-2320	55.9	3875.9				0.343	0.686	0.500
-2320	149.9	3875.9	Bx	QS	Qvgp	17.829	4.800	3.714
-2320	161.5	3874.5				3.429	4.457	0.769
-2320	148.4	3874.4	Bx	QSP	Qvg	6.857	1.714	4.000
-2320	54.4	3874.4				0.686	0.686	1.000
-2320	160.1	3873.1				6.857	1.714	4.000
-2320	53.0	3873.0				2.057	4.457	0.462
-2320	147.0	3873.0	Bx	QC	Qvg	2.400	1.714	1.400

COORDINATE			ALTERATION			VALUE		RATIO
NS	EW	ELEV	TYPE	ALT	MIN	AUppm	AGppm	AU/AG
-2320	158.7	3871.7				2.743	3.086	0.889
-2320	51.6	3871.6				4.114	4.114	1.000
-2320	145.6	3871.6	Bx	QCP	Qvg	3.771	1.371	2.750
-2320	157.3	3870.3				2.400	0.686	3.500
-2320	144.2	3870.2	Fw	Aout	Qvg	3.086	1.371	2.250
-2320	50.2	3870.2				0.343	0.686	0.500
-2320	155.9	3868.9				2.057	2.057	1.000
-2320	142.8	3868.8	Fw	Aout	Qvg	4.114	3.086	1.333
-2320	48.8	3868.8				0.686	1.029	0.667
-2320	154.4	3867.4				2.400	0.686	3.500
-2320	47.4	3867.4				1.371	4.114	0.333
-2320	141.4	3867.4	Fw	Aout	0			ERR
-2320	153.0	3866.0				3.086	0.686	4.500
-2320	46.0	3866.0				0.686	1.714	0.400
-2320	140.0	3866.0	Fw	Aout	0	2.743	1.714	1.600
-2320	151.6	3864.6				2.400	1.714	1.400
-2320	44.5	3864.5				0.686	1.029	0.667
-2320	138.5	3864.5	Fw	Pout	0	1.714	0.686	2.500
-2320	150.2	3863.2				1.371	1.714	0.800
-2320	137.1	3863.1	Fw	Pout	0	3.086	0.343	9.000
-2320	43.1	3863.1				0.686	1.371	0.500
-2320	148.8	3861.8				1.029	8.914	0.115
-2320	135.7	3861.7	Fw	Pout	0	1.029	0.343	3.000
-2320	41.7	3861.7				0.686	0.686	1.000
-2320	147.4	3860.4				3.086	3.429	0.900
-2320	40.3	3860.3				2.057	1.371	1.500
-2320	146.0	3859.0				0.686	0.686	1.000
-2320	38.9	3858.9				0.686	0.686	1.000
-2320	144.5	3857.5				3.429	3.771	0.909
-2320	37.5	3857.5				1.029	4.457	0.231
-2320	143.1	3856.1				1.714	0.686	2.500
-2320	36.1	3856.1				1.029	3.086	0.333
-2320	141.7	3854.7				1.029	1.029	1.000
-2320	34.6	3854.6				0.343	3.429	0.100
CDH-21								
-2340	168.6	3881.6	Hw	Pout	0	1.029	3.086	0.333
-2340	167.2	3880.2	Hw	Pout	Qvg	0.343	3.086	0.111
-2340	165.8	3878.8	Hw	Aout	Qvg	2.743	3.771	0.727
-2340	164.3	3877.3	Bx	QS	Qcmn	2.743	0.686	4.000
-2340	162.9	3875.9	Bx	QSP	Qvg	1.714	3.429	0.500
-2340	161.5	3874.5	Bx	QC	Qcmn	3.429	4.457	0.769
-2340	160.1	3873.1	Bx	QSP	Qvg	6.857	1.714	4.000
-2340	158.7	3871.7	Fw	QS	Qvg	2.743	3.086	0.889
-2340	157.3	3870.3	Fw	Ain	0	2.400	0.686	3.500
-2340	155.9	3868.9	Fw	Aout	Qvg	2.057	2.057	1.000
-2340	154.4	3867.4	Fw	Aout	Qvg	2.400	0.686	3.500
-2340	153.0	3866.0	Fw	Aout	Qvg	3.086	0.686	4.500
-2340	151.6	3864.6	Fw	Aout	Qvg	2.400	1.714	1.400
-2340	150.2	3863.2	Fw	Aout	Qvg	1.371	1.714	0.800
-2340	148.8	3861.8	Fw	Aout	0	1.029	8.914	0.115

COORDINATE			ALTERATION			VALUE		RATIO
NS	EW	ELEV	TYPE	ALT	MIN	AUppm	AGppm	AU/AG
-2340	147.4	3860.4	Fw	Pout	0	3.086	3.429	0.900
-2340	146.0	3859.0	Fw	Pout	0	0.686	0.686	1.000
-2340	144.5	3857.5	Fw	Pout	0	3.429	3.771	0.909
-2340	143.1	3856.1	Fw	Pout	0	1.714	0.686	2.500
-2340	141.7	3854.7	Fw	Pout	0	1.029	1.029	1.000
CDH-20								
-2384	208.6	3858.6	Hw			1.714	0.686	2.500
-2384	207.2	3857.2	Hw			7.543	5.486	1.375
-2384	205.8	3855.8	Hw	Aout	Qvgp	5.486	4.800	1.143
-2384	204.3	3854.3	Bx	QSP	Qvg	2.057	2.400	0.857
-2384	202.9	3852.9	Bx	QSP	Qvg	6.857	8.572	0.800
-2384	201.5	3851.5	Bx	QSP	Qvg	1.371	1.714	0.800
-2384	200.1	3850.1	Fw	Pout		2.743	2.743	1.000
-2384	198.7	3848.7	Fw	Pout	0	6.857	15.086	0.455
-2384	197.3	3847.3	Fw	Pout	0	2.743	2.400	1.143
-2384	195.9	3845.9	Fw	Pout	0	1.714	2.743	0.625
-2384	194.4	3844.4	Fw	Pout	0	6.857	3.429	2.000
-2384	193.0	3843.0	Fw	Pout	0	1.371	1.371	1.000
-2384	191.6	3841.6	Fw	Pout	0			
-2384	190.2	3840.2	Fw	Pout	0	1.714	1.714	1.000
-2384	188.8	3838.8	Fw	Pout	0	3.086	1.714	1.800
-2384	187.4	3837.4	Fw	Pout	0	2.057	2.057	1.000
-2384	186.0	3836.0	Fw	Pout	0	3.086	1.714	1.800
-2384	184.5	3834.5	Fw	Pout	0	1.371	1.371	1.000
-2384	183.1	3833.1	Fw	Pout	0	1.029	0.686	1.500
-2384	181.7	3831.7	Fw	Pout	0	2.057	1.029	2.000
-2384	180.3	3830.3	Fw	Pout	0	2.400	1.029	2.333
-2384	178.9	3828.9	Fw	Pout	0	2.057	1.714	1.200
-2384	177.5	3827.5	Fw	Pout	0	1.371	1.371	1.000
-2384	176.1	3826.1	Fw	Pout	0	1.029	1.371	0.750
-2384	174.6	3824.6	Fw	Pout	0	1.371	1.714	0.800
-2384	173.2	3823.2	Fw	Pout	0	1.714	1.371	1.250
-2384	171.8	3821.8	Fw	Pout	0	1.714	3.086	0.556
-2384	170.4	3820.4	Fw	Pout	0	2.400	1.714	1.400
-2384	169.0	3819.0	Hw	Pout	0	1.371	1.371	1.000
CDH-EE								
-2462	223.6	3856.6	Hw	0	0	0.686		
-2462	222.2	3855.2	Hw	0	0	0.686		
-2462	220.8	3853.8	Hw	0	0	1.714		
-2462	219.3	3852.3	Hw	Pout	0	0.686		
-2462	217.9	3850.9	Hw	Ain	0	1.029		
-2462	216.5	3849.5	Bx	QS	Qvg	0.686		
-2462	215.1	3848.1	Bx	Ain	Qvg	0.686		
-2462	213.7	3846.7	Fw	Pin	0	1.029		
-2462	212.3	3845.3	Fw	Pin	0	1.029		
-2462	210.9	3843.9	Fw	Pin	0	0.686		
-2462	209.4	3842.4	Fw	Pin	0	1.029		
-2462	208.0	3841.0	Fw	Pin	0	0.343		
-2462	206.6	3839.6	Fw	Pout	0	0.343		
-2462	205.2	3838.2	Fw	Pout	0	0.343		

COORDINATE			ALTERATION			VALUE		RATIO
NS	EW	ELEV	TYPE	ALT	MIN	AUppm	AGppm	AU/AG
-2462	203.8	3836.8	Fw	Pout	0	1.714		
-2462	202.4	3835.4	Fw	Pout	0	1.029		
-2462	201.0	3834.0	Fw	Pout	0	0.686		
-2462	199.5	3832.5	Fw	Pout	0	0.686		
-2462	198.1	3831.1	Fw	Pout	0	1.371		
-2462	196.7	3829.7	Fw	Ain	0	1.371		
-2462	195.3	3828.3	Fw	Ain	0	0.686		
-2462	193.9	3826.9	Fw	Pout	0	0.343		
-2462	192.5	3825.5	Fw	Pout	0	0.343		
-2462	191.1	3824.1	Fw	Pout	0	0.343		
-2462	189.6	3822.6	Fw	Pout	0	0.686		
-2462	188.2	3821.2	Fw	Pout	0	1.029		
-2462	186.8	3819.8	Fw	Pout	0	0.686		
-2462	185.4	3818.4	Fw	Pout	0	0.686		
CDH-FF								
-2480	223.6	3840.6				1.371		
-2480	222.2	3839.2				1.029		
-2480	220.8	3837.8				0.686		
-2480	219.3	3836.3				0.343		
-2480	217.9	3834.9				0.343		
-2480	216.5	3833.5				0.343		
-2480	215.1	3832.1				0.343		
-2480	213.7	3830.7				0.343		
-2480	212.3	3829.3				0.343		
-2480	210.9	3827.9				0.343		
-2480	209.4	3826.4				0.343		
-2480	208.0	3825.0				0.343		
-2480	206.6	3823.6				0.343		
-2480	205.2	3822.2				0.343		
-2480	203.8	3820.8				1.714		
-2480	202.4	3819.4				0.343		
-2480	201.0	3818.0				0.686		
-2480	199.5	3816.5				0.343		
-2480	198.1	3815.1				0.343		
-2480	196.7	3813.7				0.000		
-2480	195.3	3812.3				0.343		
-2480	193.9	3810.9						
CDH-GG								
-2510	223.6	3845.6				0.343		
-2510	222.2	3844.2				0.343		
-2510	220.8	3842.8				0.343		
-2510	219.3	3841.3				0.000		
-2510	217.9	3839.9				0.343		
-2510	216.5	3838.5				0.343		
-2510	215.1	3837.1				0.686		
-2510	213.7	3835.7				0.343		
-2510	212.3	3834.3				0.343		
-2510	210.9	3832.9				0.343		
-2510	209.4	3831.4				0.686		
-2510	208.0	3830.0				0.343		

COORDINATE			ALTERATION			VALUE		RATIO
NS	EW	ELEV	TYPE	ALT	MIN	AUppm	AGppm	AU/AG
-2510	206.6	3828.6				0.343		
-2510	205.2	3827.2				1.029		
-2510	203.8	3825.8				0.686		
-2510	202.4	3824.4				0.343		
-2510	201.0	3823.0				0.343		
-2510	199.5	3821.5				0.343		
-2510	198.1	3820.1				0.343		
-2510	196.7	3818.7				0.343		
-2510	195.3	3817.3				0.343		
-2510	193.9	3815.9				0.343		
-2510	192.5	3814.5				0.343		
-2510	191.1	3813.1				0.343		
-2510	189.6	3811.6				0.343		
-2510	188.2	3810.2				0.343		
-2510	186.8	3808.8				0.343		
-2510	185.4	3807.4				0.343		
-2510	184.0	3806.0				0.343		
-2510	182.6	3804.6				0.343		
-2510	178.3	3800.3						
CDH-24								
-2960	108.6	3861.6	Hw	Pout	0	0.686	1.029	0.667
-2960	107.2	3860.2	Hw	Pout	0	1.371	1.714	0.800
-2960	105.8	3858.8	Hw	Pout	0	0.343	1.371	0.250
-2960	104.3	3857.3	Hw	Pin	0	0.686	2.743	0.250
-2960	188.6	3856.6	Hw	Pin	0	1.029	2.057	0.500
-2960	102.9	3855.9	Hw	Aout	0	1.029	1.371	0.750
-2960	187.2	3855.2	Bx	QSP	0	18.172	2.743	6.625
-2960	101.5	3854.5	Hw	Aout	Qvg	5.829	2.400	2.429
-2960	185.8	3853.8	Hw	Ain	Qvg	2.743	7.543	0.364
-2960	100.1	3853.1	Hw	Aout	0	0.686	1.029	0.667
-2960	184.3	3852.3	Hw			1.371	1.371	1.000
-2960	98.7	3851.7	Hw	Pin	FeO	0.343	1.029	0.333
-2960	182.9	3850.9	Vn	0	Qfn	0.686	1.029	0.667
-2960	97.3	3850.3	Hw	0	0	0.343	1.029	0.333
-2960	181.5	3849.5	Vn	0	Qfn	1.029	0.343	3.000
-2960	95.9	3848.9	Hw	0	0	3.086	2.743	1.125
-2960	180.1	3848.1	Vn	0	Qfn	1.029	0.686	1.500
-2960	94.4	3847.4	Hw	0	0	1.029	1.371	0.750
-2960	93.0	3846.0	Hw	0	0	0.686	1.029	0.667
-2960	177.3	3845.3	Vn	0	Qfn	0.343	0.343	1.000
-2960	91.6	3844.6	Hw	Aout	Qfnp	4.457	2.400	1.857
-2960	175.9	3843.9	Vn	0	Qfn	1.371	0.686	2.000
-2960	90.2	3843.2	Bx	QSP	Qfnp	4.114	3.086	1.333
-2960	174.4	3842.4	Vn	0	Qfn	1.029	7.200	0.143
-2960	88.8	3841.8	Vn	0	Qfn	14.743	5.143	2.867
-2960	173.0	3841.0	Vn	0	Qfn	3.086	0.686	4.500
-2960	87.4	3840.4	Vn	0	Qfn	36.686	8.572	4.280
-2960	171.6	3839.6	Vn	0	Qfn	1.371	2.400	0.571
-2960	86.0	3839.0	Bx	QSP	Qvg	27.086	9.600	2.821
-2960	170.2	3838.2	Vn	0	Qfn	0.686	0.686	1.000

COORDINATE			ALTERATION			VALUE		RATIO
NS	EW	ELEV	TYPE	ALT	MIN	AUppm	AGppm	AU/AG
-2960	168.8	3836.8	Vn	0	Qfn	0.686	1.029	0.667
-2960	167.4	3835.4	Vn	0	Qfn	1.029	1.029	1.000
-2960	166.0	3834.0	Vn	0	Qfn			
-2960	164.5	3832.5	Hw	Aout	Qfn	8.914	18.514	0.481
-2960	163.1	3831.1	Bx	QSP	Qfnp	5.143	9.257	0.556
-2960	161.7	3829.7	Bx	QSP	Qvg	2.057	13.714	0.150
-2960	160.3	3828.3	Bx	QC	Qfn	6.514	14.400	0.452
-2960	158.9	3826.9	Fw	Pin	Qvg	5.143	10.972	0.469
-2960	157.5	3825.5	Fw	Pin	Qvg	5.143	12.686	0.405
-2960	156.1	3824.1	Fw	Aout	Qvg	4.457	8.914	0.500
-2960	154.6	3822.6	Bx	QSP	Qfn			
-2960	153.2	3821.2	Fw	Aout	Qvg	4.114	5.486	0.750
-2960	151.8	3819.8	Fw	Aout	Qvg	1.371	3.086	0.444
-2960	150.4	3818.4	Vn	0	Qfn	2.057	3.086	0.667
-2960	149.0	3817.0				2.057	3.086	0.667
-2960	147.6	3815.6				1.714	2.743	0.625
CDH-25/22								
-2970	108.6	3862.6				0.343	0.343	1.000
-2970	107.2	3861.2				0.686	0.343	2.000
-2970	105.8	3859.8				0.343	0.343	1.000
-2970	188.6	3859.6				7.200	12.000	0.600
-2970	104.3	3858.3				0.343	0.686	0.500
-2970	187.2	3858.2				0.686	1.029	0.667
-2970	102.9	3856.9				0.000	0.686	0.000
-2970	185.8	3856.8				0.686	1.029	0.667
-2970	101.5	3855.5				16.114	4.114	3.917
-2970	184.3	3855.3				0.686	0.343	2.000
-2970	100.1	3854.1				5.486	1.371	4.000
-2970	182.9	3853.9				0.343	0.686	0.500
-2970	98.7	3852.7				1.371	1.371	1.000
-2970	181.5	3852.5				0.686	0.343	2.000
-2970	97.3	3851.3				3.086	1.371	2.250
-2970	180.1	3851.1				1.371	1.029	1.333
-2970	95.9	3849.9				0.343	1.029	0.333
-2970	178.7	3849.7				0.686	0.686	1.000
-2970	94.4	3848.4				2.057	2.057	1.000
-2970	177.3	3848.3				0.343	0.343	1.000
-2970	93.0	3847.0				3.086	1.714	1.800
-2970	175.9	3846.9				0.343	0.343	1.000
-2970	91.6	3845.6				2.400	1.371	1.750
-2970	174.4	3845.4						
-2970	90.2	3844.2				2.057	3.429	0.600
-2970	173.0	3844.0						
-2970	88.8	3842.8				5.486	4.457	1.231
-2970	171.6	3842.6				0.686	1.029	0.667
-2970	170.2	3841.2				0.343	0.686	0.500
-2970	168.8	3839.8				1.029	0.686	1.500
-2970	167.4	3838.4				1.371	2.400	0.571
-2970	166.0	3837.0				1.371	2.057	0.667
-2970	164.5	3835.5				1.714	4.114	0.417
-2970	163.1	3834.1				5.143	13.714	0.375

COORDINATE			ALTERATION			VALUE		RATIO
NS	EW	ELEV	TYPE	ALT	MIN	AUppm	AGppm	AU/AG
CDH-23								
-2980	108.6	3865.6				2.400	1.714	1.400
-2980	107.2	3864.2				2.400	2.400	1.000
-2980	105.8	3862.8				1.714	3.429	0.500
-2980	188.6	3861.6				1.371	0.686	2.000
-2980	104.3	3861.3				0.686	2.400	0.286
-2980	187.2	3860.2				0.343	0.343	1.000
-2980	102.9	3859.9				0.686	1.371	0.500
-2980	185.8	3858.8				2.057	0.686	3.000
-2980	101.5	3858.5				0.343	1.371	0.250
-2980	184.3	3857.3				1.029	0.343	3.000
-2980	100.1	3857.1				2.400	1.371	1.750
-2980	182.9	3855.9						
-2980	98.7	3855.7				1.029	0.686	1.500
-2980	181.5	3854.5				1.029	1.371	0.750
-2980	97.3	3854.3				0.343	0.343	1.000
-2980	180.1	3853.1				0.343	1.029	0.333
-2980	95.9	3852.9				0.686	0.343	2.000
-2980	178.7	3851.7				0.686	0.686	1.000
-2980	94.4	3851.4				0.686	2.057	0.333
-2980	177.3	3850.3				0.686	1.029	0.667
-2980	93.0	3850.0				0.686	1.371	0.500
-2980	175.9	3848.9				0.686	0.686	1.000
-2980	91.6	3848.6				0.686	1.714	0.400
-2980	174.4	3847.4				0.686	1.371	0.500
-2980	90.2	3847.2				1.371	1.029	1.333
-2980	173.0	3846.0				0.343	1.029	0.333
-2980	88.8	3845.8				2.743	1.371	2.000
-2980	171.6	3844.6				1.371	1.029	1.333
-2980	87.4	3844.4				1.029	2.057	0.500
-2980	170.2	3843.2				3.429	1.029	3.333
-2980	86.0	3843.0				1.371	2.057	0.667
-2980	168.8	3841.8				0.686	0.686	1.000
-2980	84.5	3841.5				0.686	2.743	0.250
-2980	167.4	3840.4				3.086	1.371	2.250
-2980	83.1	3840.1				2.057	1.714	1.200
-2980	166.0	3839.0				1.714	1.371	1.250
-2980	81.7	3838.7				11.657	4.114	2.833
-2980	164.5	3837.5				3.429	2.057	1.667
CDH-27								
-3000	135.0	3873.0				21.943		
-3000	135.0	3868.0				3.771		
CDH-28								
-3004	162.1	3874.6				0.686		
-3004	163.2	3873.2				0.343		
-3004	164.3	3871.8				0.343		
-3004	165.3	3870.3				0.343		
-3004	166.4	3868.9				0.343		
-3004	167.5	3867.5				0.343		
-3004	168.6	3866.1				0.686		

COORDINATE			ALTERATION			VALUE		RATIO
NS	EW	ELEV	TYPE	ALT	MIN	AUppm	AGppm	AU/AG
-3050	73.0	3866.0				0.000		
-3050	71.6	3864.6				0.000		
-3050	70.2	3863.2				0.343		
-3050	68.8	3861.8				0.343		
-3050	67.4	3860.4				1.371		
-3050	66.0	3859.0				19.543		
-3050	64.5	3857.5				0.686		
-3050	63.1	3856.1				0.686		
-3050	61.7	3854.7				0.343		
-3050	60.3	3853.3				0.000		
-3050	58.9	3851.9				0.343		
-3050	57.5	3850.5				0.343		
-3050	56.1	3849.1				0.343		
-3050	54.6	3847.6				0.343		
-3050	53.2	3846.2				0.343		
-3050	51.8	3844.8				1.371		
-3050	50.4	3843.4				0.343		
-3050	49.0	3842.0				7.543		
-3050	47.6	3840.6				0.343		
CDH-35								
-3070	190.0	3865.0				1.029		
-3070	190.0	3860.0				6.171		
-3070	218.6	3856.6				0.343		
-3070	217.2	3855.2				0.343		
-3070	215.8	3853.8				0.343		
-3070	214.3	3852.3				0.343		
-3070	212.9	3850.9				0.343		
-3070	211.5	3849.5				0.343		
-3070	210.1	3848.1				0.343		
-3070	208.7	3846.7				0.343		
-3070	207.3	3845.3				0.343		
-3070	205.9	3843.9				0.343		
-3070	204.4	3842.4				0.343		
-3070	203.0	3841.0				0.343		
-3070	201.6	3839.6				0.343		
-3070	200.2	3838.2				0.343		
-3070	198.8	3836.8				2.400		
-3070	197.4	3835.4				1.371		
-3070	196.0	3834.0				1.714		
-3070	194.5	3832.5				1.371		
CDH-37								
-3135	168.6	3861.6				0.343		
-3135	167.2	3860.2				0.343		
-3135	165.8	3858.8				0.343		
-3135	164.3	3857.3				0.343		
-3135	162.9	3855.9				0.343		
-3135	161.5	3854.5				0.343		
-3135	160.1	3853.1				0.343		
-3135	158.7	3851.7				0.343		
-3135	157.3	3850.3				0.343		

COORDINATE			ALTERATION			VALUE		RATIO
NS	EW	ELEV	TYPE	ALT	MIN	AUppm	AGppm	AU/AG
-3135	155.9	3848.9				0.343		
-3135	154.4	3847.4				0.343		
-3135	153.0	3846.0				0.343		
-3135	151.6	3844.6				0.343		
-3135	150.2	3843.2				0.686		
-3135	148.8	3841.8				0.343		
-3135	147.4	3840.4				0.000		
-3135	146.0	3839.0				0.343		
-3135	144.5	3837.5				0.343		
-3135	143.1	3836.1				0.343		
-3135	141.7	3834.7				0.343		
-3135	140.3	3833.3				0.343		
-3135	138.9	3831.9				0.343		
-3135	137.5	3830.5				0.000		
-3135	136.1	3829.1				0.343		
-3135	134.6	3827.6				0.343		
-3135	133.2	3826.2				0.343		
-3135	131.8	3824.8				0.343		
-3135	130.4	3823.4				0.343		
-3135	129.0	3822.0				0.000		
-3135	127.6	3820.6				0.000		
CDH-38								
-3169	218.6	3851.6				1.371		
-3169	217.2	3850.2				0.343		
-3169	215.8	3848.8				0.343		
-3169	214.3	3847.3				0.343		
-3169	212.9	3845.9				13.029		
-3169	211.5	3844.5				8.229		
-3169	210.1	3843.1				2.400		
-3169	208.7	3841.7				0.686		
-3169	207.3	3840.3				2.057		
-3169	205.9	3838.9				0.686		
-3169	204.4	3837.4				0.686		
-3169	203.0	3836.0				0.686		
-3169	201.6	3834.6				0.686		
-3169	200.2	3833.2				0.343		
-3169	198.8	3831.8				0.686		
-3169	197.4	3830.4				0.343		
-3169	196.0	3829.0				0.343		
-3169	194.5	3827.5				0.343		
-3169	193.1	3826.1				0.343		
-3169	191.7	3824.7				0.343		
-3169	190.3	3823.3				0.000		
-3169	188.9	3821.9				0.000		
-3169	187.5	3820.5				3.771		
-3169	186.1	3819.1				0.000		
-3169	184.6	3817.6				0.343		
-3169	183.2	3816.2				0.343		
-3169	181.8	3814.8				0.343		
-3169	180.4	3813.4				0.686		

COORDINATE			ALTERATION			VALUE		RATIO
NS	EW	ELEV	TYPE	ALT	MIN	AUppm	AGppm	AU/AG
-3169	179.0	3812.0				0.343		
-3169	177.6	3810.6				1.029		

COORDINATE			ALTERATION			VALUE		RATIO
NS	EW	ELEV	TYPE	ALT	MIN	AUppm	AGppm	AU/AG
-3004	169.7	3864.7				0.343		
-3004	170.8	3863.3				0.343		
-3004	171.8	3861.9				0.343		
-3004	172.9	3860.4				0.343		
-3004	174.0	3859.0				0.686		
-3004	175.1	3857.6				0.343		
-3004	176.2	3856.2				0.343		
-3004	177.3	3854.8				0.343		
-3004	178.3	3853.4				4.800		
-3004	179.4	3852.0				20.229		
-3004	180.5	3850.5				1.029		
-3004	181.6	3849.1				1.029		
-3004	182.7	3847.7				0.686		
-3004	183.8	3846.3				1.029		
-3004	184.8	3844.9				0.343		
-3004	185.9	3843.5				4.800		
-3004	187.0	3842.1				1.714		
-3004	188.1	3840.6				0.686		
-3004	189.2	3839.2				0.686		
-3004	190.3	3837.8				0.343		
-3004	191.3	3836.4				0.686		
-3004	192.4	3835.0				0.686		
-3004	193.5	3833.6				1.029		
CDH-29								
-3021	179.1	3872.6	Hw	0	0	0.343		
-3021	180.2	3871.2	Hw	0	0	1.371		
-3021	181.3	3869.8	Hw	0	0	0.686		
-3021	182.3	3868.3	Hw	0	0	0.686		
-3021	183.4	3866.9	Hw	0	0	0.686		
-3021	184.5	3865.5	Hw	0	0	0.343		
-3021	185.6	3864.1	Hw	0	0	0.686		
-3021	186.7	3862.7	Hw	0	0	0.000		
-3021	187.8	3861.3	Hw	0	0	1.371		
-3021	188.8	3859.9	Hw	0	0	0.343		
-3021	189.9	3858.4	Hw	0	0	0.343		
-3021	191.0	3857.0	Hw	0	0	0.343		
-3021	192.1	3855.6	Hw	0	0	0.343		
-3021	193.2	3854.2	Hw	0	0	0.343		
-3021	194.3	3852.8	Hw	0	0	0.343		
-3021	195.3	3851.4	Bx	QSP	0	0.686		
-3021	196.4	3850.0	Vn	0	Qfn	10.286		
-3021	197.5	3848.5	Vn	QSP	Qfnp	21.257		
-3021	198.6	3847.1	Fw	0	Qfnp	14.743		
-3021	199.7	3845.7	Vn	QC	Qfn	9.943		
-3021	200.8	3844.3	Bx	Ain	Qfn	4.457		
-3021	201.8	3842.9	Fw	Pin	Qvg	2.743		
-3021	202.9	3841.5	Fw	Pout	Qvg	2.057		
-3021	204.0	3840.1	Fw	Pout	0	2.400		
-3021	205.1	3838.6	Fw	Pout	0	0.686		
-3021	206.2	3837.2	Fw	Pout	0	0.343		

COORDINATE			ALTERATION			VALUE		RATIO
NS	EW	ELEV	TYPE	ALT	MIN	AUppm	AGppm	AU/AG
-3021	207.3	3835.8	Fw	Pout	0	2.400		
-3021	208.3	3834.4	Fw	Pout	0	0.686		
-3021	209.4	3833.0	Fw	Pout	0	0.343		
-3021	210.5	3831.6	Fw	Pout	0	0.343		
CDH-31								
-3024	136.0	3879.0				16.457		
-3024	136.0	3874.0				16.800		
CDH-33								
-3038	196.1	3868.6	Hw	Pout	0	0.343		
-3038	197.2	3867.2	Hw	Pout	0	0.343		
-3038	198.3	3865.8	Hw	Pout	0	0.343		
-3038	199.3	3864.3	Hw	Pout	0	0.000		
-3038	200.4	3862.9	Hw	Pout	0	0.343		
-3038	201.5	3861.5	Hw	Pout	0	0.686		
-3038	202.6	3860.1	Hw	Pout	0	1.029		
-3038	203.7	3858.7	Hw	Pout	0	0.343		
-3038	204.8	3857.3	Hw	Pout	0	0.343		
-3038	205.8	3855.9	Hw	Pout	0	0.343		
-3038	206.9	3854.4	Bx	QSP	Qvg	6.171		
-3038	208.0	3853.0	Fw	Aout	Qvgp	0.686		
-3038	209.1	3851.6	Fw	QSP	Qvg	1.029		
-3038	210.2	3850.2	Fw	0	Qfn	4.457		
-3038	211.3	3848.8	Vn	0	Qfnp	2.400		
-3038	212.3	3847.4	Vn	0	Qfn	9.943		
-3038	213.4	3846.0	Fw	Aout	Qfnp	4.457		
-3038	214.5	3844.5	Fw	Aout	Qfn	2.400		
-3038	215.6	3843.1	Fw	0	0	3.429		
-3038	216.7	3841.7	Fw	0	0	2.743		
-3038	217.8	3840.3	Fw	0	0	1.029		
-3038	218.8	3838.9	Fw	0	0	0.686		
-3038	219.9	3837.5	Fw	0	0	1.029		
-3038	221.0	3836.1	Fw	0	0	2.057		
-3038	222.1	3834.6	Fw	0	0	2.743		
-3038	223.2	3833.2	Fw	0	0	3.086		
-3038	224.3	3831.8	Fw	0	0	2.400		
-3038	225.3	3830.4	Fw	0	0	1.029		
-3038	226.4	3829.0	Fw	0	0	0.686		
-3038	227.5	3827.6	Fw	0	0	1.714		
CDH-34								
-3050	88.6	3881.6				0.686		
-3050	87.2	3880.2				0.000		
-3050	85.8	3878.8				0.000		
-3050	84.3	3877.3				0.000		
-3050	82.9	3875.9				0.343		
-3050	81.5	3874.5				0.343		
-3050	80.1	3873.1				0.343		
-3050	78.7	3871.7				0.343		
-3050	77.3	3870.3				0.343		
-3050	75.9	3868.9				0.343		
-3050	74.4	3867.4				0.343		